Génération de lumière paramétrique infrarouge : des cristaux aux dispositifs

Vincent Kemlin

UNIVERSITÉ DE GRENOBLE

THÈSE

Pour obtenir le grade de

DOCTEUR DE L'UNIVERSITÉ DE GRENOBLE

Spécialité : **OPTIQUE ET RADIOFREQUENCES**

Arrêté ministériel : 7 août 2006

Présentée par

Vincent KEMLIN

Thèse dirigée par **Benoît BOULANGER** et **Patricia SEGONDS**

préparée au sein de **l'Institut Néel**
dans **l'École Doctorale EEATS**

Parametric infrared generation : from crystals to devices

Thèse soutenue publiquement le **12 juillet 2013**,
devant le jury composé de :

Monsieur Emmanuel ROSENCHER
Professeur à l'Ecole Polytechnique, Président
Monsieur Fabien BRETENAKER
Directeur de Recherches au Laboratoire Aimé Cotton, Rapporteur
Monsieur Valentin PETROV
Chercheur au Marx Born Institute, Rapporteur
Monsieur Takunori TAIRA
Professeur à l'Institute for Molecular Science, Examinateur
Monsieur Gabriel MENNERAT
Ingénieur au CEA Saclay, Examinateur
Madame Patricia SEGONDS
Professeur à l'Université de Grenoble, Directrice de thèse
Monsieur Benoît BOULANGER
Professeur à l'Université de Grenoble, Directeur de thèse

REMERCIEMENTS

C'est par cette traditionnelle section des remerciements que s'achève la rédaction de ma thèse et ainsi ces trois années riches en émotions. Des émotions, il y en a eu jusqu'à la fin... C'est ainsi que je souhaite souligner ici la mémoire d'Emmanuel Rosencher, dont le décès brutal survenu le 15 juin 2013 a laissé un grand vide dans la communauté scientifique française et en particulier celle de l'optique non-linéaire. J'ai eu l'immense privilège d'assister au cours d'optronique d'Emmanuel au cours de l'année scolaire 2007-2008. Et comme beaucoup d'autres de ses anciens élèves, j'ai moi aussi succombé à la vocation scientifique qu'il savait si bien faire naitre en ses auditeurs. A l'époque, j'ignorais encore tout des équations des modes couplés... Mais il faut croire que la passion avec laquelle Emmanuel parlait de cette "boite à outils" était si communicative que j'ai fini par faire une thèse sur le sujet. Je n'oublierai pas de sitôt cette formule si caractéristique des liens qu'il tissait entre le savoir fondamental et les application technologiques : "Sachez que les photons cela se vend cher". Il est quasiment certain que je n'aurais jamais effectué une thèse en optique non-linéaire si je n'avais pas rencontré cet immense professeur, passeur de savoir et semeur de vocations. Je tiens à remercier chaudement M. Michel Lefebvre non seulement pour sa présence et sa participation à mon jury soutenance mais aussi pour l'hommage qu'il a rendu à Emmanuel Rosencher à cette occasion.

Je tiens à remercier non moins chaleureusement les deux rapporteurs de mes travaux de thèse Valentin Petrov et Fabien Bretenaker pour leur relecture avisée et leurs remarques sans concessions... Je m'excuse par là même de leur avoir fait subir les hésitations de ma "prose" en anglais, et le détail de calculs parfois barbares. Je remercie M. Takunori Taira de m'avoir honoré de sa présence malgré les milliers de kilomètres qui séparent Grenoble et Okazaki. Enfin, j'aimerais souligner le rôle de M. Gabriel Mennerat dans toute cette aventure. Sa thèse est une "bible" à mettre en toutes les mains de jeune thésard en optique non-linéaire, et la source qu'il a conçue il y a une dizaine d'années fut le point de départ de notre travail. Je le remercie d'avoir bien voulu présider mon jury de soutenance. Enfin, comment souligner assez le rôle de Patricia Segonds et Benoit Boulanger durant ces trois années ? Ils sont le Yin et le Yang du groupe d'optique paramétrique de l'Institut Néel : aussi différents qu'indivisibles... Je leur suis infinement reconnaissant pour la qualité de leur encadrement au jour le jour et sur le long terme. Malgré leurs visions parfois opposées d'un même problème, Patricia et Benoit partagent un même enthousiasme pour la recherche et pour l'optique cristalline linéaire et non-linéaire. Ils ont su m'accorder leur confiance et me permettre de monter une manip' ce qui est assez rare pour un thésard.

J'ai eu la chance de monter cette manip' grâce au soutien précieux de Jérôme Debray et David Jegouso. Jérôme m'a transmis beaucoup des subtilités de l'orientation et du polissage des cristaux en cubes ou en cylindres. J'ai appris lors de ces longues heures de polissage/nettoyage/observation sous la bino le prix d'un piqûre laser sur un cristal. Je suis maintenant persuadé que c'est en polissant qu'on devient un bon padawan en optique non-linéaire. Merci Jérôme pour les instants passés dans cette bonne vieille salle de polissage. Je reviens dans la nouvelle salle quand tu veux ! Mais c'est bien en salle de manipe que se déroulent les principales épreuves pour passer chevalier Jedi en optique non-linéaire. Heureusement, c'est avec David que nous les avons passées les unes après les autres. Des cylindres coniques, aux piqûres intracavités en passant par les mesures au

“spectro blanc” travailler ensemble restera comme un excellent souvenir et un réel plaisir ! Cela va me manquer. Bon courage pour la suite, et bienvenue au bébé ! Plus largement, ce sont les pôles “Cristaux massifs” et “Optique” de l’Institut Néel que je remercie pour leur soutien, et en particulier Corinne et Bertrand. Je souhaite également mentionner la contribution de Hideki Ishizuki qui a accepté de me prendre sous son aile lors de mon passage express à l’Institute for Molecular Science. Ses échantillons géants de PPLN furent un élément décisif de la source que nous avons construite. Enfin, merci à l’équipe DMPH de l’ONERA pour leur accueil et leur soutien pas seulement logistique. Antoine, Myriam et Jean-Michel, j’espère qu’on aura l’occasion de retravailler ensemble.

Mention spéciale évidemment à Sandra, catalane préférée de tout MCMF. Je vous conseille ses tortillas qu’elle cuisine avec son énergie et sa bonne humeur caractéristiques. Evidemment, mieux vaut en manger un soir de victoire du Barça avec Simone, Julien et Stéphanie : c’est encore meilleur ! Un grand merci aux thésards de MCMF : Pierre, Julien, Marcio, Issam, Audrey, Marta, Damien, Emmanuelle, Anne, Mehdi, Adrien, Joséphine, Sophie et Denis pour les chouettes souvenirs comme le kayak en Ardèche ou les soirées à la Bobine. Je ne résiste pas à quelques clins d’oeil très non-linéaires en souvenir de l’OPOlette, des blagues perchées tout en haut de l’échelle, des franches rigolades, de l’Ecosse, de Lady Gaga (“because she is the best”) et du wiki de Patou censuré... Et j’en profite pour souhaiter une très bonne chance à Elodie et à Quentin qui ont déjà pris le relai des manipes infrarouges. La relève est bien assurée !

Je tiens à remercier enfin toute ma famille pour leur présence et leur amour. J’ai la chance de pouvoir témoigner ici toute mon affection et mon admiration à mes quatre grands-parents Guy et Brigitte, Geneviève et Alain. Merci à eux pour toute leur tendresse et leur générosité. Evidemment merci à mes parents, et à mes frères et soeurs Amélie, Guillaume, Claire et Delphine. Je vous aime. Last but not least : mes derniers remerciements seront évidemment pour Cécile, ma Cécile. Malgré la distance, l’internat, les canalisations et les coups de pression elle a tout suivi de ces trois années. De la Corse au Lac du Crozet, de Istanbul aux calanques de Cassis, de Londres à Paris, de la Bourgogne à Barcelone : la route ensemble est déjà belle. J’espère qu’elle sera encore longue !

CONTENTS

INTRODUCTION

Nonlinear optics has been an exciting field of research for more than 50 years triggered by the invention of the laser in 1961, which brought together the fields of parametric oscillation and optics thanks to unprecedented light powers. One of the main interest in parametric light stems from the fact that it combines some of the most desirable features of laser light such as a good coherence or a high brightness with the possibility to access wavelength ranges where no laser sources are available. In this dissertation, the infrared part of the electromagnetic spectrum will be our main focus, and we will consider wavelengths ranging from 1 to about 12 µm. There are two main reasons that drive the search for intense and coherent light sources in this part of the spectrum. The first reason comes from the transmission spectrum of the atmosphere of Earth shown on Figure (1). Our atmosphere is essentially a mixture of oxygen and nitrogen but these are the traces gases such as carbon dioxide or water vapor that contribute mostly to its transmission in the infrared: its spectrum can be split into three main transmission bands called Band I, II and III (see Figure 1). In this work, we will be interested in Band II and Band III of transmission that extend respectively from 3 to 5 µm, and from 8 to 12 µm. Coherent sources in these ranges are highly desired since they can potentially lead to faster communications. On the other hand, the infrared part of the spectrum is also the kingdom of spectroscopy where rovibrational movements of molecules and bonds can be easily probed. Thanks to specific absorption bands of chemical bonds, one of the most common applications of infrared spectroscopy is the identification of chemical species. Figure (1) shows the absorption bands of the main organic and amide compounds. Intense sources in these specific ranges have already triggered important innovations in the fields of selective chemical microscopy, mixture analysis or infrared differential absorption lidar measurements [1]. The superiority of parametric sources over laser sources can be seen from the wide tunability that can be theoretically obtained with frequency converter devices.

The first observation of frequency conversion was Second Harmonic Generation of a ruby laser in a quartz crystal in 1961. It gave an early glimpse of how future progress in frequency converter devices would be irreparably tied to advances in both fields of lasers and materials science. Parametric infrared generation has been no exception since that day. Historically speaking, two lasers have had a tremendous impact on the search for new nonlinear infrared crystals. First of all, Second Harmonic Generation of the CO_2 laser emitting around 10 µm has long been regarded as a prerequisite to the decision of developing a new nonlinear crystal. This criterion has led to the identification of a few crystals such as $ZnGeP_2$, $AgGaSe_2$, $AgGaS_2$ that are now commercially available. On the other hand this criterion of Second Harmonic Generation of the CO_2 laser can prove limited either because this frequency conversion is impossible in some crystals (including CdSe), or simply because high intensity CO_2 lasers are not widely available.

The most widely spread laser in the near infrared is undoubtedly the Nd:YAG laser emitting at 1.064 µm, and a specific focus has then been put on the search for infrared materials allowing an efficient parametric conversion of laser wavelengths close to 1 µm [5]. However limited success in *direct* generation of wavelengths above 8 µm has been seen so far, so that laser materials doped with other rare earth ions, such as Ho^{3+}, Tm^{3+} or Er^{3+} or transition metal ions such as Cr^{2+}

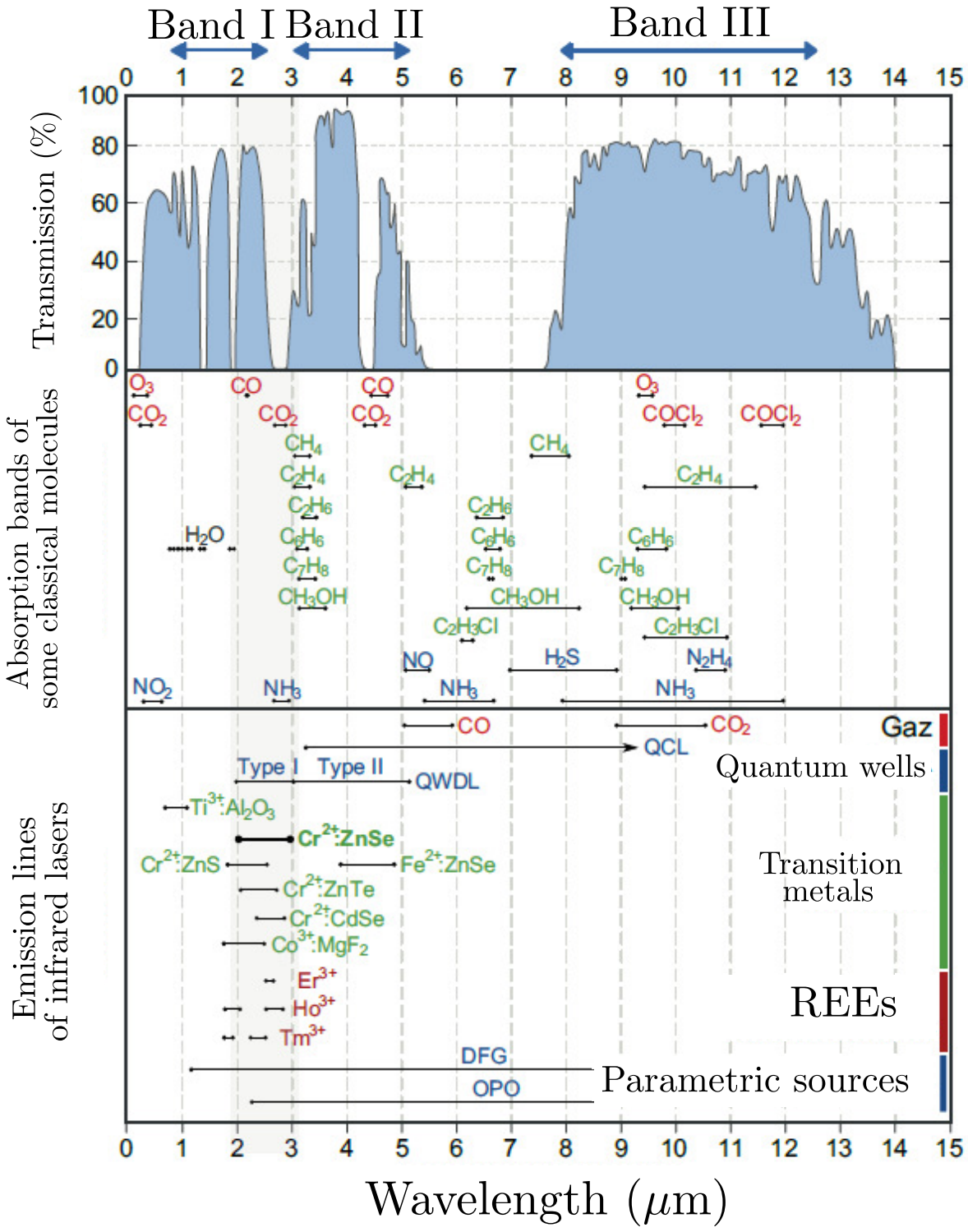

Figure 1: Illustration of the two main applications of intense coherent infrared sources and of the main laser infrared sources. This graph is taken from [2], after [3]and [4].

have been developped providing new lasers emitting at specific wavelengths in the range 2-3 µm (see [6] and Figure 1). These lasers are expected to play a key role in the generation of longer infrared wavelengths in the future. On the other hand, it is interesting to notice that despite these recent developments, there are still several nonlinear crystals with giant nonlinearities and wide transmission windows in the infrared such as $CdGeAs_2$, Te, Se that remain underused mostly because of a lack of adequate laser sources for pumping or characterization above 3 µm [5]. We advocate in this work that the search for new nonlinear infrared materials is still highly desirable not only for fundamental but also for practical reasons. However, as Optical Parametric Oscillation can hardly be demonstrated at the early stages of the development of a new crystal because of the small sizes necessarily obtained in the very first growth attempts, it is the underlying stance of this dissertation that exploratory search, early identification and better characterizations of new and small-sized nonlinear infrared crystals requires the development of better analytical as well as experimental tools. As a consequence, this dissertation falls at the interface between the fields of materials science and that of parametric nonlinear optics.

The first Part of this work provides some theoretical background on frequency conversion in nonlinear crystals. A classical picture of Optical Parametric Oscillation (OPO) and Difference Frequency Generation (DFG) is given. These two processes both involve the fission of a photon and can therefore lead to the generation of parametric light at longer wavelengths. However, a high degree of synchronism between the interacting waves in the crystal is necessary to generate such new wavelengths. An extensive comparison is provided between Birefringent Phase-Matching and Quasi-Phase-Matching, which are the two main methods that have been developed to force a photon to fission. Emphasis is put on the versatility of the Quasi-Phase-Matching technique [7] for the generation of tunable coherent radiation in the infrared.

The second Part of this work deals with the new chalcopyrite material $CdSiP_2$. Its unique phase-matching properties have been characterized using the sphere method. Contrary to $ZnGeP_2$ or $AgGaS_2$ that belong to the same family, this material is better suited for pumping with a Nd:YAG laser at 1.064 µm. In this work, we use the unique measurements of the phase-matching angles of this crystal and strive to determine its principal refractive indices with the uttermost accuracy required by the phase-matching conditions. An unusual quantitative analysis relating the accuracy of the measurements of the refractive indices of a crystal to that of the calculations of the phase-matching angles is provided. We believe that this analysis comes to fill a gap in the field of phase-matching metrology.

The two following Parts III and IV are then devoted to the design of an all-parametric source dedicated to fundamental studies of the phase-matching properties of mid to far-infrared nonlinear crystals. We first deal with the experimental realization of a widely and continuously tunable OPO that will be the cornerstone of the parametric source described in the final Part IV. This OPO is based on a 5-mm-thick crystal of 5%MgO:PPLN cut and polished to optical quality as a partial cylinder. World record conversion efficiencies for a cylindrical device as well as wide and continuous tunability from 1.4 up to 4.4 µm have been obtained. This device is perfectly suited for

applications in Band II of transmission of the atmosphere, as shown on Figure (1), but because of the limited transparency range of the crystal, generation of infrared coherent radiation in Band III is not possible with only one such device.

It is the purpose of Part IV to present how the combination of two such devices can be advantageously used to generate a tunable radiation in Band III. We have built a second partial cylinder OPO similar to the one described in Part III, so that when the two OPOs are pumped in *parallel* and with the same Nd:YAG laser, we dispose of a unique dual wavelength source with two independently and widely tunable beams. This is a unique and highly desirable feature of a dual wavelength source for characterizing new nonlinear infrared crystals since any parametric interaction between two beams between 1.4 and 4.4 microns can be foreseen. In this work, we used our source to perform DFG experiments in Band III between two beams independently tunable between 2.5 and 4.4 µm. Two different experiments have been carried out in CdSe crystals and confirmed the potentiality of our source. The many promises held by such a dual wavelength source will be stressed.

Parametric sources between 2 and 5 µm have now reached such a high degree of maturity [6, 7] that we find them better suited than solid-state lasers to match the requirements of new characterization tools of nonlinear crystals in the mid to far infrared.

Part I

ELEMENTS OF THEORY

INTRODUCTION

In this part, we consider the classical interaction between an electric field and a second order nonlinear medium. At high enough intensities, the electronic polarization induced in a material depends nonlinearly on the electric field, so that its spectrum includes additional "new" frequencies. In the general case, these new frequencies cannot be radiated efficiently: a constructive interference between the nonlinear polarization and the electric field it radiates is necessary to ensure an efficient generation or amplification of an optical wave. In this dissertation, we are essentially interested in the generation of optical waves in the infrared part of the electromagnetic spectrum through a three-wave mixing process, and the Difference Frequency Generation (DFG) process is our main focus.

In the first chapter, the linear and nonlinear polarizations induced in uniaxial crystals are derived. The electric field radiated by the second-order nonlinear polarization is then obtained as the solution of the Maxwell's equations. The resulting coupled equations governing the amplitudes of each Fourier component of the electric field are figured out. The phase velocities of the second-order nonlinear polarization and of the radiated electric field must be matched to ensure an efficient three-wave parametric mixing process. And in the second chapter, we discuss two different strategies that will ensure the efficient generation or amplification of a wave at a given optical frequency. Historically, the first strategy has been birefringent phase matching (BPM) where the required constructive interference is obtained in an anisotropic material: the dispersion is exactly compensated by the birefringence of the material in the considered direction of propagation. The second scheme is called quasi-phase matching (QPM): through a proper modulation of the sign of the non-linearity inside the material, the efficient growth of a new optical wave can be obtained even if the phase velocities are not matched. The solution of the coupled equations is given for typical DFG processes in each case. The advantages of QPM over BPM are also discussed.

Even if the phase matching condition is fulfilled, DFG conversion efficiencies in nonlinear crystals are often still low, and the third chapter is dedicated to the phenomenon of Optical Parametric Oscillation (OPO) that overcomes this limitation. Actually, the resonance of one of the newly generated wave leads to an "artificial" increase of the interaction length in the nonlinear crystal. Provided the nonlinear gain is high enough to compensate for the losses of the cavity, pump photons are efficiently converted into two photons with lower energies. OPOs are therefore very interesting devices when new wavelengths in the infrared must be efficiently generated. It is the advent of QPM materials that has contributed to a renewed interest in OPO devices.

1

PARAMETRIC THREE WAVE MIXING

1.1 CLASSICAL TREATMENT

We consider in this section the polarization induced by an electric field in a noncentrosymmetric crystal. The electric field is real and assumed to be the superposition of three waves at frequencies ω_1, ω_2 and ω_3 . It writes:

$$\vec{\mathcal{E}}(\vec{r},t) = \sum_{n=1,2,3} \vec{\mathbf{E_n}}(\vec{r},t) \tag{1}$$

where

$$\overrightarrow{\mathbf{E_n}}(\overrightarrow{r},t) = \mathcal{R}e(\vec{\mathbf{E}}(r,\omega_n)e^{j\omega_n t}) = \frac{1}{2}(\vec{\mathbf{E}}(r,\omega_n)e^{j\omega_n t} + \vec{\mathbf{E}}(r,\omega_n)^* e^{-j\omega_n t}) \tag{2}$$

with

$$\vec{\mathbf{E}}(r,-\omega_n) = \vec{\mathbf{E}}(r,\omega_n)^* \tag{3}$$

The spectrum of the full electric field is therefore made of six terms at the circular frequencies $\pm\omega_1$, $\pm\omega_2$ and $\pm\omega_3$.

Besides, the time dependent polarization induced by the electric field is assumed to be written [8] under the form :

$$\begin{aligned}
\vec{\mathcal{P}}(\vec{r},t) =& \varepsilon_0 \int_{-\infty}^{+\infty} \underline{R^{(1)}}(\tau_1) : \vec{\mathcal{E}}(\vec{r},t-\tau_1)d\tau_1 \\
&+ \varepsilon_0 \int_{-\infty}^{+\infty}\int_{-\infty}^{+\infty} \underline{\underline{R^{(2)}}}(\tau_1,\tau_2) \therefore \vec{\mathcal{E}}(\vec{r},t-\tau_1) \otimes \vec{\mathcal{E}}(\vec{r},t-\tau_2)d\tau_1 d\tau_2 \\
&+ ... \\
&+ \varepsilon_0 \int_{-\infty}^{+\infty}\int_{-\infty}^{+\infty} \underline{\vdots} \, \underline{R^{(n)}}(\tau_1,...,\tau_n) : \vec{\mathcal{E}}(\vec{r},t-\tau_1) \otimes ... \otimes \vec{\mathcal{E}}(\vec{r},t-\tau_n)d\tau
\end{aligned} \tag{4}$$

where $R^{(n)}$ are n+1 order tensors fulfilling the causality condition and describing the nth order impulse response of the material.

By combining the Maxwell's equations, one finds the Helmholtz equation (5) satisfied by the electric field in a nonmagnetic and lossless medium. The polarization term $\vec{\mathcal{P}}$ given in Equation (4) acts like a source term of the electric field $\vec{\mathcal{E}}$:

$$\nabla^2\vec{\mathcal{E}} - \frac{1}{c^2}\frac{\partial^2\vec{\mathcal{E}}}{\partial t^2} = \mu_0\frac{\partial^2\vec{\mathcal{P}}}{\partial t^2} \tag{5}$$

By taking the Fourier Transform of Equation (4), one can get the Fourier components of the polarization induced in the material by the electric field at any pulsation $\omega \in \mathbb{R}^+$(see Equation 3):

$$\vec{\mathbf{P}}(\vec{r},\omega) = \vec{\mathbf{P^{(1)}}}(\vec{r},\omega) + \vec{\mathbf{P^{(2)}}}(\vec{r},\omega) + ... + \vec{\mathbf{P^{(n)}}}(\vec{r},\omega) \tag{6}$$

The first order term $\vec{\mathbf{P^{(1)}}}$ is the linear electronic polarization, while the $\vec{\mathbf{P^{(n)}}}$ components constitute the nth-order nonlinear electronic polarizations. In the Fourier domain, Equation (5) yields the partial derivative equation governing the amplitude of each Fourier component of the electric field :

$$\forall\omega \in \mathbb{R}^+, \nabla^2\vec{\mathbf{E}}(\vec{r},\omega) + \frac{\omega^2}{c^2}\vec{\mathbf{E}}(\vec{r},\omega) = \frac{-\omega^2}{c^2\varepsilon_0}\vec{\mathbf{P}}(\vec{r},\omega) \tag{7}$$

1.1.1 *Linear optics in uniaxial crystals*

The first order Fourier component of the polarisation at ω is given by a linear term in the electric field component :

$$\vec{\mathbf{P^{(1)}}}(\vec{r},\omega) = \varepsilon_0 \underline{\chi}^{(1)}(\omega).\vec{\mathbf{E}}(\vec{r},\omega) \tag{8}$$

We have introduced the first order susceptibility tensor $\underline{\chi^{(1)}}(\omega)$, which is the Fourier Transform of the first order impulse response of the material. The real and imaginary parts of this tensor describe the linear properties, propagation as well as absorption phenomena respectively, of an electromagnetic wave at the circular frequency ω in the material. Formula (8) shows that the spectrum of the electric field is necessarily the same as the spectrum of the linear polarization.

In the linear case, the Helmholtz equation reduces to:

$$\forall \omega \in \mathbb{R}^+, \nabla^2 \vec{\mathbf{E}}(\vec{r},\omega) + \frac{\omega^2}{c^2}(\underline{1} + \underline{\chi}^{(1)}(\omega))\vec{\mathbf{E}}(\vec{r},\omega) = 0 \tag{9}$$

The number of independent eigenvalues of the relative dielectric permittivity tensor $\underline{\epsilon_r}(\omega) = \underline{1} + \underline{\chi}^{(1)}(\omega)$ sets the optical class of the crystal: for a triply degenerate eigenvalue, the crystal is isotropic; for two eigenvalues, one of which being degenerate, the crystal belongs to the uniaxial class; and for three independent eigenvalues, the crystal belongs to the biaxial class. The optical class of a crystal is set by its crystalline symmetry [8]. In this dissertation we will be dealing with crystals belonging to the uniaxial class only. For uniaxial crystals, the (x, y, z) optical frame, also called the dieletric frame, is the frame where the susceptibility and dielectric permittivity tensors are both diagonal. In this frame, the x and y axis are equivalent while z is called the optical axis of the crystal. And $\underline{\epsilon_r}(\omega)$ writes:

$$\underline{\epsilon_r(\omega)} = \begin{pmatrix} 1+\chi_{xx}(\omega) & 0 & 0 \\ 0 & 1+\chi_{xx}(\omega) & 0 \\ 0 & 0 & 1+\chi_{zz}(\omega) \end{pmatrix} \tag{10}$$

For a lossless medium, this tensor is real. We can then define two principal refractive indices $n_o(\omega)$, the ordinary index, and $n_e(\omega)$, the extraordinary index through

$$n_o^2(\omega) = 1 + \chi_{xx}(\omega) \tag{11}$$

and

$$n_e^2(\omega) = 1 + \chi_{zz}(\omega) \tag{12}$$

If $n_e > n_o$ the uniaxial is said to be positive, and if $n_e < n_o$, it is said to be negative. For an arbitrary direction of propagation $\vec{u}(\theta, \phi)$,

$$\vec{u}(\theta, \phi) = \begin{pmatrix} \sin\theta\cos\phi \\ \sin\theta\sin\phi \\ \cos\theta \end{pmatrix} \tag{13}$$

where θ and ϕ are the angles of spherical coordinates in the optical frame, the refractive index of a wave at the circular frequency ω can then take two different values given by:

$$\begin{cases} n_o(\omega, \theta, \phi) = n_o(\omega) \\ n_e(\omega, \theta, \phi) = (\dfrac{\cos^2\theta}{n_o^2(\omega)} + \dfrac{\sin^2\theta}{n_e^2(\omega)})^{-1/2} \end{cases} \tag{14}$$

The ordinary index n_o corresponds to an ordinary polarized wave, meaning that its direction of polarization $\vec{e_o}$ is always perpendicular to the optical axis z and to the Poynting vector $\vec{\Pi}_o$. The extraordinary index is that of a wave whose polarization vector $\vec{e_e}$ is perpendicular to $\vec{e_o}$, and to the Poynting vector $\vec{\Pi}_e$ but not to the z-axis. When an extraordinary polarized wave propagates in a direction $\vec{u}(\theta, \phi)$ with $\theta \neq 0°$ or $\theta \neq 90°$, the Poynting vector $\vec{\Pi}_e$ and the wavevector $\vec{k_e}$ are not parallel: there exists an angle called the walk-off angle between them. This angle ρ is given in [9]. For positive uniaxial crystals, it writes:

$$\rho^+(\theta, \omega) = \theta - \arctan(\frac{n_o^2(\omega)}{n_e^2(\omega)}\tan(\theta)) \tag{15}$$

For negative uniaxial crystals, it writes:

$$\rho^-(\theta, \omega) = \arctan(\frac{n_o^2(\omega)}{n_e^2(\omega)}\tan(\theta)) - \theta \tag{16}$$

The magnitude of this angle increases with the birefringence $(n_e - n_o)$ of a material. It is the highest for $\theta = 45°$ and vanishes for $\theta = 0°$ or $\theta = 90°$. The direction of polarisation of ordinary and extraordinary waves can then be expressed in the spherical coordinates linked to the optical frame through :

$$\begin{aligned} \vec{e_o} &= \begin{pmatrix} -\sin\phi \\ \cos\phi \\ 0 \end{pmatrix} \\ \vec{e_e} &= \begin{pmatrix} -\cos(\theta \pm \rho^{\mp}(\theta))\cos\phi \\ -\cos(\theta \pm \rho^{\mp}(\theta))\sin\phi \\ \sin(\theta \pm \rho^{\mp}(\theta)) \end{pmatrix} \end{aligned} \tag{17}$$

where $-\rho^+$ must be used for the positive class, and $+\rho^-$ for the negative class [8]. The fact that an extraordinary and an ordinary wave propagating in a uniaxial crystal at $\theta = 90°$ from

the optical axis are not spatially separated has very important consequences in nonlinear optics and leads to angular noncritical phase-matching (see section 2.1.3). Otherwise, such two waves will be spatially separated after a length that depends on the size of the beams and conditions of focalisation which eventually limits the conversion efficiency of a three-wave mixing process.

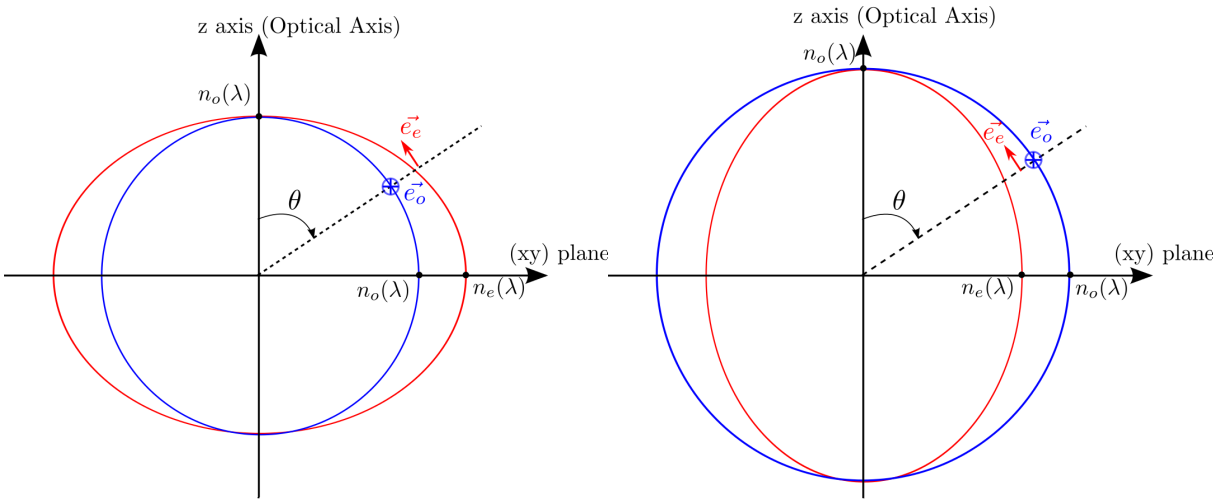

(a) Positive uniaxial crystals

(b) Negative uniaxial crystals

Figure 2: Index surface of uniaxial crystals.

The ordinary and extraordinary layers of the index surfaces are sketched in Figure (2) for optically positive and negative uniaxial crystals, based on Equations (14). The ordinary surface is spherical whereas the extraordinary surface is elliptical. These two surfaces intersect along the optical axis z and the crystal is optically isotropic along this direction of propagation.

1.1.2 *Nonlinear polarization*

Generally speaking, when two waves at ω_1 and ω_2 are incident upon the crystal the new circular frequencies of the nonlinear polarization can be $0\,(=\omega_1-\omega_1=\omega_2-\omega_2)$, $2\omega_1\,(=\omega_1+\omega_1)$, $2\omega_2\,(=\omega_2+\omega_2)$, $\omega_{SFG}=\omega_1+\omega_2$ and $\omega_{DFG_1}=\omega_2-\omega_1$, $\omega_{DFG_2}=\omega_2-\omega_1$. These six angular frequencies correspond respectively to six different physical processes of three-wave mixing: Optical Rectification, Second Harmonic Generation of the wave at ω_1, Second Harmonic Generation of the wave at ω_2, Sum Frequency Generation (SFG) between the wave at ω_1 and the wave at ω_2, and Difference Frequency Generation (DFG) between the wave at ω_2 and the wave at ω_1, or Difference Frequency Generation between the wave at ω_1 and the wave at ω_2. Any wave with an angular frequency different from the six possibilities mentioned above cannot interact with the two other waves through a second order nonlinear process.

The energy conservation between three waves at ω_1, ω_2 and ω_3 satisfying $\omega_1 \leq \omega_2 < \omega_3$ is:

$$\omega_3 = \omega_1 + \omega_2 \tag{18}$$

In the case of Sum Frequency Generation between two waves at ω_1 and ω_2 for example, the Fourier component of the second order nonlinear polarization $\vec{\mathbf{P}^{(2)}}(\vec{r}, \omega_{SFG})$ in Equation (6) is related to the Fourier transform of the second order impulse response of the material $\underline{\underline{\chi^{(2)}}}(\omega_{SFG} = \omega_1 + \omega_2)$ through:

$$\vec{\mathbf{P}^{(2)}}(\vec{r}, \omega_{SFG} = \omega_1 + \omega_2) \quad = \quad \varepsilon_0 \underline{\underline{\chi^{(2)}}}(\omega_{SFG} = \omega_1 + \omega_2) \therefore \vec{\mathbf{E}}(\vec{r}, \omega_1) \otimes \vec{\mathbf{E}}(\vec{r}, \omega_2) \tag{19}$$

We will see in the next section that an electric field at a new frequency is radiated efficiently only if the nonlinear polarization at this new frequency interferes constructively with the generated electric field it radiates at the same frequency. This is so if the phase matching condition is fulfilled.

1.1.3 *Coupled equations for propagating waves*

In this section, we consider three collinear plane waves at ω_1, ω_2 and ω_3 satisfying the energy conservation relation (18) and propagating in a noncentrosymmetric crystal. The crystal is assumed to be without losses at the given frequencies, and the diffraction and spatial walk-off effects are neglected. These waves propagate along a direction $\vec{u}(\theta, \phi)$ in the crystal with ξ being the coordinate along this direction of propagation. If these waves are assumed to be linearly polarized along the unit vectors $\vec{e_1}$, $\vec{e_2}$, $\vec{e_3}$, the Fourier component at ω_n then writes:

$$\vec{\mathbf{E}_\mathbf{n}}(\vec{r}, \omega_n) = A_n(\xi) e^{-jk_n\xi} \vec{\mathbf{e}_\mathbf{n}} \tag{20}$$

The complex amplitude of the field at ω_n is called A_n and we assume a priori that this amplitude can change along the propagation in the crystal. The wave vectors $\vec{k_n}$ are collinear to $\vec{u}(\theta, \phi)$ with amplitudes given by:

$$k_n = \frac{n(\omega_n)\omega_n}{c} = \frac{2\pi}{\lambda_n} n(\omega_n) \tag{21}$$

where $n(\omega_n)$ is the index of refraction of the wave at ω_n in the considered direction of propagation.

By keeping the first and second order terms, Equation (6) writes:

$$\vec{\mathbf{P}}(\vec{r}, \omega) \approx \vec{\mathbf{P}^{(1)}}(\vec{r}, \omega) + \vec{\mathbf{P}^{(2)}}(\vec{r}, \omega) \tag{22}$$

When plugging this equation into (7), it can be seen that the second order nonlinear polarisation acts like an additional source term in the Helmholtz equation that writes:

$$\nabla^2 \vec{\mathbf{E}}(\vec{r}, \omega) + \underline{\varepsilon_r}(\omega) \frac{\omega^2}{c^2} \vec{\mathbf{E}}(\vec{r}, \omega) = \frac{-\omega^2}{c^2 \varepsilon_0} \vec{\mathbf{P}^{(2)}}(\vec{r}, \omega) \tag{23}$$

As we have assumed that the electric field comprises only three Fourier components satisfying the energy conservation relation, it can be shown that except for a degenerate case (excluded

here), this is the only triplet satisfying such energy conservation relation. Therefore the nonlinear polarization spectrum has only three a priori nonzero components at respectively ω_1, ω_2 and ω_3. Equation (19) gives:

$$\begin{cases} \vec{\mathbf{P}^{(2)}}(\vec{r},\omega_3) = & \varepsilon_0 \underline{\underline{\chi^{(2)}}}(\omega_3 = \omega_1 + \omega_2) \therefore \vec{\mathbf{E}}(\vec{r},\omega_1) \otimes \vec{\mathbf{E}}(\vec{r},\omega_2) \\ \vec{\mathbf{P}^{(2)}}(\vec{r},\omega_2) = & \varepsilon_0 \underline{\underline{\chi^{(2)}}}(\omega_2 = \omega_3 - \omega_1) \therefore \vec{\mathbf{E}}(\vec{r},\omega_3) \otimes \vec{\mathbf{E}}^*(\vec{r},\omega_1) \\ \vec{\mathbf{P}^{(2)}}(\vec{r},\omega_1) = & \varepsilon_0 \underline{\underline{\chi^{(2)}}}(\omega_1 = \omega_3 - \omega_2) \therefore \vec{\mathbf{E}}(\vec{r},\omega_3) \otimes \vec{\mathbf{E}}^*(\vec{r},\omega_2) \end{cases} \tag{24}$$

Each Fourier component of the nonlinear polarization is created by the coupling of the two other fields through the second order susceptibility tensor. The nonlinear polarization at ω_3 is induced by the Fourier component of the fields at $+\omega_1$ and $+\omega_2$. The nonlinear polarization at ω_1 (and ω_2) are induced by the Fourier component at $+\omega_3$ and $-\omega_2$ ($+\omega_3$ and $-\omega_1$). This justifies (see Equation 3) the presence of the conjugate of the Fourier component of the electric field $\vec{\mathbf{E}}^*(\vec{r},\omega_2)$ and $\vec{\mathbf{E}}^*(\vec{r},\omega_1)$ respectively in Equations (24).

When assuming a lossless medium and a low frequency dispersion of the nonlinear medium, the three susceptibility terms in Equation (24) can be considered as equal, i.e:

$$\underline{\underline{\chi^{(2)}}}(\omega_3) = \underline{\underline{\chi^{(2)}}}(\omega_2) = \underline{\underline{\chi^{(2)}}}(\omega_1) = \underline{\underline{\chi^{(2)}}} \tag{25}$$

This corresponds to the ABDP symmetry [10]. It will be the framework of the following calculations. We also consider the approximation of the slowly varying envelope which assumes that the spatial variation of the envelope along the $\vec{u}$ direction is small on a distance comparable with the wavelength. This is the case if the nonlinear interaction is weak enough. Then, it is correct to assume that

$$\left| \frac{\partial^2 A_n}{\partial \xi^2} \right| \ll \left| 2jk_n \frac{\partial A_n}{\partial \xi} \right| \propto \left| \frac{1}{\lambda_n} \frac{\partial A_n}{\partial \xi} \right| \tag{26}$$

The full system governing the amplitudes of the fields in the crystal is:

$$\begin{cases} \dfrac{\partial A_1}{\partial \xi} = \dfrac{-j\omega_1}{2n(\omega_1)c} A_3 A_2^* \chi_{eff} e^{-j\Delta k \xi} \\ \dfrac{\partial A_2}{\partial \xi} = \dfrac{-j\omega_2}{2n(\omega_2)c} A_3 A_1^* \chi_{eff} e^{-j\Delta k \xi} \\ \dfrac{\partial A_3}{\partial \xi} = \dfrac{-j\omega_3}{2n(\omega_3)c} A_1 A_2 \chi_{eff} e^{j\Delta k \xi} \end{cases} \tag{27}$$

This first order nonlinear system provides the coupled equations governing the evolution of the complex amplitudes of the three interacting waves in the crystal.

We have introduced two key parameters of a second order parametric process: the collinear phase mismatch Δk and the effective coefficient χ_{eff}:

$$\Delta k = k_3 - k_2 - k_1 \tag{28}$$

and

$$\chi_{eff} = \vec{\mathbf{e_1}}.\underline{\underline{\chi^{(2)}}}:\vec{\mathbf{e_3}} \otimes \vec{\mathbf{e_2}} = \vec{\mathbf{e_2}}.\underline{\underline{\chi^{(2)}}}:\vec{\mathbf{e_1}} \otimes \vec{\mathbf{e_3}} = \vec{\mathbf{e_3}}.\underline{\underline{\chi^{(2)}}}:\vec{\mathbf{e_1}} \otimes \vec{\mathbf{e_2}} \tag{29}$$

The expression of the effective coefficient χ_{eff} involves the three directions of polarization of the interacting waves. This coefficient is invariant upon any permutation of these three vectors [10]. The importance of this coefficient will be discussed extensively in the BPM section (2.1.2). It is common to define the nonlinear effective coefficient as :

$$d_{eff} = \frac{1}{2}\chi_{eff} \tag{30}$$

We also put

$$a_n = \frac{A_n}{\sqrt{2Z_n\hbar\omega_n}} \tag{31}$$

as well as

$$\kappa = d_{eff}\sqrt{\frac{2\omega_1\omega_2\omega_3}{c^2 n(\omega_1)n(\omega_2)n(\omega_3)}\hbar Z_0} \tag{32}$$

where Z_0 is the vaccum free impedance ($Z_0 = 377\,\Omega$) and Z_n is the impedance of the medium at ω_n: $Z_n = \dfrac{Z_0}{n(\omega_n)}$, so that system of coupled equations is reduced to:

$$\begin{cases} \dfrac{\partial a_1}{\partial \xi} = -j\kappa a_3 a_2^* e^{-j\Delta k\xi} \\ \dfrac{\partial a_2}{\partial \xi} = -j\kappa a_3 a_1^* e^{-j\Delta k\xi} \\ \dfrac{\partial a_3}{\partial \xi} = -j\kappa a_1 a_2 e^{j\Delta k\xi} \end{cases} \tag{33}$$

These new variables are useful since now the intensity I_n of a wave at the frequency ω_n is proportional to the photon flux density $|a_n|^2$:

$$I_n = \hbar\omega_n |a_n|^2 = \frac{1}{2} n(\omega_n)\epsilon_0 c |A_n|^2 \tag{34}$$

And one can show that the coupled equations imply the Manley Rowe relations:

$$\frac{d(|a_1|^2)}{d\xi} = \frac{d(|a_2|^2)}{d\xi} = \frac{-d(|a_3|^2)}{d\xi} \tag{35}$$

These equations state that in a three wave parametric process, the annihilation of a photon at ω_3 always goes along with the creation of two photons, at ω_1 and ω_2: the global photon number is not conserved in a parametric process, contrary to the sum of the intensities of the three waves.

1.2 DIFFERENCE FREQUENCY GENERATION

1.2.1 *Principle*

So far, three waves at ω_1, ω_2 and ω_3 satisfying $\omega_1 \leq \omega_2 < \omega_3$ and $\omega_1 + \omega_2 = \omega_3$ have been considered. From now, the circular frequencies of these waves are called ω_p, ω_s and ω_i for the pump, signal and idler waves respectively, and the condition $\omega_i \leq \omega_s < \omega_p$ is valid. Difference Frequency Generation consists in the generation of a wave at the circular frequency ω_i from two initial waves at ω_p and ω_s so that :

$$\omega_i = \omega_p - \omega_s \tag{36}$$

We are interested here in the efficiency of the generation of a wave at ω_i. The intensity of this wave in the crystal is governed by the system of coupled equations (33). Fully analytical solutions of this system can be worked out, without assumptions on the relative intensities of the three waves. This was done in 1962 in the seminal paper of nonlinear optics [10], but we do not give this full solution here. We would rather make some necessary and realistic assumptions so that the system (33) can be further simplified and solved out.

1.2.2 *Solution in the case of no depletion*

In a typical case of DFG between one wave at ω_p and one wave at ω_s, the intensities of the two incoming waves are comparable. The efficiency of conversion at $\omega_i = \omega_p - \omega_s$ is usually low enough so that the amplitudes of the two incident waves $I_{p,0}$ and $I_{s,0}$ (with corresponding reduced amplitudes $a_{p,0}$ and $a_{s,0}$) can be regarded as constant throughout the crystal of length L. This assumption, called the undepleted pump approximation (UPA), was discussed elsewhere [11] and has the main advantage of giving a result that can be easily and physically interpreted. In this case, the system (33) gets down to only one equation governing the amplitude of the new wave at ω_i:

$$\frac{\partial a_i}{\partial \xi} = -j\kappa a_{p,0} a_{s,0}^* e^{-j\Delta k \xi} \tag{37}$$

After a length L, the amplitude and intensity of the wave at ω_i turn out to be:

$$a_i(L) = -j\kappa a_{p,0} a_{s,0} L e^{-j\frac{\Delta k}{2}L} sinc(\frac{\Delta k L}{2}) \tag{38}$$

and

$$I_i(L) = \frac{2\omega_i^2}{n(\omega_i)n(\omega_s)n(\omega_p)} Z_0 d_{eff}^2 I_{p,0} I_{s,0} L^2 sinc^2(\frac{\Delta k L}{2}) \tag{39}$$

This behavior is typical of an interference: the two waves that interfere in the crystal are the nonlinear polarization at ω_i and the electric field at the same frequency. The amplitude of the electric electric field grows in the crystal if this interference is constructive. When the phase mismatch Δk is not nil, these two waves do propagate in the crystal at different phase velocities: after propagation over a length L_c given by

$$L_c = \frac{\pi}{|\Delta k|} \tag{40}$$

these two waves get dephased by a factor of π, so that the interference is successively constructive and destructive. However, if the phase-mismatch is zero, then the coherence length on which the energy transfer can take place is supposedly infinite, and only restricted by the crystal length available L. This is the optimal situation for a high conversion efficiency. This condition $\Delta k = 0$ is the phase-matching condition. In the case of three collinear interacting waves, it writes, in the direction of propagation considered :

$$\Delta k = 0 \Longleftrightarrow \frac{n(\lambda_p)}{\lambda_p} = \frac{n(\lambda_s)}{\lambda_s} + \frac{n(\lambda_i)}{\lambda_i} \tag{41}$$

We have plotted a typical gain curve of a DFG process in Figure (3). The intensity of the wave at λ_i is given as a function of the wavelength λ_s. The pump wavelength is assumed to be set at a constant value λ_p. Thus, the wavelength λ_i satisifies the energy conservation relation for each value of λ_s (see Equation 18):

$$\lambda_i = (\frac{1}{\lambda_p} - \frac{1}{\lambda_s})^{-1} \tag{42}$$

The wavelength $\lambda_{s,PM}$ corresponding to the maximum of Equation (39) satisfies the phase-matching condition

$$\Delta k(\lambda_{s,PM}) = \frac{n(\lambda_p)}{\lambda_p} - (\frac{n(\lambda_{s,PM})}{\lambda_{s,PM}} + \frac{n(\lambda_{i,PM})}{\lambda_{i,PM}}) = 0 \tag{43}$$

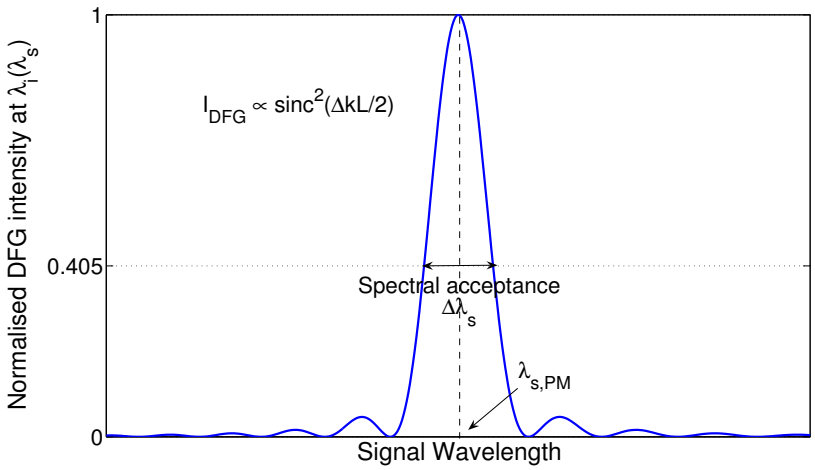

Figure 3: Normalized intensity of the generated idler wave at λ_i as a function of the signal wavelength λ_s, from Equation (39).

The gain on the idler is the highest for this signal wavelength. But waves with phase mismatches that satisfy the condition

$$|\Delta k| < \frac{2\pi}{L} \tag{44}$$

can still be amplified. The longer the crystal, the narrower this spectral acceptance. It is usual to consider that the acceptance of a phase matching process is given by the range of wavelengths satisfying

$$sinc(\frac{\Delta kL}{2})^2 \geq \left(\frac{2}{\pi}\right)^2 \approx 0.405 \tag{45}$$

In this case, the phase-mismatch condition writes:

$$|\Delta k|_{0.405} < \frac{\pi}{L} \tag{46}$$

This is a general feature of phase-matching conditions. Whenever phase-matching is obtained for a given parameter α_{PM} (such as temperature, angle, dopant concentration etc...) there is always a range of α parameters around α_{PM} that will contribute to the parametric processes with a non negligible intensity. Spectral acceptances are of prime importance in nonlinear parametric processes. More work on the specific acceptances of Birefringent Phase Matching and Quasi-Phase Matching will be discussed in sections (2.1.3) and (2.2.3).

1.2.3 *Quantum interpretation*

Difference Frequency Generation can be seen as the fission of the high frequency photon at ω_p into two photons of lower frequency (ω_s and ω_i). The phase-matching condition and

(a) Spontaneous photon splitting (i.e. parametric fluorescence)

(b) Stimulated photon splitting (i.e. optical parametric amplification at ω_s and DFG at ω_i)

Figure 4: 3-photon scission schemes

(a) Collinear phase-matching

(b) Noncollinear phase-matching with angles α (and β) between the signal (and idler) and the pump momenta.

Figure 5: 3-photon momentum conservation schemes

energy conservation relation can be understood as conservation relations in a scattering process between three photons at ω_p, ω_s and ω_i. The energy conservation relation can be restated as $\hbar\omega_p = \hbar\omega_s + \hbar\omega_i$ which is nothing else than the energy conservation between one photon at ω_p and two photons at ω_s and ω_i. The scattering process can be either spontaneous or stimulated (See Figure 4), meaning that the fission of a pump photon can happen spontaneously or through the stimulation by another signal photon. As for the phase matching condition, it should be interpreted as the momentum conservation relation $\hbar\vec{k_p} = \hbar\vec{k_s} + \hbar\vec{k_i}$. In the collinear case, the three photons have their momenta along the same direction. In the noncollinear case, the momenta are no longer aligned (see Figure 5).

1.3 OPTICAL PARAMETRIC AMPLIFICATION

1.3.1 *Solutions in the Undepleted Pump Approximation*

In this section, contrary to what was assumed for a DFG conversion process, only the depletion of the pump wave is negligible. On the opposite, the amplitude of the two other waves can evolve in the crystal. Then, the system of coupled equations becomes:

$$\begin{cases} \frac{\partial a_i}{\partial \xi} = -j\kappa a_{p,0} a_s^* e^{-j\Delta k \xi} \\ \frac{\partial a_s}{\partial \xi} = -j\kappa a_{p,0} a_i^* e^{-j\Delta k \xi} \end{cases} \tag{47}$$

By combining these two equations, one finds that a_s and a_i fulfill the same following partial differential equation:

$$\frac{\partial^2 a}{\partial \xi^2} + j\Delta k \frac{\partial a}{\partial \xi} - \gamma_0^2 a = 0 \tag{48}$$

where we have defined the gain coefficient γ_0 as:

$$\gamma_0^2 = \kappa^2 \frac{I_{p,0}}{\hbar \omega_p} = \frac{2\omega_s \omega_i d_{eff}^2}{c^2 n(\omega_s) n(\omega_i) n(\omega_p)} Z_0 I_{p,0} = \frac{8\pi^2 d_{eff}^2}{\lambda_s \lambda_i n(\lambda_s) n(\lambda_i) n(\lambda_p)} Z_0 I_{p,0} \tag{49}$$

We also define the pseudo-gain coefficient γ through:

$$\gamma^2 = \gamma_0^2 - (\frac{\Delta k}{2})^2 \tag{50}$$

Depending on the relative values of the phase mismatch and of the intensity of the pump wave, the behavior of the complex amplitudes of the fields is dramatically different. The exact solution depends on the relative position of Δk and γ_0 so that γ can be either purely real or purely imaginary. In the realistic case where one wave at λ_s is incident on the crystal, (still in addition of a strong and undepleted pump), the initial boundary conditions write $a_i(0) = a_i^*(0) = 0$ and we get the solution of (47):

$$\begin{cases} a_i(L) = j a_s^*(0) \frac{\kappa a_{p,0}}{\gamma} \sinh(\gamma L) e^{-j\frac{\Delta k}{2} L} \\ a_s(L) = a_s(0)[\cosh(\gamma L) + j\frac{\Delta k}{2\gamma} \sinh(\gamma L)] e^{-j\frac{\Delta k}{2} L} \end{cases} \tag{51}$$

From there we can derive the intensity of the two waves in the crystal:

$$\begin{cases} I_i(L) = I_s(0) \frac{\lambda_s}{\lambda_i} \frac{\gamma_0^2}{\gamma^2} \sinh^2(\gamma L) \\ I_s(L) = I_s(0)[1 + \frac{\gamma_0^2}{\gamma^2} \sinh^2(\gamma L)] \end{cases} \tag{52}$$

It appears that the intensities of the signal and idler waves increase in the crystal (see Figure 6), including the generation of new optical wave at λ_i and the amplification of the other wave at λ_s. This phenomenon corresponds to Optical Parametric Amplification (OPA) and is the principal mechanism involved in Optical Parametric Oscillators.

In the limit of very low gains (in the first order in γ_0^2, and for arbitrary Δk), the formulas (52) can be simplified in:

$$\begin{cases} I_i(L) \approx I_s(0)\dfrac{\lambda_s}{\lambda_i}\gamma_0^2 L^2 sinc^2(\dfrac{\Delta kL}{2}) \\ I_s(L) \approx I_s(0) \end{cases} \tag{53}$$

These two formulas coincide with the expressions derived in section (1.2.2) for the DFG situation. At small gains the DFG equation does provide a good approximation of the intensity generated at λ_i, while the amplification at λ_s can be neglected.

When the phase-mismatch vanishes ($\Delta k = 0$, γ_0 arbitrary), the formulas (52) give:

$$\begin{cases} I_i(L) = I_s(0)\dfrac{\lambda_s}{\lambda_i}\sinh^2(\gamma_0 L) \\ I_s(L) = I_s(0)\cosh^2(\gamma_0 L) \end{cases} \tag{54}$$

And for high gains in formulas (52), the intensities are approximated by:

$$\begin{cases} I_i(L) = \dfrac{1}{4}I_s(0)\dfrac{\lambda_s}{\lambda_i}e^{2\gamma L} \\ I_s(L) = \dfrac{1}{4}I_s(0)e^{2\gamma L} \end{cases} \tag{55}$$

This shows that for large gains, the intensities of the waves grow exponentially in the crystal (see insert of Figure 6). And the meaning of γ_0 and γ as amplification coefficients is now clear. These coefficients increase when the pump intensity increases (see Equation 49). For high conversion efficiencies, the pump will start to be depleted, and the solutions of the coupled equations provided here are no longer valid. At this point, pump depletion must be taken into account, and the elliptical functions must be used to derive the proper solution of the coupled equations [10].

1.3.2 *Comments and numerical estimates*

First of all, it is important to notice that the gain coefficient given in Equation (49) is very dispersive. If we exclude the dispersion of the effective coefficient, the product $\omega_s\omega_i$ shows that the gain coefficient, γ_0, is the highest at degeneracy for

$$\omega_s = \omega_i = \frac{\omega_p}{2} \tag{56}$$

This is an important remark for our future work in Part III: it is usually more difficult to trigger the oscillation of an OPO far from degeneracy.

In this dissertation, we will be dealing mainly with two different crystals CdSe and 5%MgO:PPLN for which we provide two numerical estimates of the gain coefficient. These values are not only useful for the sake of comparison but also for the prospects of CW OPO operation (see section 3.2.2). The gain coefficient of CdSe is worked out for typical values corresponding to angular noncritical phase-matching ($\theta = 90°$). For a pump, signal and idler wavelength at respectively 2.7,

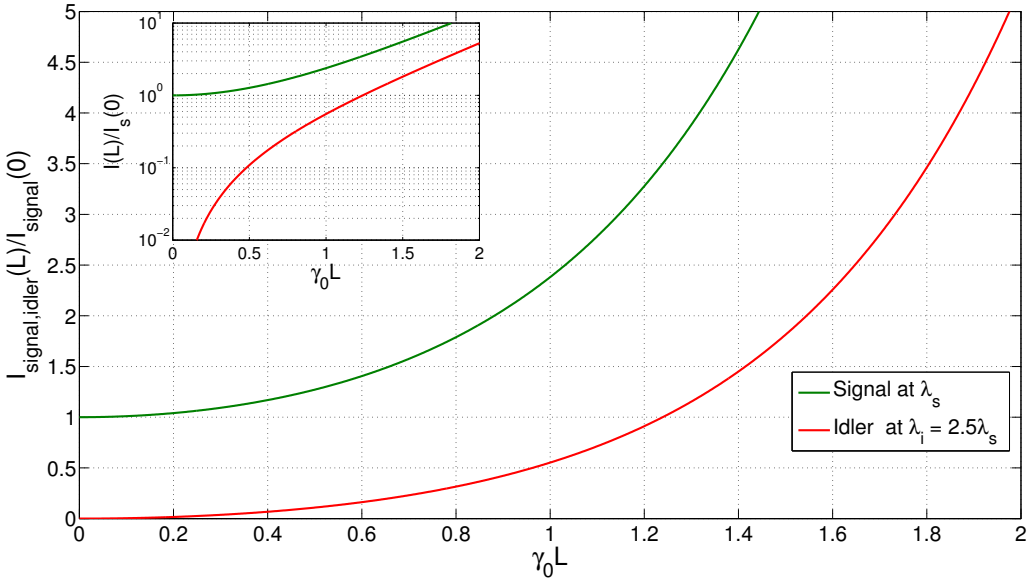

Figure 6: Example of intensities of the amplified signal and generated idler waves in an Optical Parametric Amplifier. The exponential behavior at high gains predicted in Equation (55) is shown in insert on a logarithmic plot.

4.0 and 8.3 µm, an effective coefficient $d_{eff} = 18$ pm/V, and a pump intensity $I_{p,0} = 30\,MW/cm^2$, we find:

$$\gamma_0^2 = 0.57\,cm^{-2} \tag{57}$$

As for 5%MgO:PPLN, we take here numerical values typical of the OPO described in Part III. The pump wavelength is 1.064 µm and the downconverted signal and idler wavelengths are taken far from degeneracy ($\lambda_s = 1.45$ µm and $\lambda_i = 4.0$ µm). For the sake of comparison, we take the same pump intensity as for the calculations in CdSe. And the effective coefficient for the QPM process is here $d_{eff} = \frac{2}{\pi} d_{33} = -17.3$ pm/V (See section 2.2.2.2 and reference [12]). We find:

$$\gamma_0^2 = 4.8\,cm^{-2} \tag{58}$$

The gain coefficient is therefore almost 3 times higher in 5%MgO:PPLN sample than in CdSe. This discrepancy comes from the fact that the idler and pump wavelengths considered in the case of CdSe are longer than in 5%MgO:PPLN.

The last comment that can be done here is about the ratio of the wavelengths appearing in Equations (53) or (54). For a given idler wavelength, the idler conversion efficiency is proportional to the ratio between the signal and the idler wavelengths, which increases with the pump wavelength as shown on Figure (7). The efficiency of conversion of a given idler wavelength is higher if longer pump wavelengths are used: the quantum defect is reduced. This is an important feature of Optical Parametric Amplification.

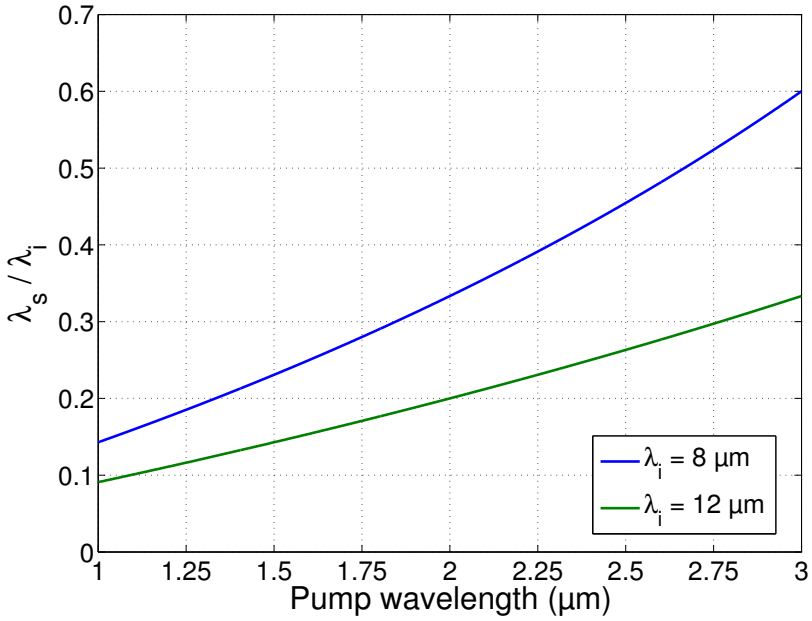

Figure 7: Influence of the pump wavelength on the ratio between the signal and idler wavelength $\frac{\lambda_s}{\lambda_i}$ appearing in Equation (52) for two different idler wavelengths.

2

BIREFRINGENT PHASE-MATCHING VERSUS QUASI-PHASE-MATCHING

2.1 BIREFRINGENT PHASE-MATCHING

2.1.1 *Principle*

In an isotropic crystal with normal dispersion over the range λ_p and λ_i , the phase-matching relation (41) cannot be fulfilled. But, in an anisotropic medium, such as an uniaxial crystal, since the index of a wave can take two values, $n^+(\lambda)$ or $n^-(\lambda)$, with the convention $n^-(\lambda) < n^+(\lambda)$, it is possible to achieve the phase-matching condition. Among the $2^3 = 8$ different configurations of polarizations allowed in a three wave process, it is necessary but far from being sufficient for the highest circular frequency wave (or pump wavelength) to propagate along the fast axis of the crystal. In its most general form, the BPM condition then writes [13]:

$$\frac{n^-(\lambda_p,\theta)}{\lambda_p} = \frac{n^{-,+}(\lambda_s,\theta)}{\lambda_s} + \frac{n^{-,+}(\lambda_i,\theta)}{\lambda_i} \tag{59}$$

with three possible different configurations called Type I, Type II and Type III depending on the idler and signal polarizations. In this work, Type I corresponds to the two waves λ_s and λ_i with the same polarization, whereas Type II is chosen to be the configuration with the signal λ_s in the same state of polarization as the pump. The extraordinary refractive index varying with the direction of propagation in the crystal (Equation 14), the phase mismatch parameters are functions of the azimuthal angle θ in uniaxial crystals, and Table (1) gives the expression of the phase matching condition for the three types in unaxial negative and positive crystals.

For a given set of wavelengths $\{\lambda_p,\lambda_s,\lambda_i\}$ satisfying the energy conservation relation and with $\lambda_p < \lambda_s \leq \lambda_i$, phase matching condition is usually not satisfied for a random direction of propagation in a crystal. The angle of propagation θ must be chosen equal to the phase-matching angle θ_{PM} defined by $\Delta k(\theta_{PM}) = 0$. The requirements on the birefringence of the crystal to fulfill the BPM condition have been discussed elsewhere [13]. Except for Type II and Type III of positive uniaxial crystals and Type I of a negative uniaxial crystals, there is no analytical solution for the phase matching angle θ_{PM} since two extraordinary waves are involved in Equation (59). Numerical estimates can be found in [9].

Type I	$\frac{n_e(\lambda_p,\theta)}{\lambda_p} = \frac{n_o(\lambda_s)}{\lambda_s} + \frac{n_o(\lambda_i)}{\lambda_i}$
Type II	$\frac{n_e(\lambda_p,\theta)}{\lambda_p} = \frac{n_e(\lambda_s,\theta)}{\lambda_s} + \frac{n_o(\lambda_i)}{\lambda_i}$
Type III	$\frac{n_e(\lambda_p,\theta)}{\lambda_p} = \frac{n_o(\lambda_s)}{\lambda_s} + \frac{n_e(\lambda_i,\theta)}{\lambda_i}$

(a) Negative uniaxial crystals ($n_e < n_o$)

Type I	$\frac{n_o(\lambda_p)}{\lambda_p} = \frac{n_e(\lambda_s,\theta)}{\lambda_s} + \frac{n_e(\lambda_i,\theta)}{\lambda_i}$
Type II	$\frac{n_o(\lambda_p)}{\lambda_p} = \frac{n_o(\lambda_s)}{\lambda_s} + \frac{n_e(\lambda_i,\theta)}{\lambda_i}$
Type III	$\frac{n_o(\lambda_p)}{\lambda_p} = \frac{n_e(\lambda_s,\theta)}{\lambda_s} + \frac{n_o(\lambda_i)}{\lambda_i}$

(b) Positive uniaxial crystals ($n_e > n_o$)

Table 1: Type I, II and III phase-matching conditions in uniaxial crystals.

It is important to notice that when the energy conservation relation (42) is taken into account, the BPM condition (59) reduces to three unknowns: the pump wavelength λ_p, the signal wavelength λ_s, and the direction in the crystal θ.

It is common to set the pump wavelength to a given value, such as a typical common laser wavelength, and to look for the phase-matching signal wavelength $\lambda_{s,PM}$ at different phase matching angles θ_{PM}. The curve giving the phase-matching wavelengths as a function of the phase matching angle is called the angular tuning curve of the crystal. But the other option is to keep the angle constant (so that the effective coefficient is maximum for example) and to look for the phase-matching signal wavelength at different pump wavelengths.

2.1.2 *Effective coefficient*

It is clear from Equation (39) that the effective coefficient should not vanish in order to have an efficient generation of a new optical wave. In BPM, the effective coefficient is given by Equation (29) as a contraction product between the second order nonlinear susceptibility tensor and the unit vectors of the polarization waves $\vec{\mathbf{e}}_{\mathbf{p}}^{-}(\theta,\phi)$, $\vec{\mathbf{e}}_{\mathbf{s}}^{+,-}(\theta,\phi)$, $\vec{\mathbf{e}}_{\mathbf{i}}^{+,-}(\theta,\phi)$:

$$\chi_{eff} = \vec{\mathbf{e}}_{\mathbf{p}}^{-}(\theta,\phi).\underline{\underline{\chi^{(2)}}}.\vec{\mathbf{e}}_{\mathbf{s}}^{+,-}(\theta,\phi) \otimes \vec{\mathbf{e}}_{\mathbf{i}}^{+,-}(\theta,\phi) \tag{60}$$

The second order susceptibility tensor for DFG has in the most general case 27 independent coefficients. Under Kleimann [14] and ABDP symmetries [10], the dispersion of the second order susceptibility is neglected and it is valid to calculate the effective coefficient of any three-wave-mixing process with the contracted tensor $\underline{\underline{d^{(2)}}}$ corresponding to Second Harmonic Generation, and that has only 18 components. This tensor writes:

$$\underline{\underline{d^{(2)}}} = \begin{pmatrix} d_{11} & d_{12} & d_{13} & d_{14} & d_{15} & d_{16} \\ d_{21} & d_{22} & d_{23} & d_{24} & d_{25} & d_{26} \\ d_{31} & d_{32} & d_{33} & d_{34} & d_{35} & d_{36} \end{pmatrix} \tag{61}$$

The number and position of zero coefficients $d_{ij} = 0$ are imposed by the symmetry of the crystal [15]. In addition, under Kleinmann symmetry, some relations between the non-zero d_{ij} coefficients can be derived [14]:

$$d_{21} = d_{16},\ d_{25} = d_{36},\ d_{26} = d_{12},\ d_{31} = d_{15}, d_{32} = d_{24},\ d_{34} = d_{23},\ d_{35} = d_{13},\ d_{36} = d_{14} \tag{62}$$

In the case of an uniaxial crystal, the polarization vectors are given in Equation (17) for the ordinary and extraordinary rays, and the effective coefficients can be worked out for different crystal classes. We will be using these coefficients several times in this dissertation. That is why we recall here the effective coefficients for all the uniaxial crystal classes when the walk-off angles are neglected [9].

Crystal classes	Negative crystals Type I: $\lambda_p^e, \lambda_s^o, \lambda_i^o$ Positive crystals Type II and III: $\lambda_p^o, \lambda_s^o, \lambda_i^e$ and $\lambda_p^o, \lambda_s^e, \lambda_i^o$
4, 4mm, 6, 6mm	$d_{15}\sin\theta$
$\bar{6}m2$	$d_{22}\cos\theta\sin 3\phi$
$3m$	$d_{15}\sin\theta - d_{22}cos\theta\sin 3\phi$
$\bar{6}$	$(d_{11}\cos 3\phi - d_{22}\sin 3\phi)\cos\theta$
3	$(d_{11}\cos 3\phi - d_{22}\sin 3\phi)\cos\theta + d_{15}\sin\theta$
32	$d_{11}\cos\theta\cos 3\phi$
$\bar{4}$	$(d_{14}\sin 2\phi + d_{15}\cos 2\phi)\sin\theta$
$\bar{4}2m$	$d_{36}\sin\theta\sin 2\phi$

Crystal classes	Negative crystals Type II and III: $\lambda_p^e, \lambda_s^e, \lambda_i^o$ and $\lambda_p^e, \lambda_s^o, \lambda_i^e$ Positive crystals Type I: $\lambda_p^o, \lambda_s^e, \lambda_i^e$
4, 4mm, 6, 6mm	0
$\bar{6}m2$	$d_{22}\cos^2\theta\cos\phi$
$3m$	$d_{22}\cos^2\theta\cos 3\phi$
$\bar{6}$	$(d_{11}\sin 3\phi + d_{22}\cos 3\phi)\cos^2\theta$
3	$(d_{11}\sin 3\phi + d_{22}\cos 3\phi)\cos^2\theta$
32	$d_{11}\cos^2\theta\sin 3\phi$
$\bar{4}$	$(d_{14}\cos 2\phi - d_{15}\sin 2\phi)\sin 2\theta$
$\bar{4}2m$	$d_{36}\sin 2\theta\cos 2\phi$

Table 2: Effective coefficients of positive and negative uniaxial crystals for the three types of phase matching, when walk off is neglected and under Kleinmann assumption [9].

2.1.3 *Angular acceptances and noncritical phase matching*

For values θ close to the phase matching angle θ_{PM} , the interference function described in Equation (39) has not dropped substantially, meaning that the conversion efficiency can still be non negligible. This range of θ angles is called the angular acceptance of the crystal. It can be worked out with a Taylor Young expansion of the phase mismatch around the value θ_{PM} :

$$\Delta k(\theta) \approx \Delta k(\theta_{PM}) + (\theta - \theta_{PM}) \left.\frac{\partial \Delta k}{\partial \theta}\right)_{\theta=\theta_{PM}} + \frac{1}{2}(\theta - \theta_{PM})^2 \left.\frac{\partial^2 \Delta k}{\partial \theta^2}\right)_{\theta=\theta_{PM}} \tag{63}$$

The first nonzero term of this expansion is related to the acceptance of the nonlinear process. If the first order term dominates, then the condition (45) writes:

$$|\theta - \theta_{PM}| \leq \frac{2\pi}{L} \left[\left.\frac{\partial \Delta k}{\partial \theta}\right)_{\theta=\theta_{PM}}\right]^{-1} \tag{64}$$

And the acceptance of the crystal varies as the inverse of the length of the crystal. If the first order term is null then the second order term dominates, and the condition (45) writes:

$$|\theta - \theta_{PM}| \leq \sqrt{\frac{4\pi}{L} \left[\left.\frac{\partial^2 \Delta k}{\partial \theta^2}\right)_{\theta=\theta_{PM}}\right]^{-1}} \tag{65}$$

The acceptance of the crystal varies then as the inverse of the square root of the length of the crystal.

The first case corresponds to a so-called critical phase matching situation (See Figure 8a), whereas the second case is a noncritical phase-matching situation (See Figure 8b). These two situations are very different in terms of tuning strategy for example. A very critical case will be favored when a wide range of wavelengths must be covered with a very small change in the angle of propagation. The noncritical phase-matching situation has to be favored when a wide range of wavelengths can be accessed with a broader change in angle. The angular tuning rate in noncritical phase-matching situations is of course much lower, yielding better control as well as higher accuracies.

It can be shown that noncritical phase-matching in an uniaxial crystal is achieved whenever the phase-matching angle lies in the (xy) plane of the crystal. In this case $\theta_{PM} = 90°$ and the walk-off angle $\rho(\theta_{PM})$ given in Equation (15) vanishes. This situation is very favorable because the waves do not suffer from any spatial deviation, which allows a higher conversion efficiency due to a longer interacting length. Besides, the noncritical phase-matching scheme is very favorable when dealing with pointing instabilities.

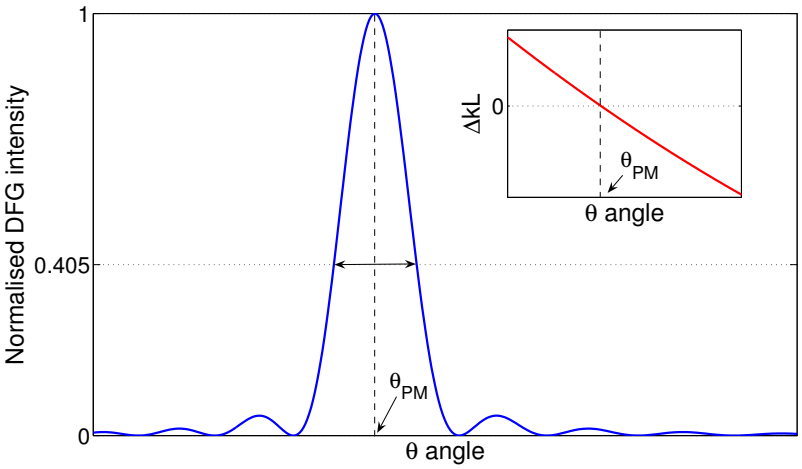

(a) Critical phase-matching scheme.

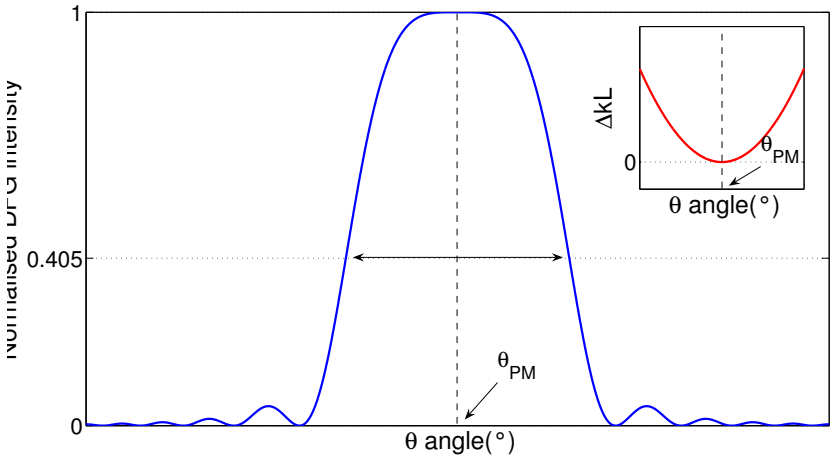

(b) Noncritical phase-matching scheme.

Figure 8: Angular critical (a) versus Angular noncritical phase-matching (b) schemes.

2.1.4 *Conclusion on BPM*

Birefringent Phase-Matching enabled the first experimental achievement of Second Harmonic Generation in the history of nonlinear optics. It allows the efficient generation of additional optical waves provided several conditions are fulfilled: the BPM phase matching-condition $\Delta k_{BPM} = 0$ is necessary but far from being sufficient; the effective coefficient χ_{eff} must also be taken into account: the higher the amplitude of χ_{eff}, the stronger the interaction. The parametric conversion is not possible in any direction where this effective coefficient vanishes.

2.2 QUASI-PHASE MATCHING

Quasi-Phase matching (QPM) was foreseen since the early days of nonlinear optics [10], but achieved experimentally only in 1992 [16]. In this section, we give two different but equivalent representations of Quasi-Phase-Matching, and we derive the conversion efficiency of a QPM process. The main advantages of QPM will be stressed.

2.2.1 *Physical representation*

When the phase-matching condition between three waves at ω_p, ω_s and ω_i is not fulfilled ($\Delta k \neq 0$), the intensity of the wave at ω_i cannot grow monotonically in the crystal. Its amplitude oscillates (see Figure 9) because the interference between the nonlinear polarisation $P^{(2)}(\omega_i = \omega_p - \omega_s)$ and the field radiated at the same frequency $E(\omega_i)$ is successively constructive and destructive. Among other alternatives [10, 17], the most promising solution to overcome this problem consists in switching the sign of the nonlinear polarisation every coherence length (See equation 40). On the first coherence length, the interference is still constructive, but over the second coherence length, instead of interfering destructively with the nonlinear polarisation, the electric field will now interfere constructively with -$P^{(2)}(\omega_i)$. Thanks to the periodic switching, the interference can be constructive all along the crystal length, and QPM eventually ensures the growth of the idler wave in a DFG process even if the phase matching condition is not fulfilled (See Figure 9). The QPM period Λ_{QPM} must be set equal to twice this coherence length in order to ensure a proper compensation of these phase shifts. This QPM condition writes:

$$\Lambda_{QPM} = 2L_c = \frac{2\pi}{|\Delta k|} \tag{66}$$

In ferroelectric materials, the inversion of the sign of the nonlinear coefficient is done by flipping the spontaneous polarisation of the material using a strong external electric field through a high voltage applied to electrodes deposited on the surface of the oriented material [16]. This method is called electric-field poling. After such a process, the material consists of domains with

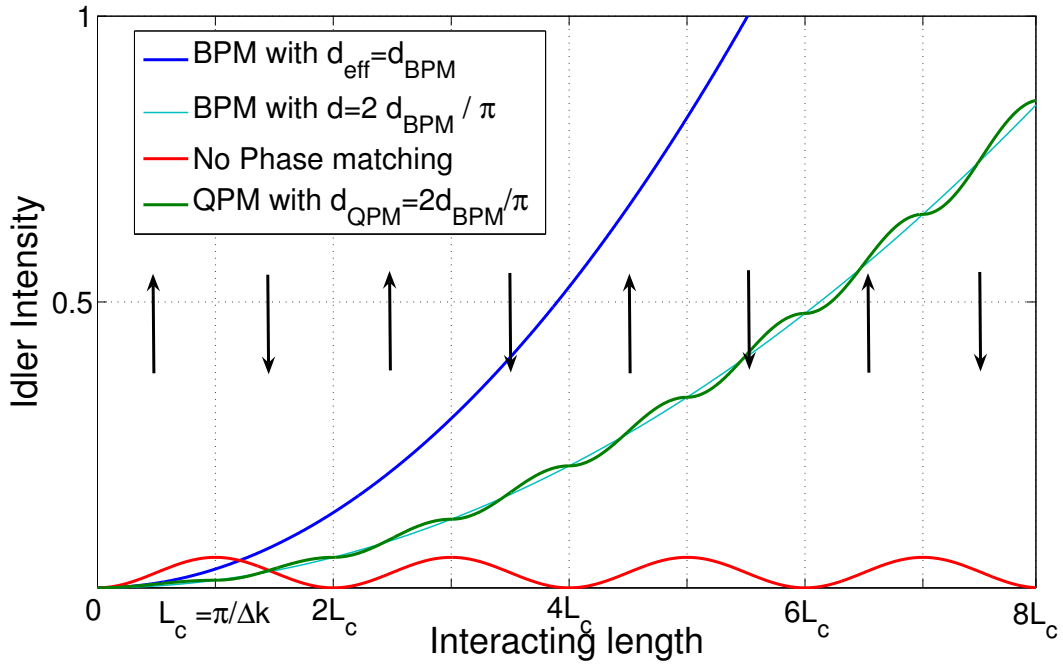

Figure 9: Intensity of a DFG wave generated in three different phase matching conditions $\Delta k_{BPM} = 0$ (blue), $\Delta k_{BPM} \neq 0$ (red), and $\Delta k_{QPM} = 0$ (green).

polarizations successively flipped by 180°, which leads to a successive reversal of the sign of the effective coefficient with the same periodicity Λ_{QPM} (See Figure 10).

This physical representation of QPM is good enough to provide some physical insight on QPM. It is nevertheless limited and cannot account for neither the conversion efficiency of a QPM process nor the appearance of higher order QPM processes. A mathematical representation based on the Fourier Transform is much more helpful in grasping the wealth of QPM.

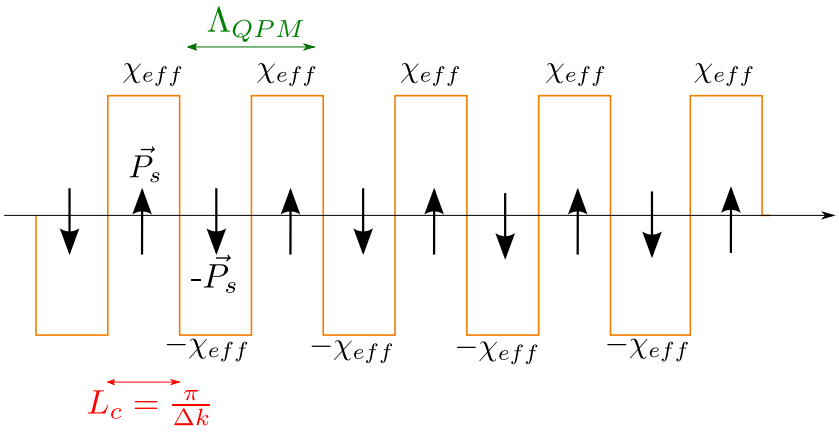

Figure 10: Modulation of the direction of the spontaneous polarization $\vec{P}_s$ and of the sign of the effective coefficient χ_{eff} of an ideal periodically poled material, i.e. with a duty ratio of 0.5.

2.2.2 *First-order QPM*

2.2.2.1 *Mathematical representation*

Quasi-Phase Matching relies on the spatial modulation of the effective coefficient along the direction of propagation. It is useful to incorporate this dependency of the effective coefficient in the coupled Equations (33) to get:

$$\begin{cases} \dfrac{\partial a_i}{\partial \xi} = j\kappa(\xi) a_p a_s^* e^{-j\Delta k \xi} \\ \dfrac{\partial a_s}{\partial \xi} = j\kappa(\xi) a_p a_i^* e^{-j\Delta k \xi} \\ \dfrac{\partial a_p}{\partial \xi} = j\kappa(\xi) a_i a_s e^{j\Delta k \xi} \end{cases} \tag{67}$$

In the case of DFG, and under the UPA, the complex amplitude of the field at ω_i at the exit of the crystal of length L is given by the line integral:

$$a_i(L) = a_i(0) + \int_0^L \frac{\partial a_1}{\partial \xi} d\xi \tag{68}$$

or

$$a_i(L) = j a_{p,0} a_{s,0} T F_\kappa(\Delta k) \tag{69}$$

where TF_κ is the Fourier Transform of the grating along the direction of propagation. The relation between the phase-mismatch and the QPM grating is now clear: the complex amplitude of the wave at ω_i will be non zero only if the Fourier component of the spatial susceptibility profile at Δk is different from zero. And reciprocally, any susceptibility profile that can be engineered with a non zero Fourier component at the value Δk will allow the growth of a wave at ω_i. It is practically very difficult to make structures where the nonlinear coefficient is continuously modulated and for which the Fourier Transform is a mere Dirac peak at Δk. An easier approach is the realization of a periodic door-like profile sketched in Figure (10), where the nonlinear coefficient is switched periodically. The spatial modulation of such a QPM grating is given by:

$$\kappa(\xi) = \kappa_0(-1)^{E(\xi/L_c)} \tag{70}$$

where E is the floor function.

And the Fourier Transform of such a structure is given by:

$$\begin{aligned} TF_\kappa(u) &= \frac{2}{\pi}\kappa_0\delta(u - \frac{2\pi}{\Lambda_{QPM}})\text{-}\frac{2}{3\pi}\kappa_0\delta(u - \frac{2\pi}{3\Lambda_{QPM}}) \\ &\quad +\ldots+(-1)^m(\frac{2}{(2m+1)\pi})\kappa_0\delta(u - \frac{2\pi}{(2m+1)\Lambda_{QPM}}) \end{aligned} \tag{71}$$

where δ is the Kronecker symbol. It has a infinite number of components all of which can participate in the QPM process. Fortunately enough, only one Fourier component usually satisfies the QPM condition. When it is the first component, the QPM is said to be of the first order. When it is the mth component that is involved, the QPM process is said to be of the m-th order.

The first-order QPM condition is exactly equivalent to the condition given in Equation (66). Since the amplitude of the first Fourier component in Equation (71) is $\frac{2}{\pi}d_{eff} \approx 0.64 d_{eff}$, the complex amplitude of the wave grown at ω_i given in Equation (69) is reduced by the same factor. And the intensity of the wave is reduced by $(\frac{2}{\pi})^2$ i.e. almost 40%:

$$I_i(L) = (\frac{2}{\pi})^2\kappa_0 I_{p,0} I_{s,0} L^2 sinc^2((\Delta k - \frac{2\pi}{\Lambda_{QPM}})\frac{L}{2}) \tag{72}$$

From this equation, first order QPM is seen to be formally equivalent to BPM using the proper expression of the effective coefficient in κ_0. For a perfect door-like profile, and a first order QPM process, the effective coefficient writes:

$$d_{QPM} = \frac{2}{\pi}d_{eff} \tag{73}$$

And the QPM phase-mismatch is given by:

$$\Delta k_{QPM} = \Delta k - \frac{2\pi}{\Lambda_{QPM}} \tag{74}$$

We have plotted in Figure (9) the typical profile of the generated idler wave when the phase-matching condition is fulfilled, when it is not fulfilled and when the first order QPM condition is met. These curves are given for the same effective coefficient.

2.2.2.2 *Main advantages*

QPM presents several advantages over BPM that make it a versatile and widely used technique nowadays. One of the most noticeable achievements of QPM is the extension of parametric conversion to isotropic crystals. This extension is made possible because in QPM, three waves of the same polarizations are allowed to interact efficiently. More specifically, the polarization of the pump wave is not predetermined by the structure of the crystal. This has far reaching consequences : the three polarizations of the waves in interaction can be chosen so that the higher component of the second order nonlinear susceptibility tensor is solicited. As a consequence, QPM does enhance the conversion efficiency of a parametric process, contrary to what could be guessed from Equation (73). For example, we give here the full second-order susceptibility tensor of $LiNbO_3$ [12]: the coefficient d_{33} is more than fives times higher than the other coefficients, which can represent a 25 fold increase in efficiency of conversion compared to what is possible in BPM. The reduction factor $(2/\pi)^2$ is then more than compensated. In KTP, the d_{33} factor is also 5 times higher than the other coefficients [18].

$$\underline{\underline{d^{(2)}}} = \begin{pmatrix} 0 & 0 & 0 & 0 & -4.35 & -2.1 \\ -2.1 & 2.1 & 0 & -4.35 & 0 & 0 \\ -4.35 & -4.35 & -27.2 & 0 & 0 & 0 \end{pmatrix}$$

Table 3: Contracted second order susceptibility tensor of $LiNbO_3$ in pm/V, after [12].

Following Equation (29), d_{33} is solicited i.e.

$$d_{eff} = d_{33} \tag{75}$$

if the three interacting waves are all polarized along the z direction. When propagating in the (xy) plane, the QPM condition in a uniaxial crystal (whatever its sign) therefore writes:

$$\frac{n^e(\lambda_p)}{\lambda_p} - \frac{n^e(\lambda_s)}{\lambda_s} - \frac{n^e(\lambda_i)}{\lambda_i} = \frac{1}{\Lambda_{QPM}} \tag{76}$$

2.2.3 *Duty ratio*

For an ideal sample such as the one sketched in Figure (10), the size of the domains with a positive sign (L_+), and a negative sign (L_-) is the same so that the duty ratio η defined as:

$$\eta = \frac{L_+}{L_+ + L_-} \tag{77}$$

is equal to 0.5:

$$\eta_{ideal} = 0.5 \tag{78}$$

Unfortunately, the poling process may result in structures where the sizes of the positive and negative domains are not equal. The duty ratio can therefore be different from its optimal value of 0.5. When this duty ratio deviates from 0.5, the effective coefficient of a first order QPM process decreases [16, 19] (see Figure 12) according to :

$$d_{QPM}(\eta) = d_{QPM}(\eta_{ideal}) sin(\pi\eta) \tag{79}$$

where $d_{QPM}(\eta_{ideal})$ was given in Equations (73).

2.2.4 *Higher order QPM*

An additional interest in QPM comes from the fact that different parametric mixing processes can be envisioned with a single grating sample since there are some non-vanishing higher order Fourier components of the susceptibility profile. For an ideal QPM structure, the amplitude of the (2m+1)th order Fourier component is given in Equation (71). The corresponding effective coefficient is:

$$d_{2m+1} = \frac{2}{(2m+1)\pi} d_{eff} \tag{80}$$

And the corresponding QPM period is:

$$\Lambda_{2m+1} = (2m+1)\Lambda_{QPM} = (2m+1)\frac{2\pi}{\Delta k} \tag{81}$$

Even if the efficiency of such higher order QPM processes drops sharply with the order m, it can be interesting to use such possibilities for characterization purpose for example. By choosing the proper QPM period, it may also be possible to achieve phase matching for different QPM processes in one monograting sample. We have sketched in Figure (11) the evolution of an idler wave in a QPM material with an ideal duty ratio $\eta = 0.5$ (see Equation 78) for different QPM odd orders. When the mth order QPM is considered, the idler wave is forced to grow every m coherence lengths.

The effective coefficient of a m^{th} order QPM process is of course still dependent on the quality of the grating. For a duty ratio η, its amplitude is modified according to [16, 19]:

$$d_m(\eta) = \frac{2}{m\pi} sin(m\pi\eta) d_{eff} \tag{82}$$

This equation shows that the absolute value of all the even coefficients decreases when the duty ratio deviates from its ideal value of 0.5: for a first order QPM process, it is reduced by 20% for a duty ratio of 0.3 (See Figure 12). This implies that the conversion efficiency is decreased by almost 35%. Conversely, when the duty ratio worsens, it is interesting to see that the effective coefficient of even order terms increases and can be non-zero: mathematically speaking, some new nonzero even order terms appear in the Fourier expansion, thus opening new QPM possibilities. In Figure (12), we have plotted the effective coefficient of a first and of a second order QPM process in 5%MgO:PPLN. The second order term is forbidden in an ideal structure with a duty ratio of 0.5 but it becomes possible as soon as the duty ratio deviates from its optimal value. The effective coefficient of a second order QPM process can be seen to be maximum for $\eta = 0.25$. In the range of duty ratios $\eta \in [0.2; 0.3]$, the effective coefficients of the first and second orders are comparable.

2.2.4.1 *Tunable QPM*

Besides this gain in efficiency, QPM introduces one additional degree of engineering to the parametric processes. Engineering samples with different QPM periods has eased the way to tunable parametric generation. Samples with multigratings or with a fan shape grating have been the first solutions put ahead. Later on, the advent of angular quasi-phase matching has allowed continuous and very broad tunability in QPM crystals cut as spheres or cylinders. Part III will make great use of the wide and continuous tuning capability of a 5%MgO:PPLN crystal engineered as a partial cylinder. The tunability of QPM devices will be addressed there.

2.2.4.2 *Conclusion on QPM*

QPM has undoubtedly contributed to a renewal of the field of nonlinear optics. It has not only increased the conversion efficiency of parametric processes but also allowed more phase-matching scenarii. The possibility to use three interacting waves with the same polarization is fundamental in QPM devices and has allowed isotropic materials to be used [20]. The tunability of QPM devices is now a clear advantage over solid state laser sources [7].

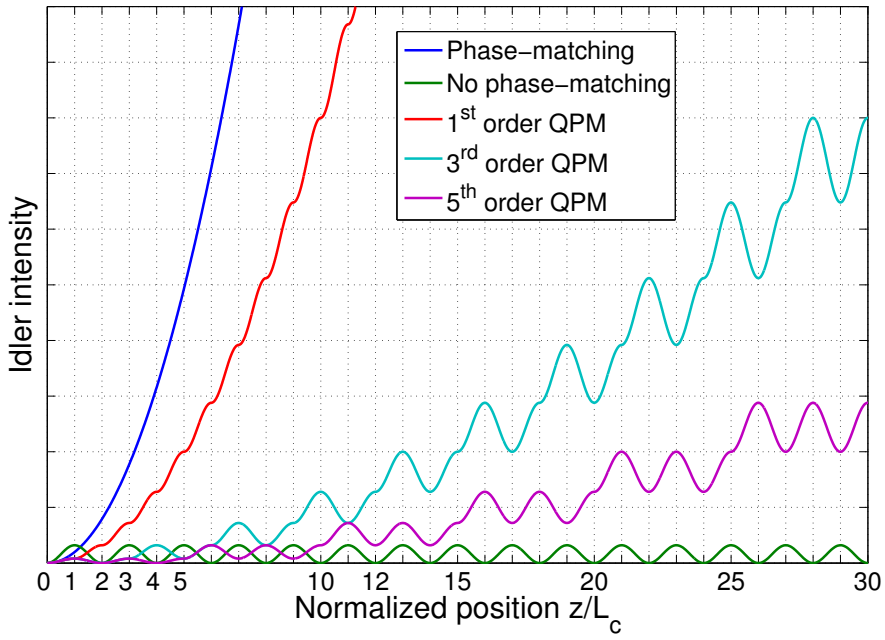

Figure 11: Illustration of the generation of an idler wave under different phase-matching or quasi-phase matching conditions. The effective coefficient is the same for all these curves, and the duty ratio is $\eta = 0.5$. The coherence length L_c is given by Equation (66).

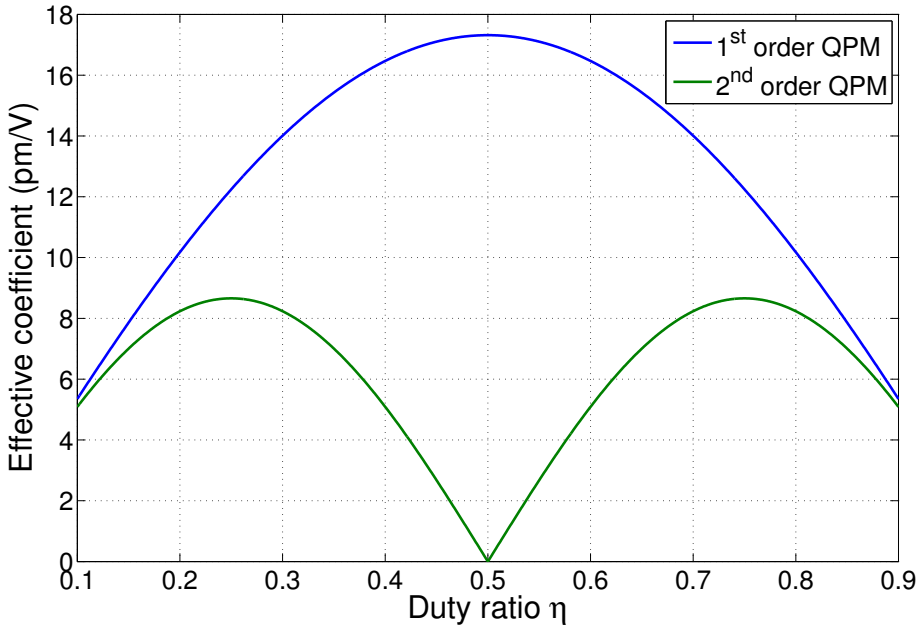

Figure 12: Absolute value of the effective coefficient of a first and second order QPM process in 5%MgO:PPLN as a function of the duty ratio η. The d_{33} coefficient is equal to -25.2 pm/V after [12].

3

OPTICAL PARAMETRIC OSCILLATION

In the first section of this chapter we have seen that Optical Parametric Amplification leads to the amplification of one wave and to the generation of another wave. Optical Parametric Oscillation consists in the generation of two new waves (the signal and the idler) from only one pump wave in a nonlinear crystal inserted inside a resonating cavity. The principle of an OPO is very similar to a laser operation where an amplification medium provides gain at the resonated wavelength: the oscillation kicks off as soon as the gain of the resonated wave(s) in the medium is above the reflection and propagation losses. But one major difference between a laser and an OPO is that the amplification of the resonating wave(s) in an OPO takes place through the instantaneous nonlinear process of Optical Parametric Amplification that we described previously. Oscillation is possible if the pumping intensity is high enough for the nonlinear gain to overcome the losses of the cavity. Another major distinction between laser and OPOs is that an Optical Parametric Oscillator does not depend on resonant transitions, which implies that an OPO can be theoretically tuned over a wider spectral range. This is done when the phase-matching condition can be fulfilled over a wide range of wavelengths, the limitations of the tunability being set by either the transmission of the mirrors or that of the crystal.

However, the classical treatment of OPA that we provided (see section 1.3.1) is not able to predict the purely quantum phenomenon of parametric fluorescence, an elementary process playing the same role as spontaneous emission in a laser and being the cornerstone of parametric oscillation. A semi-quantum derivation can be used to predict the number of signal and idler photons spontaneously emitted by a nonlinear crystal. From there, rate equations of an Optical Parametric Oscillator are derived, and the two regimes of operation of an OPO are clearly identified.

There exists many different configurations of OPOs depending on the number of resonated waves and on the level of recycling of the pump. OPOs have been used in CW, low repetition rate nanosecond regime or high repetition rate picosecond regime. Optical Parametric Oscillation has been developed as soon as 1965 by Giordmaine and Miller [21] and CW OPOs were demonstrated 3 years later by Smith [22]. Reaching the threshold of an OPO is no longer a challenge nowadays. Commercial devices are available, and so far the record output for a CW OPO is 17.5 W [23]. On the other hand, in the nanosecond regime, more than half a joule have been obtained from a 10 mm thick 5%MgO:PPLN OPO [24]. These two world records illustrate the progress in Optical

Parametric Oscillators that were made possible thanks to the use of improved QPM materials. The main characteristics of CW and nanosecond OPOs are compared in this work.

3.1 PARAMETRIC FLUORESCENCE

A semi-quantum treatment must be used to explain the "first" spontaneous splitting of a pump photon in a pair of signal and idler photons. An illuminating treatment of quantum fluctuations and parametric processes was given in 1966 by Yariv. Following his work [25, 26], we now derive the expressions of the numbers of signal and idler photons produced by parametric amplification in a semi-quantum approach.

We consider that the pump field can be treated classically whereas the signal and idler fields are quantized, and we assume that phase-matching is realized, which considerably simplifies the calculations. Rather than the classical expressions of their amplitudes, the creation $a^\dagger$ and annihilation a operators shall be used [26, 27]. If the fields are initially in the state $< \Psi(0)|$, then the average number of signal and idler photons after a time t are given by:

$$< n_s(t) >= < \Psi(0)|\, a_s^\dagger(t) a_s(t)\, |\Psi(0) > \tag{83}$$

$$< n_i(t) >= < \Psi(0)|\, a_i^\dagger(t) a_i(t)\, |\Psi(0) > \tag{84}$$

And the time dependence of the operators can be solved thanks to the equation of motion in the Heisenberg representation:

$$\frac{da_s}{dt} = -\frac{i}{\hbar}[a_s, \mathcal{H}] \tag{85}$$

and

$$\frac{da_i}{dt} = -\frac{i}{\hbar}[a_i, \mathcal{H}] \tag{86}$$

The Hamiltonian $\mathcal{H}$ describing the system of a strong coherent pump field in quantized signal and idler fields, under phase matching conditions can be written as the sum of the unperturbated Hamiltonian and of the interaction Hamiltonian taking into account the nonlinear coupling between the classical undepleted pump and the two other fields:

$$\mathcal{H} = \hbar\omega_s(a_s^\dagger a_s + \frac{1}{2}) + \hbar\omega_i(a_i^\dagger a_i + \frac{1}{2}) + \frac{1}{2}\hbar G_0(a_s a_i e^{i\omega_p t} + a_s^\dagger a_i^\dagger e^{-i\omega_p t}) \tag{87}$$

where the coefficient G_0 is proportional [28, 27] to the gain coefficient given in Equation (49) through :

$$G_0^2 = \gamma_0^2 \frac{c^2}{n(\omega_s)n(\omega_i)} \tag{88}$$

And equations (85), (86) and (87) provide the system of coupled equations describing the evolution of the operators:

$$\frac{da_s}{dt} = -i\omega_s a_s - \frac{1}{2} i G_0 a_i^\dagger e^{-i\omega_p t} \tag{89}$$

$$\frac{da_i^\dagger}{dt} = i\omega_i a_i^\dagger + \frac{1}{2} i G_0 a_s e^{i\omega_p t} \tag{90}$$

These equations give the temporal evolution of the operators and are exactly what we would have obtained if the temporal evolution of the fields in a cavity had been considered [27] classically. The time dependency of the operators takes a similar expression compared with Equation (51):

$$a_s(t) = \left[a_s(0)\cosh(G_0 t) - i a_i^\dagger(0)\sinh(G_0 t) \right] e^{-i\omega_s t} \tag{91}$$

$$a_i^\dagger(t) = \left[a_i^\dagger(0)\cosh(G_0 t) + i a_s(0)\sinh(G_0 t) \right] e^{i\omega_i t} \tag{92}$$

It is a linear combination of cosh and sinh functions. But contrary to the classical case, the expression of the number of photons is not simply the sum of the number of photons amplified in each field. Because of the non-commutativity of operators, i.e:

$$[a_l(t),\, a_m^\dagger(t)] = a_l(t)a_m^\dagger(t) - a_m^\dagger(t)a_l(t) = \delta_{lm} \tag{93}$$

then the average number of photons given in Equations (83) and (84) writes [25]:

$$\begin{aligned} < n_s(t) > &= \left[n_{s,0}\cosh^2(G_0 t) + n_{i,0}\sinh^2(G_0 t) \right] + \sinh^2(G_0 t) \\ < n_i(t) > &= \left[n_{s,0}\sinh^2(G_0 t) + n_{i,0}\cosh^2(G_0 t) \right] + \sinh^2(G_0 t) \end{aligned} \tag{94}$$

When, the number of idler photon at $t = 0$ is neglected ($n_{i,0} = 0$), we get:

$$\begin{aligned} < n_s(t) > &= n_{s,0}\cosh^2(G_0 t) + \sinh^2(G_0 t) \\ < n_i(t) > &= n_{s,0}\sinh^2(G_0 t) + \sinh^2(G_0 t) \end{aligned} \tag{95}$$

Compared with expressions (52) obtained in the case of classical parametric amplification these quantum expressions contain an additionnal term, i.e. $+\sinh^2(G_0 t)$, in the expression of the amplified fields. Even when no signal or idler are incident on the crystal, the generation of an idler and of a signal photon is still possible. The non-coherent zero-point fluctuations are responsible for the generation of the "first" photons in an OPO. These "first" photons are then

amplified classically following Equation (52). Parametric fluorescence can be seen as an analogy of spontaneous emission in a real laser system [29], but they arise from different elementary processes: parametric fluorescence depends on the real part of the second order electric susceptibility, while the spontaneous emission is governed by the imaginary part of the first order electric susceptibility.

3.2 A LASER-LIKE PROCESS

3.2.1 *Cavity stability and mode matching of an OPO*

The simpler OPO configuration (See Figure 13a) which is not strictly speaking stable is made of two plane mirrors with a crystal cut as slab. This configuration has the main advantage of its simplicity since it does not require too much care in the alignment procedure, but it is not very selective. Even though operation of OPOs with unstable resonator configurations has been reported [30], cavity stability is an important requirement of Optical Parametric Oscillators since it improves the quality of the profiles of the generated beams. Practically, the stability of an OPO can be achieved thanks to different cavity architectures. The use of a slab crystal with concave mirrors is a good option (See Figure 13b). When a crystal cut as slab is used, the stable configuration is achieved if the criterion of stability is valid [29]. When the crystal inserted in the cavity is cut as a cylinder, the shape of the crystal itself is the stabilizing element. Plane mirrors can then be used in this case (See Figure 13c), with a cavity still exhibiting a good filtering effect [31].

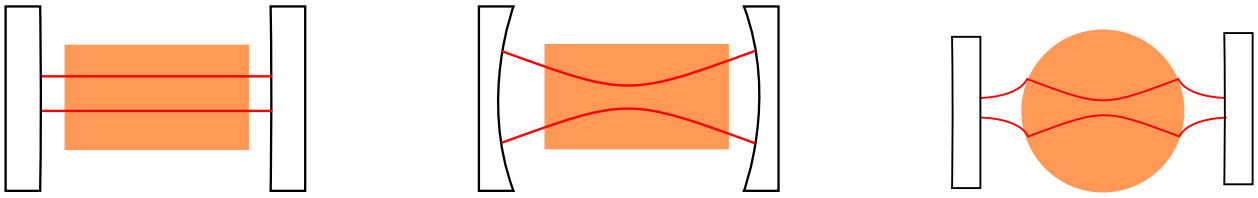

(a) Plano-Plano cavity with a crystal cut as a slab.

(b) Concave Concave Cavity with crystal cut as a slab.

(c) Plano-Plano cavity with a crystal cut as cylinder.

Figure 13: Examples of simple configurations of OPO cavities.

For a given stable cavity configuration, only the modes that remain identical after one round trip are allowed to resonate. These eigenmodes of the cavity impose a comb of circular frequencies (or wavelengths) likely to be amplified. These eigenfrequencies will be amplified only if the parametric gain at these frequencies is above the reflection and propagation losses.

As in any other resonator, the coupling between the source term and the eigenmodes dictates the efficiency of the transfer between the waves. In an OPO where the signal is resonant, the polarization wave driving the signal at λ_s must be expanded in terms of cavity modes. As a consequence, only a fraction of the generated signal field will be coupled into the modes of the resonator. Much work has been done on the optimal conditions of focusing in an OPO [32, 33]. The optimal overlap corresponds to the pump beam and the resonant signal having the same confocal parameters. It was also shown that a poor overlap between the driving nonlinear polarization

and the resonant Gaussian modes can be qualitatively taken into account through a coefficient of coupling g_s that reduces the gain coefficient. This coefficient g_s is given as a function of the pump and signal beam radii by [33]:

$$g_s = \frac{w_p^2}{w_p^2 + w_s^2} \leq 1 \tag{96}$$

Taking into account such a coefficient is equivalent to considering a reduced parametric gain coefficient $\gamma_{0,OPO}$ given by:

$$\gamma_{0,OPO}^2 = g_s \gamma_0^2 \leq \gamma_0^2 \tag{97}$$

3.2.2 *CW OPO*

Singly Resonant Optical Parametric Oscillators (SROPO) where only one of the two generated waves is resonated, drastically reduces stability issues of Doubly Resonant OPOs (DROPO) but at the price of higher pump thresholds. In this work, we will focus only on singly resonant OPOs. They are much simpler and cheaper to build than doubly resonant OPOs.

We have sketched on Figure (14) the profiles of the intensity of the signal and idler waves inside an OPO made of plane mirrors with a crystal cut as a slab and without recycling of the pump. This sketch is shown for a pump input energy above threshold so that oscillation of the signal wave is possible.

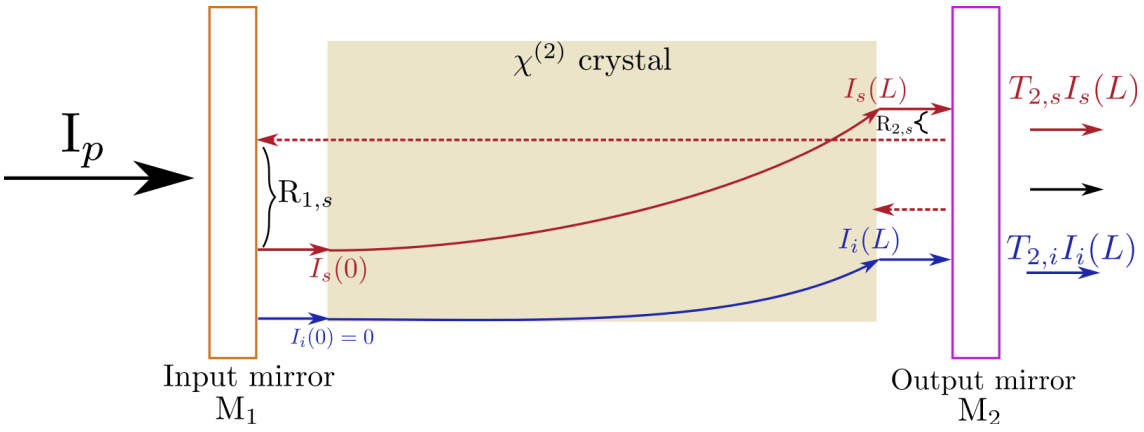

Figure 14: Schematic view of the signal (red) and idler (blue) intensity profiles in an Optical Parametric Oscillator above threshold. The parametric gain compensates exactly for the losses at the resonated signal wavelength. The idler and signal classical intensities are given in Equations (54). The reflection and transmission coefficients of the two mirrors are R and T with clear indexations.

We now want to derive the basic equation of the threshold of a CW SROPO . To do so, we get back to the classical picture of optical parametric amplification. The OPA gain Equation (54) is:

$$I_s(L) = I_s(0) cosh^2(\gamma_0 L) \tag{98}$$

The threshold of a CW OPO can be worked out by putting that the gain on the resonated wave matches the losses $R_s = R_{1,s}R_{2,s}$ of the cavity at the same wavelength (see Figure 14):

$$R_s cosh^2(\gamma_0 L) = 1 \tag{99}$$

where γ_0 is given in Equation (49).

The pump threshold intensity is therefore:

$$I_{p,th} = \hbar\omega_p \left[\frac{1}{\kappa L} \cosh^{-1} \left(\frac{1}{\sqrt{R_s}} \right) \right]^2 \tag{100}$$

where κ was given in Equation (32).

The full expressions of the output of a CW OPO were derived by Rosencher and Fabre [34], by resorting to the exact solution of the coupled equations [10]. The expression of signal intensity at the output of the crystal was also derived. It is given through an implicit formula of the pump power that accounts for pump back conversion processes [34].

3.2.3 *Gain clamping*

When the pump power is increased above the threshold value, a process similar to the gain clamping in lasers does take place. Yariv has shown that when the steady state is reached, the pump power inside the cavity cannot exceed its threshold value [35] : if the intracavity pump power is lower than its threshold value, then the oscillation is not be possible because there is not be enough parametric gain on the signal; on the other hand, if the pump power is higher than its threshold value, then the intracavity signal power cannot increase with time because of the steady state regime. The conservation of power law then states that the whole pump power above this threshold $P_p - P_p)_{th}$ value must be converted in signal and idler photons. Because of the Manley Rowe relation, the parametric annihilation of one pump photon must result into the creation of one idler and one signal photons. And the following energy relation holds inside the cavity:

$$\frac{P_s}{\omega_s} = \frac{P_i}{\omega_i} = \frac{P_p - P_p)_{th}}{\omega_p} \tag{101}$$

This relation is of course valid only inside the resonator. The output powers must take into account the respective transmission coefficients of the cavity.

3.3 SINGLY RESONANT OPOS IN THE NANOSECOND REGIME

Nanosecond OPOs have several advantages over CW OPOs. As the peak power is higher, the nonlinear gain coefficient is higher and the threshold is lower. But, nanosecond OPOs also have some drawbacks. The pulse takes some time to build up from zero to threshold which may prevent oscillation for too short pulses. In the nanosecond regime, the linewidths emitted by an OPO are also larger than in a CW OPO. The required linewidth depends of course on the applications targeted with the generated wavelengths. But since pulsed OPOs have lower thresholds, it is usually possible to insert filtering elements inside the cavity without quenching oscillation.

3.3.1 *The two models*

Two different approaches have been taken to derive the main properties of pulsed nanosecond OPOs. The first one is typically the one used by by Brosnan and Byer [32]. Their model makes extensive use of the "constant at each pass" approximation. In this approximation, the pump pulse is divided into small time steps with a length equal to the round-trip time of the signal in the cavity. This model has been the first modelization of the temporal dynamics of a pulsed OPO. A more recent model by Godard et al. [36] uses the exact solutions of the coupled equations to derive the threshold, build-up time as well as efficiency of an OPO. Despite heavier mathematics, this model provides very good insight on the dynamics of pulsed nanosecond OPOs, and especially close to threshold.

3.3.2 *Model with analytical solutions*

The model developed by Godard et al. resorts to the exact solutions of the coupled equations [36, 34]. The intensity of the signal at the ouput of the crystal of length L, $I_s(L)$, was given as a function of the input $I_s(0)$ and for any pump values $I_p(0)$ [10]. With the notations used in this work, it writes:

$$I_s(L) = I_s(0)\left[1 - sn^2(j\kappa L\sqrt{\frac{I_p(0)}{\hbar\omega_p}}|\frac{-\omega_p I_s(0)}{\omega_s I_p(0)})\right] \tag{102}$$

As the intuitive time constant of an OPO is the round trip time of the signal given by:

$$\tau = \frac{L_{cav} + (n(\lambda_s) - 1)L}{c} \tag{103}$$

where L_{cav} is the cavity length. It can be shown that the output power of an OPO at the signal wavelength $I_{s,out}$ must satisfy the first order differential equation [36]:

$$\frac{d}{dt}(I_{s,out}) + \frac{1}{\tau}I_{s,out} = \frac{-R}{\tau(1-R)}I_{s,out}sn^2(j\kappa L\sqrt{\frac{I_p(t)}{\hbar\omega_p}}|\frac{-R\omega_p I_{s,out}}{(1-R)\omega_s I_p(t)}) \tag{104}$$

This equation has the big advantage of giving direct access to the time dependence of the output of a nanosecond OPO as a function of the time dependent pump input $I_p(t)$ and reflectivity at the signal R. It can be solved using standard mathematical softwares. For a refractive index close to n=2.5, and a crystal of length L=40 mm inside a cavity of length $L_{cav} = 60$ mm, the round trip time is approximately $\tau = 0.4$ ns. A 10 ns pulse corresponds to about 25 roundtrips then. The signal wave is not instantaneously amplified from noise to the threshold values. It takes a few round trips for the signal to reach the required level of amplification. Figure (15) shows the typical profiles of the signal and pump pulses, as well as the build-up time of the signal beam, as measured by Bjorkholm and co-workers at the output of their first singly resonant OPO [37]. The model by Godard and Rosencher allowed the derivation of the expression of the build up time of a SRO in the case of a square input pump pulse [36].

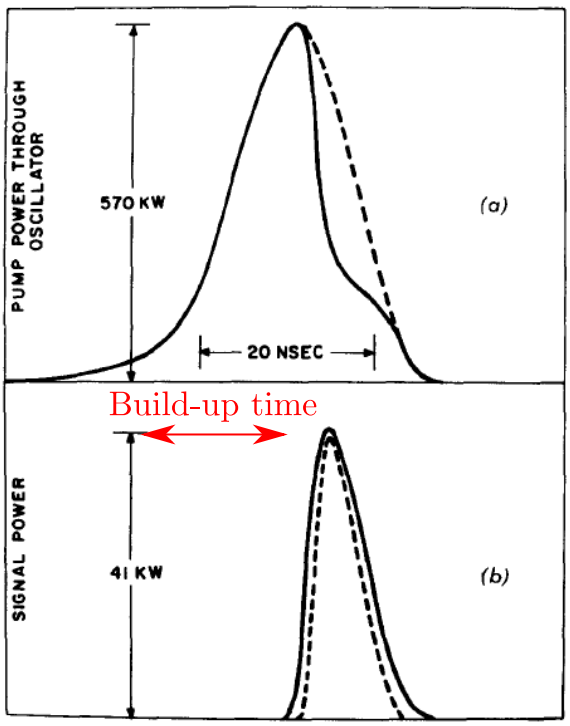

Figure 15: Temporal profiles of the pump and resonated signal wave of the first singly resonant $LiNbO_3$ OPO (continuous lines). The build up time corresponds to the delay between the onset of the pump pulse and the onset of the signal pulse. These graphs are taken from [37]. The dashed line in Figure (a) corresponds to the pump profile without oscillation while the dashed line in Figure (b) corresponds to the difference between the two waveforms of Figure (a). The agreement between the solid and dashed lines in Figure (b) illustrates that the depletion of the pump in Figure (a) is directly related to the growth of the signal wave.

3.3.3 *Oscillation threshold*

Pulsed nanosecond OPOs are more difficult to modelize than CW OPOs because of the time dependent gain function induced by the propagating pump pulse. Nevertheless, the threshold of an OPO can still be roughly worked out, given some approximations. Brosnan and Byer [32] have obtained Equation (105) for the threshold of a SRO with recycling of the pump. This formula is derived by assuming that at each pass in the crystal, the pump intensity is constant. This is equivalent to assuming that the round trip duration is much shorter than the pump pulse duration τ. The pump energy fluence at threshold J_0 then writes:

$$J_0 = \frac{2.25\tau}{4\kappa g_s L^2}[\frac{L}{2c\tau}\ln(\frac{P_n}{P_0}) + 2\alpha L + ln(\frac{1}{\sqrt{R}}) + \ln 4]^2 \tag{105}$$

κ is the gain coefficient given in Equation (32). And g_s is the coupling factor that accounts for the mode-matching of the nonlinear polarization at λ_s with the eigenmodes of the cavity as given in Equation (96). The factor 4 accounts for the recycling of the pump. The term $\frac{P_n}{P_0}$ is related to the level of amplification to reach threshold: Brosnan and Byer assumed that this level of amplification should be 33 dB in the case of OPOs.The absorption losses are included in the absorption coefficient α. The reflection of the cavity is given through the R coefficient that is the product of the reflectivities of the input and output mirros.

If we put Equation (105) under the form

$$4\kappa g_s L^2 J_0 = 2.25\tau[\frac{L}{2c\tau}\ln(\frac{P_n}{P_0}) + 2\alpha L + ln(\frac{1}{\sqrt{R}}) + \ln 4]^2 \tag{106}$$

a clear competition appears between gain and losses at stake under the threshold of an OPO. On the left side of equation (106), the gain term is typical of a second order nonlinear phase-matched conversion process. It is given by:

$$Gain = 4J_0\kappa g_s L^2 \tag{107}$$

On the right side of Equation (105), the total losses are given by:

$$Losses = 2.25\tau[\frac{L}{2c\tau}\ln(\frac{P_n}{P_0}) + 2\alpha L + ln(\frac{1}{\sqrt{R}}) + \ln 4]^2 \tag{108}$$

This formula has been able to give only rough estimates of the threshold of pulsed nanosecond OPOs so far. This can be owed to the fact that this model assumes perfect collimation of the pump, and neglects the divergence of the beams. A better analysis should include the effects of angular and spectral acceptances. The main advantage of this formula is to give a physical interpretation of the balance between the losses and the gain in an Optical Parametric Oscillator.

CONCLUSION

The first Part of this dissertation deals with the basic elements of theory of three-wave mixing processes in nonlinear uniaxial crystals. The phase-matching (or quasi-phase-matching) condition and the amplitude of the effective coefficient drive their efficiency. The expression of the DFG intensity has been recalled in the realistic cases of undepletion of one or two input waves. Optical Parametric Oscillators artificially increase the interaction length in the crystal and thus enhance this conversion efficiency.

These elements of theory will find direct applications in the following Parts of this dissertation whose focus is on Difference Frequency Generation and Optical Parametric Oscillation. The second Part of this work is indeed dedicated to the study of the phase-matching conditions of the new nonlinear crystal $CdSiP_2$. Optical Parametric Oscillation with a 1.064 µm pump has been reported under noncritical phase matching condition [38], and Difference Frequency Generation can be phase-matched up to 9.5 µm in this crystal [39].

Part II

$CdSiP_2$: A PROMISING INFRARED NONLINEAR CRYSTAL

4

INTRODUCTION

Parametric down conversion of laser pulses appears nowadays as one of the most promising routes to the generation of tunable coherent radiation above 3 µm where very few other kinds of laser sources are available. Tunable coherent sources at always longer wavelengths require the use of a nonlinear crystal where the down conversion parametric process described in Part I can take place. The choice of a nonlinear crystal gets down to a compromise between different characteristics, among which: a high figure of merit, a good transmission window covering the working wavelengths, and a high optical damage threshold. So far, mainly five crystals have exhibited a good enough tradeoff between these three requirements to become "available" commercially: $ZnGeP_2$, $AgGaS_2$, $AgGaSe_2$, CdSe and GaSe. Nonetheless, the search for new nonlinear crystals whose phase-matching properties can either better match the available pump laser wavelengths or allow longer wavelengths to be generated is still desirable [5]. The new infrared nonlinear crystal $CdSiP_2$ was recently identified as a very promising solution with this respect. Because of its high (negative) birefringence and on the basis of early reports on the value of its band gap ($\lambda_G = 506$ nm [40]), noncritical phase-matching with a 1.064 µm pump wavelength with limited two photon absorption had been predicted and achieved experimentally [41, 42] in this crystal. An extensive characterization of the phase-matching directions of $CdSiP_2$ has been carried out at the Néel Institute using the sphere method [43, 44]. Based on these new measurements [45], two methods are proposed in this work to provide reliable new Sellmeier equations for this crystal. The first method that we implemented relies upon the simultaneous fit of the measured phase-matching curves [39] and was applied previously to other crystals [46, 47]. Another new method is also proposed. It provides a direct determination of the values of the ordinary and extraordinary refractive indices in the mid-infrared from the DFG phase-matching angles measurements. These two methods are compared in this work. Lastly, on the basis of the new Sellmeier equations for $CdSiP_2$, we investigate the phase-matching conditions through which a broadband infrared supercontinuum [48] can be generated. We also perform a comparison with other infrared nonlinear crystals. The $CdSiP_2$ crystal we studied was provided by Pete Schunemann from BAE System, Nashua NH, USA within a collaboration.

5

PHASE-MATCHING PROPERTIES OF $CdSiP_2$

5.1 INTRODUCTION

The nonlinear optical crystal $CdSiP_2$ (CSP) belongs to the tetragonal crystal system with point group $\bar{4}2m$, and the optical frame coincides with the crystallographic frame. Its lattice constants are $a = 5.68$ Å, $c = 10.431$ Å, and the unit cell number is Z = 4. It was grown in the past in small sizes that did not allow measurements of essential physical properties. Recently, high optical quality crystals of CSP with sizes reaching 70×25×8 mm^3 were grown successfully from the melt via the horizontal gradient freeze technique [41, 42] by using high purity starting materials. Even more recently, the growth of 35 mm long $CdSiP_2$ crystals using the modified vertical Bridgman method has been reported [49]. Important physical characteristics, including transparency, birefringence, and thermo-mechanical properties have already been measured and can be found in the literature [42]. One noticeable advantage of $CdSiP_2$ over other NLO materials is its high thermal conductivity: it was measured to be 13.6 $W.m^{-1}.K^{-1}$, which is ten times higher than that of $AgGaS_2$. This makes CSP very attractive for future high average power mid-IR OPO applications where thermal issues are involved.

CSP is an optically negative uniaxial chalcopyrite so that angular non-critical type I phase-matching is possible in contrast to the positive $ZnGeP_2$ (ZGP) which is the only commercially available II-IV-V_2 type chalcopyrite. Indeed, the effective coefficient for Type I DFG (λ_p^o, λ_s^e, λ_i^e) in a

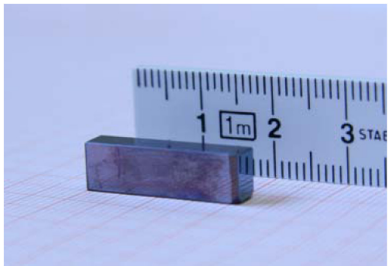

(a) 2.5 cm long $CdSiP_2$ crystal used for OPG experiments [50]

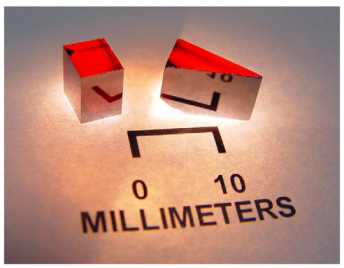

(b) $CdSiP_2$ crystal and prism used for refractive index measurements [42]

Figure 16: Pictures of $CdSiP_2$ crystals

$\bar{4}2m$ positive crystal such as $ZnGeP_2$ vanishes for $\theta = 90°$, whereas it is maximum for Type I DFG (λ_p^e, λ_s^o, λ_i^o) for a $\bar{4}2m$ negative uniaxial crystal such as $CdSiP_2$ (See Table 2) when $\theta = 90°$ and $\phi = 45°$. The birefringence ($n_e - n_o$) of CSP was found to be -0.051 near 2 µm [42]. An isotropic point, i.e. $n_e = n_o$, was also observed close to the band-edge : at room temperature this point occurs at 2.41 eV (514.5 nm) and near this point, optical activity can be observed [51].

The absorption coefficient of CSP is shown on Figure (17) and compared to that of ZGP. On the one hand, the band gap of CSP is larger than ZGP and pumping at shorter wavelength is possible, but on the other hand, because of three phonon absorption starting around 6.6 µm, the spectrum of CSP does not extent much above 8.5 µm. As any absorption of the idler beam generated from DFG in the crystal can be detrimental in terms of heat deposition in the crystal and in terms of conversion efficiency, the use of CSP to Band III applications (from 8 to 12 µm) seems compromised.

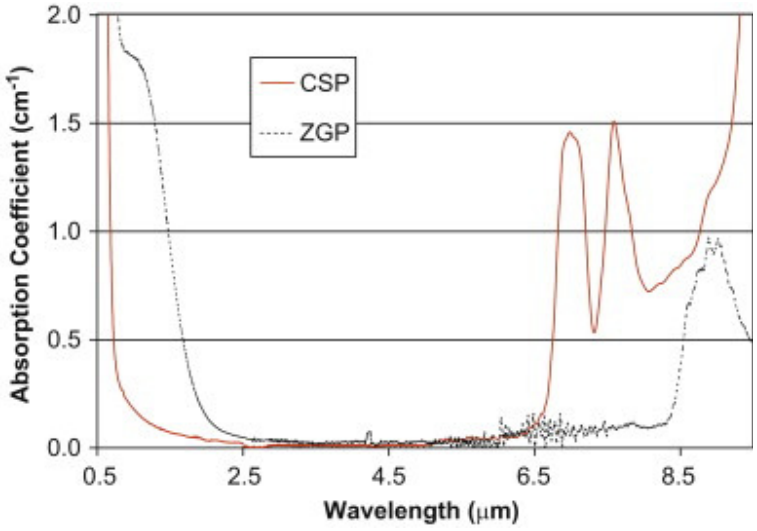

Figure 17: Comparison between the absorption coefficient of $CdSiP_2$ and $ZnGeP_2$. This graph is taken from [42].

The lower transmission wavelength of a nonlinear crystal is a counterintuitive but very important feature for infrared generation. Two photon absorption (TPA) consists in the detrimental nonlinear absorption process of two photons at the same energy [27, 52]. In a semiconducting crystal, TPA happens whenever the pump field is intense enough to trigger the nonlinear absorption of two pump photons at the same wavelength λ_p. In terms of wavelengths, the condition to avoid TPA in a semiconducting materials with a bandgap E_G (and corresponding wavelength λ_G) writes:

$$\lambda_p > \frac{4\pi\hbar c}{E_G} = 2\lambda_G \tag{109}$$

The shorter the cut-on wavelength, the shorter the minimum pump wavelength. For example, pumping with a Nd:YAG laser at $\lambda_p = 1.064$ µm requires a band gap higher than 2.33 eV. The most recent measurements of the value of the band-gap of $CdSiP_2$ were made on samples of improved crystalline quality and yielded $E_G = 2.08$ eV [53] which is lower than earlier estimates

[40] that gave $E_G = 2.45$ eV. These new measurements are therefore important since they suggest that TPA at 1.064 µm in $CdSiP_2$ could have been underestimated so far. This was indeed confirmed experimentally by two-photon absorption measurements [53]. The TPA absorption coefficients β (see [52] for a definition) of an ordinary and extraordinary polarized 1.064 µm pump were extrapolated from the decrease in transmission of the samples with increasing pump intensities (See Figure 18). The authors found $\beta = 2.6$ cm/GW for an ordinary polarized pump beam at 1.064 µm, showing that this detrimental phenomenon cannot be neglected in the picosecond or femtosecond regime.

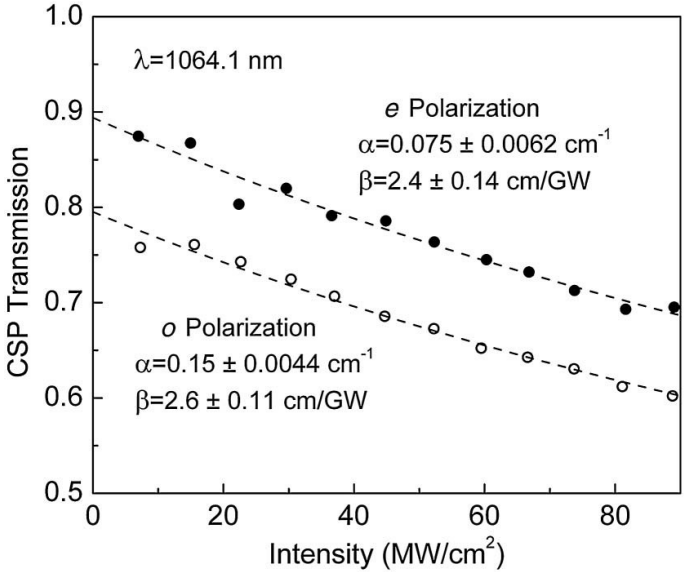

Figure 18: Two-photon absorption indirect measurement in a 12.1 mm long AR-coated $CdSiP_2$ crystal. The transmission at 1.064 µm is plotted as a function of the laser intensity. The absorption and TPA coefficients were obtained from the fit of the data shown in dashed line. This graph is taken from [53].

Due to its orientation symmetry class, the only nonzero component of the second order electric susceptibility tensor of CSP far from any transition is $d_{zxy} = d_{zyx}$ or d_{36} in the contracted form. It was measured using femtosecond pulses near 4.6 µm [54]. A comparison with ZGP yielded $d_{36}(CSP) = 1.07 d_{36}(ZGP)$ with a relative error estimate of ±5%. Assuming $d_{36} = 75\, pm/V$ for ZGP at $9.6\,\mu m$ [55], it was then found $d_{36} = 84.5 pm/V$ for CSP at $4.56\,\mu m$. At this wavelength, the value of its nonlinear figure of merit FOM is:

$$FOM = \frac{d_{36}^2}{n^3} \approx 250\, pm^2/V^2 \tag{110}$$

For the sake of comparison, the nonlinear figures of merit $\frac{d^2}{n^3}$ of the main nonlinear crystals are presented in Figure (19) as a function of their short cut-on wavelength. On this logarithmic plot, most nonlinear crystals fall on a line with a slope between 4 and 5. And the interest in $CdSiP_2$ can be seen from its relatively high figure of merit compared to its short wavelength cut-on, since it falls slightly above the other crystals.

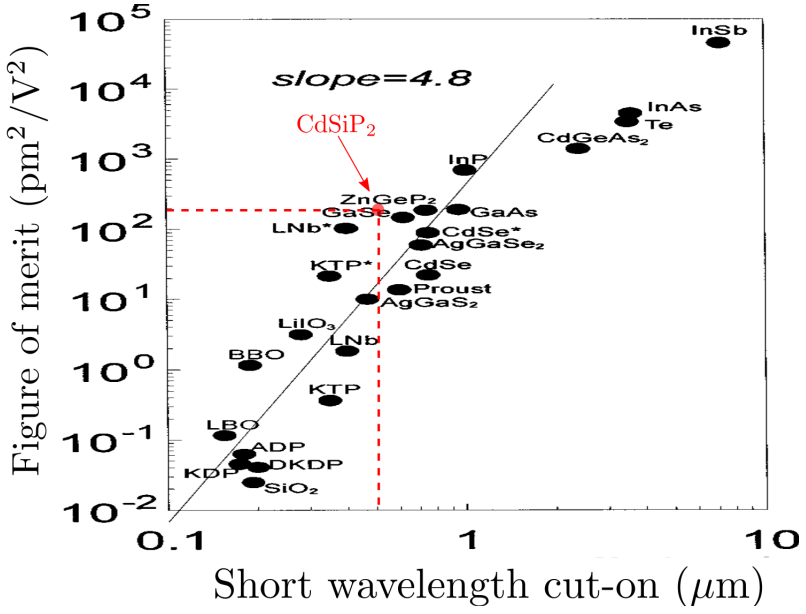

Figure 19: Effective figure of merit of the main nonlinear crystals as a function of their wavelength cut-on, from [56]

The ordinary and extraordinary principal refractive indices of $CdSiP_2$ were measured using the minimum deviation technique between 0.66 µm and 5 µm (See Figure 20), using the prism shown in Figure (16b). The following dispersion Sellmeier equations were obtained [42], where the wavelength is expressed in microns :

$$\begin{aligned} n_o^2(\lambda) &= 3.0811 + \frac{6.2791\,\lambda^2}{\lambda^2 - 0.10452} - 0.0034888\,\lambda^2 \\ n_e^2(\lambda) &= 3.4343 + \frac{5.6137\,\lambda^2}{\lambda^2 - 0.11609} - 0.0034264\,\lambda^2 \end{aligned} \tag{111}$$

5.2 ANGULAR NONCRITICAL PHASE-MATCHING WITH A 1.064 µM PUMP WAVELENGTH

Today, the Nd:YAG laser is one the most widespread infrared lasers. As angular noncritical phase-matching (ANCPM) i.e. $\theta = 90°$ is a highly desired phase-matching scheme (see figure 8b and discussion thereof), the prospect of ANCPM with a pump wavelength at 1.064 µm is very attractive [5].

Quasi-phase-matching with a 1.064 µm pump wavelength is of course the best example of ANCPM with a Nd:YAG laser pump. But, most QPM materials are oxides and cannot transmit above 5 µm so that direct and efficient generation from 1.064 µm to wavelengths longer than 5

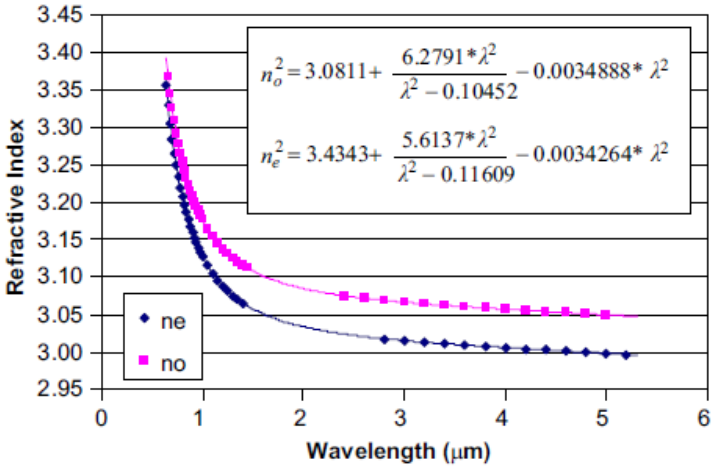

Figure 20: Measured and extrapolated values of the principal refractive indices of CSP, from [42]

µm is not possible. Birefringent phase-matching in materials with a longer transmission in the infrared is the other alternative.

Because of its high band gap, TPA at 1.064 µm is also limited in $AgGaS_2$. But ANCPM Type I DFG ($\lambda_p^e, \lambda_s^o, \lambda_i^o$) is only possible in this crystal with pump wavelength below 0.9 µm. A beautiful application of this feature is CW OPO operation with $\lambda_p = 0.845$ µm [57]. On the other hand, highly critical phase-matching ($\theta = 45.1°$) has been achieved in a 1.064 µm pumped $AgGaS_2$ OPO and resulted in an impressive idler tuning range [58].

The first report of ANCPM Optical Parametric Oscillation with a 1.064 µm pump wavelength involved a solid solution of $Cd_xHg_{1-x}Ga_2S_4$. Tuning the idler was obtained thanks to a translation of the pump beam along the composition gradient. This tuning scheme is very original but resulted in a limited idler tuning range from 2.85 to 3.27 µm [59].

The first device reported with CSP was such an ANCPM nanosecond OPO pumped at 1.064 µm [38]. The phase-matched signal wavelength was measured to be 1.285 µm, with the corresponding idler at 6.193 µm. The maximum idler output was 0.47 mJ for an incident pump pulse energy of 21.7 mJ corresponding to a pump to idler conversion efficiency of 2.2%. Later on, temperature tuning of the idler from 6.12 µm to 6.55 µm was also demonstrated [60] in a CSP OPO with a 1 ns pump pulse duration. Synchronously pumped OPOs were also reported in collinear [23] or noncollinear [61] configurations. Eventually, Optical Parametric Generation was demonstrated in seeded [50] or unseeded [62] conditions. The seeding process drastically reduced the bandwidth of the idler [50] down to less than 1 nm. Note that seeding was made possible thanks to the temperature tuning that enabled the perfect matching between the diode laser seeding wavelength and the parametric fluorescence.

Figure 21: Picture of the 4.99 mm diameter oriented $CdSiP_2$ sphere, polished to optical quality, used for the phase-matching studies and stuck on a goniometric head.

5.3 CDSIP$_2$ PHASE-MATCHING CURVES

Before Pierre Brand's PhD at Néel Institute [45], phase-matching studies of $CdSiP_2$ had been restricted to Type I ANCPM with $\theta = 90°$ and $\phi = 45°$. Besides this attractive phase-matching scheme, it is interesting to investigate other phase-matching directions of $CdSiP_2$ for which the idler wavelength could be higher than 6.15 µm. Moreover, the full characterization of the phase-matching directions of $CdSiP_2$ could lead to the refinement of the Sellmeier equations of this new crystal as done previously in our team [46, 47].

5.3.1 *Experimental set-up*

The experimental set-up used to measure the phase-matching directions in the CSP sphere that is shown in Figure (21) was described extensively in Pierre Brand's PhD thesis [45]. A multistage parametric source from Excel Technology and Light Conversion is used. The first stage delivers 15 ps pulses at 1.064 µm and with a repetition rate of 10 Hz. An infrared tunable beam is then obtained thanks to a noncollinear DFG stage between the 1.064 µm pump beam and the idler beam generated from a 355 nm pumped LBO OPG-OPA and tunable between 0.7 and 2.4 µm. The DFG crystal is $AgGaS_2$ cut at $\theta = 45°$ and $\phi = 45°$. The generated DFG beam is tunable between 2 and 10 µm and its energy per pulse decreases from about 200 µJ at 2 µm down to a few µJ at 10 µm. It is then coupled inside the CSP sample cut and polished as a sphere, with or without the 1.064 µm input beam depending on whether SHG or DFG experiments are performed.

The focalisation issue is very critical when DFG and SHG phase-matching directions are measured in a sphere [44, 45]. Indeed, because of its curved surface, a sphere of radius R is equivalent to a thick converging boule lens with focal length given by:

$$f_{sphere}(\lambda) = \frac{n(\lambda)R}{2(n(\lambda)-1)} \tag{112}$$

This focal length is shorter than the radius of the sphere as soon as the index is higher than 2. For CSP the indices are close to 3 (see Figure 20) meaning that the focus point of a plane wave incident on the sphere will be in the bulk of the crystal, which could damage the crystal. In order to avoid any surface and bulk damage, the beams must hit the sphere with a slightly diverging profile while propagating along the diameter. If the input beam focal point is located at a distance $2f_{sphere}$ from the center of the sphere, then parallel propagation of the beam inside the sphere is achieved. This is the best configuration, not only in terms of a lower pump intensity, but also in terms of accuracy in the measurements of the phase-matching directions. This topic has already been extensively covered in [44] or [45].

5.3.2 *Measurement of the phase-matching directions*

$CdSiP_2$ being optically negative, phase-matching can be achieved only if the highest frequency wave is polarized extraordinarily, because this polarization is associated with the lower refractive index in the considered direction (See Equation 59). The conversion efficiency of the two types of SHG and the three types of DFG is the highest when the BPM conditions given in Table (4) are fulfilled i.e. when the beams propagate along the phase-matching directions marked out by the phase-matching angles θ_{PM}.

	BPM condition
SHG Type II	$n_e(\frac{\lambda_\omega}{2}, \theta_{PM}) = \frac{1}{2}(n_o(\lambda_\omega) + n_e(\lambda_\omega, \theta_{PM}))$
SHG Type I	$n_e(\frac{\lambda_\omega}{2}, \theta_{PM}) = n_o(\lambda_\omega)$
DFG Type I	$\frac{n_e(\lambda_p, \theta_{PM})}{\lambda_p} = \frac{n_o(\lambda_s)}{\lambda_s} + \frac{n_o(\lambda_i)}{\lambda_i}$
DFG Type II	$\frac{n_e(\lambda_p, \theta_{PM})}{\lambda_p} = \frac{n_e(\lambda_s, \theta_{PM})}{\lambda_s} + \frac{n_o(\lambda_i)}{\lambda_i}$
DFG Type III	$\frac{n_e(\lambda_p, \theta_{PM})}{\lambda_p} = \frac{n_o(\lambda_s)}{\lambda_s} + \frac{n_e(\lambda_i, \theta_{PM})}{\lambda_i}$

Table 4: Second Harmonic Generation and Difference Frequency Generation phase-matching conditions in a negative uniaxial crystal such as CSP.

The measurement of the SHG and DFG phase-matching curves has to be carried out in the planes of the dielectric frame where the effective coefficient of the considered interaction does not vanish, and if possible where it reaches the highest value. In the case of DFG or SHG in CSP, the expressions of the different effective coefficients were given in Table (2):

$$\begin{aligned} d_{eff}^{DFG\ Type\ I} &= d_{eff}^{SHG\ Type\ I} = d_{36} \sin\theta \sin 2\phi \\ d_{eff}^{DFG\ Type\ II,III} &= d_{eff}^{SHG\ Type\ II} = d_{36} \sin 2\theta \cos 2\phi \end{aligned} \tag{113}$$

Type I and Type II SHG as well as Type I and Type III DFG have been measured (See Figures 22 and 23). No Type II DFG could be found. The measurements of Type I DFG and Type I SHG were done in the plane $\phi = 30°$, because the plane $\phi = 45°$ was not accessible in the sphere due to a dead angle (see Figure 21). Measurements of Type III DFG as well as Type II SHG were done in the plane $\phi = 0°$.

In addition, the DFG phase-matching directions were measured by maximizing the SFG intensity between the idler beam tunable above 6 µm and the pump beam at 1.064 µm. Since SFG and DFG phase-matching directions are equivalent when keeping the same set of wavelengths, it is more convenient to generate SFG because it is in the range 1-1.3 µm where detection is much simpler.

These measurements provide the first extensive characterization of the SHG and DFG phase-matching directions of $CdSiP_2$. The DFG measurements were performed up to 9.5 µm which is well above the onset of the three-phonon absorption of CSP (See Figure 17). Figures (22) and (23) show that the SHG phase-matching directions are in good agreement with the calculations derived from Equations (111) and that were obtained from the fit of the indices measured with the minimum deviation technique. The calculations and measurements of the DFG curves do exhibit some discrepancies higher than the 0.5° experimental accuracy. It is the goal of the next section to provide new Sellmeier equations for $CdSiP_2$ that match our measurements and that could eventually lead to a better prediction of the phase-matching angles in future experiments.

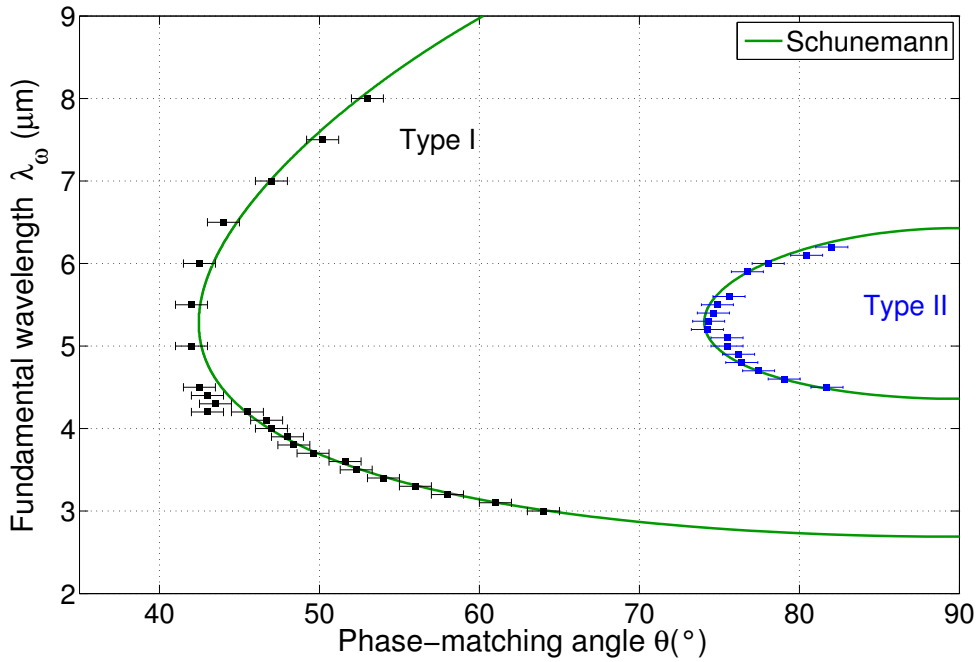

Figure 22: Type I SHG (λ^o_ω, $\lambda^e_{2\omega}$) and Type II SHG ($\lambda^{o,e}_\omega$, $\lambda^e_{2\omega}$) tuning curves of $CdSiP_2$. Squares stand for experimental data. The green curves correspond to calculations from Equations (111).

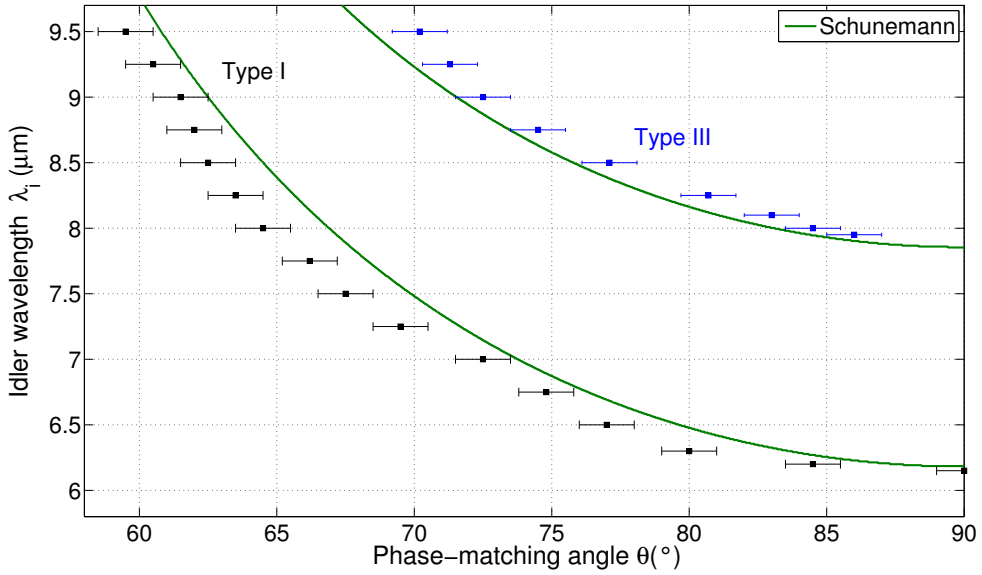

Figure 23: Type I DFG (λ^e_p, λ^o_s, λ^o_i) and type III DFG (λ^e_p, λ^o_s, λ^e_i) tuning curves of $CdSiP_2$ with a pump at $\lambda_p = 1.064\,\mu m$. Squares are the experimental data. The green curves correspond to calculations from Equations (111).

6

IMPROVING SELLMEIER EQUATIONS FOR $CdSiP_2$

The direct measurements of phase-matching directions using the sphere method are highly valuable since these data can be used directly when a crystal has to be oriented for a specific targeted frequency conversion process. The goal of this section is to take advantage of all the measurements performed on $CdSiP_2$ to provide new and more accurate Sellmeier equations for this crystal over its entire transparency range. Two different and separate methods have been implemented to do so. In the first part of this section, the same method that was used for RTP, RTA and CTA [46] as well as for YCOB [47] is implemented. It is referred to as the "classical method". On the other hand, the "new method" uses a different approach and strives to determine the values of the principal refractive indices directly from the phase-matching angles measurements. This chapter therefore constitutes a comparison between these two methods. It also includes some calculations that relate the accuracy of the measurements of refractive indices to that of the calculations of the phase-matching angles. As far as we know, such calculations have never been reported. They provide useful insight to interpret the results obtained with the "classical" and "new" methods.

6.1 SIMULTANEOUS FIT OF THE PHASE-MATCHING CURVES

In order to derive new Sellmeier coefficients of $CdSiP_2$, the first method that we carried out is the simultaneous nonlinear fit of the four phase-matching curves. In this section, the procedure to do so is described, and the results obtained with this "classical method" are discussed.

6.1.1 *The "classical" method*

The method used for the nonlinear fit of the phase-matching curves is now described. First of all, we assume that the ordinary and extraordinary dispersion formulas can be well described by a two independent oscillators Sellmeier expression in the transparency range of the crystal:

$$n_{o,e}^2(\lambda) = A_{o,e} + \frac{B_{o,e}\,\lambda^2}{\lambda^2 - C_{o,e}} + \frac{D_{o,e}\,\lambda^2}{\lambda^2 - E_{o,e}} \tag{114}$$

Since $CdSiP_2$ is known to be optically isotropic for $\overline{\lambda} = 0.5145\,\mu m$ [51], the ten Sellmeier coefficients must satisfy the condition:

$$A_o + \frac{B_o\overline{\lambda}^2}{\overline{\lambda}^2 - C_o} + \frac{D_o\overline{\lambda}^2}{\overline{\lambda}^2 - E_o} = A_e + \frac{B_e\overline{\lambda}^2}{\overline{\lambda}^2 - C_e} + \frac{D_e\overline{\lambda}^2}{\overline{\lambda}^2 - E_e} \tag{115}$$

And we decide here to express the coefficient B_e as a function of the other nine coefficients. A nonlinear algorithm is then implemented in order to find the values of these nine coefficients fitting at best the phase-matching curves of Figures (22) and (23).

The phase-matching angles for Type I SHG and Type I DFG can be expressed analytically as a function of the principal refractive indexes through:

$$\sin^2(\theta_{PM}^{SHG\,TypeI}) = \frac{n_o(\lambda_\omega)^{-2} - n_o(\frac{\lambda_\omega}{2})^{-2}}{n_e(\frac{\lambda_\omega}{2})^{-2} - n_o(\frac{\lambda_\omega}{2})^{-2}} \tag{116}$$

And

$$\sin^2(\theta_{PM}^{DFG\,Type\,I}) = \frac{\left(\frac{\lambda_p}{\lambda_s}n_o(\lambda_s) + \frac{\lambda_p}{\lambda_i}n_o(\lambda_i)\right)^{-2} - n_o(\lambda_p)^{-2}}{n_e(\lambda_p)^{-2} - n_o(\lambda_p)^{-2}} \tag{117}$$

But for type II SHG, and type III DFG, only numerical estimates can be obtained for the phase-matching angles $\theta_{PM}^{SHG\,Type\,II}$ and $\theta_{PM}^{DFG\,Type\,III}$ since the BPM condition involves two extraordinary indexes. By plugging Equation (114) in the analytical and numerical expressions of the phase-matching angles and by numerically evaluating the phase-matching angles for different sets of the nine Sellmeier coefficients, it is possible to find their values that fit the four phase-matching curves simultaneously. The algorithm implemented is the nonlinear Levenberg Marquardt algorithm as we did in previous studies of the same kind [46]. The Matlab code and some details regarding the theory of this algorithm can be found here [63]. The convergence of the simultaneous fit of the four phase-matching curves is not an easy thing to obtain though. As it is fairly easy to fit the four phase-matching curves separately, the idea to succeed in the convergence of the simultaneous fit is to look for a set of nine Sellmeier coefficients that is a linear combination of the parameters fitting the curves separately. This procedure has a priori no mathematical justification but it allows us to derive some sets of parameters that fit first two out of four curves, then three out of four curves and eventually the simultaneous fit of the four phase-matching curves.

Practically speaking, this process leads to the convergence of the algorithm, and the four phase-matching curves are fitted successfully. It yields the first set of "good" parameters of the simultaneous fit. Nevertheless, unrealistic values of the refractive indices $n \approx 8$ are obtained with the new coefficients. In order to correct for these unrealistic values, a multiplication factor was applied to all the Sellmeier coefficients. This coefficient was chosen to match the values of the indices with the values measured on prism at 1.064 µm. Because the phase-matching conditions remain unchanged when the same multiplicative factor is applied to the ordinary and

extraordinary refractive indices (see Equations 116 and 117 for example), such a procedure does not affect the phase-matching angles. The choice of 1.064 µm was arbitrary.

Figures (25) and (24) display the results of the fit in terms of predicting the phase-matching angles of $CdSiP_2$ with these new dispersion equations. They are as good as the Equations (111) to predict the SHG phase-matching curves, but much better in terms of type III DFG. However, even if the type I DFG is improved, it is still not perfect.

6.1.2 *Results and discussion*

The resulting new Sellmeier equations are:

$$\begin{aligned} n_o^2(\lambda) &= 3.72202 + \frac{5.91985\,\lambda^2}{\lambda^2 - 0.06408} + \frac{3.92371\,\lambda^2}{\lambda^2 - 2071.59} \\ n_e^2(\lambda) &= 4.68981 + \frac{4.77331\,\lambda^2}{\lambda^2 - 0.08006} + \frac{0.91879\,\lambda^2}{\lambda^2 - 496.71} \end{aligned} \tag{118}$$

where λ is in microns. The refractive indices obtained with these new Sellmeier coefficients are valid between 2.5 µm and 9 µm and plotted in Figure (26). They can be compared with the equations from the values measured on prism. It is clear that these new Sellmeier coefficients suffer from two main problems. First, the corresponding birefringence value differs from two previous measurements on $CdSiP_2$ [42, 40]. Second, the values of the principal refractive indexes obtained with these new coefficients deviate by a factor of 0.02 from the measurements performed using the minimum deviation technique. However, the value of the ANCPM idler that can be calculated from Equations (118) with a 1064 nm pump at 21°C is 6.10 µm. This value is in perfect agreement with the latest NCPM idler value reported for $CdSiP_2$ [23]. The Sellmeier Equations (111) overestimate this value and predict an idler wavelength at 6.18 µm.

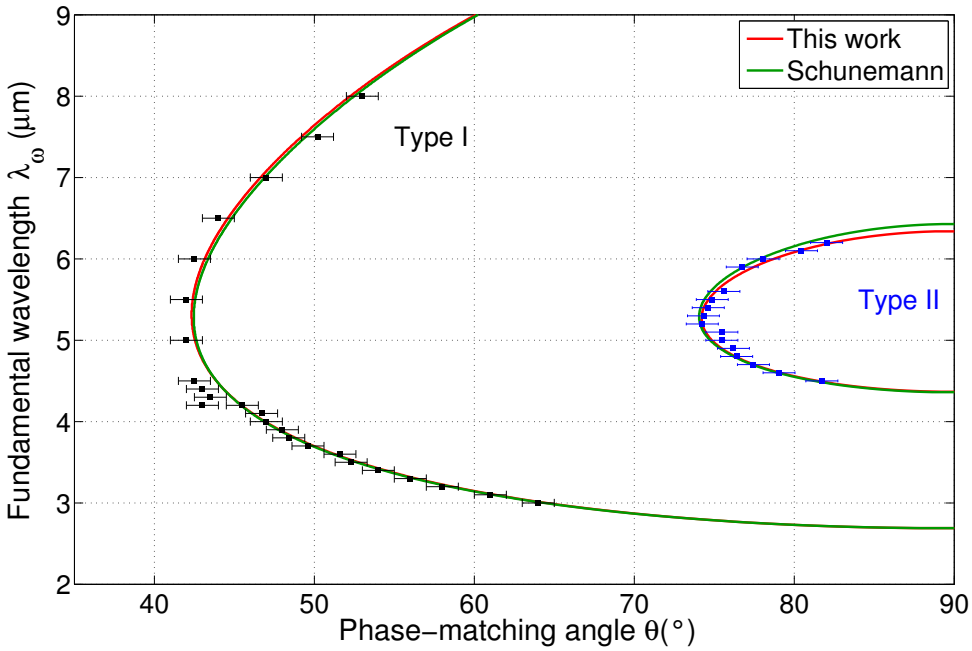

Figure 24: Type I SHG (λ^o_ω, $\lambda^e_{2\omega}$) and type II SHG ($\lambda^{o,e}_\omega$, $\lambda^e_{2\omega}$) tuning curves of $CdSiP_2$. The red curves are calculated with Equations (118) from this work. The green curves still correspond to calculations from Equations (111).

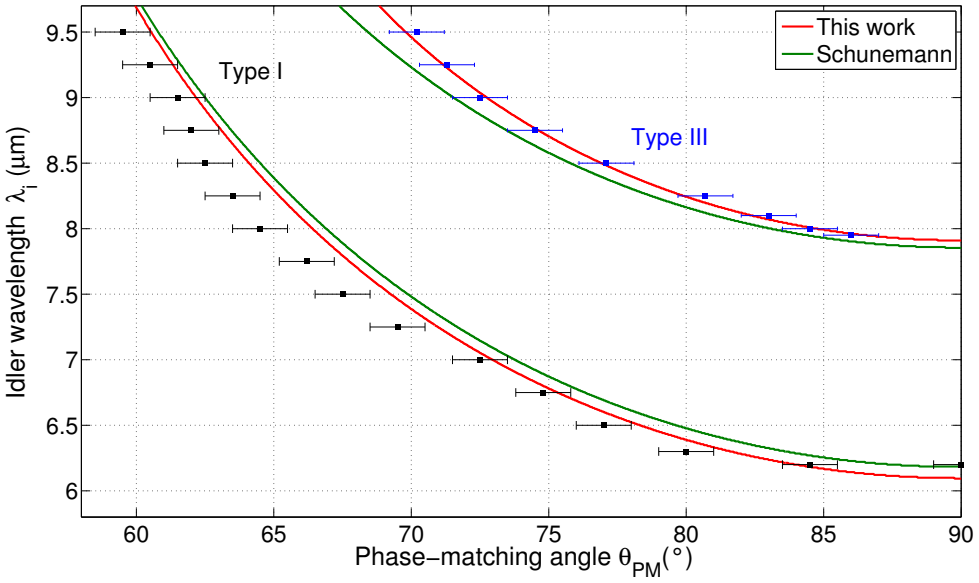

Figure 25: Type I DFG (λ^e_p, λ^o_s, λ^o_i) and type III DFG (λ^e_p, λ^o_s, λ^e_i) tuning curves of $CdSiP_2$ with a pump at $\lambda_p = 1.064\,\mu m$ The red curves are calculated with Equations (118) from this work. The green curves still correspond to calculations from Equations (111).

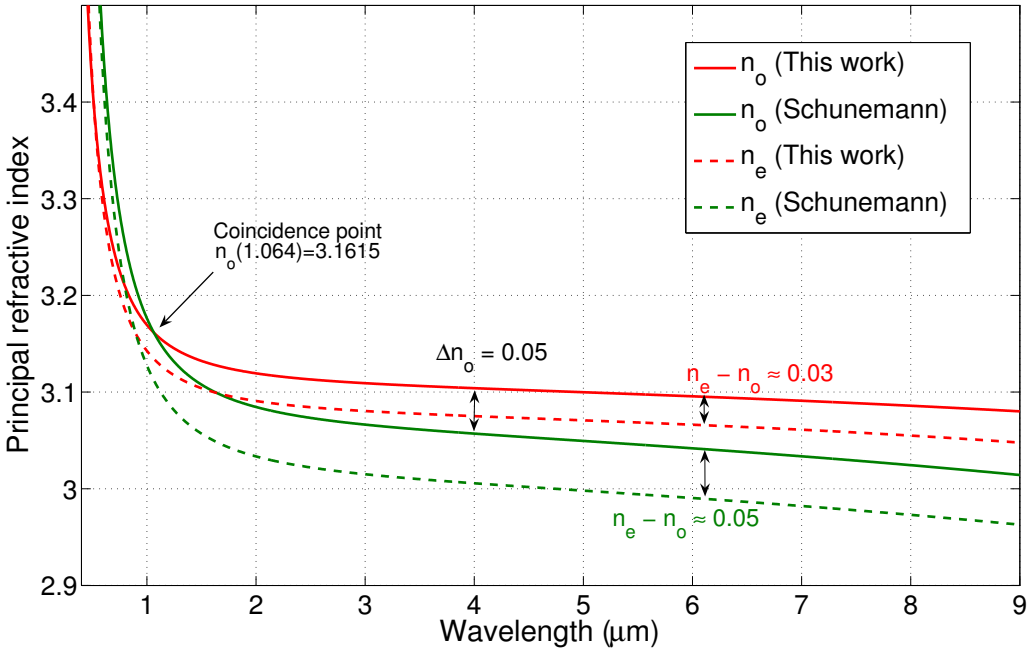

Figure 26: Comparison between the principal refractive indices obtained by Schunemann (Equations 111) and those obtained from the classical method (Equations 118).

6.2 DETERMINATION OF REFRACTIVE INDICES ABOVE 6 µM

In this section, the "new method" that we have designed is presented and applied to CSP. Its starting point is the fact that the discrepancy between the experimental phase-matching curves and the calculations from Equation (111) is more noticeable on the DFG curves than on the SHG curves (See Figures 22 and 23). As the DFG experiments solicit the indices at the pump wavelength 1.064 µm, the signal wavelength between 1.2 µm and 1.3 µm and the corresponding idler wavelength in the range 6 - 9.5 µm where no refractive index measurements have been reported (See Figure 20), it is legitimate to assume that the discrepancies observed in Figure (23) arise from this lack of measurements at long wavelengths. In this section, we will present a new method of determination of the principal refractive indices of CSP above 6 µm which relies on a careful exploitation of the measured DFG phase-matching angles.

6.2.1 *The new method*

Here we show that a proper exploitation of the DFG phase-matching angles measured with the sphere method can give access to the values of the principal ordinary and extraordinary refractive indices at the idler wavelengths for which DFG has been measured, if we assume that the refractive indices are known in the range of pump and signal wavelengths.

The main idea of this method is that if we want to determine the two principal indices at a given wavelength λ_i, $n_o(\lambda_i)$ and $n_e(\lambda_i)$, it is sufficient to know two values of the extraordinary index $n_e(\lambda_i, \theta_1)$ and $n_e(\lambda_i, \theta_2)$ at the same idler wavelength λ_i but corresponding to two different angles θ_1 and θ_2. These two values are indeed related to the two unknowns of our problem $n_o(\lambda_i)$ and $n_e(\lambda_i)$ through the expression of the extraordinary index in a uniaxial crystal at θ_1 and θ_2 (see equation 14) :

$$\begin{cases} n_e(\lambda_i, \theta_1) = \left(\dfrac{\cos^2\theta_1}{n_o^2(\lambda_i)} + \dfrac{\sin^2\theta_1}{n_e^2(\lambda_i)}\right)^{-1/2} \\ \\ n_e(\lambda_i, \theta_2) = \left(\dfrac{\cos^2\theta_2}{n_o^2(\lambda_i)} + \dfrac{\sin^2\theta_2}{n_e^2(\lambda_i)}\right)^{-1/2} \end{cases} \tag{119}$$

And it turns out that this system has a unique solution in terms of $n_o(\lambda_i)$ and $n_e(\lambda_i)$ if $\theta_1 \neq \theta_2$, which can be found by inverting a 2×2 matrix. The principal ordinary index is given by:

$$n_o(\lambda_i)^{-2} = \frac{\sin^2\theta_2 n_e(\lambda_i, \theta_1)^{-2} - \sin^2\theta_1 n_e(\lambda_i, \theta_2)^{-2}}{\cos^2\theta_1 \sin^2\theta_2 - \cos^2\theta_2 \sin^2\theta_1} \tag{120}$$

While the expression of the principal extraordinary index is:

$$n_e(\lambda_i)^{-2} = \frac{-\cos^2\theta_2 n_e(\lambda_i, \theta_1)^2 + \cos^2\theta_1 n_e(\lambda_i, \theta_2)^2}{\cos^2\theta_1 \sin^2\theta_2 - \cos^2\theta_2 \sin^2\theta_1} \tag{121}$$

In our case, we obtain the two values of the extraordinary index at θ_1 and θ_2 by exploiting the type I DFG ($\lambda_p^e, \lambda_s^o, \lambda_i^o$) and type III DFG ($\lambda_p^e, \lambda_s^o, \lambda_i^e$) tuning curves measured experimentally. The corresponding BPM conditions that we use were given in Table (4):

$$\begin{cases} n_o(\lambda_i) &= \dfrac{\lambda_i}{\lambda_p} n_e(\lambda_p, \theta_{PM}^I) - \dfrac{\lambda_i}{\lambda_s} n_o(\lambda_s) \\ n_e(\lambda_i, \theta_{PM}^{III}) &= \dfrac{\lambda_i}{\lambda_p} n_e(\lambda_p, \theta_{PM}^{III}) - \dfrac{\lambda_i}{\lambda_s} n_o(\lambda_s) \end{cases} \tag{122}$$

If the refractive indices of CSP are known in the range of pump and signal wavelengths (from measurements on prisms or interferometric measurements for example), and the phase-matching angles θ_{PM}^I and θ_{PM}^{III} have been measured experimentally, it is possible to determine $n_o(\lambda_i) = n_e(\lambda_i, \theta = 0)$ and $n_e(\lambda_i, \theta_{PM}^{III})$ from Equations (122).

On Figure (23) one sees that type I DFG is possible for an idler wavelength between 6.15 and 9.5 µm, while type III DFG is only possible above 8 µm. For idler wavelengths where type I only is possible (i.e. between 6.15 and 8 µm) the ordinary refractive index is the only principal index that can be determined directly. For idler wavelengths where both type I and type III have been found (i.e. above 8 µm), the principal extraordinary refractive index can also be obtained by putting $\theta_1 = 0$ and $\theta_2 = \theta_{PM}^{III}$ in Equation (121):

$$n_e(\lambda_i) = \left(\frac{n_e(\lambda_i, \theta_{PM}^{III})^{-2} - n_o(\lambda_i)^{-2} \cos^2 \theta_{PM}^{III}}{\sin^2 \theta_{PM}^{III}} \right)^{-1/2} \tag{123}$$

Table (5) gives the resulting values of the principal ordinary and extraordinary refractive indices at the idler wavelength based on the values of the refractive index at the signal and pump wavelengths measured on a prism. The ordinary refractive index is given from 6.15 up to 9.5 µm, whereas the value of the extraordinary refractive index is given only above 8 µm. It is worth stressing here that these two values are the only ones that are in agreement with both the measurements made using the minimum deviation technique and the direct measurement of the phase-matching angles.

Since the determinations that we perform here are based in part on the values of refractive indices determined using the prism technique, we cannot expect a better accuracy for our results. Because of the centimetrical size of the prism, and because of the range of pump and signal wavelengths considered here (1 to 1.3 µm) , the accuracy of these measurements is quite good and can be estimated to be lower than 0.0005 (see section 6.3.3 for more numerical justification). For a conservative accuracy of 0.5° on the measurements of the phase-matching angles, the error bars can be computed according to the formulas (122) and (123). The experimental error bars are then between five and ten times higher than the accuracy on the measurements on the prisms, this ratio coming primarily from the ratios between the wavelengths in Equation (122). In our case, the error bars end up in the range 0.002 to 0.005. Despite such error bars (that could be reduced with a better precision in the phase-matching angle measurements), Table (5) shows that these new values differ significantly from the values extrapolated from prism measurements.

λ_i (µm)	New method				Extrapolation from prism method	
	θ_{PM}^{I} (°)	θ_{PM}^{III} (°)	$n_o(\lambda_i)$	$n_e(\lambda_i)$	n_o	n_e
6.15	90		3.041(6)		3.0407	
6.2	84.5		3.042(3)		3.0403	
6.3	80		3.044(5)		3.0395	
6.5	77		3.043(2)		3.0378	
6.75	74.8		3.039(6)		3.0357	
7	72.5		3.037(5)		3.0336	
7.25	69.5		3.039(2)		3.0314	
7.5	67.5		3.038(7)		3.0291	
7.75	66.2		3.036(1)		3.0268	
7.95		86				
8	64.5	84.5	3.035(9)	2.971(3)	3.0244	2.9730
8.1		83				
8.25	63.5	80.7	3.032(9)	2.966(3)	3.0220	2.9706
8.5	62.5	77.1	3.030(3)	2.963(8)	3.0195	2.9681
8.75	62	74.5	3.025(2)	2.961(3)	3.0169	2.9655
9	61.5	72.5	3.020(2)	2.958(4)	3.0143	2.9629
9.25	60.5	71.3	3.018(5)	2.953(0)	3.0115	2.9601
9.5	59.5	70.2	3.017(3)	2.947(5)	3.0088	2.9574

Table 5: DFG phase-matching angles and principal refractive indices of CSP determined between 6.15 and 9.5 µm with the new method. The extrapolated values from Equations (111) are shown for comparison.

6.2.2 *Comments*

We would like to stress here, that this method is nothing else than the inversion of the expression of the extraordinary refractive index. What is new to us is the way to obtain the values of the extraordinary refractive index at different angles. The use of the DFG phase-matching angles is a direct way to relate the index of the material at long wavelengths based on the values of the indices at short wavelengths. Such direct measurements of the DFG phase-matching angles can only be obtained with the sphere or cylinder method, that find here a beautiful fundamental application.

It is worth mentioning that with very little modifications, this method should be applicable to many more DFG types, and many more nonlinear crystals. Moreover, we find it very powerful to determine the refractive indices of a crystal in remote part of the spectrum where no sources are available.

Eventually, note that the determination of the two principal refractive indices of a crystal at a given idler wavelength will be all the more accurate as more values of the extraordinary index at different angles are known. A very nice way to obtain these different values is by measuring the phase-matching curves at different pump wavelengths, for example.

6.2.3 *Results and discussion*

Once the values of the two refractive indices were obtained for wavelengths above 6 µm, we looked for new Sellmeier equations in agreement with both the measurements made using the minimum deviation technique and our latest values between 6.15 and 9.5 µm. Two separate and independent fits (see Figure 27) of the ordinary and extraordinary refractive indices yielded the new Sellmeier coefficients displayed in Equation (124). The resulting dispersion curves do reconcile the measurements made on prism and our new measurements.

They are given by:

$$\begin{aligned} n_o^2(\lambda) &= 2.59322 + \frac{6.75619\,\lambda^2}{\lambda^2 - 0.09928} - 0.00267\,\lambda^2 \\ n_e^2(\lambda) &= 3.65508 + \frac{5.39945\,\lambda^2}{\lambda^2 - 0.11911} - 0.00389\,\lambda^2 \end{aligned} \tag{124}$$

These new dispersion curves match better not only our new values of refractive indices but also the values measured on prism. This makes these equations a priori more reliable than those obtained from the classical method (See Figure 26). The tuning curves predicted with these new Sellmeier equations were calculated and are shown in Figure (28) and (29). The strength of the new method to predict the DFG tuning curves is clear: there is an obvious improvement in the prediction of the DFG tuning curves (See Figure 28). On the other hand, these new Sellmeier coefficients worsen the prediction of the SHG phase-matching angles (See Figure 29). This new

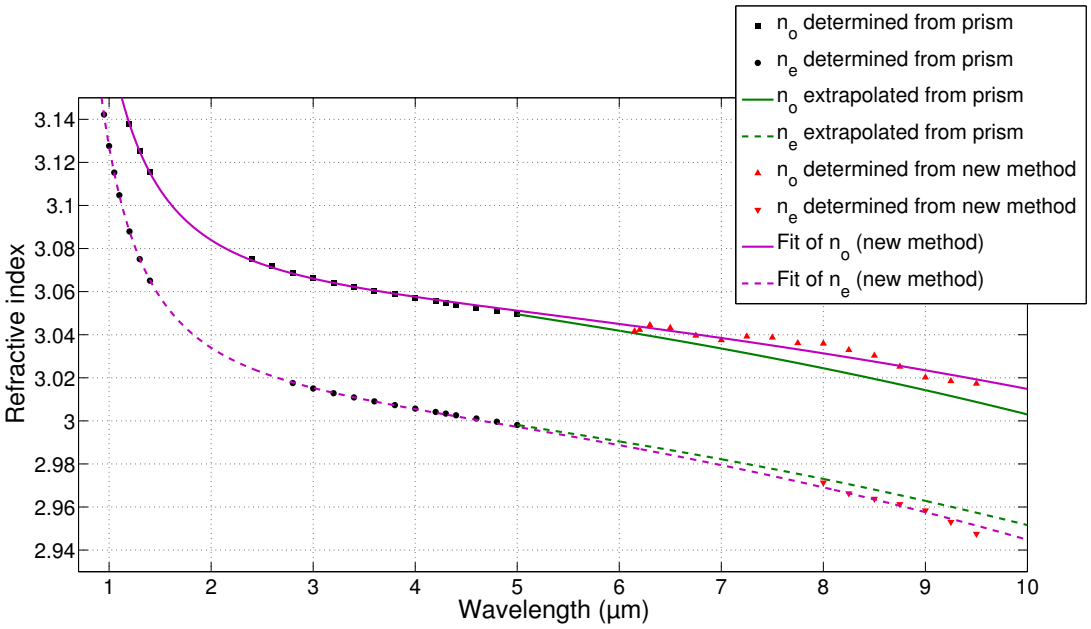

Figure 27: Refractive indices of $CdSiP_2$ determined with our new method and comparison between the new Sellmeier equations given in Equation (124) and the extrapolation above 6 µm of the Sellmeier equations (111).

discrepancy can be attributed to the fact that the large corrections imposed on the indices at the idler wavelengths (above 6 µm) have substantially modified the refractive indices in the range 3 to 5 µm, and by the same extent the SHG phase-matching angles. As a result, this new method does not turn out to be more successful than the "classical" method in terms of predicting all the phase-matching directions measured experimentally. Nevertheless, the strongest argument in favor of this new method is the unicity of the values of the two indices that we can determine. This determination is straightforward and does not require a complicated and nonlinear algorithm involving 12 parameters.

6.3 REFRACTIVE INDEX ACCURACY AND PHASE-MATCHING MEASUREMENTS

The work presented so far illustrates how difficult it can be to obtain Sellmeier equations capable to predict both the values of the principal refractive indices and the phase-matching angles of a nonlinear crystal. The measurements performed by Schunemann et al. show that the prediction of the DFG phase-matching angles is problematic even when good measurements are made on a centimetric prism. The comparison between all the Sellmeier equations available for CSP given in [48] has stressed upon the fact that the prediction of both SHG and DFG phase-matching angles is still an issue in CSP. The case of $CdSiP_2$ presented in this dissertation is by no mean an isolated case in the field of phase-matching metrology, as suggested by the controversy on the phase-matching angle of SHG at 10.6 µm in ZGP [64]. It is widely acknowledged that the principal refractive indices must be known with an accuracy in the order of $\delta n = \pm 10^{-4}$ to predict

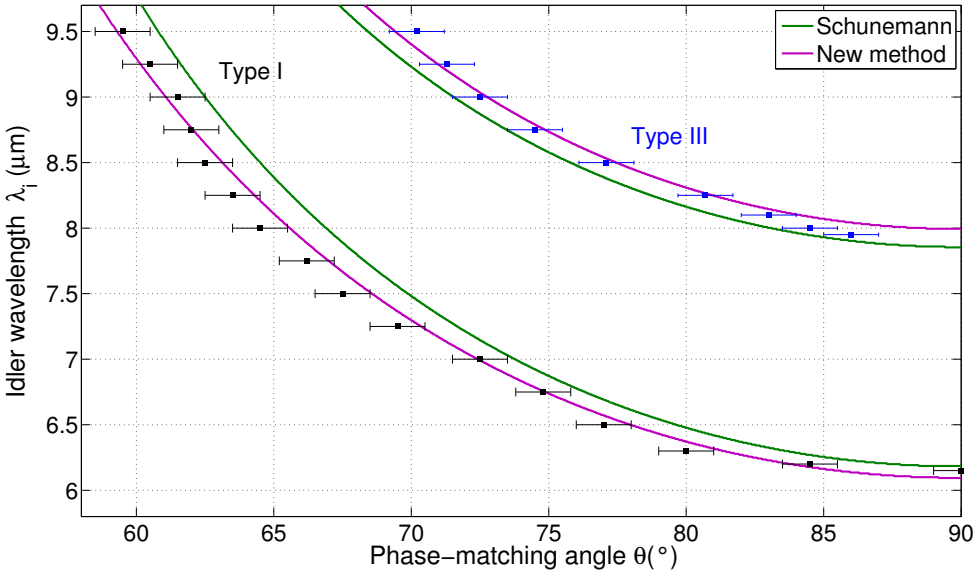

Figure 28: Type I DFG (λ_p^e, λ_s^o, λ_i^o) and type III DFG (λ_p^e, λ_s^o, λ_i^e) tuning curves of $CdSiP_2$ with a pump at $\lambda_p = 1.064\,\mu m$ The purple curves are calculated with Equations (124). The green curves still correspond to calculations from Equations (111).

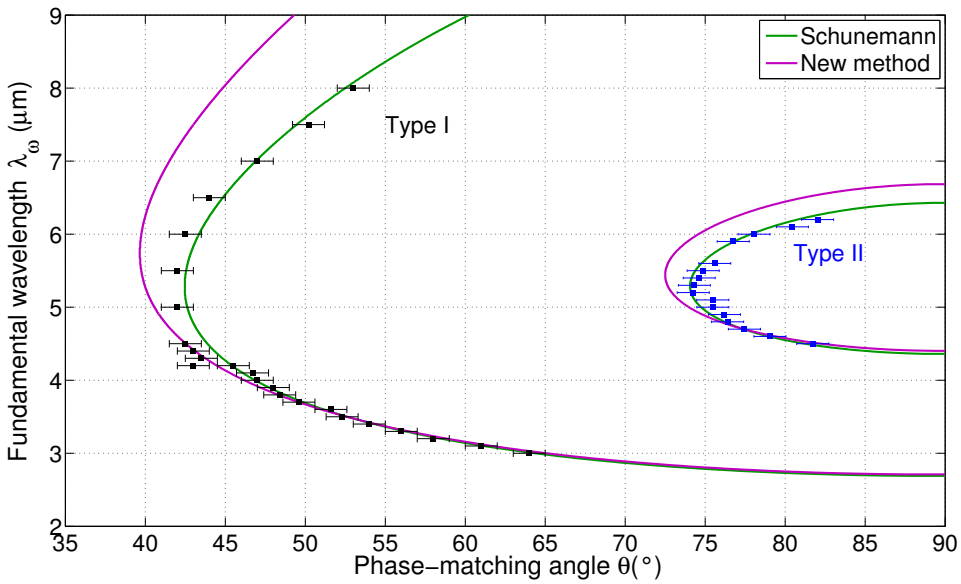

Figure 29: Type I SHG (λ_ω^o, $\lambda_{2\omega}^e$) and type II SHG ($\lambda_\omega^{o,e}$, $\lambda_{2\omega}^e$) tuning curves of $CdSiP_2$. The purple curves are calculated with Equations (124). The green curves still correspond to calculations from Equations (111).

the phase-matching angles with an accuracy better than 0.5°. In this work we want to discuss this statement: we provide an exhaustive and qualitative analysis that relates the accuracy of the principal refractive indices to that of the phase-matching angle calculations. As far as we know, such a study has never been reported, mostly because of the heavy and tedious calculations it requires. We have carried out all these calculations and we present now some of the results that we obtained with a specific focus on negative uniaxial crystals such as CSP.

6.3.1 *Example of calculation procedure*

We develop here the classical uncertainty calculation procedure that we carried out. For the sake of clarity, we chose to present only the calculation for Type I DFG in CSP.

We first assume that the phase-matching condition is fulfilled. And this constitutes the zeroth order of our calculation:

$$\frac{n_e(\lambda_p, \theta_{PM})}{\lambda_p} = \frac{n_o(\lambda_s)}{\lambda_s} + \frac{n_o(\lambda_i)}{\lambda_i} \tag{125}$$

When small variations δn_o^p, δn_e^p, δn_o^s, and δn_o^i of the principal refractive indices $n_o(\lambda_p)$, $n_e(\lambda_p)$, $n_o(\lambda_s)$, and $n_o(\lambda_i)$ are taken into account, the phase-matching angle is varied by a small amount $\delta\theta_{PM}$. The phase-matching condition (125) can then be rewritten as:

$$\frac{n_{ex}(\lambda_p, \theta_{PM}) + \delta n_{ex}(\lambda_p, \theta_{PM})}{\lambda_p} = \frac{n_o(\lambda_s) + \delta n_o^s}{\lambda_s} + \frac{n_o(\lambda_i) + \delta n_o^i}{\lambda_i} \tag{126}$$

And in order to relate the variation of the phase-matching angle, $\delta\theta_{PM}$, to the variations δn_o^p, δn_e^p, δn_o^s, and δn_o^i, we first need to differentiate the expression of the extraordinary index given in Equation (14):

$$n_{ex}(\lambda, \theta) = \left[\frac{\cos^2\theta}{n_o^2(\lambda)} + \frac{\sin^2\theta}{n_e^2(\lambda)}\right]^{-1/2} \tag{127}$$

The subsript $-ex$ means that we refer to the spatially dependent value of the extraordinary index and not to the principal value of the extraordinary index. Small variations of the principal refractive indices δn_o or δn_e and of the angle $\delta\theta$ will modify n_{ex} through its partial derivatives and according to :

$$\delta n_{ex}(\lambda, \theta) = \frac{\partial n_{ex}}{\partial \theta}\delta\theta + \frac{\partial n_{ex}}{\partial n_o}\delta n_o + \frac{\partial n_{ex}}{\partial n_e}\delta n_e \tag{128}$$

The three partial derivatives in Equation (128) can be worked out and one finds :

$$\delta n_{ex}(\lambda, \theta) = \frac{1}{2}\sin(2\theta)(n_e(\lambda)^{-2} - n_o(\lambda)^{-2})n_{ex}(\lambda, \theta)^3\delta\theta + \cos^2\theta\frac{n_{ex}(\lambda, \theta)^3}{n_o(\lambda)^3}\delta n_o + \sin^2\theta\frac{n_{ex}(\lambda, \theta)^3}{n_e(\lambda)^3}\delta n_e$$

By plugging this equation into Equation (126) and developing $n_{ex}(\lambda_p, \theta)$ one finds:

$$\frac{1}{2}\sin(2\theta_{PM})(n_e(\lambda_p)^{-2} - n_o(\lambda_p)^{-2})n_{ex}(\lambda_p,\theta_{PM})^3\delta\theta_{PM} \quad + \cos^2\theta_{PM}\frac{n_{ex}(\lambda_p,\theta_{PM})^3}{n_o(\lambda_p)^3}\delta n_o^p + \sin^2\theta_{PM}\frac{n_{ex}(\lambda_p,\theta_{PM})^3}{n_e(\lambda_p)^3}\delta n_e^p$$
$$= \quad \lambda_p\left(\frac{\delta n_o^s}{\lambda_s} + \frac{\delta n_o^i}{\lambda_i}\right)$$

For $\theta_{PM} \neq 90°$, and this is an important assumption for the following work that we present here, we then get:

$$\delta\theta_{PM} = \frac{-\cos^2\theta\frac{n_{ex}^3(\lambda_p,\theta_{PM})}{n_o(\lambda_p)^3}\delta n_o^p - \sin^2\theta\frac{n_{ex}^3(\lambda_p,\theta_{PM})}{n_e(\lambda_p)^3}\delta n_e^p + \lambda_p\left(\frac{\delta n_o^s}{\lambda_s} + \frac{\delta n_o^i}{\lambda_i}\right)}{\frac{1}{2}\sin(2\theta_{PM})(n_e(\lambda_p)^{-2} - n_o(\lambda_p)^{-2})n_{ex}^3(\lambda_p,\theta_{PM})}$$

After some simplifications, it then comes:

$$\begin{aligned}\delta\theta_{PM} \quad = \quad & \frac{1}{\Delta n(\lambda_p)}\left(-\frac{\cot\theta_{PM}}{2}\delta n_o^p - \frac{\tan\theta_{PM}}{2}\frac{n_o(\lambda_p)^3}{n_e(\lambda_p)^3}\delta n_e^p\right) \\ & + \frac{1}{\Delta n(\lambda_p)}\left(\frac{\lambda_p}{\lambda_s}\frac{1}{\sin 2\theta_{PM}}\frac{n_o(\lambda_p)^3}{n_{ex}(\lambda_p,\theta_{PM})^3}\delta n_o^s + \frac{\lambda_p}{\lambda_i}\frac{1}{\sin 2\theta_{PM}}\frac{n_o(\lambda_p)^3}{n_{ex}(\lambda_p,\theta_{PM})^3}\delta n_o^i\right)\end{aligned} \tag{129}$$

where we have used the value of the birefringence at the pump wavelength :

$$\Delta n(\lambda_p) = n_e(\lambda_p) - n_o(\lambda_p) \tag{130}$$

The expression (129) gives directly the change in the phase-matching angle $\delta\theta_{PM}$ due to small variations of the refractive indices δn_o^p, δn_e^p, δn_o^s, and δn_o^i. And the partial derivatives of the phase-matching angle are (now !) easily obtained by identifying Equation (129) with:

$$\delta\theta_{PM} = \frac{\partial\theta_{PM}}{\partial n_o(\lambda_p)}\delta n_o^p + \frac{\partial\theta_{PM}}{\partial n_o(\lambda_s)}\delta n_o^s + \frac{\partial\theta_{PM}}{\partial n_o(\lambda_i)}\delta n_o^i + \frac{\partial\theta_{PM}}{\partial n_e(\lambda_p)}\delta n_e^p + \frac{\partial\theta_{PM}}{\partial n_e(\lambda_s)}\delta n_s^s + \frac{\partial\theta_{PM}}{\partial n_e(\lambda_i)}\delta n_e^i \tag{131}$$

6.3.2 *Matrix formalism and results for CSP*

For DFG, the partial derivatives of the phase-matching angle with respect to the refractive indices can be summarized in a matrix J_{DFG} that we define as:

$$J_{DFG} = \begin{pmatrix} \frac{\partial \theta_{PM}}{\partial n_o(\lambda_p)} & \frac{\partial \theta_{PM}}{\partial n_e(\lambda_p)} \\ \frac{\partial \theta_{PM}}{\partial n_o(\lambda_s)} & \frac{\partial \theta_{PM}}{\partial n_e(\lambda_s)} \\ \frac{\partial \theta_{PM}}{\partial n_o(\lambda_i)} & \frac{\partial \theta_{PM}}{\partial n_e(\lambda_i)} \end{pmatrix} \tag{132}$$

– For type I DFG, the corresponding matrix is obtained directly from Equations (129) and (131). It writes:

$$J_{DFG\,TypeI} = \frac{1}{\Delta n(\lambda_p)} \begin{pmatrix} -\frac{\cot\theta_{PM}}{2} & -\frac{\tan\theta_{PM}}{2} \times \frac{n_o(\lambda_p)^3}{n_e(\lambda_p)^3} \\ \frac{\lambda_p}{\lambda_s} \times \frac{1}{\sin 2\theta_{PM}} \times \frac{n_o(\lambda_p)^3}{n_{ex}(\lambda_p,\theta_{PM})^3} & 0 \\ \frac{\lambda_p}{\lambda_i} \times \frac{1}{\sin 2\theta_{PM}} \times \frac{n_o(\lambda_p)^3}{n_{ex}(\lambda_p,\theta_{PM})^3} & 0 \end{pmatrix} \tag{133}$$

where $\Delta n(\lambda_p) = n_e(\lambda_p) - n_o(\lambda_p)$.

– The matrix corresponding to type III DFG was also obtained in a similar manner. It writes:

$$J_{DFG\,TypeIII} = \frac{1}{(\Delta n_{DFG\,III})} \begin{pmatrix} -\frac{\lambda_s}{\lambda_p}\frac{\cot\theta}{2}\frac{n_{ex}(\lambda_p,\theta)^3}{n_o(\lambda_p)^3} & -\frac{\lambda_s}{\lambda_p}\frac{\tan\theta}{2}\frac{n_{ex}(\lambda_p,\theta)^3}{n_e(\lambda_p)^3} \\ \frac{1}{sin2\theta} & 0 \\ \frac{\lambda_s}{\lambda_i}\frac{\cot\theta}{2}\frac{n_{ex}(\lambda_i,\theta)^3}{n_o(\lambda_i)^3} & \frac{\lambda_s}{\lambda_i}\frac{\tan\theta}{2}\frac{n_{ex}(\lambda_i,\theta)^3}{n_e(\lambda_i)^3} \end{pmatrix} \tag{134}$$

where

$$\Delta n_{DFG\,III} = \frac{\lambda_s}{\lambda_p}\frac{n_{ex}(\lambda_p,\theta)^3}{n_o(\lambda_p)^3}\Delta n(\lambda_p) - \frac{\lambda_s}{\lambda_i}\frac{n_{ex}(\lambda_i,\theta)^3}{n_o(\lambda_i)^3}\Delta n(\lambda_i) \tag{135}$$

Similarly to the case of DFG, we can use a 2×2 matrix J_{SHG} to represent the results of the uncertainty on the types I and II SHG phase-matching angles. This matrix is chosen as:

$$J_{SHG} = \begin{pmatrix} \frac{\partial \theta_{PM}}{\partial n_o(\lambda_\omega)} & \frac{\partial \theta_{PM}}{\partial n_e(\lambda_\omega)} \\ \frac{\partial \theta_{PM}}{\partial n_o(\lambda_{2\omega})} & \frac{\partial \theta_{PM}}{\partial n_e(\lambda_{2\omega})} \end{pmatrix} \tag{136}$$

– For Type I SHG, we obtained the following matrix:

$$J_{SHG\,I} = \frac{1}{\Delta n(\lambda_{2\omega})} \begin{pmatrix} \frac{1}{\sin 2\theta_{PM}} \times \frac{n_o(\lambda_{2\omega})^3}{n_{ex}(\lambda_{2\omega},\theta)^3} & 0 \\ -\frac{\cot\theta_{PM}}{2} & -\frac{\tan\theta_{PM}}{2}\frac{n_o(\lambda_{2\omega})^3}{n_e(\lambda_{2\omega})^3} \end{pmatrix} \tag{137}$$

where $\Delta n(\lambda_{2\omega})$ is the birefingence at $\lambda_{2\omega}$.

– For Type II SHG, the matrix has four non-vanishing elements and writes :

$$J_{SHG\,II} = \frac{1}{(\Delta n_{SHG\,II})} \begin{pmatrix} \frac{1}{\sin 2\theta_{PM}} + \frac{\cot\theta_{PM}}{2} \times \frac{n_{ex}(\lambda_\omega,\theta_{PM})^3}{n_o(\lambda_\omega)^3} & \frac{\tan\theta_{PM}}{2} \times \frac{n_{ex}(\lambda_\omega,\theta_{PM})^3}{n_e(\lambda_\omega)^3} \\ -\cot\theta_{PM}\frac{n_{ex}(\lambda_{2\omega},\theta_{PM})^3}{n_o(\lambda_{2\omega})^3} & -\tan\theta_{PM}\frac{n_{ex}(\lambda_{2\omega},\theta_{PM})^3}{n_e(\lambda_{2\omega})^3} \end{pmatrix} \tag{138}$$

where

$$\Delta n_{SHG\,II} = 2\frac{n_{ex}(\lambda_{2\omega},\theta_{PM})^3}{n_o(\lambda_{2\omega})^3}\Delta n(\lambda_{2\omega}) - \frac{n_{ex}(\lambda_\omega,\theta_{PM})^3}{n_o(\lambda_\omega)^3}\Delta n(\lambda_\omega) \tag{139}$$

Once again, the most important aspect of this (heavy) formalism is probably that it allows to separate the contributions of the different principal refractive indices to the error made on the prediction of the phase-matching angle. For example for type I DFG, a small variation of the principal ordinary refractive index at the idler wavelength δn_o^i leads to a variation of the phase-matching angle $\delta\theta_{PM})_{n_o^i}$ given by :

$$\delta\theta_{PM})_{n_o^i} = \frac{\partial\theta_{PM}}{\partial n_o(\lambda_i)}\delta n_o^i \tag{140}$$

Using the matrix $J_{DFG\,TypeI}$ in Equation (133) one finds:

$$\delta\theta_{PM})_{n_o^i} = \frac{1}{\Delta n(\lambda_p)} \times \frac{\lambda_p}{\lambda_i} \times \frac{1}{\sin 2\theta_{PM}} \times \frac{n_o(\lambda_p)^3}{n_{ex}(\lambda_p,\theta)^3}\delta n_o^i \tag{141}$$

The role of the birefringence must be stressed here. Equation (141) shows that in crystals with a large birefringence, the change (or uncertainty) in the phase-matching angles due to variations (or uncertainties) on the refractive indices will be lower. It also shows that the phase-matching angles of crystals with a large birefringence are more tolerant to refractive indices uncertainties. In the case of CSP, the birefringence is large [42]: $n_e - n_o \approx -0.05$, and it can be expected that small uncertainties in the values of the refractive indices will not impact too much the calculations of the phase-matching angles.

6.3.3 *Numerical results*

We now use the analytical results obtained previously to shine a new light on the work presented so far on the phase-matching angles in CSP. It is important to mention that the contribution of

the different refractive indices given in the J matrices above are strictly speaking depending on the wavelength at which the measurements are done (through either the dispersion of the birefrigence or the dispersion of the indices). Nevertheless, in the case of SHG, the variations of these contributions and especially of the ratio of the refractive indices appearing in the J matrices in Equations (137) and (138) are very small. As a consequence, the angular dependency of these contributions will be only analyzed in the case of a fixed fundamental wavelength at 6 µm. This wavelength corresponds to an "average" value of the fundamental SHG phase-matching wavelengths of CSP as shown on Figure (22). As for the DFG, the dispersion of the contributions cannot usually be neglected. It turns out that when the idler and signal wavelengths are far from degeneracy, the terms in the J matrices (133) and (134) are much less dispersive and the angular dependency takes over. We will then consider an idler wavelength of 8 µm for the calculations shown thereafter, since the two types of DFG have been measured for this idler wavelength in CSP (see Figure 23).

Lastly, the acceptable level of accuracy for the phase-matching measurements will be 0.5°.

6.3.3.1 *Second Harmonic Generation*

In this section we assume that all the refractive indices are measured (or determined) with an accuracy of $\delta n = \pm 0.0001$. And we want to compare the overall error it induces in the prediction of the phase-matching angles.

We start with type I SHG. We have plotted on Figure (30) the absolute values of the individual contributions of the three principal refractive indices to the phase-matching angle accuracy. These contributions are given as a function of the phase-matching angle and for a fundamental wavelength of λ_ω = 6 µm.

We see that the contributions of the three principal refractive indices are equivalent and remain below 0.15° when the phase-matching angle is between 45° and 60°, with the corresponding overall accuracy (sum of errors) falling below 0.3°. Above 60°, the contribution of the principal ordinary refractive index at $\lambda_{2\omega}$, has decreased to below 0.05° and this refractive index does not impact much the phase-matching angle calculations. On the other hand, the phase-matching angle is more strongly affected by the uncertainties in the values of the ordinary index at λ_ω and of the extraordinary index at $\lambda_{2\omega}$, so that their contributions dominate in the overall error $\delta\theta_{PM}$. This is a general feature that we have identified: there is always one or two principal refractive indices whose measurements limit the accuracy of the phase-matching angle calculations more than the others.

The phase-matching angles of Type I SHG in CSP have been found to lie in the range 40°-60° (see Figure 22). Around $\theta_{PM} = 45°$, the contributions of the three refractive indices can be seen to be equivalent. For the same theoretical uncertainty $\delta n = \pm 0.0001$ the phase-matching uncertainty is $\delta\theta_{PM} = 0.23°$.

Type II SHG on the other hand is much more demanding, mostly because the phase-matching angles are much closer to 90°. We have plotted the same curves as Figure (30) for Type II SHG on Figure (31). In the range where type II SHG phase-matching angles were measured, the same error

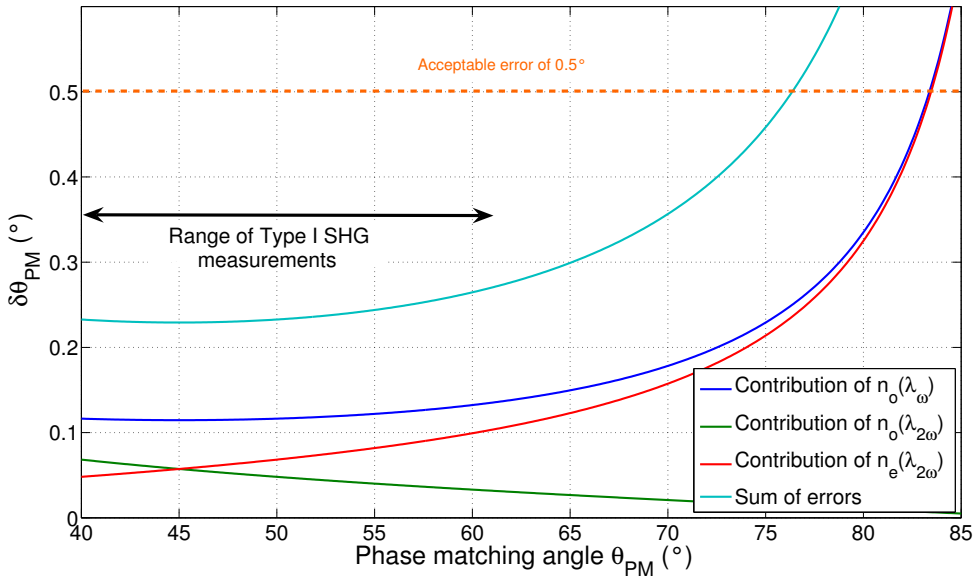

Figure 30: Plot of the absolute values of the different contributions of the principal refractive indices to the phase-mismatch error as a function of the phase-matching angle for type I SHG in $CdSiP_2$. An error of 0.0001 is assumed on each refractive index, the fundamental wavelength is set at 6 µm for the calculations presented here. The birefringence is -0.05.

$\delta n = \pm 0.0001$ results in an uncertainty of about 1.2° on the phase-matching angle. But contrary to Type I SHG, the contributions of the four indices are not equivalent, $n_e(\lambda_{2\omega})$ having a much stronger contribution than the others.

Based on these results it is possible to determine the maximum allowable uncertainty on each refractive index that would result in a prediction of the SHG phase-matching angles with an accuracy better than 0.5°. The results are shown for a fundamental wavelength at 6 µm in Table (6). As expected, the refractive indices with the higher contributions have the tightest requirements. For Type I SHG, there is only the refractive index at λ_ω that must be known with a good accuracy. For Type II SHG, three of the four indices must be known with an accuracy of 0.0025. This is the consequence of higher phase-matching angles as shown on Figure (31).

	Type I SHG	Type II SHG
θ_{PM}	43°	77°
$\delta n_o(\lambda_\omega)$	$\mathbf{4.5 \times 10^{-4}}$	2.0×10^{-4}
$\delta n_e(\lambda_\omega)$	Infinite	2.3×10^{-4}
$\delta n_o(\lambda_{2\omega})$	1×10^{-3}	1.6×10^{-3}
$\delta n_e(\lambda_{2\omega})$	1×10^{-3}	$\mathbf{1.2 \times 10^{-4}}$

Table 6: Maximum uncertainties on the principal refractive indices that can be tolerated if an accuracy better than 0.5 ° is targeted on the SHG phase-matching angles. The fundamental wavelength is $\lambda_\omega = 6$ µm.. The numbers appearing in bold heading are the most stringent requirements.

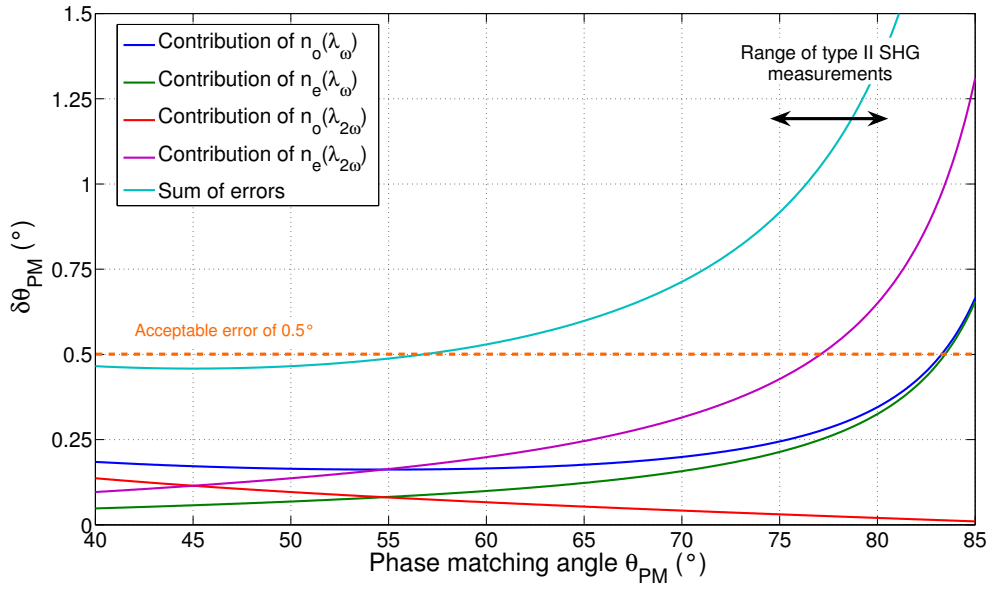

Figure 31: Plot of the absolute values of the different contributions of the principal refractive indices to the phase-mismatch error as a function of the phase-matching angle for type II SHG in $CdSiP_2$, when an error of 0.0001 is assumed on each refractive index. The birefringence is -0.05, and the fundamental wavelength is set at 6 µm for the calculations presented here.

Based on these calculations, we now try to give an estimation of the accuracy of the measurements made by Schunemann on prism. The difference between the calculations from Equation (111) and the measurements of the SHG phase-matching angles are shown on Figure (32). For Type I SHG, and except at 43°, these differences are randomly distributed around 0°, with an amplitude that does not exceed 0.7° (see Figure 32). Since for uncertainties of 0.0001, the scattering of the phase-matching angles is predicted to be about 0.13° (see Figure 30), the accuracy of the measurements on prism can then be assessed to be at least as good as ±0.0004 or ±0.0005 over the range of wavelengths solicited in type I SHG (i.e. between 2 and 8 µm). The fact that the measurements are performed over the range 40 to 60° must be stressed: predicting type I SHG phase-matching angles around 45° is the least problematic situation. In this range, the uncertainties on the refractive indices induce small modifications of the phase-matching angles. As for Type II SHG, calculations made with Equations (111) predict the phase-matching angles with a constant error of 0.5° and a random distribution of amplitude about 0.7° (see Figure 32). The index with the strongest contribution is $n_e(\lambda_{2\omega})$. And one sees on Figure (31) how critical this value is. An uncertainty or mistake as low as 0.0001 would induce an error on the calculation of the phase-matching angle between 0.5 and 1°. The other indices have smaller contributions, and a scattering of the measurements of 0.7° remains possible with uncertainties in the range of 0.0004. This value probably constitutes the average accuracy of the measurements made on prism between 2 and 8 µm.

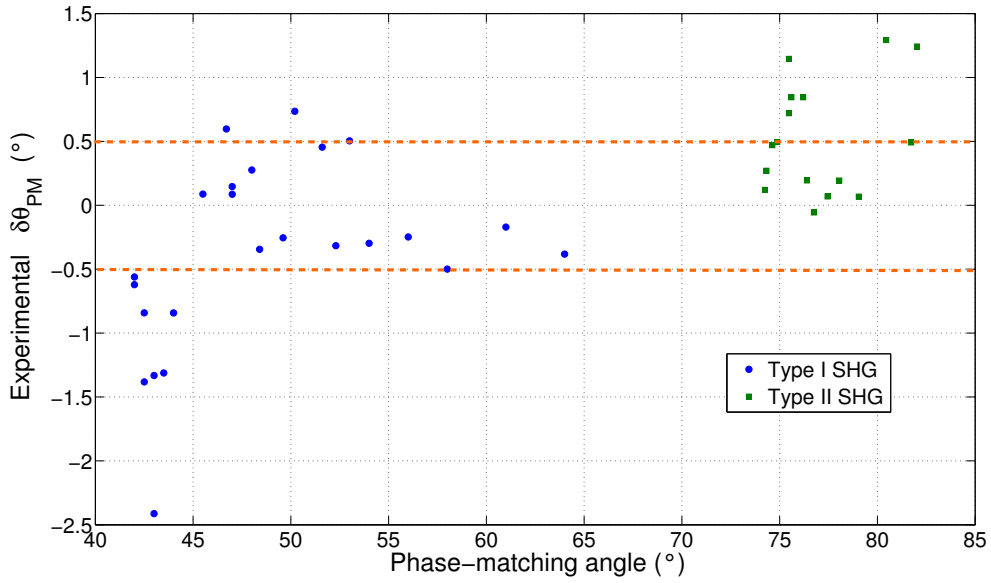

Figure 32: Deviations between the SHG phase-matching angles from our measurements and the calculations from Equations (111).

6.3.3.2 *Difference Frequency Generation*

We now present the numerical simulations for Type I DFG. The theoretical uncertainty on the indices is still taken as $\delta n = \pm 0.0001$ for the numerical simulations. Figure (33) gives the separate and overall contributions of the different refractive indices involved in the phase-matching calculations. The phase-matching angles of Type I DFG are in the range 60° to 90° as shown on Figure (23).

An accuracy as good as 0.0001 on all the refractive indices induces an error on the calculation of the phase-matching angles smaller than 0.5° if the phase-matching angle is below 75°, and between 0.5° and 1.5° for $\theta_{PM} > 75°$. The two refractive indices that contribute the most to the uncertainty of the phase-matching angle calculations are $n_o(\lambda_s)$ and $n_e(\lambda_p)$. This seems to confirm our analysis from Section (6.2.3) where we have found that the hypothesis of a mistake on the values of the indices at long wavelengths was not satisfactory to account for the discrepancies observed in Figure (23). The accuracy of $n_o(\lambda_s)$ and $n_e(\lambda_p)$ is actually dominating the accuracy with which one can predict the DFG phase-matching angles. This finding is even more strongly supported by the analysis of the different contributions of the refractive indices to Type III DFG phase-matching calculations, as shown on Figure (34). In the range where Type III DFG measurements have been performed, the extraordinary refractive index at the pump wavelength can be seen to have an impact almost five times stronger than the other indices on the uncertainty of the phase-matching angles.

We have plotted on Figure (35) the discrepancy between the measurements of the DFG phase-matching angles and the results obtained from calculations with Equations (111). In these measurements it is important to see that since the pump wavelength is fixed, $n_e(\lambda_p)$ and $n_o(\lambda_p)$

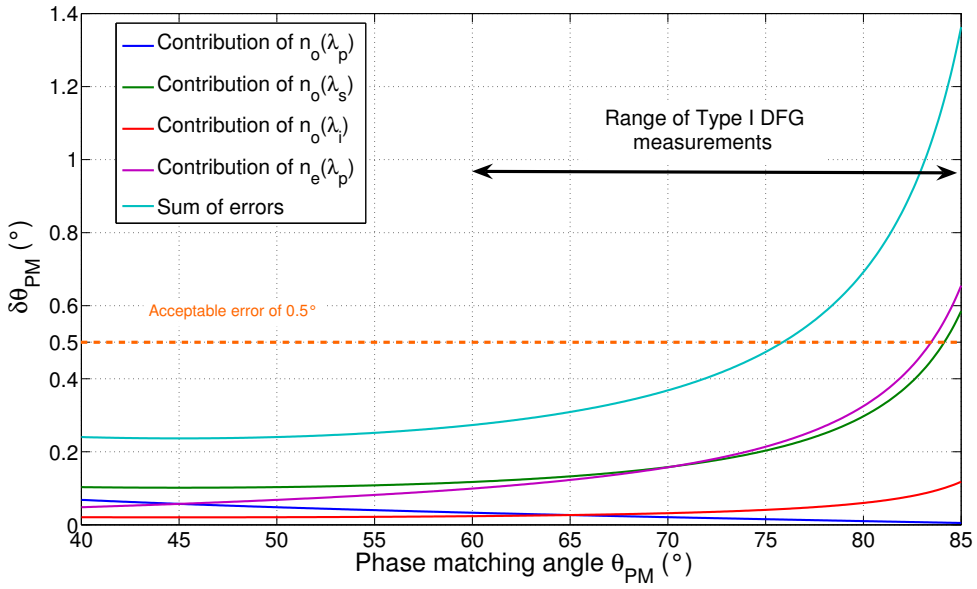

Figure 33: Plot of the absolute values of the different contributions of the principal refractive indices to the phase-mismatch error as a function of the phase-matching angle for type I DFG in $CdSiP_2$, when an error of 0.0001 is assumed on each refractive index. The birefringence is -0.05.

are constant, while $n_o(\lambda_s)$, $n_o(\lambda_i)$, $n_e(\lambda_s)$, $n_e(\lambda_i)$ change because of the changes of the phase-matching wavelengths. It is therefore legitimate to assume that the amplitude of the scattering of the deviations observed on Figure (35) arise from a scattering of the values of the refractive indices over the range of signal and idler, while the constant deviations of these measurements are due to a mistake on the value of the indices at the pump wavelength.

We will not go further in the numerical analysis of the deviations between the experimental and calculated DFG phase-matching angles because of the experimental uncertainties involved in the measurements on sphere. However, we believe that such an analysis could lead to the implementation of a fast and efficient algorithm that makes the best use of the phase-matching angle measurements to refine the values of the refractive indices of a crystal.

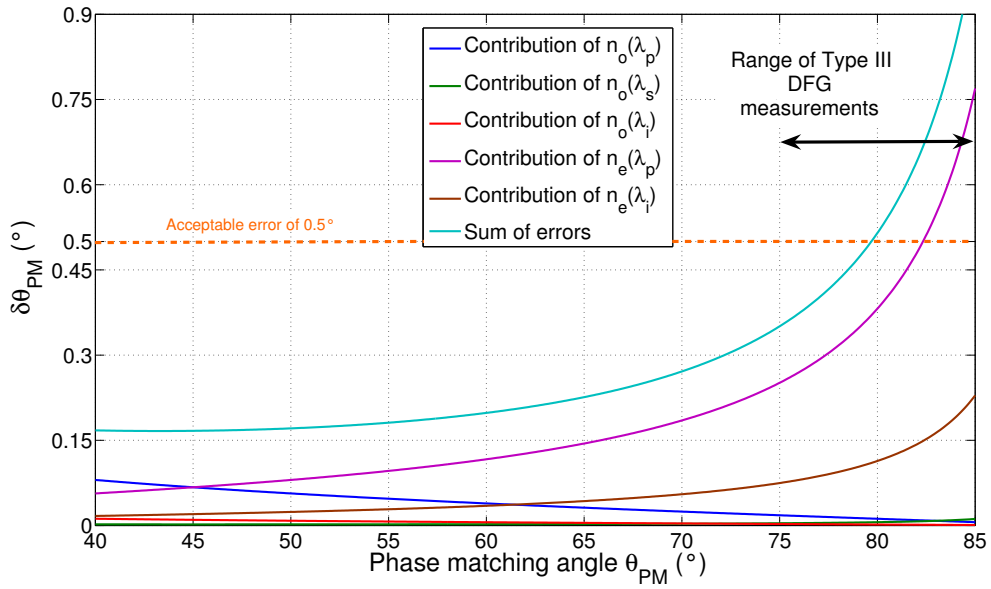

Figure 34: Plot of the absolute values of the different contributions of the principal refractive indices to the phase-mismatch error as a function of the phase-matching angle for type III DFG in $CdSiP_2$, when an error of 0.0001 is assumed on each refractive index. The birefringence is -0.05.

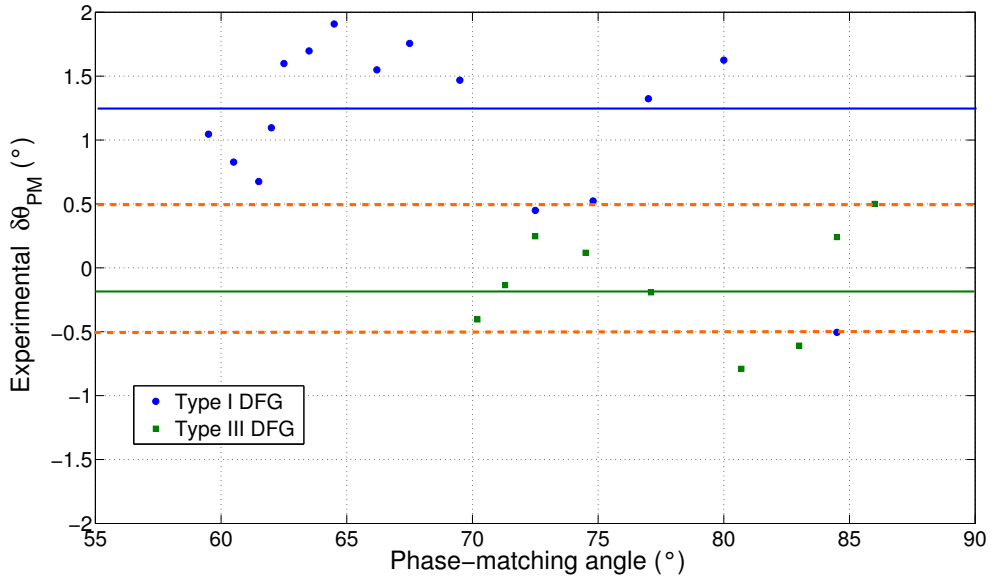

Figure 35: Deviations between the DFG phase-matching angles measurements and the calculations from Equations (111).

6.4 CONCLUSION

The first part of this work consisted in the simultaneous fit of the four tuning curves measured experimentally. The convergence of a nonlinear algorithm yielded a first set of new Sellmeier coefficients for CSP (Equations 118) that predicts the SHG phase-matching curves with a very good accuracy, as well as the DFG tuning curves with a better overall accuracy than any other coefficients [48] proposed for CSP including Equations (111). Nevertheless, the birefringence obtained with these coefficients is substantially lower than what was measured previously in $CdSiP_2$. The values of the principal refractive indices are also higher by 0.2 than what was measured on prisms.

As a consequence, in the second part, we tried to reconcile the measurements made on sphere and the measurements made on prism. A new method has been proposed to do so. We assumed that the measurements of the refractive indices on prisms were correct between 1 and 1.3 µm, and by combining properly the BPM conditions it was possible to determine the values of the refractive indices of the crystal above 6 µm in agreement with the DFG phase-matching directions. Sellmeier Equations (124) were then obtained from the fits of both the values measured on prism and the new values determined with our new method. These Sellmeier coefficients are in good agreement with the refractive indices measured by Schunemann on prism up to 3 µm, and they turn out to be the best coefficients to predict the DFG tuning curves measured on $CdSiP_2$. However they are unable to predict the SHG tuning curves obtained experimentally when the fundamental wavelength is above 5 µm.

As it was very difficult to obtain new Sellmeier equations giving both a good estimate of the values of the refractive indices and a good prediction of the phase-matching directions, we decided to investigate more in depth the relation between the accuracy of the refractive index measurements and that of the calculations of the phase-matching angles. The analytical expressions of the partial derivatives of the phase-matching angles that we obtained turn out to be very useful for the interpretation of the phase-matching curves. We have separated the different contributions of all the principal refractive indices involved in the calculations of the phase-matching angles and found that their different contributions vary strongly with the phase-matching angle. We emphasized the role of the birefringence in these calculations: we have seen that crystals with a large birefringence are more tolerant towards uncertainties of the refractive indices. Thanks to to its high birefringence, CSP is a very favorable case when the phase-matching must be predicted. For SHG in this crystal, when the phase-matching angle is near 45°, an accuracy of 0.0004 on all the refractive indices is good enough to predict the phase-matching angles within 0.5°. On the other hand, when the phase-matching gets closer to 70°, there is always one or two principal refractive indices that limit the accuracy more than the others. And it is the uncertainty on these indices that should be taken into account when one wants to predict the SHG phase-matching angles with a good accuracy. For Type II SHG it is the refractive index at the fundamental wavelength that must be determined with the best accuracy. The case of DFG phase-matching angles is even more demanding in terms of accuracy on the refractive indices. We have estimated that an accuracy of

0.0004, which is generally sufficient to predict the SHG phase-matching angles, is by no means capable of predicting the DFG phase-matching angles with a good accuracy. We advocate that measuring the DFG phase-matching directions with another pump wavelength should solve the too high dependency of the phase-matching angles on the ordinary and extraordinary refractive index at the pump wavelength.

7

INFRARED SUPERCONTINUUM GENERATION IN CSP

In this short chapter, we adress another topic: we investigate the conditions required to generate the broadest spectrum in a BPM crystal, and we apply these results to CSP.

7.1 INTEREST OF A SUPERCONTINUUM

Broadband as a lamp, bright as a laser [65]... Supercontinuum sources bridge the gap between classical incoherent but wide spectrum lamps and laser with a good spatial coherence and a high brightness. By combining the properties of these two types of light sources, supercontinua are expected to become highly useful in many different fields including gas detection or metrology [65]. Multispectral imaging has already opened new possibilities in the the field of microscopy [66]. Supercontinuum in the visible spectrum is now available commercially [67]. Photonic fibers provide single mode operation with very little pointing instability which are highly desirable features. The main physical mechanisms responsible for broadening in photonic crystal fibers have been identified [68]. Nevertheless, the longest wavelength of a supercontinuum generated in a photonic fiber is intrinsically limited by the onset of absorption of the fiber material. In the case of ZBLAN fiber, the spectra are typically restricted to below 4.5 µm [69]. New solutions leading to supercontinuum spanning the mid-infrared are still needed. Pumping an OPO at degeneracy with femtosecond pulses [70] is a very promising solution. Intracavity spectroscopy in broadband degenerate OPOs was recently applied successfully to the detection of traces of the main greenhouse gases [71], and could lead to applications in human breath analysis. Other options to generate mid-IR supercontinua are the use of chirped QPM gratings [72] or non-collinear phase-matching [73]. In this work we investigate the possibilities of using collinear birefringent phase-matching. It is shown that a good choice of the pump wavelength and BPM angle can lead to a "superdegeneracy" [48].

7.2 THEORETICAL TREATMENT

Here we are interested in deriving the conditions leading to the parametric generation of a spectrum as broad as possible in the transparency range of a second order nonlinear crystal. Only collinear type I DFG interactions are considered because Type I spectral acceptances are greater

than Type II and Type III. Let ω_p, ω_s and ω_i be the pump, signal and idler circular frequencies, with $\omega_p = \omega_s + \omega_i$. Type I collinear phase-mismatch Δk^I writes:

$$\Delta k^I = k^-(\omega_p, \theta) - k^+(\omega_s, \theta) - k^+(\omega_i, \theta) \tag{142}$$

For a given pump frequency $\overline{\omega_p}$, in a given direction of propagation $\overline{\theta}$, the phase mismatch can be expanded around degeneracy $2\omega_s \to \overline{\omega_p}$ as:

$$\Delta k^I(\omega_s, \overline{\theta}) \underset{\omega_s \to \overline{\omega_p}/2}{\approx} \begin{cases} \Delta k^I(\dfrac{\overline{\omega_p}}{2}, \overline{\theta}) \\ -(\omega_s - \dfrac{\overline{\omega_p}}{2})^2 \dfrac{\partial^2 k^+}{\partial \omega^2}\Big)_{\overline{\omega_p}/2} \\ -\dfrac{1}{12}(\omega_s - \dfrac{\overline{\omega_p}}{2})^4 \dfrac{\partial^4 k^+}{\partial \omega^4}\Big)_{\overline{\omega_p}/2} \end{cases} \tag{143}$$

If the direction of propagation $\overline{\theta}$ is chosen as the phase-matching direction at degeneracy, i.e.:

$$\Delta k^I(\frac{\overline{\omega_p}}{2}, \overline{\theta}) = 0 \tag{144}$$

then, the first term in Equation (143) vanishes and in the most general case, the Taylor Young expansion becomes:

$$\Delta k^I(\omega_s, \overline{\theta}) \underset{\omega_s \to \overline{\omega_p}/2}{\approx} -(\omega_s - \frac{\overline{\omega_p}}{2})^2 \frac{\partial^2 k^+}{\partial \omega^2}\Big)_{\overline{\omega_p}/2} \tag{145}$$

The phase-matching is therefore of a second order type, which is the usual case around degeneracy. But this expression is valid only if the second order derivative does not vanish. When it vanishes, i.e. for a specific pump frequency ω_p^* that satisfies the following relation:

$$\frac{\partial^2 k^+}{\partial \omega^2}\Big)_{\omega_p^*/2} = 0 \tag{146}$$

In this case, and only in this case, the phase-mismatch is given by a fourth order term with much smoother variations:

$$\Delta k(\omega_s, \overline{\theta}) \underset{\omega_s \to \omega_p^*/2}{\approx} -\frac{1}{12}(\omega_s - \frac{\omega_p^*}{2})^4 \frac{\partial^4 k^+}{\partial \omega^4}\Big)_{\omega_p^*/2} \tag{147}$$

And Equations (144) and (146) are the two mathematical conditions on the phase-matching angle and pump wavelength required to generate a supercontinuum in a BPM crystal. Physically

speaking, the condition (146) states that the signal and idler must be generated close to the zero dispersion wavelength (ZDW), λ_{ZDW}, of the higher index of a crystal, and given by:

$$\left.\frac{d^2 n^+}{d\lambda^2}\right)_{\lambda_{ZDW}} = 0 \tag{148}$$

The pump wavelength for which the supercontinuum is possible, λ_p^*, must be computed as half this ZDW (See Figure 36a):

$$\lambda_p^* = \frac{\lambda_{ZDW}}{2} \tag{149}$$

Once this pump wavelength has been determined, the optimal phase-matching angle, θ_{PM}^*, can be calculated or determined experimentally as the phase-matching angle of type I SHG for this specific fundamental ZDW (See Figure 36b).

For $CdSiP_2$, it is surprising to notice that the zero dispersion wavelengths calculated from Equations (111) and (118) are respectively 4.868 µm and 4.873 µm. The optimal pump wavelengths λ_p^* calculated with two different sets of Sellmeier equation for this crystal are therefore very close and between 2.434 µm and 2.436 µm. The optimal phase-matching angle is 42.8°. The spectrum that can be generated in this crystal when such a pump wavelength and such a phase-matching direction are used is shown on Figure (37). This spectrum spans roughly from 3.7 up to 7 µm.

7.3 COMPARISON BETWEEN INFRARED NONLINEAR CRYSTALS

7.3.1 *Optimal parameters*

The ability to produce a supercontinuum from commercially available lasers or "classical" lasers can be a strong argument when choosing a new nonlinear infrared material. We have computed the main conditions for such a supercontinuum to be generated in different BPM and QPM materials. In the case of QPM, instead of an optimal phase-matching angle, there is an optimal QPM period that must be chosen.

	λ_p^*(µm)	θ_{PM}^* (°)	d_{eff} (pm/V)	References
$CdSiP_2$	2.43	42.8	84.1/57.2	[39, 54]
$ZnGeP_2$	2.63	46.7	77.8/77.6	[55, 74]
$AgGaS_2$	2.04	30.9	13.1/6.7	[75, 76]
$AgGaSe_2$	2.86	40.0	31.0/19.9	[77, 78]
OP-GaAs	3.29	$\Lambda^* = 173\,\mu m$	91/57.9	[79, 80]

Table 7: Comparison between the optimal parameters leading to the generation of an infrared supercontinuum in uniaxial BPM materials and OP-GaAs.

Table (7) shows that the optimal phase-matching angles for BPM materials usually lie in the range 30-50° where the walk-off angle is the highest. This is a detrimental aspect of supercontinuum

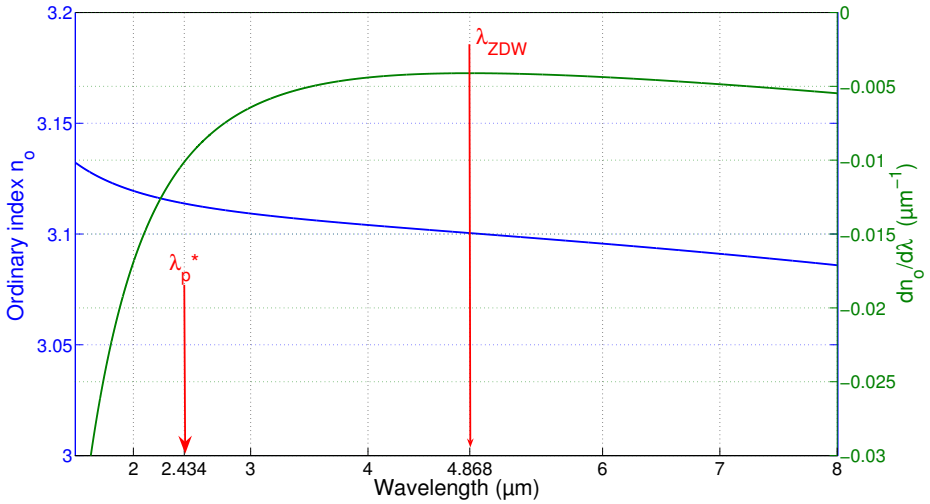

(a) Determination of the optimal pump wavelength $\lambda_p^* = \frac{\lambda_{ZDW}}{2}$ in $CdSiP_2$ ($n^+ = n_o$) based on Equations (118). The value of the ZDW is found as the wavelength for which the first order partial derivative of the higher refractive index reaches an extremum.

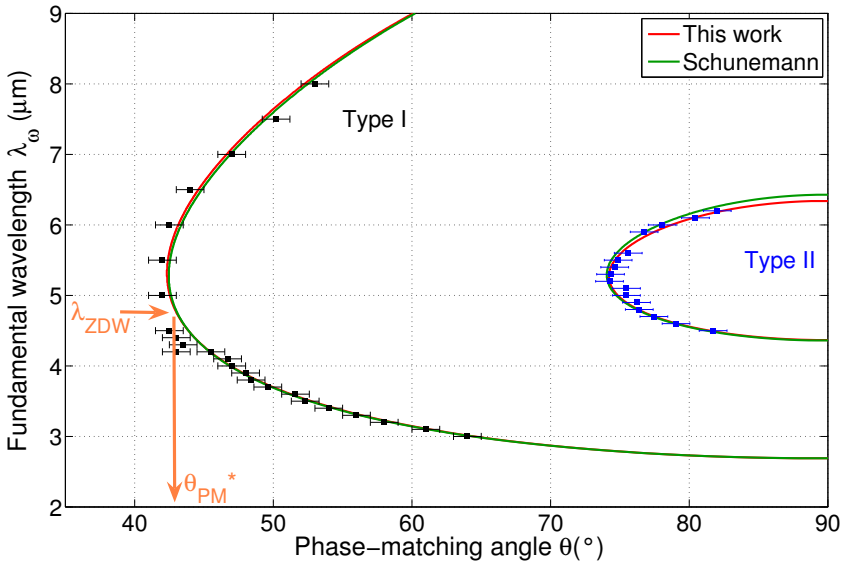

(b) Determination of the optimal phase-matching angle θ_{PM}^*

Figure 36: Practical determination of λ_p^* and $\theta_{PM}{}^*$ for generating a mid-IR supercontinuum in $CdSiP_2$

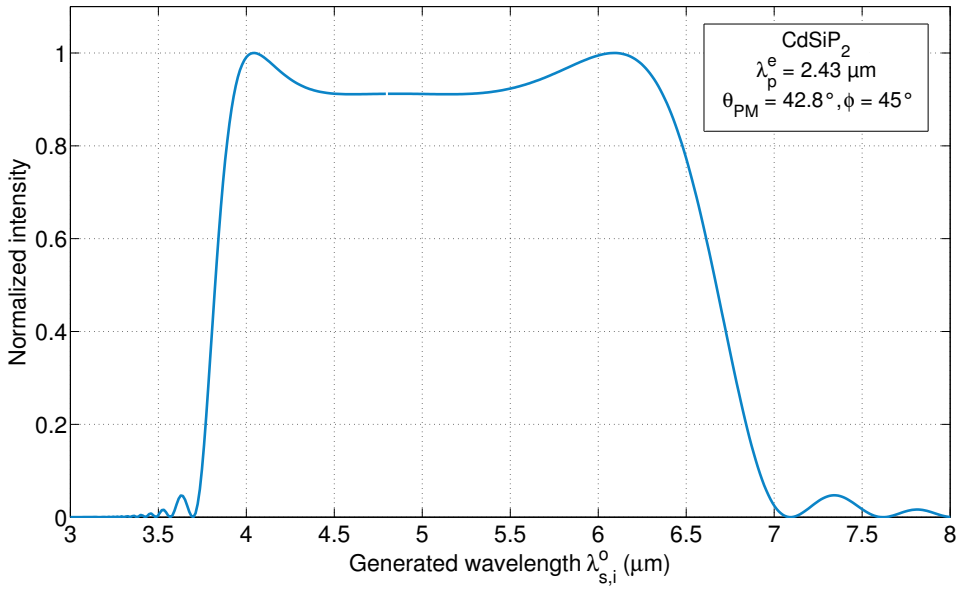

Figure 37: Normalized spectrum of the mid-IR Type I supercontinuum that can be generated in a 1 cm long CSP crystal oriented at $\theta^*_{PM} = 42.8°$. The pump wavelength must be $\lambda^*_p = 2.43$ µm.

generation in birefringent crystals because the interaction length will be reduced. The intrinsic noncriticity of quasi-phase-matching is very favorable compared with BPM here. OP-GaAs clearly stands out of the list of candidates, and several demonstrations of supercontinuum generation have been reported at Stanford University including an OPG spanning from 3 to 9 µm [81] and an OPO from 4.4 up to 5.4 µm [70].

7.3.2 *Spectral acceptances*

Depending on the applications and on the temporal regime of the pump source, different expressions of the spectral acceptance can be worked out. The first case is typical of low gains. In that case the spectral acceptance is imposed by the shape of the interference function in Equation (39) and fulfills:

$$sinc^2(\frac{\Delta kL}{2}) \geq 0.405 \tag{150}$$

When combined with Equation (147), the spectral accpetance at low gains writes:

$$\Delta\lambda_{low\,gains} = \frac{2}{\pi c}\left(\lambda^*_p\right)^2 \left(\frac{9.72}{L\beta_4}\right)^{1/4} \tag{151}$$

In the case of higher intensities, the equation ruling the gain of an OPG was given in Equations (50) and (55). The spectral acceptance can be taken as the bandwidth across which the gain coefficient is higher than half its maximal value (FWHM) which writes [73]:

$$\Delta k \leq \left(\frac{4\gamma_0 \ln 2}{L}\right)^{1/2} \tag{152}$$

When combined with Equation (147), this yields the spectral acceptance at high gains:

$$\Delta\lambda_{high\,gains} = \frac{2}{\pi c}\left(\lambda_p^*\right)^2 \left(\frac{24}{\beta_4}\right)^{1/4} \left(\frac{\gamma_0 \ln 2}{L}\right)^{1/8} \tag{153}$$

In every case, the coefficient β_4 is given by (see Equation 147):

$$\beta_4 = \left.\frac{\partial^4 k^+}{\partial\omega^4}\right)_{\omega_p^*/2} \tag{154}$$

Its amplitude drives the bandwidth of the fourth-order parametric process. It can be calculated numerically with available Sellmeier equations of a crystal. Moreover, since the gain coefficient increases with the pump intensity (See Equation 49), the high gain FWHM given in Equation (153) will also increase with the pump intensity. This dependency of the FWHM on the pump intensity could provide an efficient way to extrapolate the value of the coefficient β_4 from the values of FWHM measured at different pump intensities. Such direct measurements of β_4 are valuable tools when designing a supercontinuum source. Based on available Sellmeier equations for the different materials under comparison, we calculated the high gain spectral linewidths of a supercontinuum generated in the main nonlinear infrared crystals available commercially (See Table 8). Note that such a supercontinuum is not possible in CdSe for which no Type I DFG is possible.

	β_4 (10^{-54} s/m)	$\gamma_0(cm^{-1})$	$\Delta\lambda_{high\,gains}$ (µm) (Eq. 153)
$CdSiP_2$	18	12.0	3.6
$ZnGeP_2$	37	14.5	3.5
$AgGaS_2$	9.7	2.4	2.3
$AgGaSe_2$	4.5	4.5	0.9
OP-GaAs	130	8.0	3.7

Table 8: Broadband continuum phase-matching parameters for the four birefringent chalcopyrite crystals considered and OP-GaAs High gain bandwidths are given for L = 1cm, $I_{p,0} = 1\,GW/cm^2$ and parameters in Table (7). References used for the calculations of β_4 are the same as in Table (7).

Laser material	Wavelengths
$Nd^{3+} : YAG$	1.064 µm
$Er^{3+} : YAG$	1.645 µm; 2.94 µm
$Ho^{3+} : YAG$	2.09 µm
He/Ne	3.39 µm
$Cr^{2+} : ZnSe$	tunable from 2.4 to 2.6 µm
$Er^{3+} : YSGG$	2.79 µm
$Tm^{3+} : YAG$	2.0 µm

Table 9: Main infrared laser lines wavelengths [6, 82, 83].

7.4 INFRARED PUMP LASERS

The availability of commercial or classical laser wavelengths corresponding to the optimal pump wavelengths calculated above will probably be the major argument in the choice of a given material. In Table (9), we have summarized the wavelengths of the main infrared lasers, some of which may not be commercially available.

The generation of a supercontinuum was performed in a nanosecond OPO with a ZnSe:Cr^{2+} pump laser tuned at 2.35 µm and a $ZnGeP_2$ crystal cut at $\theta = 49.5°$, $\phi = 0°$ [84]. The linewidth of the OPO was only 1.2 µm which turns out to be smaller than what we calculated above. This can come from the fact that the optimal parameters that we calculated in Table (7) are somewhat different from those used in this experiment, and that the linewidth of such a supercontinuum is probably limited by the reflectivity of the OPO mirrors.

The tunable Cr^{2+}:ZnSe laser could be also perfectly matched with a $CdSiP_2$ crystal to build a compact mid-IR supercontinuum. If the wavelength of this laser is set at 2.43 µm, a broadband source spanning 3.5 to 6.5 µm (See Figure 37) could be obtained. Femtosecond Cr^{2+}:ZnSe lasers have been recently built [85], and the very high peak powers make the prospect of Optical Parametric Generators (OPG) based on CSP even more appealing. OPGs are better suited than OPOs when a very broadband spectrum must be generated because there is no cavity to restrict the supercontinuum linewidth.

8

CONCLUSION

The new nonlinear crystal CSP has been successfully grown in large enough sizes to allow optical parametric devices to be built. The interest in this crystal lies in its high figure of merit compared with its wide band gap. Angular noncritical temperature-tuned phase-matching is possible with a 1.064 µm pump wavelength enabling continuous tuning of the idler between 6.1 and 6.5 µm. Such a range of wavelengths may prove highly useful for future surgery applications [86]. Pumping at 1.064 µm is a strong advantage for this crystal compared to $ZnGeP_2$. Nevertheless, two-photon absorption at 1.064 µm in $CdSiP_2$ was recently found to be stronger than the primary estimations, primarily because of an overestimation of the band gap of CSP.

The extensive characterization of the phase-matching properties of CSP has been carried out using the sphere method. The phase-matching directions of SHG and DFG with a 1.064 µm pump wavelength have been measured directly. Two new sets of Sellmeier equations have been proposed in this work. The first set of Sellmeier equations was obtained through the simultaneous fit of the four phase-matching curves [39]. Despite the fact that these coefficients predict a birefringence (-0.03) lower than what has been reported for CSP (-0.05), they do a better job to predict the NCPM idler wavelength at room temperature.The second set of coefficients (Equation 124) takes advantage of a somewhat underestimated capability of the sphere method. The determination of the refractive indices is possible in the mid to far infrared when the DFG phase-matching directions are combined properly. Contrary to the SHG tuning curves, the DFG phase-matching curves of CSP are very well predicted by these coefficients.

An exhaustive analysis of the impact of uncertainties in the measurements of the refractive indices upon the calculations of the phase matching angles has been presented for the case of a negative uniaxial crystal such as CSP. The large birefringence of CSP makes this crystal less sensitive to the uncertainties on the values of the refractive indices. We have also shown numerically that for a given uncertainty, predicting the phase-matching angles at large θ angles is more difficult. The direct measurement of the DFG phase-matching angles provides valuable information with this respect. We believe that measuring the DFG tuning curves at different pump wavelengths can pave the way to a powerful and reliable method of refinement of the dispersion equations of nonlinear crystals.

Lastly, we have identified that type I DFG in a $CdSiP_2$ crystal cut at $\theta = 42.8°$ and $\phi = 45°$ and pumped with a ZnSe:Cr^{2+}laser emitting at 2.43 µm could generate an infrared supercontinuum

spectrum spanning from 3.5 to 7 µm. Optical Parametric Generation seems the most convenient way to do so. The interest in femtosecond ZnSe:Cr^{2+}lasers is clear. Noncritical phase-matching with a Nd:YAG laser pump wavelength and the prospect of a supercontinuum pumped by a ZnSe:Cr^{2+}laser make CSP very well suited for operation with available lasers, which is of course highly desirable when compact and coherent sources have to be designed.

Part III

WIDELY AND CONTINUOUSLY TUNABLE OPTICAL PARAMETRIC OSCILLATOR BASED ON A 5%MGO:PPLN CRYSTAL CUT AS PARTIAL CYLINDER

INTRODUCTION

This third Part is devoted to the experimental realization of the widely and continuously tunable optical parametric oscillator that will be the cornerstone of the all-parametric source described in the fourth Part of this dissertation. This optical parametric oscillator is based on a 5-mm-thick crystal of 5%MgO:PPLN that was periodically-poled at the Institute for Molecular Science at Okazaki in Japan and then cut and polished to optical quality as a partial cylinder in Grenoble, France. The interest of using a QPM crystal cut as a cylinder was already demonstrated ten years ago: this is the best way to achieve a wide, agile and continuous tunability with a monograting QPM sample. However, in these experiments the conversion efficiencies were low and limited by the optical damage threshold of the materials: because of the small thickness of the cylinders it was necessary to strongly focus the beams. In this work, two main steps have been taken to increase the output of a cylindrical OPO: firstly, the advent of 5-mm-thick samples allows one to increase the size of the beams in the OPO which leads to higher energetical output while avoiding damage; secondly, it is the first time that a partial cylinder is used in a frequency converter device.

Periodical poling of thick QPM materials in the transverse dimensions is a desperate need in nonlinear optics and a challenge in materials science. However, few crystals have been so far successfully poled on more than 5 mm. The first part of this chapter is therefore devoted to a quick overview of the massive QPM crystals and to the challenge of achieving a good and homogeneous grating structure over the entire thickness. 5%MgO:PPLN was the first crystal in which the inversion of the domains was reported on the full 5 mm thickness. The second part of this chapter then addresses the different steps necessary to build the partial cylinder OPO from the design of the partial cylinder to the optimization of the cavity. The choice of making a partial cylinder is driven by the need of both a high conversion efficiency and of a wide tuning range. The process to make such a partial cylinder is revealed and illustrated. The design of the resonating cavity is carefully described with great emphasis put on the search for the conditions of an operation of the OPO without any optical damage. Once the conditions of a safe operation are found, the output curves of the OPO are given. We demonstrate that the energetical performance of our partial cylinder OPO is similar to that of a 5-mm-thick 5%MgO:PPLN crystal cut as a slab. It is the first time that more than 2 mJ have been generated on the entire tuning range of a cylindrical OPO. The spectral and spatial properties of the signal beam generated in the OPO are presented and analyzed to obtain useful information on the performance of the partial cylinder OPO.

9

5-MM-THICK PERIODICALLY POLED 5%MGO:PPLN CYLINDERS

9.1 MASSIVE QPM MATERIALS

9.1.1 *5%MgO:PPLN versus other QPM materials*

Homogeneous poling of QPM materials with a wide aperture is nowadays a challenge at the edge of materials science [7] and driven by the need of always higher energetical optical parametric sources. The interest in large aperture QPM materials comes from the possibility of using beams with larger dimensions which lets one work with higher energetical pump input and thus higher output while avoiding damaging the sample. A few materials have been recently successfully poled with thickness above 3 mm, among which PPRTA [87], PPRKTP [88], 5%MgO:PPLN [89] and PPMgLT [90]. Commercial devices based on 1-mm-thick PPKTP or 3-mm-thick 5%MgO:PPLN samples are now available [91, 92]. The challenge in making thick periodically poled materials is two-fold. First of all, the electrical voltages required to switch the spontaneous polarisation increases with the crystal thickness. The electric field required to switch the polarisation over 1 mm is known as the coercive electric field of the material, and most of the recent work has focused on the search for lower coercive field materials. We give in Table (10) the values of the coercive field for the most common QPM materials. Since periodic-poling of massive samples requires high voltage power amplifiers delivering more than 20 kV per electrical pulse, the availability of higher power amplifiers is expected to become the limiting factor in the making of thicker periodically poled materials.

The second challenge in making such crystals is to keep the propagation of the domains vertical throughout the poling process [95]. Any deviation in the direction of propagation of the walls of the domains will result in inhomogeneous grating structures such as those depicted on Figure (38). Such defects in the propagation of the domains have been observed in situ by Kuroda et al. [95]. Inhomogeneous domains are detrimental not only because of a reduced effective gain coefficient associated with a duty ratio different from the ideal value of 0.5 (see section 2.2.3), but also because of the spectral inhomogeneities in the profile of the generated beams.

One major advantage of periodically-poled lithium niobate crystals (PPLN) is their transmission in the infrared. Even though oxide based materials are limited to Band II applications below 5 µm, the transmission of lithium niobate crystals extents further in the infrared than KTP,

QPM Material	Coercive field	Reference
PP-LN	22 kV/mm	[93]
PP-KTP	2.3 kV/mm	[94]
PP-RKTP	3.7 kV/mm	[88]
PP-RTA	1.8 kV/mm	[94]
5%MgO:PPLN	4.45 kV/mm	[95]
	3.4 kV/mm at T=120°C	[89]
7%MgO:PPLT	3.4 kV/mm at T = 23°C	[90]
	2.0 kV/mm at T = 150°C	

Table 10: Coercive field of the main QPM materials. Unless specified, these values are given at room temperature $T = 21°C$.

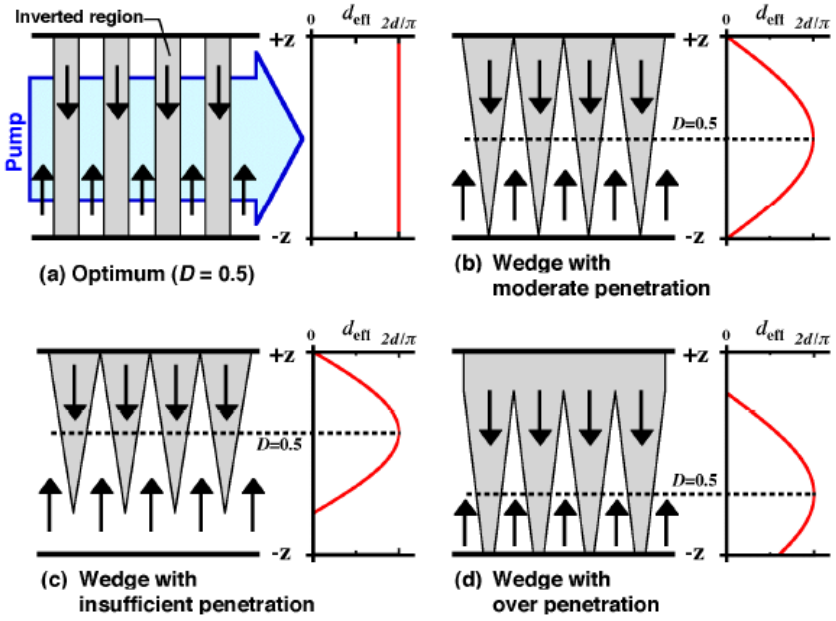

Figure 38: Illustration of the different vertical profiles of thick periodically poled materials with the corresponding vertical variation of the effective coefficient. The ideal case (a) is an effective coefficient without any vertical variation. This picture is taken from [24].

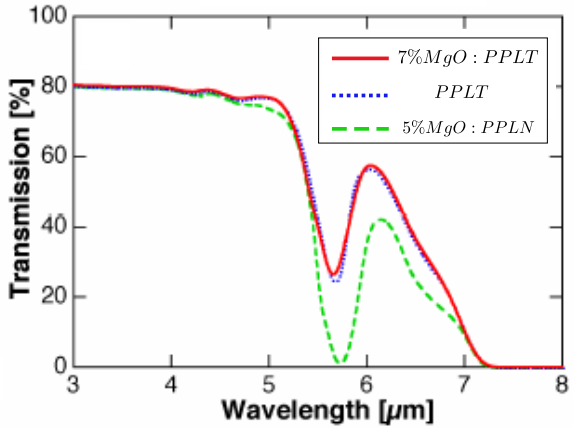

Figure 39: Transmission spectra in the mid infrared for the extraordinary polarization (along the z-axis) of 1-mm-thick samples: 5%MgO:PPLN (green), PPLT (blue) and 7%MgO:PPLT (red). This graph is taken from [103].

which is limited to 4.5 µm [96]. 5%MgO:PPLN transmits very well up to 5 µm from where the transmission starts decreasing as shown on Figure (39). On this graph, we have also represented the transmission spectra of two periodically-poled lithium tantalate crystals: 7%MgO:PPLT and PPLT. These two crystals have a better transmission in the infrared than 5%MgO:PPLN, as well as a lower coercive field (See Table 10).

Generation of an idler beam in the absorption band of a crystal reduces the interaction length and necessarily deposits heat in the crystal. Nevertheless, idler wavelengths as long as 6.6 µm have been generated in PPLN crystals [97, 98]. Figure (39) shows that PPLT is more promising than 5%MgO:PPLN when one is trying to generate wavelengths above 6 µm.

Another important criteria of comparison between different QPM materials used in nanosecond OPO is of course the optical damage threshold. For 5%MgO:PPLN it was found to be 95 MW/cm^2 [89]. It is lower than that of PPKTP by a factor of 2 [99]. Periodically-poled undoped $LiNbO_3$ crystals have been shown to be subject to a photorefractive damage, a phenomenom that is considerably reduced under doping with 5% MgO [100] or at higher temperature [101]. On the other hand, although PPKTP crystals are not subject to photorefractive damage, green-light induced infrared absorption (GRIIRA) has been identified in this material. Of course, the optical damage threshold value of a sample should be discussed in the light of the value of the effective coefficient of the parametric process. In the case of QPM, it is fair to compare the value of the d_{33} coefficient of the different ferroelectric materials that are considered: for KTP this coefficient is equal to 15.4 pm/V [102, 18]; it is smaller in amplitude than that of 5%MgO doped $LiNbO_3$ that has been measured to be -25.2 pm/V [12].

9.1.2 *Phase-matching properties of 5%MgO:PPLN*

The calculation of the quasi-phase-matching properties requires an accurate knowledge of the refractive indices of the crystal. In the case where the spontaneous polarization $\vec{P}_s$ is collinear to the z axis, the strongest nonlinear coefficient d_{33} is solicited (See section 2.2.2.2) if the three interacting waves are polarized along this z direction, i.e. the polar axis. This DFG between three extraordinary polarized waves is called Type 0. Based on previous measurements using the minimum deviation technique [104, 105], Paul et al. have provided a reliable Sellmeier equation for the extraordinary refractive index of 5%MgO:PPLN [106]. This dispersion relation was obtained by fitting additional experimental QPM phase-matching curves of an OPG pumped at 1.064 µm in a 12 channel multigratings sample.

The Sellmeier equation for the extraordinary refractive index obtained by Paul et al. [106] that we will be using extensively in this work is :

$$n_e^2(\lambda, T) = a_1 + b_1 f(T) + \frac{a_2 + b_2 f(T)}{\lambda^2 - a_3^2} + \frac{a_4 + b_3 f(T)}{\lambda^2 - a_5^2} - a_6 \lambda^2 \tag{155}$$

where the temperature T is given in °C, and the wavelength in microns. It is valid over the whole transparency range of the crystal. The coefficients appearing in Equation (155) are:

Coefficient	Value
a_1	5.319725
a_2	0.09147285
a_3	0.3165008
a_4	100.2028
a_5	11.37639
a_6	0.01497046
b_1	4.753469×10^{-7}
b_2	3.310965×10^{-8}
b_3	2.760513×10^{-5}

and

$$f(T) = (T - 24.5)(T + 570.82)$$

Based on this Sellmeier equation, it is possible to compute the solutions of the collinear quasi-phase-matching equation in 5%MgO:PPLN at $T_0 = 21°C$, i.e.:

$$\frac{n_e(\lambda_p, T_0)}{\lambda_p} - \frac{n_e(\lambda_s, T_0)}{\lambda_s} - \frac{n_e(\lambda_i, T_0)}{\lambda_i} = \frac{1}{\Lambda_{QPM}} \tag{156}$$

to find the first order Type 0 QPM phase-matching curve of an OPO or OPG with a pump wavelength of 1.064 µm. This curve is shown on Figure (40).

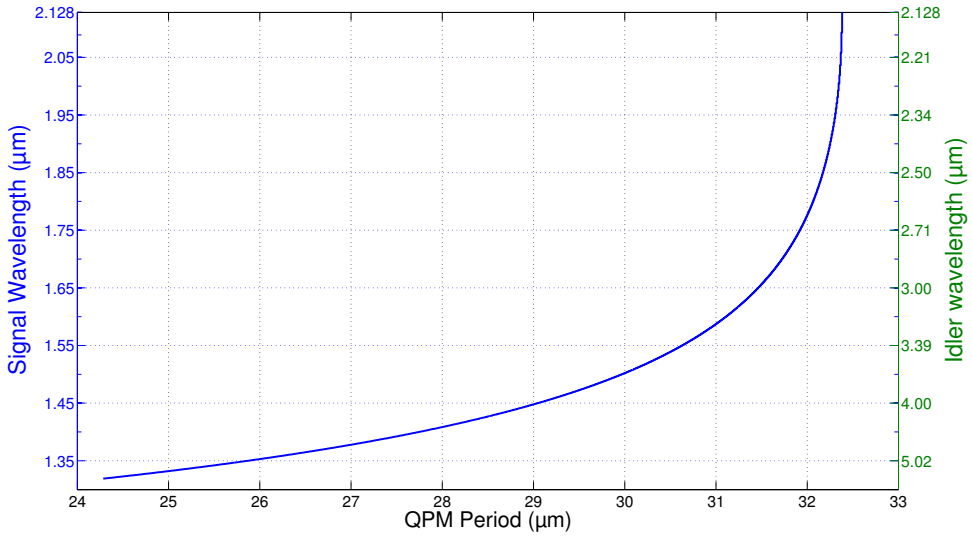

Figure 40: First order QPM DFG tuning curve of 5%MgO:PPLN with $\lambda_p = 1.064$ µm and $T = 21°C$.

This Sellmeier equation should predict the signal wavelength of a 5%MgO:PPLN OPO with an accuracy below 4 nm far from degeneracy and below 10 nm closer to degeneracy [106]. Idler wavelengths longer than 4 µm are obtained for QPM periods smaller than 29 µm and this will be one of our target in this work.

9.2 TUNABLE QUASI-PHASE-MATCHED OPO

The first experimental demonstration of QPM OPO dates back to the year 1994 at Stanford University [93, 107] and was accomplished thanks to advances in the field of electric periodical poling. Since then, QPM OPO have been reported in many different materials, and the state of the art in this field has been changing rapidly [7] because of a fierce competition between laboratories and quick transfer to companies worldwide. This section is by no means an extensive review of the work on this topic, but provides some insight on the different tunability strategies that have been implemented in nanosecond QPM OPOs. Note that Optical Parametric Oscillation has been achieved in almost any possible temporal regime from CW to femtosecond regime [93, 108], with synchronous pumping at high repetition rates for pulse durations in the picosecond or femtosecond regime. The engineering of QPM periods offers great possibilities in terms of tuning the OPO output wavelengths.

9.2.1 *Multigratings and fan QPM samples*

The use of multigrating QPM samples [109] such as shown on Figure (41) is an interesting prospect for the generation of coherent tunable radiation. It was demonstrated very soon after

the realization of the first QPM OPO and takes advantage of the versatility of the lithography process used to make the gratings. A continuous tuning can be obtained if the temperature of the sample is controlled [89]. Multigrating MgO:PPLN samples are commercially available [92, 110]. As far as we know, 2D structures such as fan-shaped gratings or multigratings in massive QPM crystals exceeding 3 mm thickness have not been reported. It is expected that the engineering of QPM structures such as a fan or a multigrating will be more difficult in thicker samples. The other option that takes advantage of the versatility of the lithography process is the use of a fan shaped grating [111]. This type of grating provides a continuous tunability of the idler and signal beams emitted by the OPO. The angle at which the fan grating "opens" should not be too big in order to avoid spectral inhomogeneities over the transversal section of the generated beams. In this case, it is the width of the sample that ultimately limits the tuning range that can be achieved with a single crystal.

9.2.2 *Cylindrical crystals*

The theory of Angular Quasi-Phase-Matching [31, 112] (AQPM) has been developed and experimentally validated first in 2D in a cylindrical PPKTP OPO [113] and a cylindrical PPLN OPG [114] and then in 3D in a 5%MgO:PPLN sphere [45]. The interest in this technique stems from the enhanced tunability obtained when the beams propagate no longer perpendicularly to the inverted domains. In the case of the first cylindrical OPO, the PPKTP crystal was 0.5 mm-thick. It was cut and polished as a full cylinder with a diameter of 12.1 mm [115]. We denote by ϕ the angle between the pump wavevector $\vec{k}_p$ and the direction perpendicular to the grating (with period Λ_0) as shown on Figure (42a). When the cylinder is rotated the effective QPM period $\Lambda_{eff}(\phi)$ seen by the pump is :

$$\Lambda_{eff}(\phi) = \frac{\Lambda_0}{\cos\phi} \tag{157}$$

The collinear condition for 2D AQPM was given in [112] and writes:

$$\frac{n_e(\lambda_p)}{\lambda_p} - \frac{n_e(\lambda_s)}{\lambda_s} - \frac{n_e(\lambda_i)}{\lambda_i} = \frac{1}{\Lambda_{eff}(\phi)} = \frac{\cos\phi}{\Lambda_0} \tag{158}$$

The corresponding angular tunability obtained wth a cylindrical PPKTP OPO is shown on Figure (42b).

9.3 OUR SAMPLES

9.3.1 *From slabs to partial cylinders*

The samples that we used in this work are 5-mm-thick 5%MgO:PPLN crystals [89]. The poling was performed in the group of Professor Taira at the Institute for Molecular Science (IMS) in

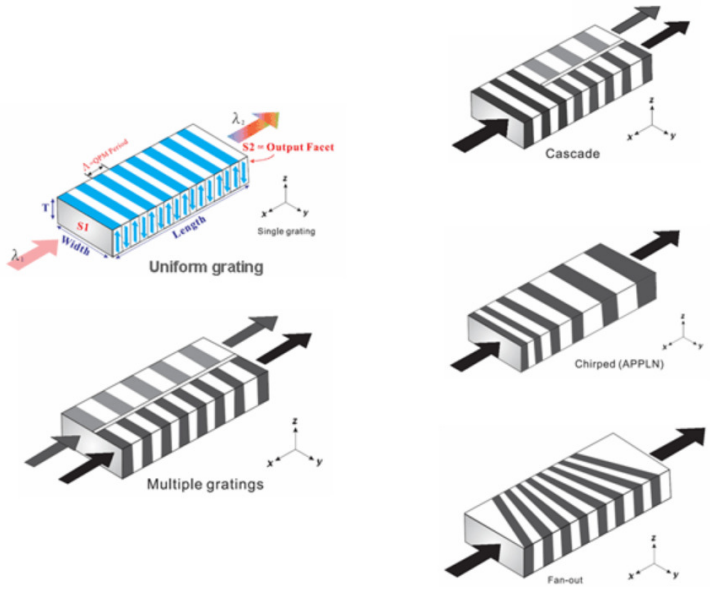

Figure 41: Examples of grating engineering in PPLN samples available commercially [92].

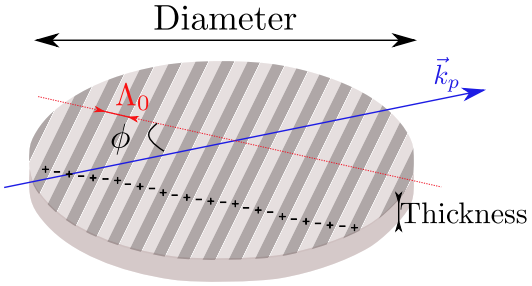

(a) Sketch of a full cylinder such as the one used in previous devices including a PPLN cylindrical OPG [114] or a cylindrical PPKTP OPO [113].

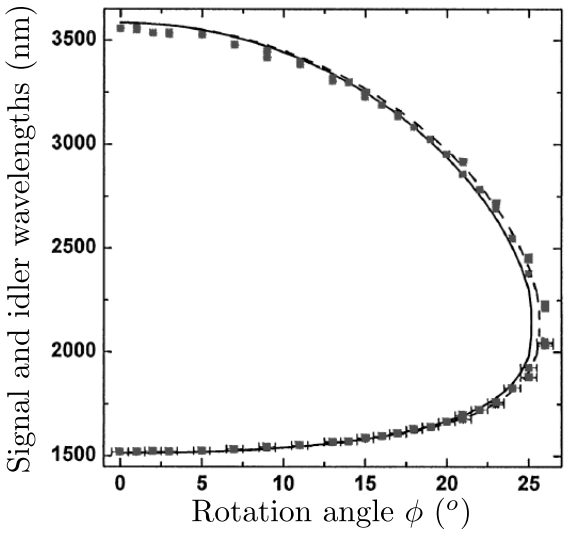

(b) Experimental tunability measured with the first cylindrical PPKTP OPO [113]. The continuous line corresponds to the noncollinear case, while the dashed line corresponds to the collinear case. (see Figure 58)

Figure 42: Interest in full cylinders QPM materials for widely tunable infrared radiation.

Okazaki. Because of the decreasing coercive field with increasing temperature, these samples have been poled at 120°C. The electric tension that was necessary to achieve the periodical flipping of the domains over the 5 mm thickness is approximately 17.5 kV [116]. Three samples whose characteristics are given in Table (11) have been obtained within a collaboration between our group and the group of IMS. The QPM grating of these samples is tilted with an angle ψ with respect to the normal of the slabs [117], as shown on Figure (43). The dimensions of the slabs that we received from Japan are W = 16 mm and L = 40 mm.

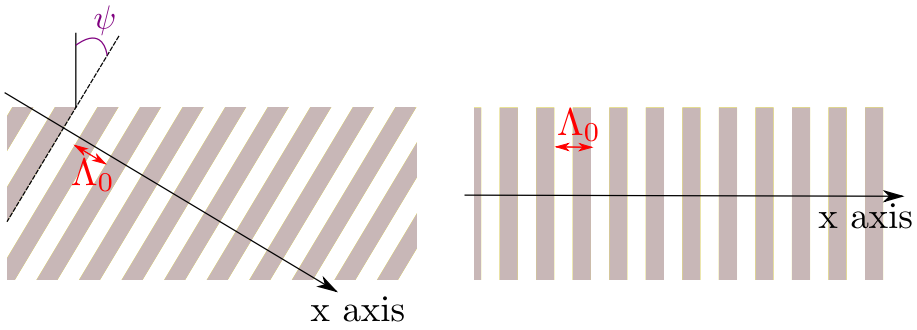

Figure 43: Sketch of a QPM crystal with domains tilted with respect to the normal of the sample (left) and of a crystal with a "classical" grating perpendicular to the faces of the crystal (right).

	Sample A	Sample B	Sample C
QPM period Λ_0	28 µm		26 µm
Tilt angle ψ	20°		30°
Technical name	PF145	PF146	PF171

Table 11: Characteristics of the three 5%MgO:PPLN crystals cut as partial cylinders. The parameters used are shown on Figure (43).

When a partial cylinder is made out of these slabs (see Figure 44), the resulting partial cylinder has an aperture angle Θ whose value is dictated by the diameter of the cylinder D and the width W of the sample. Note that D is usually a little smaller than L. In our case, D = 38 mm while L = 40 mm, because 2 mm were "lost" during the machining and polishing process. The aperture angle of the partial cylinder is then given by:

$$\Theta = 2 \arctan \frac{W}{D} \tag{159}$$

And in our case, we find:

$$\Theta = 45.6° \tag{160}$$

The maximal corresponding effective QPM period is therefore:

$$\Lambda_{max} = \frac{\Lambda_0}{cos(\Theta)} \tag{161}$$

For sample A and B with $\Lambda_0 = 28\,\mu m$, we get:

$$\Lambda_{max} = 40.0\,\mu m \tag{162}$$

meaning that when the angle ϕ is varies over Θ, the QPM period is increased from $\Lambda_0 = 28\,\mu m$ up to $\Lambda_{max} = 40.0\,\mu m$. Based on Figure (40), this is sufficient to cover the widest tuning range allowed by such a sample. Note that the tuning range is only limited by the shortest signal wavelength and corresponding longest idler wavelength that can be generated at $\phi = 0°$, i.e. along the x-axis. The smaller Λ_0, the wider the tunability.

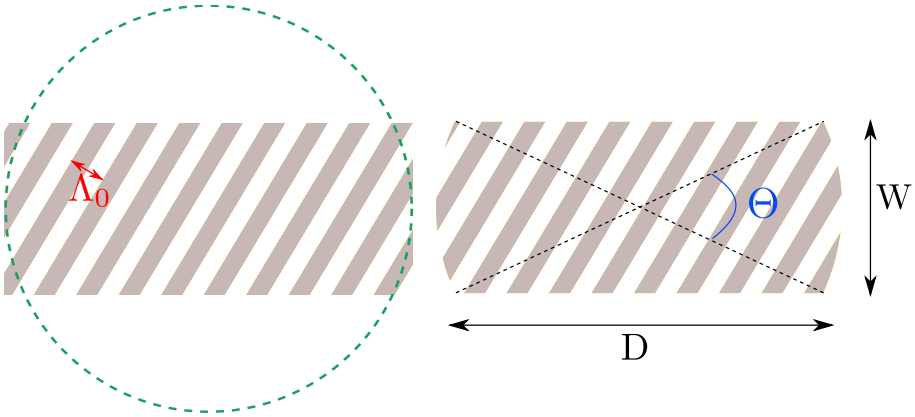

Figure 44: Sketch of the design of a partial cylinder in a sample with a tilted QPM grating.

From Figure (40), one sees that a variation of QPM period from 28 to 33 µm is large enough to cover the entire tuning range of the sample. Actually, for sample A with $\Lambda_0 = 28\,\mu m$, since the QPM condition is lost for $\Lambda_{QPM} > 32.4$ µm, the minimum aperture angle needed to cover the widest tuning range is smaller than Θ. It is $\Delta\phi = 30.1°$, as shown on Figure (45).

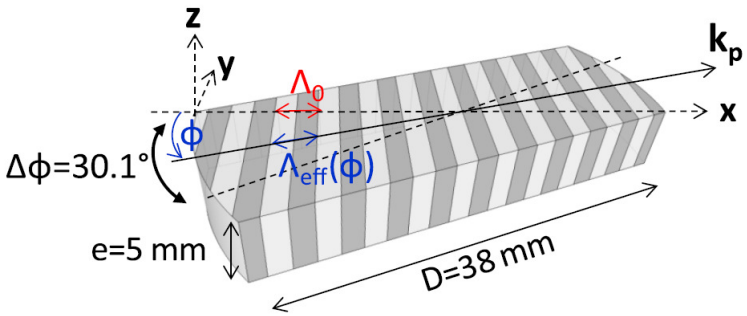

Figure 45: Schematic view of a partial cylinder such as the one used in this work.

The interest of using a crystal with a tilted grating can be seen from Figures (43) and (44). In the case of a "classical" sample without any tilt, only half the aperture angle would be useful to tune the wavelengths. But when a tilted grating is used, the QPM period keeps increasing when the crystal is rotated, and the corresponding tuning range is wider.

9.3.2 *Making the partial cylinders*

The setup used to make the cylinders was designed by Bertrand Ménaert and Benoit Boulanger [115]. It is sketched on Figure (46). Since it is easier to directly cut a full cylinder instead of a partial one, we stuck two slabs of silica on each side of the 5%MgO:PPLN rectangular sample. We then obtained a 40 x 40 x 5 mm^3 square in which a full cylinder can be cut. This square sample was finally stuck at the top of a stiff arm held by a goniometric head. The head was screwed to a motorized home-made rotating arm in order to be able to sweep onto a Logitech PM5 polishing plate as shown in Figure (46). Precession and centering settings were based on the tilt and translation of the goniometric head. A laser allowed us to align the revolution axis of the stiff arm with the z-axis of the samples with an accuracy of ±0.1°. The cylindrical shape and the optical quality of the side surfaces were obtained by polishing the side of the sample using different abrasives of decreasing grain sizes. After this process, the two silica parts were removed leading to the partial cylinders of 5%MgO:PPLN shown in Figure (47). The entire process to make one partial cylinder takes about one month. Making three such samples would not have been possible without the strong commitment of Jérôme Debray.

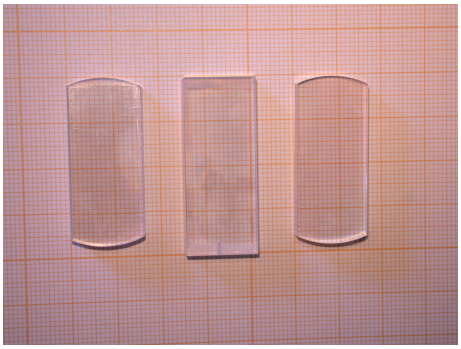

(a) Samples A (left) and C (right) after being made and polished as partial cylinders, and sample B (middle) before making process.

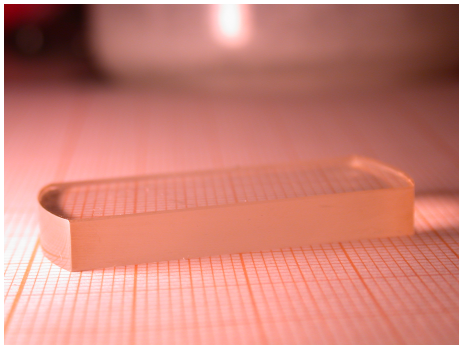

(b) Sample B where most measurements were made.

Figure 47: Pictures of 5 mm thick partial cylinders

We now discuss two defects that may result from the machining of the partial cylinders. These difficulties are worth being mentioned since we truly hope that they will spare much time to anyone willing to make even better partial cylinders. The first defect does not have any implications on the OPO conversion efficiency, and results from a poor design of the glass pieces shown in Figure (48). Measuring the glass pieces should be done very carefully because different

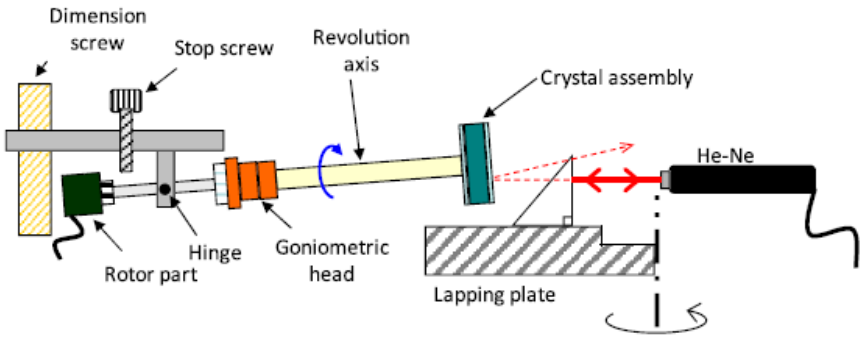

(a) Sketch of the experimental setup.

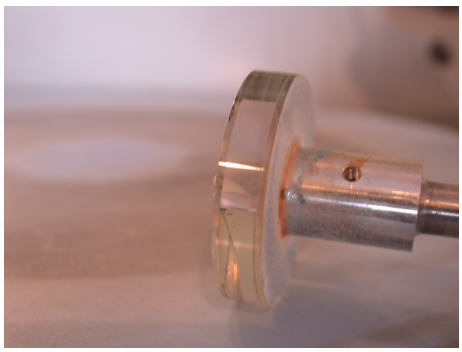

(b) Picture of the stiff arm with the full cylinder being polished to optical quality.

Figure 46: Experimental setup used to make and polish a full cylinder.

widths of the glass pieces will result in a poor centering of the partial cylinder and thus in a reduced aperture angle. In our case, the glass pieces were 12-mm-wide and 40-mm-long initially, so that the resulting diameter of the cylinder (after polishing) is 38 mm. Measuring the glass pieces was done with an accuracy of +/- 1 mm. The potential reduction of the aperture angle is only 2°. Note that if the glass pieces are not wide enough, the length of the cylinder will be reduced. If the glass pieces are too wide, the machining of the cylinder will take too long.

Another defect of the current apparatus used to make the cylinders is the defect of conicity. Indeed, it turned out that instead of having perfect parallel faces, one cylinder (sample C) had tilted faces. This defect is depicted on Figure (49), and comes from the fact that the stiff arm holding the cylinder had not reached yet the required horizontal position when we stopped the machining of the cylinder. This defect of conicity can be easily avoided by leaving the process last longer so that the dimension screw and the stop screw depicted on Figure (46) are perfectly aligned. However, it is difficult to monitor this defect of conicity, which can only be revealed once an He/Ne laser is autocollimated on the polished face of the cylinder. It will be useful to improve the current system by adding an option that gives this information during the machining. We chose the sample A to carry out all the measurements presented in this chapter since it had the smallest conicity defect. The autocollimation of the sample was good to within 1 mm on a 50 cm arm, so that the defect of conicity is below 0.1°.

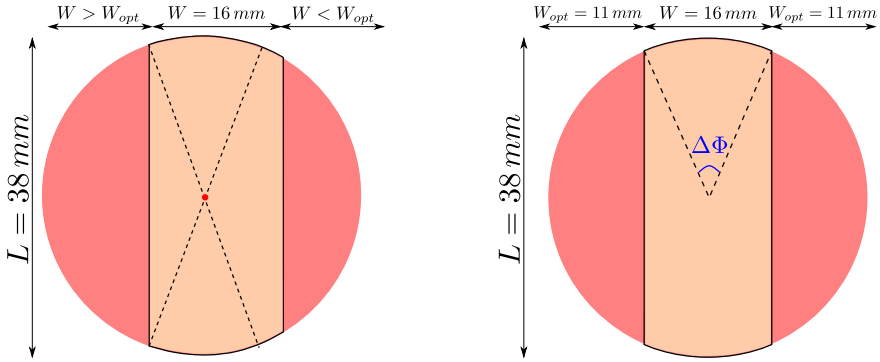

(a) Poor centering of the glass pieces: the aperture angle is reduced.

(b) Optimal position of the glass pieces. The aperture angle is 45°.

Figure 48: Effect of a poor (a) and optimal (b) design of the glass pieces on the aperture angle of the partical cylinder.

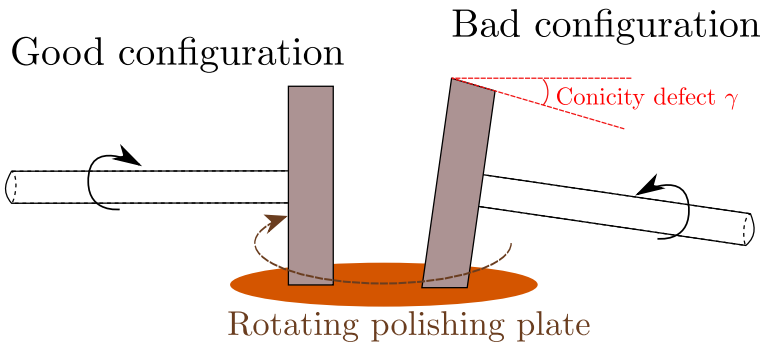

Figure 49: Exagerated schematic view of the origin of the conicity defect. The good situation is depicted on the left: the stiff arm has reached its horizontal position. On the right, the stiff arm has not yet reached its horizontal position.

10

EXPERIMENTAL SET-UP AND TUNABILITY

In this section, we present the experimental setup of the partial cylinder OPO, as well the tunability of the beams generated from such a device. The method implemented to measure the signal and idler wavelengths is emphasized. The last section is devoted to the debate on the collinear versus noncollinear QPM configuration.

10.1 EXPERIMENTAL SET-UP

The experimental setup of a partial cylinder OPO is shown on Figure (50). In this section, we deal with the pump focalisation first, then with the choice of the mirrors and eventually with the cavity stability. The following notations are used in this work: d is the distance between the partial cylinder and the mirrors, while D_0 is the distance from the cylindrical lens to the input mirror (see Figure 50). The center of the cavity is taken as the reference plane for future ABCD matrix calculations.

10.1.1 *Pump focalisation*

The pump beam that we use is emitted from a 10-Hz-repetition rate and a 10-ns-FWHM Nd:YAG laser Surelite from Continuum. This laser can provide up to 300 mJ per pulse but we inserted a hole inside the cavity in order to reduce both the size of the TEM00 mode and the pulse energy. This spatial filtering also improves the beam quality factor. The maximum available energy is therefore limited to 10 mJ in the experiments reported in this chapter.

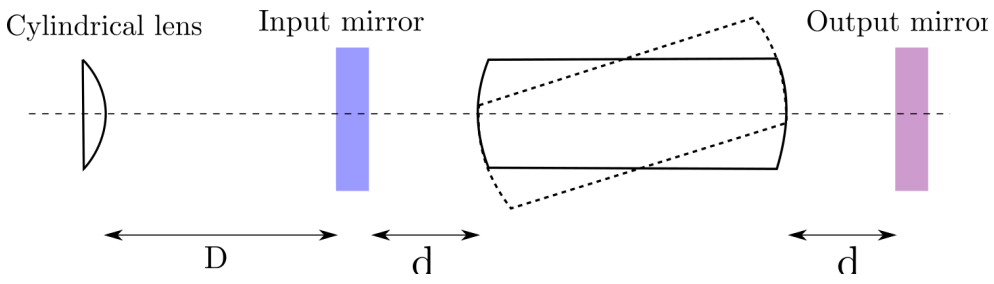

Figure 50: Schematic view of the cylindrical OPO from sample A and B.

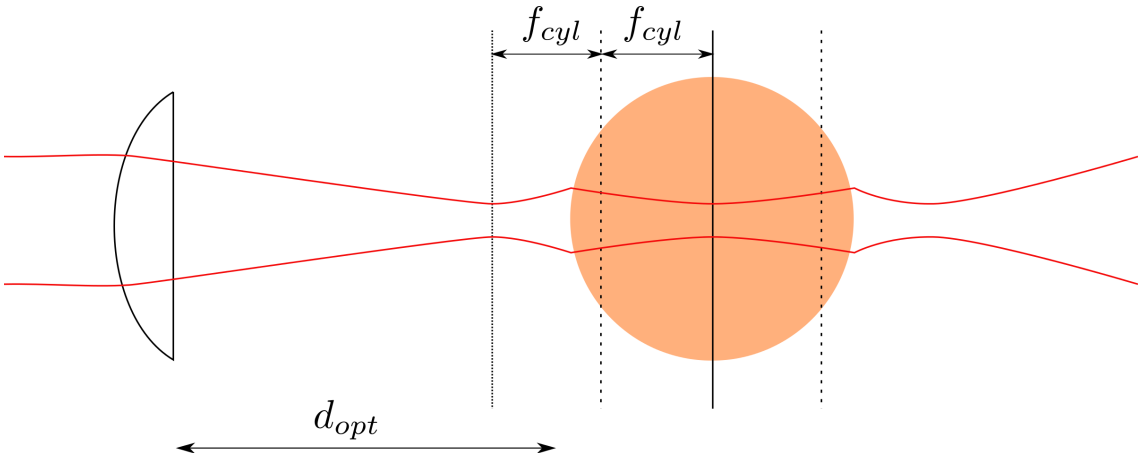

Figure 51: Configuration of focalisation of the pump beam.

The main drawback of a partial cylinder OPO is the need to focus the pump beam in the plane of rotation of the crystal because of the curvature of the two faces [44]. In the case of a crystal cut as cylinder or partial cylinder, cylindrical lenses can be used because the pump beam needs only be focused in the horizontal plane. The beam size in the vertical direction can then be kept maximum so that the pump intensity on the crystal is reduced. The extraordinary refractive index of the 5%MgO:PPLN crystal at λ_p = 1.064 µm is 2.1472 [106]. And the focal length of a partial cylinder [44] with radius R=19 mm is :

$$f_{cyl}(\lambda_p) = \frac{n^e(\lambda_p)R}{2(n^e(\lambda_p)-1)} = 17.8\,mm \tag{163}$$

This focal length is shorter than the radius of the partial cylinder because the index at the pump is greater than 2. Following Pierre Brand's PhD thesis [45], there exists an optimal position of the lens $D_0 = D_{opt}$ where the propagation of the pump beam inside the partial cylinder is nearly parallel [44] (see Figure 51). This optimal position must take into account the presence of the input mirror, but does not vary with the position of this input mirror since it is the optical path between the lens and the cylinder that determines the value of D_{opt}.

In our case, when the mirror to partial cylinder distance is d = 15 mm, the lens must be positioned at

$$D_{opt} = 72.4\,mm \tag{164}$$

At the first order, the size of the pump beam inside the partial cylinder can be worked out with the classical formula of the telescope:

$$w_{p,cyl} = \frac{f_{lens}}{2f_{cyl}} w_{p,0} \tag{165}$$

Before the cylindrical lens, the pump beam is nearly TEM_{00} with a beam waist radius $w_{p,0} = 2\,mm$, so that the transversal dimension of the pump beam in the partial cylinder is:

$$w_{p,cyl} = 0.42\,mm \tag{166}$$

Our pump beam is then elliptical inside the partial cylinder with a horizontal beam waist radius of 0.42 mm and a vertical beam waist radius of 2 mm. These values must be compared to the dimensions of the pump beam that were used in a cylindrical 500 µm thick PPKTP OPO [113]. After proper focalisation, the pump beam transverse dimensions were 50 µm and 250 µm. The use of a 5-mm-thick sample lets us work with 67 times lower pump intensities. Note that increasing the beam spot size in the horizontal direction can still be done by increasing the focal length.

10.1.2 *Cavity design and alignement*

The transmission spectra of our cavity mirrors in the range 1.3-2.8 µm are shown on Figure (52). At the pump wavelength λ_p = 1.064 µm (not shown on Figure (52)), the input mirror is highly transmitting (T > 97%) while the output mirror is highly reflecting (T> 99%) . The cylindrical OPO is therefore singly resonant at the signal wavelength, with one recycling of the pump. The choice of these mirrors will be discussed later on in this work (see section 11.1.1). But let us stress now that this cavity is designed to have a high reflectivity at short QPM signal wavelengths where the nonlinear gain (see Equation 49) is the smallest.

The better the shape of the partial cylinder, the easier the alignment of the cavity. For a partial cylinder without any defect of conicity, the alignement of the cavity gets down to three main steps. First of all, the partial cylinder has to be perfectly centered on a goniometric head such as shown in Figure (53). Aligning the axis of rotation of the partial cylinder with the axis of rotation of the goniometer is performed using a microscope with an accuracy of 15 µm. Then, the partial cylinder is centered by making sure that a He-Ne laser collinear to the pump beam is not deviated when propagating through the crystal.

For a pump energy of 2 mJ, the oscillation is "immediately" obtained if the two mirrors are nearly autocollimated. Oscillation in the cavity can be recognized from the emission of an orange (reddish) beam from the crystal that corresponds to the non phase-matched sum-frequency-generation between the signal and the pump beams. In addition to this orange beam, there is always some residual green at 532 nm exiting the cavity, and corresponding to the non-phase-matched second harmonic generation of the pump. The orange beam provides a very convenient way to align the cavity in the vertical direction. We have found experimentally that the brighter this beam, the higher the conversion efficiency of the OPO. It is worth mentioning that when the cavity is optimized, the intensity of the green beam has sharply decreased while the intensity of the orange beam has increased, showing that the pump beam is preferentially downconverted into the QPM signal wavelength. A finer alignement procedure of the cavity in the horizontal plane can also be done by using a spectrometer in the range 1.35-1.7 µm to reduce the linewidth

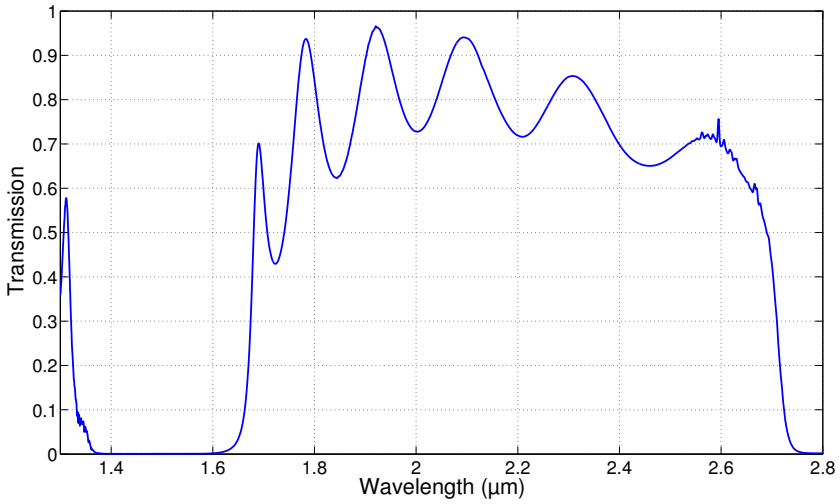

(a) Transmission spectrum of the input mirror used in this work. This mirror is made of BK7 and absorbs the idler wavelengths above 2.7 μm.

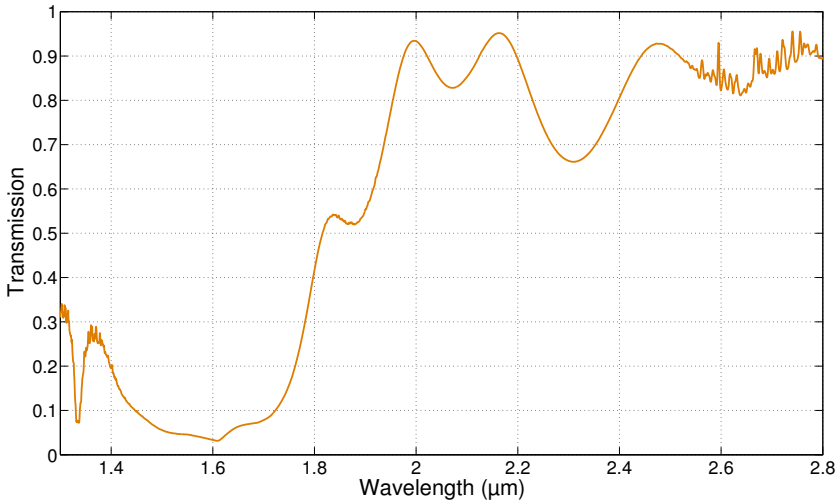

(b) Transmission spectrum of the output coupler used in this work. This mirror is made of CaF_2 and has transmission above 2.8 μm superior to 85%.

Figure 52: Transmission spectra of the input and output mirrors used in this work.

of the emitted signal beam. This reduction in linewidth corresponds to a better alignment of the different passes of the resonating signal in the crystal.

The alignment procedure can be a little trickier when the partial cylinder exhibits some of conicity. Instead of using autocollimated mirrors, the best empirical solution that we have found consists in aligning the cavity on the non-phase-matched 532 nm beam. A good way to do so is to set the output mirror first and then to optimize the cavity with the entrance coupler so that the reflections of the 532 nm beam inside the cavity are not too much spaced apart. The procedure of alignement is then similar to what we described above.

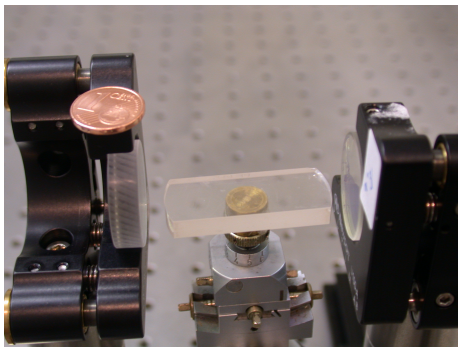

Figure 53: Picture of the partial cylinder inserted inside the resonating cavity. The partial cylinder is stuck on a goniometric head for fine centring settings.

10.1.3 *Cavity stability*

In this section we give the analytical expression of the ABCD matrix corresponding to the round trip propagation of a gaussian beam in a symmetrical cavity made of two plane mirrors and of a cylinder (partial or full). If we take the center of the cavity as the reference plane (see Figure 50), the ABCD matrix for a round trip M_{RT} can be worked out in the horizontal plane following the guidelines given in [29]:

$$M_{RT} = \left[\begin{pmatrix} 1 & \frac{R}{n(\lambda_s)} \\ 0 & 1 \end{pmatrix} \begin{pmatrix} 1 & 0 \\ \frac{1-n(\lambda_s)}{R} & 1 \end{pmatrix} \begin{pmatrix} 1 & 2d \\ 0 & 1 \end{pmatrix} \begin{pmatrix} 1 & 0 \\ \frac{1-n(\lambda_s)}{R} & 1 \end{pmatrix} \begin{pmatrix} 1 & \frac{R}{n(\lambda_s)} \\ 0 & 1 \end{pmatrix} \right]^2$$

which gives

$$M_{RT}(\lambda_s) = \begin{pmatrix} A & B \\ C & D \end{pmatrix} = \begin{pmatrix} \frac{R+(2d+R)(1-n(\lambda_s))}{n(\lambda_s)R} & \frac{2(d+R)}{n(\lambda_s)^2} \\ \frac{2(1-n(\lambda_s))(R+d(1-n(\lambda_s)))}{R^2} & \frac{2-n(\lambda_s)}{n(\lambda_s)} + \frac{2d(1-n(\lambda_s))n(\lambda_s)}{n(\lambda_s)R} \end{pmatrix}^2 \tag{167}$$

The cavity is stable whenever the condition

$$\left|\frac{A+D}{2}\right| < 1 \tag{168}$$

is valid. We have plotted this condition for three different signal wavelengths and for a mirror to partial cylinder distance d varying from 0 up to 18 mm on Figure (54). It can be seen that the cavity is stable for any wavelengths of interest in this work and for any values of d below 17 mm.

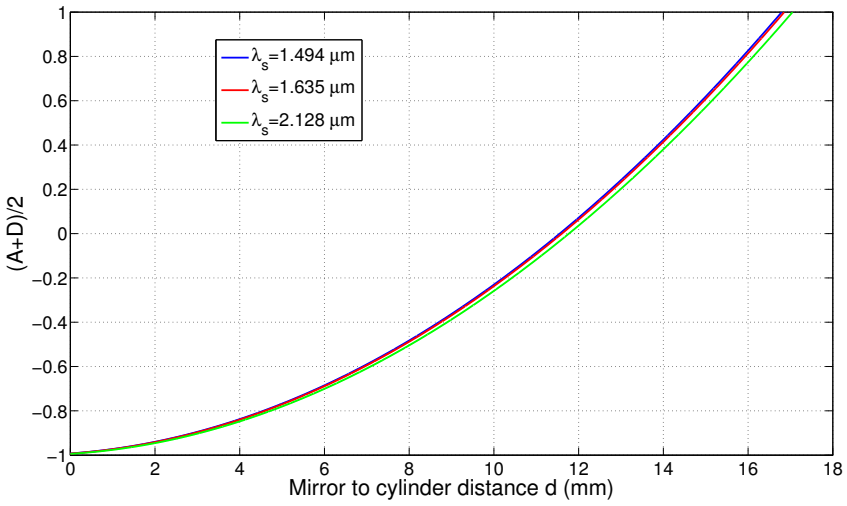

Figure 54: Stability condition of the cavity studied in this work.

10.2 MEASURING THE DOWN-CONVERTED WAVELENGTHS

Two different methods have been used to measure the signal and idler wavelengths generated in the OPO.

The first method is a direct measurement of the signal wavelength. It is performed with a NIRQuest spectrometer whose spectral response covers the range 0.9-1.72 µm. This spectrometer is well suited for measuring the signal wavelength, λ_s, far from degeneracy. Its resolution is $\delta\lambda_s = \pm 2\,nm$. The idler wavelength, λ_i, can be calculated using the conservation of energy: the error on the idler wavelength $\delta\lambda_i$ increases with the wavelength. By differentiating the relation

$$\frac{1}{\lambda_i} = \frac{1}{\lambda_p} - \frac{1}{\lambda_i} \tag{169}$$

we find:

$$\delta\lambda_i = \left(\frac{\lambda_i}{\lambda_s}\right)^2 \delta\lambda_s \tag{170}$$

At degeneracy, the idler and signal wavelengths are equal and there is no difference in the error bars on the signal and idler. But when the idler reaches 4 µm for example, the corresponding signal is 1.45 µm and the error bar on the measurement of the idler is 7.6 times higher than that of the signal. At 4 µm, the error bar is close to 15 nm. It even reaches 25 nm at 4.8 µm.

Another method has therefore been used to improve the accuracy of our measurements. It turns out that there are four new wavelengths that can be detected at the exit of the cavity and in the range 0.5 to 0.85 µm. The first wavelength is of course the 532 nm beam, but we use the three other upconverted wavelengths as shown on Figure (Fig 55) to measure the signal and idler wavelengths of the OPO. These three wavalengths correspond to the non-phase-matched sum-frequency generation between the pump and the signal, second harmonic generation of the signal and sum-frequency generation between the idler and the pump. The energy conservation can be used to relate these three separate values to the single QPM signal wavelength generated in the OPO. By averaging the three different values of the signal corresponding to each upconverted wavelength, the accuracy of our measurement of the single signal wavelength is improved (see Table 12). This method has three other advantages. First of all, since the three up-converted wavelengths always lie in the range 0.6-1 µm, measurements can be performed on the entire tuning range of the OPO and especially closer to degeneracy than with the previous method. Then, this method is much quicker and much more convenient to implement than the use of grating spectrometer. Eventually, it will not be difficult to integrate this procedure under a LabView interface.

Raw measurements	SFG signal + pump (nm)	657.3 ± 0.3
	SHG signal (nm)	770.6 ± 0.3
	SFG idler + pump (nm)	860.3 ± 0.3
Average signal wavelength λ_s (nm)		1720 ± 1
Average idler wavelength λ_i (nm)		2791 ± 3

Table 12: Typical measurement procedure of the signal and idler wavelengths generated from the OPO. The pump wavelength is 1.064 µm.

10.3 WIDE AND CONTINUOUS TUNABILITY

Using the second method described above and sample A for which $\Lambda_0 = 28$ µm , we were able to measure the signal and idler wavelengths for every angle of rotation of the partial cylinder OPO. At every angle, the four up-converted wavelengths are detected as shown on Figure (55), and the signal and idler wavelengths of the OPO are determined within an accuracy of 1 nm for the signal and 3 nm for the idler.

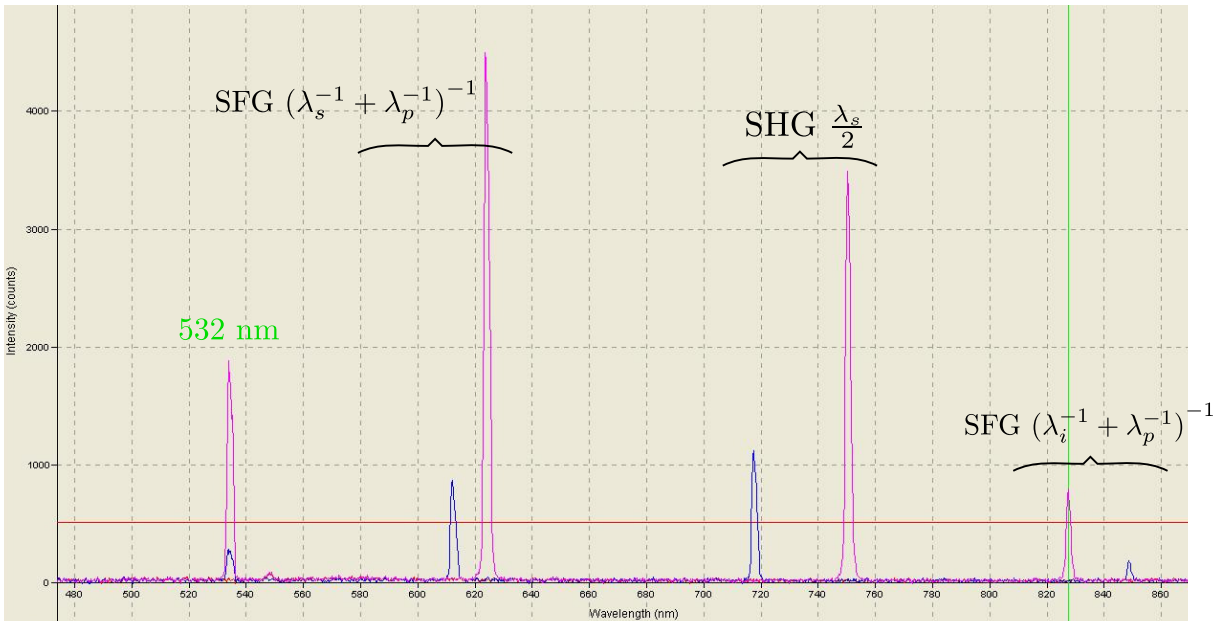

Figure 55: Visualisation of the trace of the visible spectrometer at the output of the OPO for two different angles of rotation of the cylinder. The first angle corresponds to the blue peaks. The second angle corresponds to the pink peaks. At each angle, four up-converted wavelengths are shown, and only the peak at 532 nm remains constant when the cylinder is rotated.

The measured tuning range is shown on Figure (56). It extends from 1.42 µm up to 4.4 µm. The calculated curve on Figure (56) assumes a collinear QPM scheme meaning that the three interacting wavelengths fulfill the QPM relation [112]:

$$\frac{n_e(\lambda_p, T_0)}{\lambda_p} - \frac{n_e(\lambda_s, T_0)}{\lambda_s} - \frac{n_e(\lambda_i, T_0)}{\lambda_i} = \frac{\cos\phi}{\Lambda_0} \tag{171}$$

where $T_0 = 21°C$ is the controlled room temperature.

The tunability displayed on Figure (56) is continuous since it is obtained through the continuous rotation of the crystal inside the cavity. The accuracy on the ϕ angle is limited by the goniometer on which the partial cylinder is mounted. It is between 0.25° and 0.5°. Motorized rotations are available commercially with much finer rotation steps. No temperature tuning nor temperature control is used in this experiment.

The tuning rate is a very important characteristics of our partial cylinder OPO and it corresponds to the rate at which the signal or idler are modified when the crystal is rotated in the cavity. This tuning rate is the lowest at the bottom and top of the tuning curve, where it is easier to work. When the signal and idler get closer to degeneracy, the tuning rate increases very quickly and it becomes very difficult to work with a signal above 1.8 µm. Numerically speaking, a tunability of 150 nm (between 1.42 and 1.57 µm) is obtained with a rotation of about 25°. The corresponding tuning rate is as low as 6 nm per degree, and the crystal can then be positioned at any signal wavelength in this range within 1 nm with our manual goniometer.

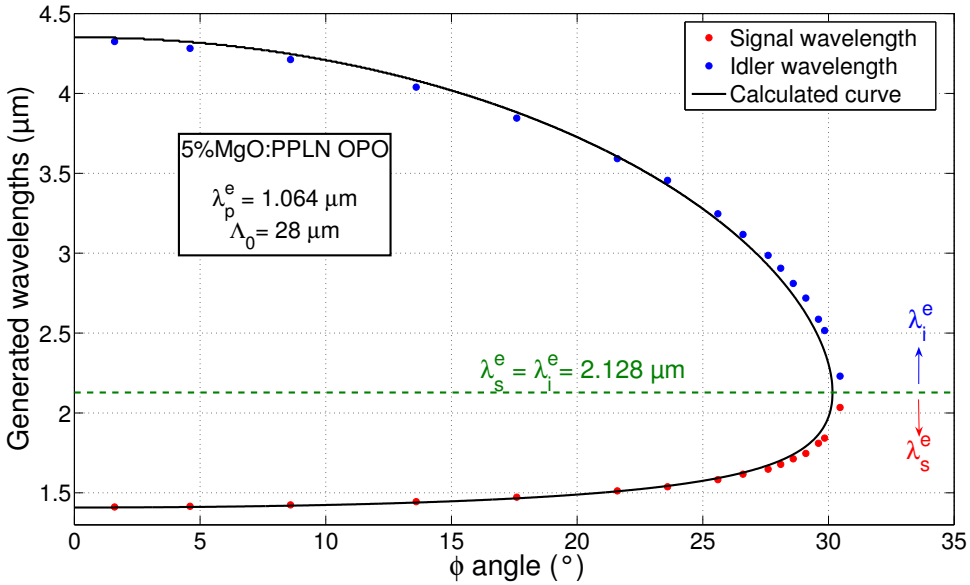

Figure 56: Type 0 angular QPM curve of the 5%MgO:PPLN cylinder at room temperature $T_0 = 21°C$; (e) refers to the extraordinary polarization. The angular accuracy is between 0.25° and 0.5°. The calculation uses Sellmeier equations (155) from [106].

The spectra of the signal and idler get very broad closer to degeneracy for $\lambda_s \approx \lambda_i \approx 2.128\,\mu m$, and this is another reason to work far from that point. The spectral properties of our OPO will be discussed extensively at the end of this Part.

10.4 COLLINEAR OR NON COLLINEAR QPM ?

Quasi-phase-matching with a tilted grating is a controversial and exciting issue. The controversy deals with the QPM configuration of the wavevectors. We have sketched the two possible configurations under debate on Figure (57). In the collinear QPM scheme, the three beams are all collinear because the QPM length that contributes to the parametric process is the effective QPM length given in Equation (157) and shown in yellow on Figure (57a). The three beams share the same direction for their $\vec{k}$ vectors. This representation of angular QPM [112] is in line with the underlying idea of QPM that consists in imposing a π phase shift to the polarization wave every coherence length along the direction of propagation. This is the configuration that we have considered so far in this work. On the other hand, in the non-collinear QPM configuration [7], the grating vector is always perpendicular to the domains. The idler wavevector $\vec{k_i}$ adapts itself to close the vectorial QPM relation imposed by the QPM vector and the signal wave vector $\vec{k_s}$ which is set by the resonating cavity (See Figure 57b). This representation is more in line with a "diffraction-like" process. This controversy has of course a fundamental interest but also practical consequences. It is important to make sure that the signal and idler beams emitted from the OPO are collinear for the future alignment of the dual source described in Part IV.

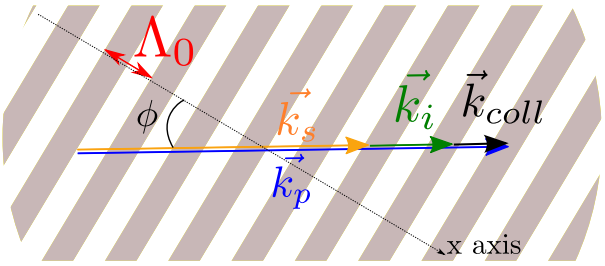

(a) Collinear QPM scheme

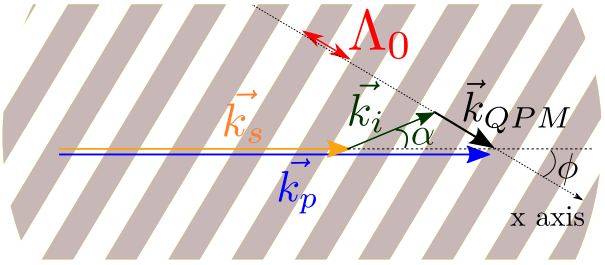

(b) Noncollinear QPM scheme

Figure 57: Comparison between the momentum conservation relation in a collinear (a) and non collinear (b) QPM schemes. The wavevector of the resonating signal is imposed by the cavity .

Let us remind that the equation ruling the collinear QPM condition writes:

$$\frac{n^e(\lambda_p)}{\lambda_p} - \frac{n^e(\lambda_s)}{\lambda_s} - \frac{n^e(\lambda_i)}{\lambda_i} = \frac{\cos\phi}{\Lambda_0} \tag{172}$$

In the case of noncollinear QPM, Equation (172) is no longer valid. There are two unknowns in the QPM condition: the direction of propagation of the idler beam that makes an angle α with the pump beam direction of propagation and the idler wavelength itself. The two equations ruling the non-collinear QPM momentum conservation can be easily worked out, and lead to a slight modification of the collinear QPM equation given in (172). They write:

$$\frac{n^e(\lambda_p)}{\lambda_p} - \frac{n^e(\lambda_s)}{\lambda_s} - \frac{n^e(\lambda_i)}{\lambda_i}\sqrt{1 - \left(\frac{\lambda_i \sin\phi}{\Lambda_0 n^e(\lambda_i)}\right)^2} = \frac{\cos\phi}{\Lambda_0} \tag{173}$$

and

$$\sin\alpha = \frac{\lambda_i}{n^e(\lambda_i)\Lambda_0}\sin\phi \tag{174}$$

We have added on Figure (58) the solution of the noncollinear phase-matching Equation (173) to the tuning curve that we measured. The deviation between the collinear case and the noncollinear case is low and increases with the signal wavelength. We see that the collinear case is in better agreement with our measurements, and especially towards degeneracy. This better agreement

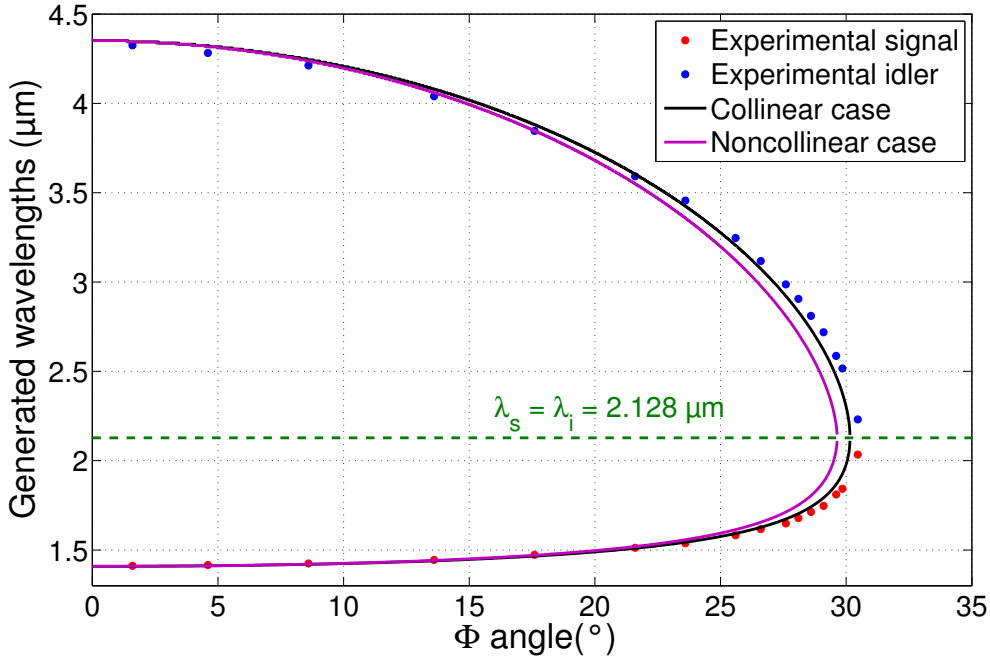

Figure 58: Comparison between the collinear (Equation 171) and the non collinear QPM solution (Equation 173) in terms of predicting the generated wavelengths of the 5% cylindrical OPO. Sellmeier equations (155) are used.

between the collinear case and the measured phase-matching curves of a cylindrical QPM OPO is here reported for the second time. Indeed, the same discrepancy between the collinear and the noncollinear case was already observed in the first QPM cylinder OPO [113] as shown on Figure (42b).

On the other hand, Liang and al. carried out a study dealing with an OPO where the pump beam propagates in a QPM crystal cut as a slab with 60° tilted domain walls and $\Lambda_0 = 13.6$ µm [118]. An external angle of 12.6° between the pump and the idler was measured. This deviation of the idler beam was found to be in good agreement with the internal angle of 5.8° predicted by Equation (174). We have plotted the internal deviation angle α solution of Equations (173) and (174) as a function of the angle of rotation ϕ for the same parameters as used in our experiment. We see that there is no deviation ($\alpha = 0°$) between the pump and the idler when the beams propagate perpendicularly to the grating (i.e. $\phi = 0°$). The deviation angle then increases with the angle ϕ up to reaching a maximum when the tilt angle is close to 24.5°. This is where we would expect the signal to be the most separated from the idler. For the parameters used in our experiment, the maximum deviation angle would remain below 1.3° on the entire tuning range. The deviation angle α would be 5 times smaller than the angle measured by Liang and al., mostly because our principal QPM period is larger than that used by these authors in [118].

We tried to image a spatial separation between the different beams of our OPO with a Pyrocam camera from Ophir Photonics to discriminate between the collinear and noncollinear case. But this turned out to be much more difficult than what we had imagined. First of all, since our OPO

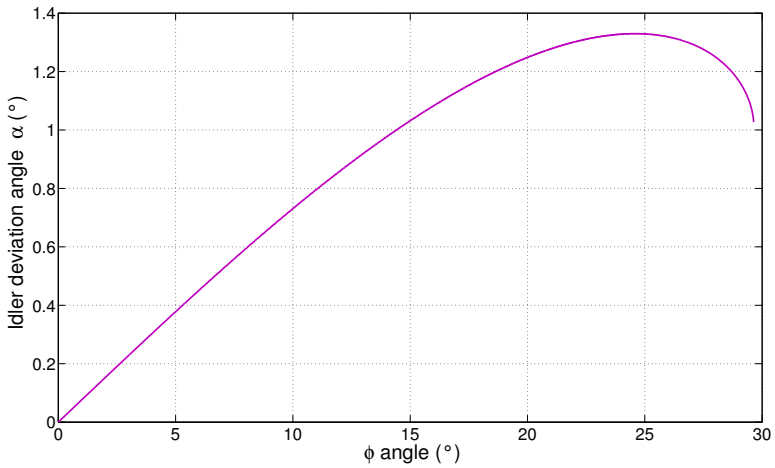

Figure 59: Plot of the angle α between the signal and the idler beam in the case of a noncollinear QPM configuration (See Figure 57b). The QPM period used for calculations here is $\Lambda_0 = 28\,\mu m$, which corresponds to sample A.

recycles the pump back in the cavity, it is impossible to image the pump at the output of the cavity. And we must image the signal and the idler beams. Far from degeneracy the signal and idler can be easily separated with a Ge filter but the angle α given in Figure 59 is very small. Closer to degeneracy, the wavelengths are too close to be separated. Moreover, separating the signal and idler is all the more difficult as the beams are elliptically focused and rapidly diverging at the output of the cavity. As a result, we could not find any deviation between the signal and the idler beams.

One additional comment can be done: in the experiment done by Liang et al., the noncollinear QPM case was considered in the case of a nondegenerate three wave process where the signal and idler are different and distinguishable. The reader is free to ask himself what would be the QPM configuration in a degenerate non-collinear OPO. Since at degeneracy the signal and idler are no longer distinguishable, what is the wavelength that is free to adapt itself to close the QPM relation shown on Figure (57) ? Is there part of the signal that is resonated and part of the signal that is not ? Collinear QPM seems more likely to reconcile the symmetry imposed by a degenerate OPO.

11

RAMPING UP THE GENERATED ENERGY

In the previous section, we have seen that cutting a crystal as a partial cylinder is as good a solution as a full cylinder to achieve a wide and continuous tunability of a QPM OPO. This section is now devoted to the energetical performances of our OPO.

We first analyze the intracavity signal damage phenomenom that we identified as the main problem to ramp up the conversion efficiency. We address this issue by increasing the cavity length of the OPO. By taking into account additional constraints related to the recycling of the pump, we are eventually able to find the optimal cavity length for which the crystal does not suffer any damage and for which the conversion efficiency is high. We then compare the energetical conversion efficiency of our partial cylinder OPO to that of a slab OPO.

11.1 INTRACAVITY SIGNAL DAMAGE

Intracavity signal damage corresponds to the damage of the crystal inside the cavity because of a too high intensity of the resonating signal beam. This detrimental phenomenom can be due to either a too high resonating signal energy stored in the cavity, or to a too small resonating signal beam radius. There are basically two convenient ways to tackle this issue. The first one is to use mirrors with lower reflectivity. This is not the route chosen in this work, and we justify our choice of mirrors in the first part of this section. The other available option is to increase the signal beam waist radius. This can be done in the partial cylinder OPO by increasing the cavity length.

11.1.1 *Choice of the mirrors*

The choice of the mirrors for our partial cylinder OPO is not easy for at least two different reasons. First of all, since the beams generated in the OPO are elliptically focused, the mirrors should have a quite high damage threshold. Then, as the tunability of the signal wavelength is broad, the best solution is potentially to use broadband mirrors. But this is usually done at the price of a lower damage threshold or higher cost. In this work, we have tested four different sets of mirrors including those whose spectra are shown on Figure (52), and three other sets of mirrors cordially loaned by Pr Taira from IMS.

We have found that the set of mirrors whose transmissions are given on Figure (52) gave the best result in terms of overall energy generated on the full tuning range. Each set of mirrors

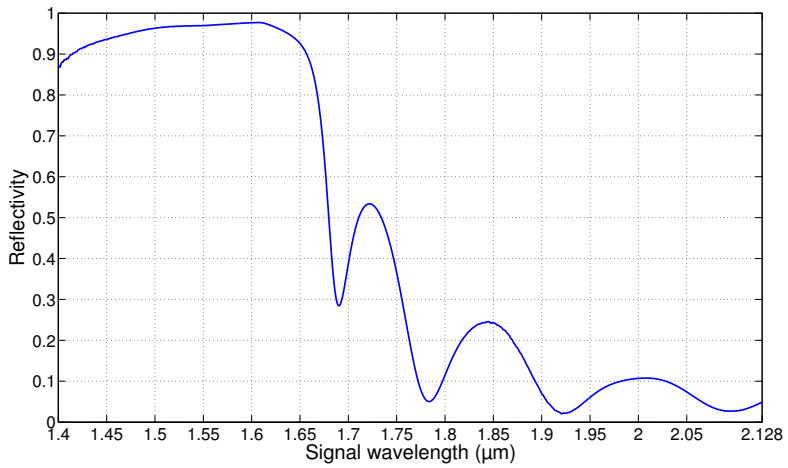

Figure 60: Reflectivity of the cavity used for the partial cylinder OPO cavity.

coming from Japan is optimized for a given range of signal and idler wavelengths: we have found that the conversion efficiency of the OPO with these mirrors is usually higher in the ranges of wavelengths for which the reflection coefficients have been optimized, but much lower in other ranges. In addition, the mirrors from IMS have a lower damage threshold. Lastly, note that using only one set of mirrors on the entire tuning range of our OPO is very convenient from a practical point of view.

We have plotted the reflectivity of the cavity with "our" mirrors on Figure (60): the cavity is highly reflective at the signal in the range 1.4-1.65 µm with an overall reflection coefficient higher than 90%. Above 1.65 µm, its reflectivity decreases. We clearly see here the consequences of our choice of set of mirrors: despite a better overall conversion efficiency and a higher damage threshold, the very high reflectivity of our mirrors in the range 1.4-1.65 µm is detrimental in terms of intracavity signal damage since more than 90% of the signal energy is trapped inside the cavity. The last option to reduce the risk of intracavity signal damage is therefore to increase the size of the beam waist of the resonating signal.

We believe that there is still a lot of improvement that can be done in the choice of the mirrors of the cavity. Such a wide tunability of the OPO can be seen as a potential problem (or opportunity...) here, because broadband and resistant mirrors need to be used.

11.1.2 *Increasing the signal beam radius in the cavity*

The Gaussian profile of the resonating signal inside the cavity of the partial cylinder OPO can be worked out by looking for the Gaussian beam that is reproduced identical to itself after one round trip [29]. To do so, the ABCD matrix given in Equation (167) is highly useful. We present here the simulations that we obtained regarding the size of the horizontal waist radius of the resonating signal (Figure 61).

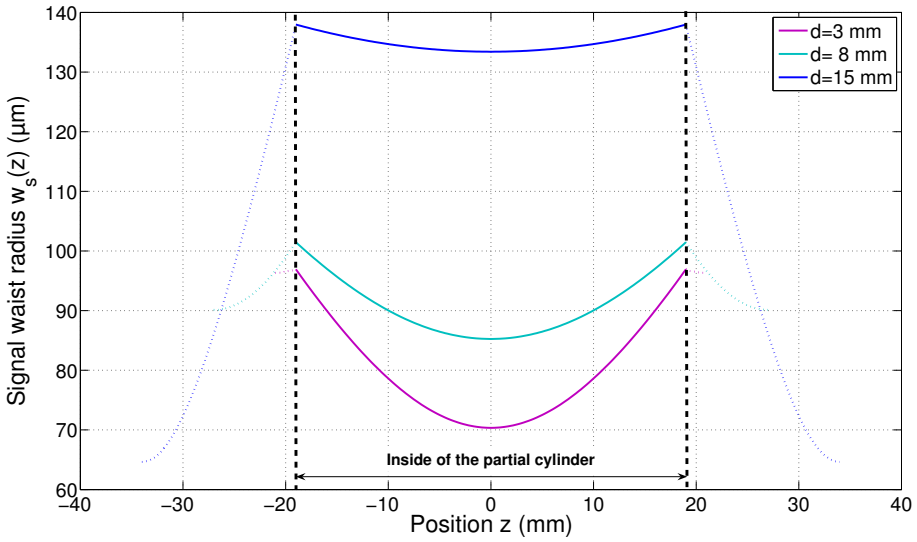

Figure 61: Effect of the cavity length on the horizontal beam profile of the resonating signal. The black dotted lines represents the faces of the cylinder, and the full lines corresponds to the profile inside the crystal. The signal wavelength is 1.67 µm in these simulations and the M^2 coefficient is assumed to be 1.

One sees that when the cavity length is increased, the size of the resonating signal inside the partial cylinder OPO is also increased. In terms of intracavity signal damage, the intensity *inside* the crystal can be reduced by a factor of four when the cavity length is increased, resulting in a decrease of the intensity on the *surface* of the partial cylinder by a factor of 2.5. This explains why we have chosen this solution to reduce the risk of intracavity signal damage. Modifying the cavity length has another effect on the horizontal resonating profile: the shorter the cavity, the smaller the divergence of the beams at the output of the OPO.

11.2 CAVITY LENGTH OPTIMIZATION

Increasing the cavity length of an OPO usually decreases the conversion efficieny because the number of passes in the crystal is reduced. In this section we investigate the effects of increasing the cavity length of our partial cylinder OPO. We first deal with the consequences of the recycling of the pump on the risk of damaging the crystal or the mirrors. Then, we present the experimental results on the influence of the cavity length on the energetical performances of the OPO. These two discussions are useful in determining the optimal cavity length for which the risk of damaging the crystal or the mirrors is the lowest while the conversion efficiency is the highest.

11.2.1 *Constraints induced by the pump recycling*

Reflecting the pump on the output mirror of an OPO has the clear advantage of artificially doubling the parametric interaction length since the down-conversion of the pump photons can now take place on the first and backward passes. It turns out that in our case, recycling the pump can lead to damaging the back surface of the partial cylinder.

We have sketched the profile of the pump beam inside the cavity on its forward and backward passes on Figure (62) for three mirror to partial cylinder distances d. On these figures, the pump beam propagates from left to right on the first pass (shown in red), and from right to left on the backward pass (shown in blue). The solid line represents the profile of the pump inside the partial cylinder, while the dashed lines represent the profile of the pump between the partial cylinder and the mirrors. The center of the cavity is still chosen as $z = 0$. The mirrors are represented by thick vertical black lines.

We assume that the cylindrical lens is located at the optimal distance D_{opt} so that the pump beam is parallel on its first pass as shown in Figure (51). But because of the curvature of the second face of the cylinder and because of the plane surface of the output coupler, the pump beam is no longer parallel on the backward pass. The position of the focal point actually depends on the distance betwen the cylinder and the output coupler, d. We see that when the cavity length is increased from 1 mm up to 15 mm, the focal point of the pump is translated from the center of the cavity to the surface of the output coupler. The pump beam propagates over $2d$ between the exit of the partial cylinder on its first pass and its re-entrance in the partial cylinder on the backward pass. When the following condition

$$2d = 2f_{cyl} - R \tag{175}$$

is satisfied, the pump beam is focused right on the back surface of the cylinder.

Numerically, this corresponds to

$$d = 8.25\,mm \tag{176}$$

And this is the situation shown on Figure (62b). As a "safety" margin , we will consider that the cavity length d should not be between 5 and 10 mm. The two other cases shown on Figure (62a) and Figure (62c) correspond to a very short cavity with d = 1 mm, and a long cavity with d = 15 mm, respectively.

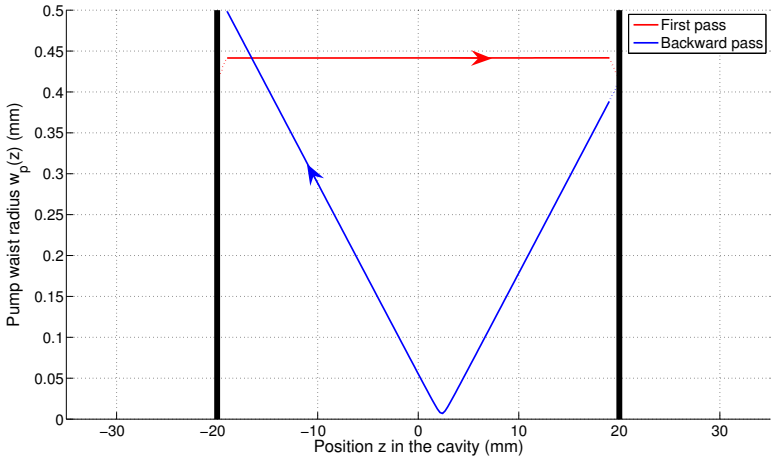

(a) Mirror to cylinder distance d = 1 mm. The pump beam is focused inside the cylinder.

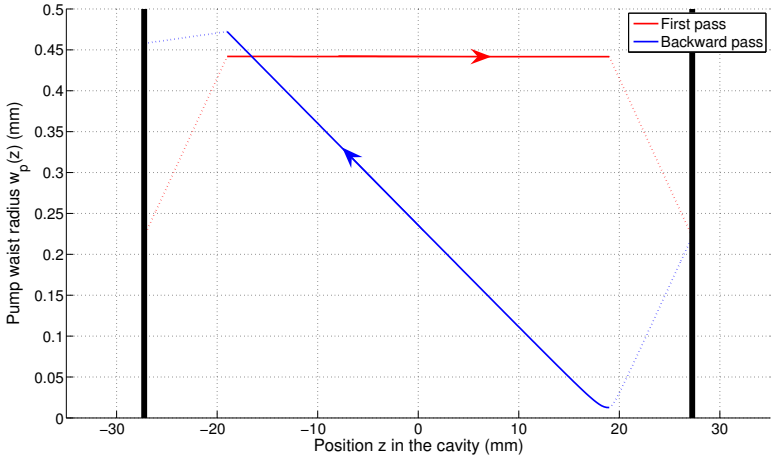

(b) Mirror to cylinder distance d = 8.25 mm. The pump beam is focused right on the surface of the cylinder.

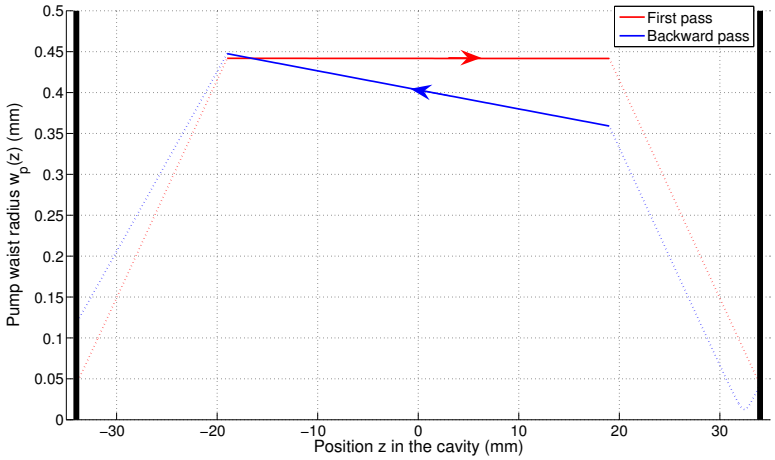

(c) Mirror to cylinder distance d = 15 mm. The pump beam is focused between the cylinder and the output mirror.

Figure 62: Horizontal profile of the pump beam inside the cavity on its first and reflected pass for three different cavity lengths.

11.2.2 *Energetical conversion efficiency and thresholds*

We have performed a series of measurements of the unfiltered output energy of the OPO versus input pump energy at different cavity lengths as shown in Figure (63). Above threshold, each curve was fitted with a two parameter linear relation (See equation 101):

$$E_{out} = \eta(E_p - E_{p,th}) \tag{177}$$

which gives a straightforward access to the values of the pump energy threshold $E_{p,th}$ and OPO conversion efficiency η.

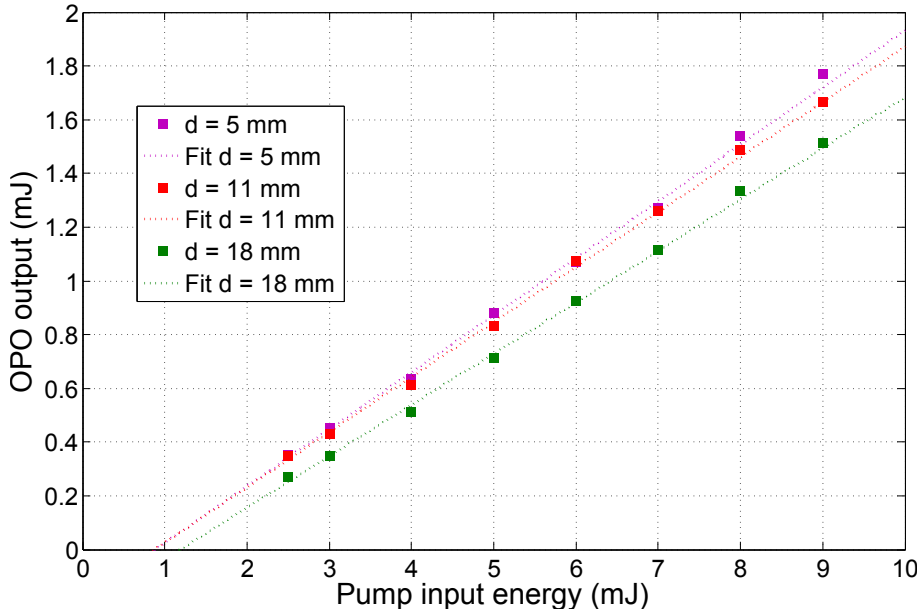

Figure 63: Effect of the cavity length on the output energy of the cylindrical OPO. Only three measured (squares) and fitted (dashed) curves are shown for more clarity. The signal wavelength is 1.67 µm.

These two parameters are then given as a function of the cavity length on Figure (64), which shows that there are basically two different regimes of operation for the cylindrical OPO. The first regime corresponds to short cavity lengths: the threshold of the OPO is low and constant throughout this range whereas the conversion efficiency is almost constant too. This regime extends from the shortest cavity lengths up to a distance d that we found to be between 12.5 mm and 15 mm. The second regime is obtained for cavities longer than that. There, the corresponding efficiency of the OPO drops sharply while the threshold of the OPO increases almost linearly so that the energetical performance is poor in this regime.

If we want to keep a good conversion efficiency, the mirror to cylinder distance d should belong to the so-called "short cavity regime". On the other hand, we see on Figure (61) that the longer the cavity length, the bigger the size of the signal beam in the cavity. The best tradeoff between a low risk of intracavity signal damage and a good conversion efficiency corresponds to a mirror to

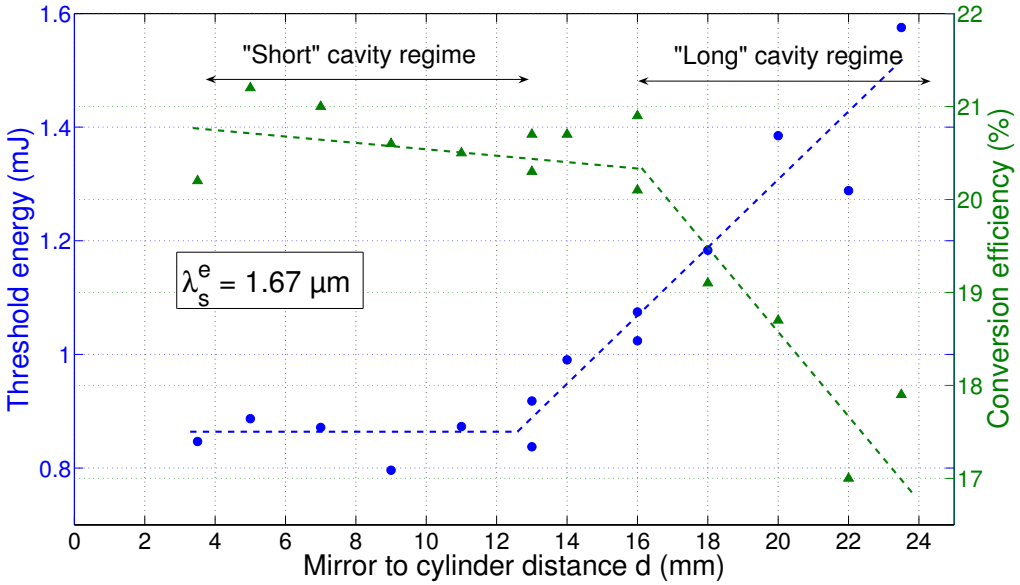

Figure 64: Effect of the cavity length on the threshold (blue circles) and energy efficiency (green triangles) of the OPO. The lines are guides for the eyes.

cylinder distance d between 12.5 mm and 15 mm. In the rest of this work, we will then choose d = 15 mm.

11.3 PARTIAL CYLINDER OPO EFFICIENCY

In this section, the cavity length is set at d = 15 mm, and we report the efficiency of the OPO at several signal wavelengths.

11.3.1 *Generated energy*

The unfiltered OPO output energy versus pump input energy was measured for three different rotation angles corresponding to three different signal wavelengths: 1.497 µm, 1.65 µm and 2.02 µm as shown on Figure (65). The pump energy is varied from 0 to 10 mJ.

The corresponding pump thresholds in energy and fluence, as well as conversion efficiencies η are given in Table (13). The pump thresholds in energy are between 1.1 and 1.9 mJ. We have obtained conversion efficiencies as high as 32.7 % close to 2 µm, and above 23% on the entire tuning range of the OPO. These conversion efficiencies are the highest ever reported for cylindrical devices. Our strategy of a thick partial cylinder OPO is validated by these results.

We have measured separately the idler and signal contributions to the unfiltered output by measuring the generated energy after two different filters. The results are shown in Figure (66). These curves show that when the pump energy is about 5 mJ, our source delivers more than 0.5

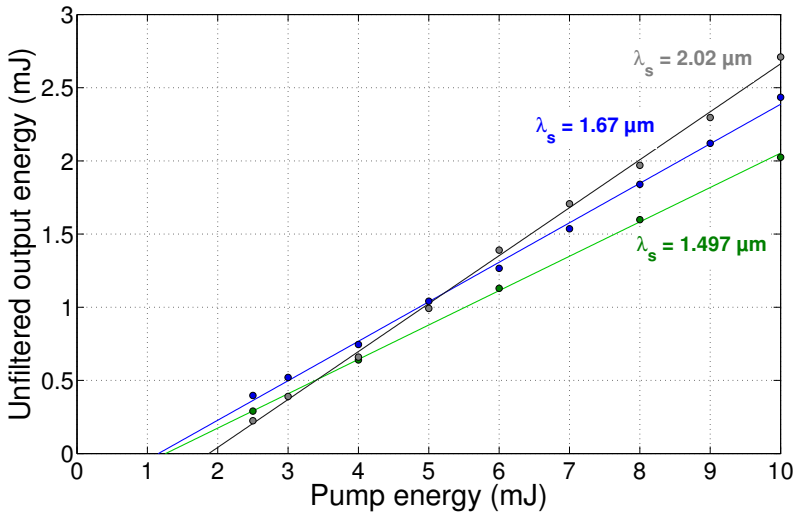

Figure 65: Best output versus input curves of the cylindrical OPO measured at three different sets of signal and idler wavelengths with the same set of mirrors (n°4 and n°31).

Signal Wavelength (µm)	Idler wavelength (µm)	Pump energy threshold (mJ)	Pump intensity fluence (mJ/cm^2)	Conversion efficiency η
1.497	3.68	1.26	44.5	23.5 %
1.67	2.93	1.16	41.0	27.0 %
2.02	2.25	1.87	66.1	32.7%

Table 13: Thresholds and efficiency of the OPO at three different signal wavelengths.

mJ at 3.7 µm. These conversion efficiencies above 3 µm were our initial target in terms of future DFG experiments in small crystals.

The stability of the OPO output was also measured. The standard deviation of the generated energy for 100 pulses is constant over the tuning range and scales with the pump laser stability, i.e. between 2 to 3%. We have also checked that the non-phase matched upconverted wavelengths measured at the output of the OPO do not account for more than 5% of the unfiltered output.

Contrary to most OPO curves usually reported, the top of the output curves shown in Figure (65) does not correspond to the surface damage of the sample. Even though it was very tempting to keep increasing the pump energy, we did not try to do so because the availability of about 500 µJ around 4 µm was our initial target in terms of generated energy for future DFG experiments, and we did not take the risk to damage a so unique sample.

We have also measured the unfiltered output of the OPO as a function of the rotation angle. The results are displayed on Figure (67). The pump input energy used for these experiments is 5 mJ and corresponds to a moderate and routine value. The output of the OPO increases from 600 µJ at 1.41 µm up to 1.4 mJ at degeneracy where it reaches its maximum. Note that this curve has been obtained without tilting the mirrors of the cavity. We could also assess the influence of the presence of OH^- impurities on the OPO conversion efficiency. These impurities cause some idler

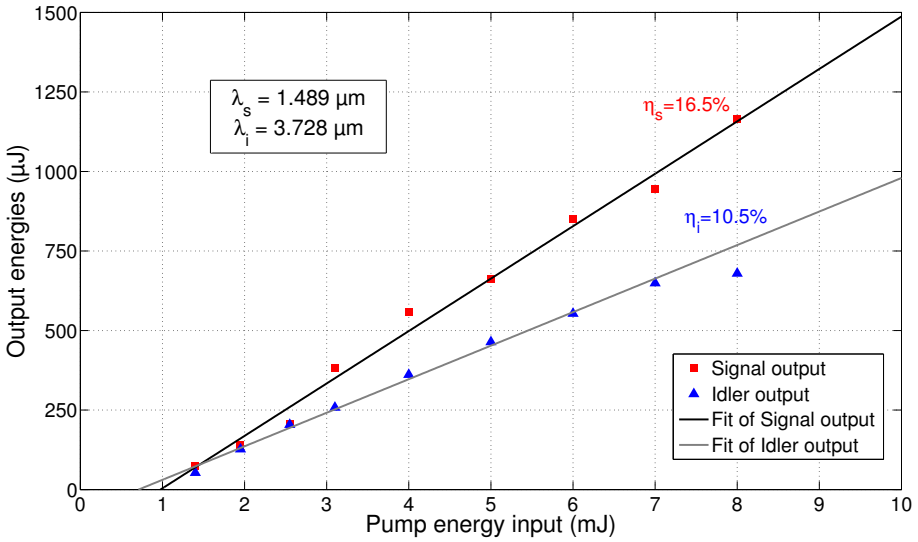

Figure 66: Signal and idler conversion efficiency for a signal wavelength at 1.489 µm and the idler at 3.728 µm.

absorption around 2.9 µm, and the idler absorption translates into a drop of efficiency as high as 30 %.

11.3.2 *Comparison with a slab and discussion*

The values of the pump fluence thresholds of our partial cylinder OPO (in mJ/cm^2) are given in Table (13) and fall in the range 40-70 mJ/cm^2, which is still almost an order of magnitude higher than what our colleagues from IMS obtained in similar slab samples [89]: in 2005, optical parametric oscillation close to 2 µm was obtained with a fluence threshold around 6 mJ/cm^2. However, because of the different pump profiles and cavity mirrors used in their experiment, we find it difficult to compare our values with these values.

That is why we performed another comparison at Néel Institute between a slab OPO and our partial cylinder OPO. The slab used for comparison (PF 147) comes from the same batch as our partial cylinder A (PF 145), but contrary to our cylinder, it is anti-reflection coated. The QPM period and tilt of the grating are identical for the two samples. In order to perform a fair comparison, the slab was inserted in the same cavity as that of the partial cylinder OPO, but we removed the focusing cylindrical lens in the case of the slab OPO. The comparison between the output energy curves obtained with the partial cylinder and the slab is shown on Figure (68). We found that the output energy of the two devices is very similar. The threshold of the slab OPO (1.16 mJ) is somewhat smaller than that of the cylindrical OPO (1.26 mJ), but the efficiency of the cylindrical OPO (η = 23.5%) is somewhat higher than that of the slab OPO (η = 22.7%). Despite equivalent generated energies, the pump intensity focused in the partial cylinder is between 15 and 20 times higher than that in the slab OPO. The origin of this need fo a higher intensity in the

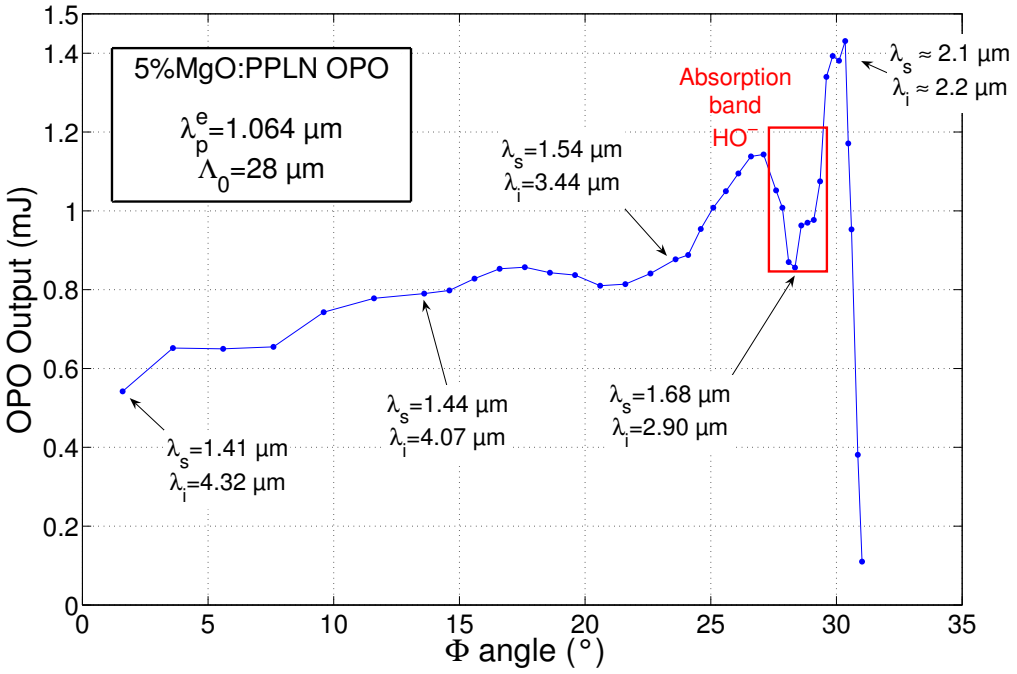

Figure 67: Output energy of the partial cylinder OPO as a function of the angle of rotation. The pump energy is 5 mJ.

case of the cylindrical OPO stems probably from a poor coupling between the waves in the cavity. Assessing the overlap between the pump and resonating signal wave in a partial cylinder OPO is not something easy because of the profiles of the pump beam over its two passes. Nevertheless, ABCD matrix calculations show that for a 15 mm cavity length, the horizontal beam waist radius of a resonating signal around 1.5 µm is about 130 µm, while the pump beam waist is around 420 µm (See Figure 69). Such a discrepancy undoubtedly alters the efficiency of the OPO since only the center of the pump beam is likely to be efficiently coupled in the resonating signal mode.

More calculations should be performed to give a quantitative assessment of the coupling between the waves and find the optimal combination of cylindrical focal length and mirror curvatures.

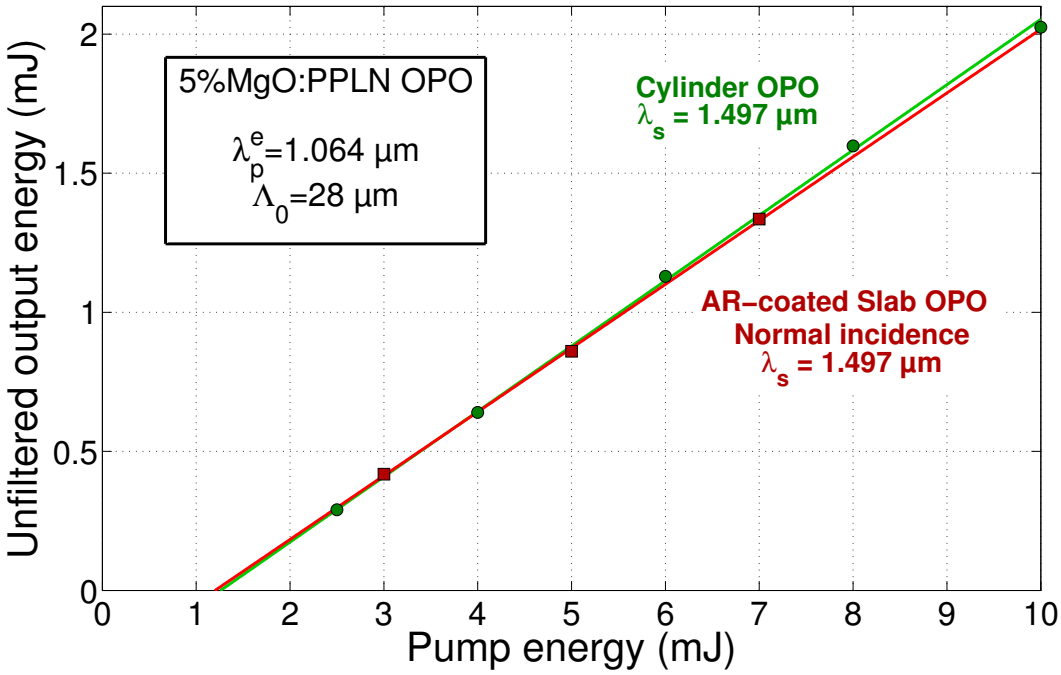

Figure 68: Comparison between the output energy of the uncoated partial cylinder OPO and the antireflection coated slab OPO at the same QPM wavelength λ_s=1.497 µm.

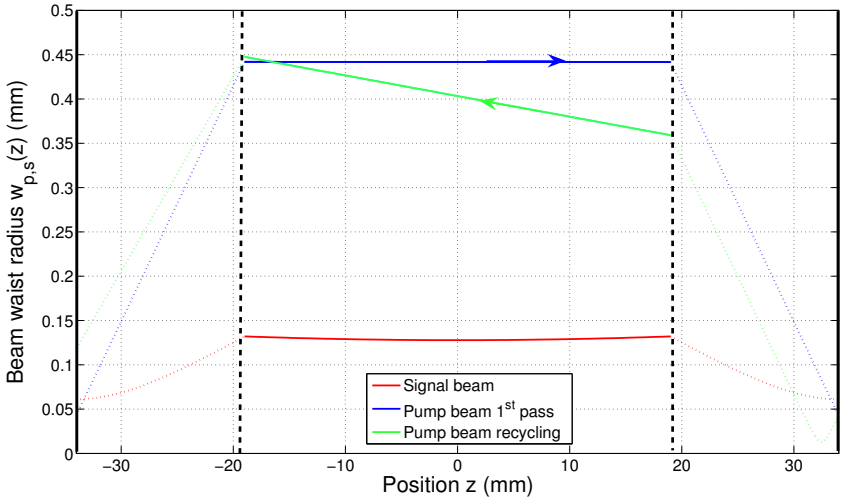

Figure 69: Spatial overlap between the pump and the resonating signal beams for d =15 mm and a signal wavelength $\lambda_s = 1.497$ µm.

12

SPECTRAL CHARACTERIZATIONS OF THE OPO

This chapter is dedicated to the spectral characterizations of the signal beams generated by the partial cylinder OPO. We first present the measurements of the linewidth of the signal beam at three different wavelengths and pump intensities. Then, we analyze several interesting features of the experimental curves in order to get some new insight on the performance of the partial cylinder OPO. This spectral analysis comes to supplement the previous results on the conversion efficiency and performance of the OPO.

12.1 RAW MEASUREMENTS

We now describe briefly the procedure that was implemented for the measurements of the spectral linewidths of the generated signal beam at three different angles of rotation and several pump energies (see Figures (70), (71) and (72)). For each angle of rotation, we first measure the signal wavelength with the usual method described in Table (12) and a low pump energy of 2 mJ. Then, we record the spectrum of the signal beam with a Chromex 250 SM spectrometer and an InGaAs photodiode DET 410 from Thorlabs, at different pump energies. The spectra measured with the Chromex spectrometer were found to be consistently shifted by 25 ± 1 nm from our measurements with the first method. Such a deviation was attributed to a constant error on the calibration of the spectrometer, and as a consequence, the spectra showed thereafter are given taking into account this constant deviation. Their resulting accuracy is ± 1 nm.

Figures (70), (71) and (72) show the results of these measurements for 2 mJ, 6 mJ and 10 mJ pump energies while Table (14) summarizes the main characteristics of all the measurements we performed.

Based on these measurements, we will now develop an extensive analysis of the spectral properties of the signal beam. It is organized as follows: first of all, two main characteristic features of these spectra are analyzed: the shift of the QPM wavelength and the broadening of the spectrum when the pump energy is increased. An effective interaction length in agreement with the linewidths of the spectra measured at the two shorter signal wavelengths 1.43 and 1.64 µm (Figures 70 and 71) will be found. The second part of the analysis focuses more specifically on the third set of spectra measured close to 2 µm as shown on Figure (72). The "chaotic" shape of these spectra will be analyzed in detail and highly valuable information will be obtained.

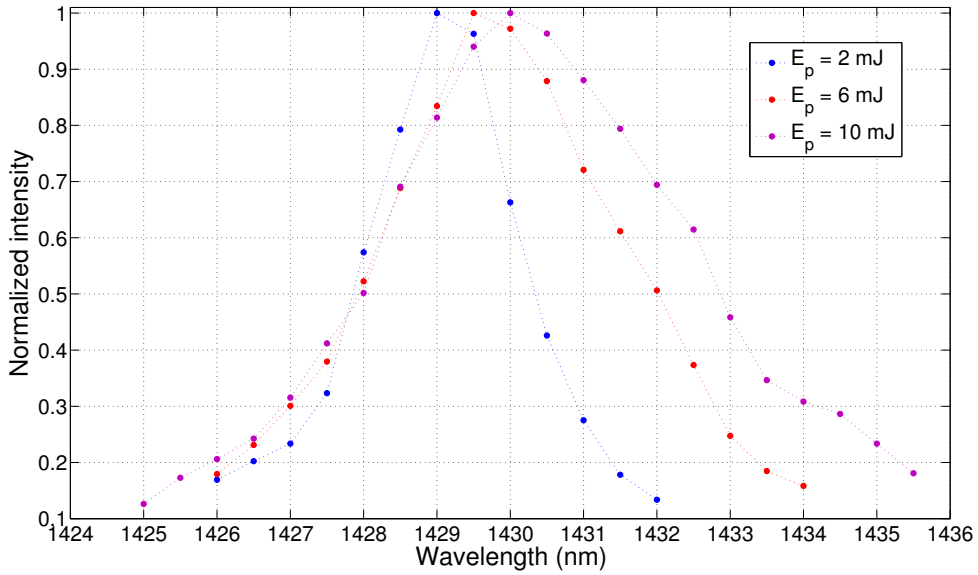

Figure 70: Spectrum of the generated signal around 1.43 µm for different pump intensities.

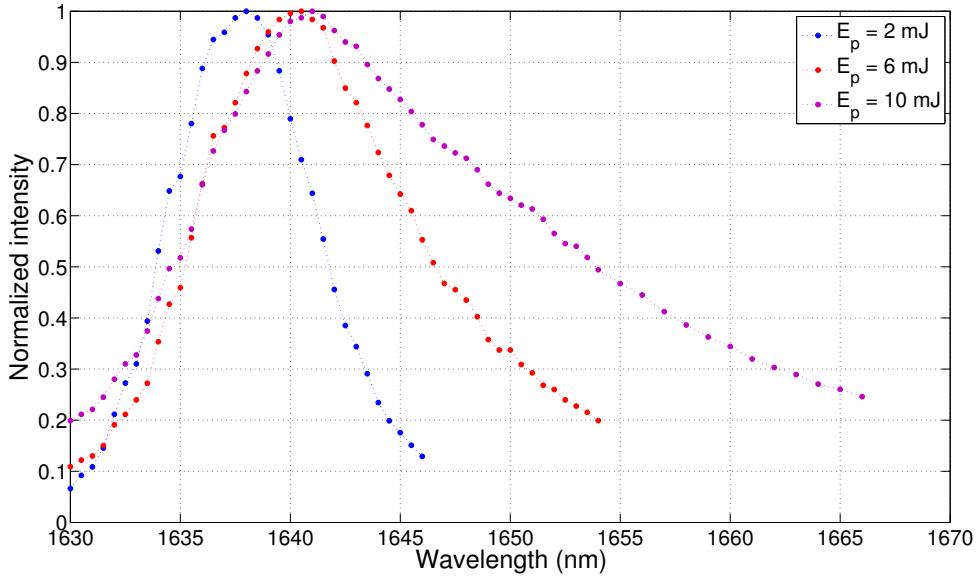

Figure 71: Spectrum of the generated signal around 1.64 µm for different pump intensities.

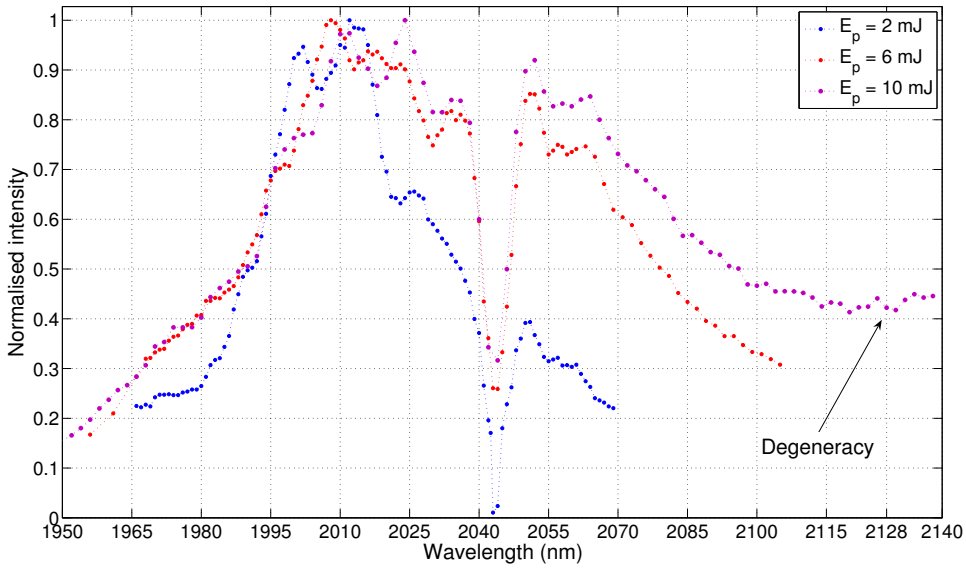

Figure 72: Spectrum of the generated signal around 2.05 µm for different pump intensities.

Pump Energy (mJ)	Figure (70)		Figure (71)		Figure (72)	
	QPM wavelength (µm)	FWHM (nm)	QPM wavelength (µm)	FWHM (nm)	QPM wavelength (µm)	FWHM (nm)
2.0	1.429	2.5	1.628	8.0	2.012	46
4.0	1.4295	3.35	1.6297	10.1	Not measured	
6.0	1.4295	4.1	1.6305	11.85	2.008	89
8.0	1.430	4.65	1.631	13.4	Not measured	
10.0	1.430	4.7	1.631	18.2	2.024	107

Table 14: Spectral properties of the signal beams measured experimentally. The QPM signal wavelength is taken as the wavelength for which the spectral density is the highest.

12.2 INCREASE IN TEMPERATURE

A common feature to the three sets of spectra displayed on Figure (70), (71) and (72) is the shift of the QPM wavelength when the pump energy is increased. Experimentally, the QPM wavelength was found to increase by 1 nm, 3 nm and 12 nm at 1.43 µm, 1.628 µm and 2.01 µm when the pump energy is increased from 2 mJ up to 10 mJ respectively. This shift of the QPM signal wavelength can be related to an increase of the temperature of the crystal, which is legitimate since no temperature control is implemented in our device.

When the temperature of a QPM crystal is changed, the refractive indices as well as the QPM period may vary a priori. However, the expansion coefficient of 5%MgO:PPLN given in [106] suggests that the QPM period cannot be modified by more than 0.05% when variations of temperature smaller than 30° are considered. Since small temperature variations are considered in

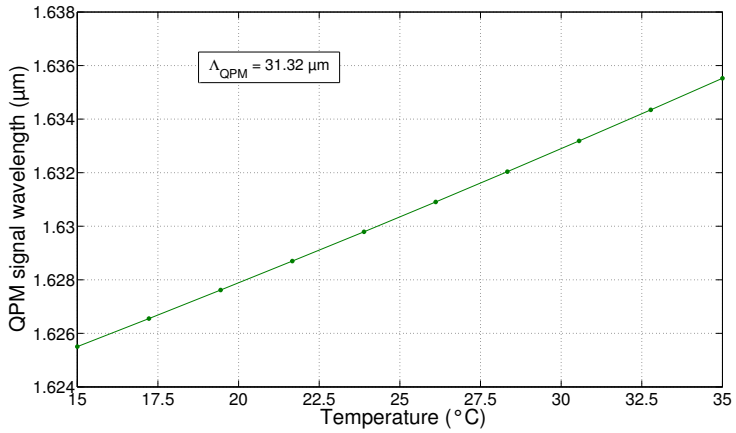

Figure 73: Effect of the temperature on the QPM signal wavelength at a fixed QPM period of 31.32 µm corresponding to a QPM signal of 1.628 µm at T=21°C. Sellmeier equations from reference [106] have been used.

this section, this remark allows us to neglect the variations of the QPM period.The temperature dependence of the refractive indices, i.e. the thermo-optical effect, will only be used to relate the shift of the QPM wavelength to an increase in the temperature of the crystal. Based on Equation (155), we could calculate the theoretical variations of the QPM signal wavelength between 15 °C and 35 °C. At 1.429 µm and 1.635 nm the temperature tuning rates are constant and equal respectively to 0.11 nm/°C and 0.5 nm/°C (see Figure 73). The 1 nm and 3 nm shifts in wavelength observed experimentally therefore would correspond to an increase in temperature of 10 °C at 1.429 µm and 6 °C at 1.628 µm. Around 2 µm, the temperature tuning rate increases much faster with the wavelength as shown on Figure (74): it is 0.7 nm/°C at 21 °C, but it becomes infinite when the upper QPM temperature is reached. It is more difficult to assess the temperature increase close to 2 µm because the shift in QPM wavelength is not determined accurately. Nevertheless, a shift of 12 nm as seen on Table (14) corresponds to a rise of temperature of about 17 ° C.

The variations of these temperature changes with the QPM signal wavelength suggest that they cannot be only attributed to a stronger pump energy. A higher absorption coefficient at the idler wavelength (4.15 µm versus 3.0 µm) could explain the difference between the temperature rise at 1.43 µm and 1.64 µm. The fact that the temperature rise is higher at 2.0 µm than at 1.429 µm and 1.628 µm is more surprising: it does not correlate with a higher reflectivity of the mirrors (see Figure 60). It is maybe due to the fact that the idler wavelength is no longer absorbed by the input mirror (See figure 52) but reflected inside the cavity closer to degeneracy, which would increase the conversion efficiency and thus rise even more the temperature.

12.3 SPECTRAL LINEWIDTH STUDIES

In addition to a small shift of the QPM signal wavelength at higher pump energy, the linewidth of the spectrum also increases with the pump energy. In this section, we give theoretical justification

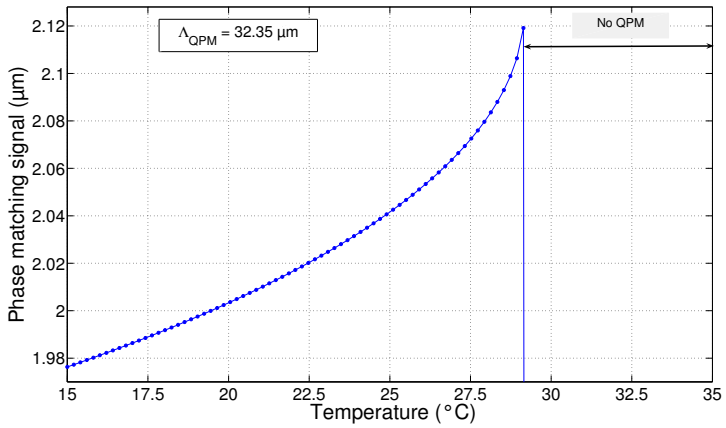

Figure 74: Effect of the temperature on the QPM signal wavelength for a fixed QPM period of 32.35 µm corresponding to a signal wavelength of 2.01 µm at T=21°C. Sellmeier equations from reference [106] have been used.

of the model that we use to analyse the values of the linewidth measured experimentally at low pump energy, and at higher energies.

12.3.1 *Gain function of an OPO*

The spectral properties of the signal emitted by an OPO have been studied both theoretically [33, 32] and experimentally [119, 120] in the past, and the model to determine the FWHM of the signal generated by and OPO is now well established. We use such a model following the main ideas given in [33].

The expression of the gain function of an Optical Parametric Amplifier was derived in the first chapter of this dissertation (see Equation 52). It writes:

$$G_{OPA} = \frac{I_s(L)}{I_s(0)} = 1 + \frac{\gamma_0^2}{\sqrt{\gamma_0^2 - (\frac{\Delta k}{2})^2}} \sinh^2(\sqrt{\gamma_0^2 - (\frac{\Delta k}{2})^2} L) \tag{178}$$

where L is the length of the sample and γ_0 is the amplification coefficient given in Equation (49):

$$\gamma_0^2 = \frac{8\pi^2 d_{eff}^2}{\lambda_s \lambda_i n(\lambda_s) n(\lambda_i) n(\lambda_p)} Z_0 I_{p,0} \tag{179}$$

When plugging the value of the effective coefficient

$$|d_{eff}| = \frac{2}{\pi} |d_{33}| = 16.0\, pm/V \tag{180}$$

based on measurements from [12], in Equations (178) and (179), it is possible to compute the gain function of an Optical Parametric Amplifier for a crystal of 5%MgO:PPLN of length L and for any arbitrary values of the signal wavelength and pump energy. At small energies, the gain function has the classical "sinc" dependency. But at higher gains, the gain function broadens, and the FWHM is increased. An Optical Parametric Oscillator can be regarded formally as a succession of several OPAs in series. And the gain function of such a device is then given by:

$$G_{OPO} = (G_{OPA})^M \tag{181}$$

where M is the number of round trips of the signal in the cavity before reaching threshold [32]. A higher number of passes in the crystal tends to reduce the linewidth of the generated beams.

Note that this model is oversimplified since it neglects the divergence of the beams and assumes a perfect QPM grating without any transversal variations or inhomogeneities. Moreover, it assumes that the interaction between the beams takes place over the entire length of the sample. This might not be the case so that we allow L to be the interaction length rather than the crystal length. A shorter interaction length inevitably broadens the spectra generated in the cavity.

12.3.2 *Analysis of our measurements*

In this section we try to relate the linewidth of the spectra measured experimentally to the prediction of the model that we just presented. The interaction length of the sample L as well as the number of passes in the crystal will be adjusted to match the shape of the gain function calculated from Equations (181) to our experimental spectra.

It turns out that the linewidths of the signal wavelengths at 1.43 µm and 1.65 µm are in good agreement with a single pass (M = 1) model of Optical Parametric Amplification considering a reduced interaction length in the crystal sample. We have shown on Figure (75) that the best agreement is obtained for a length L = 13 mm if $\lambda_s = 1.43$ µm and for a length L = 19 mm if $\lambda_s = 1.64$ µm. In every case, the spectrum calculated for a single pass and L = 38 mm, which corresponds to the diameter D of the partial cylinder, is also shown for the sake of comparison. The effect of a reduced interaction length is the broadening of the spectra as shown on Figure (75).

These conclusions on a shorter interaction length are somehow surprising because the interaction length is much reduced compared with the partial cylinder diameter D = 38 mm. At 1.43 µm, the effective interaction length derived from the fit of the spectral profiles is close to one third of the crystal diameter. It increases to one half of the diameter of the cylinder at 1.64 µm. In addition, the fact that the best agreement was obtained for a single pass gain model is also surprising. In order to further check the validity of the single pass gain model, we investigated the effect of an increase of the pump energy on the linewidth of the spectra. We have compared the spectra measured at 10 mJ pump energy to the single pass OPA gain function given in Equation (178) and for a pump intensity corresponding to 10 mJ. The results are plotted on Figures (76a) and (76b). It turns out that the gain function of the single pass OPA does not widen as fast as the

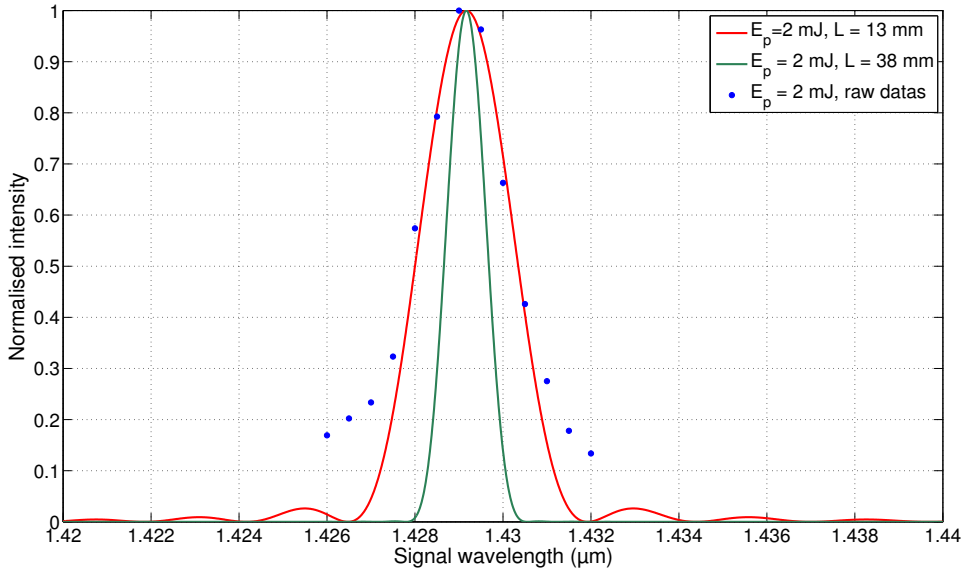

(a) The best agreement is obtained for $\lambda_s = 1.428$ µm when an interaction length L = 13 mm is considered in Equation (178).

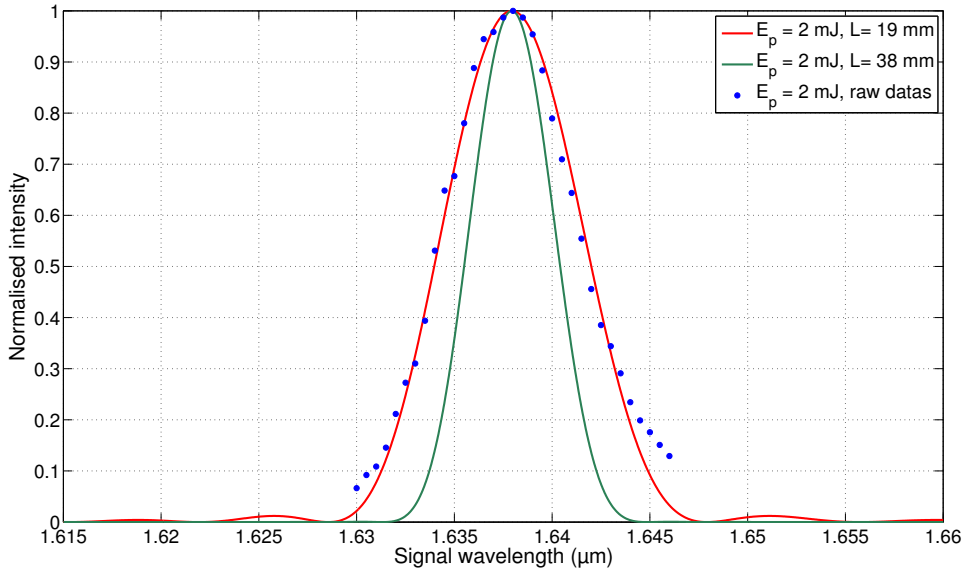

(b) The best agreement is obtained at $\lambda_s = 1.64$ µm when an interaction length L = 19 mm is considered in Equation (178).

Figure 75: Determination of the effective length of interaction in the crystal from the fit of the signal spectral profile at 1.43 µm (a) and 1.64 µm (b). The pump energy is 2 mJ corresponding to a pump intensity of 7.5 MW/cm^2.

real spectra when the pump energy is increased. Even though the broadening of the left wing of the spectrum is fairly well predicted by our model, the discrepancy between the calculations and the experiments are mostly seen on the right wing of the spectra: the upper part of the spectra broadens much faster than the lower part.

The role of temperature fluctuations identified in the previous section deserves more investigation with this respect. One way to check for the influence of the temperature would be to carry out the same analysis with the same crystal but with a regulated temperature. Another hypothesis could be the contribution of the divergence of the beam, the different "rays" over the beam aperture propagating at different effective QPM periods due to the asymetry of the grating geometry. We also think that it would be interesting to check the distribution of wavelengths over the beam cross section. This would be a highly efficient way to probe the quality of the QPM grating but also to make sure that the asymmetrical broadening does not come from spectral inhomogeneities over the beam profiles.

Eventually, if we take L = 15 mm as an average interaction length, we found that M = 11 round trips for the signal at low pump energy and M = 7 round trips at 10 mJ pump energy give the best agreement between the spectra measured experimentally and the calculations from Equation (181), as shown on Figure (77).

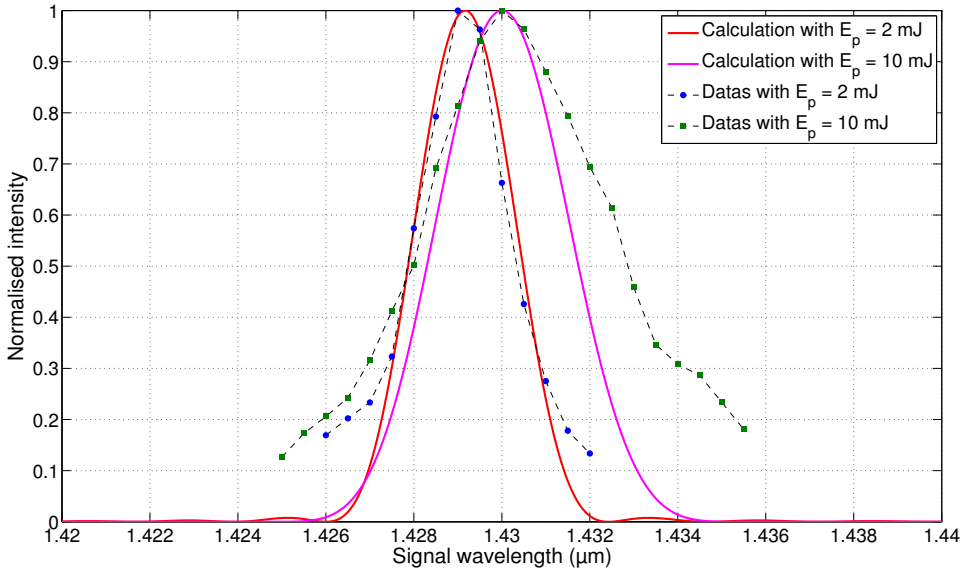

(a) Spectral broadening around 1.43 µm. The length of the crystal used for calculation corresponds to that determined on Figure (75) i.e. L = 13 mm here.

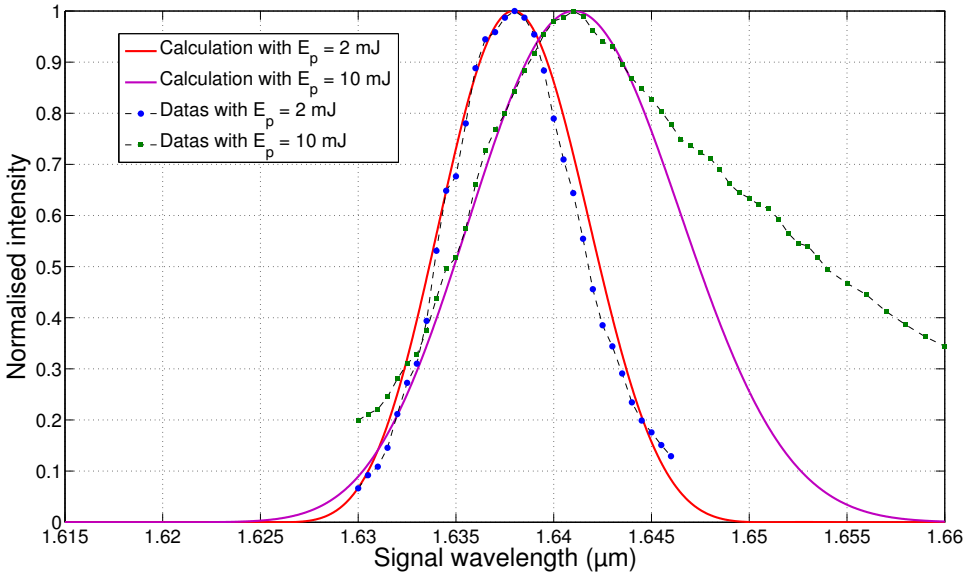

(b) Spectral braodening around 1.64 µm. The length of the crystal used for calculation corresponds to that determined on Figure (75) i.e. L = 19 mm here.

Figure 76: Effect of the pump energy on the linewidth of the signal.

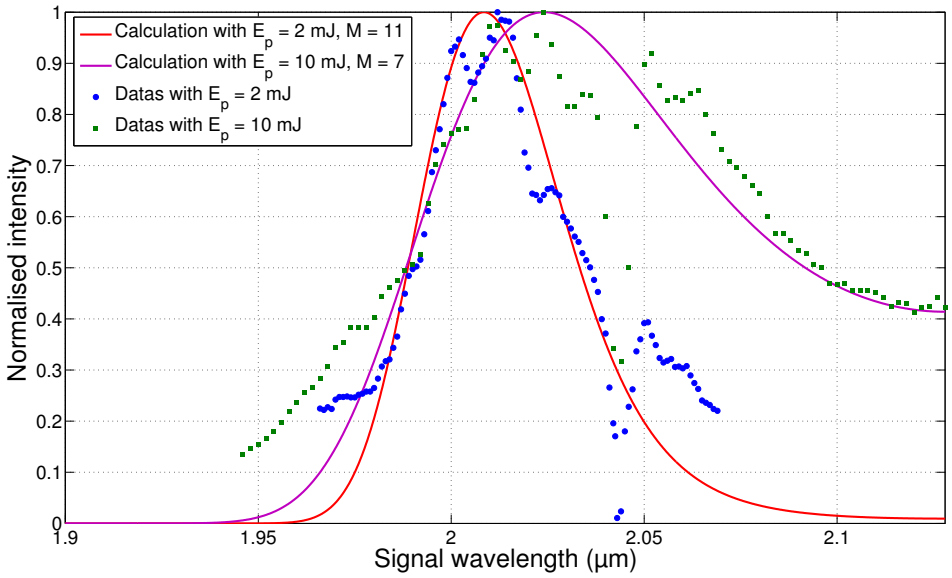

Figure 77: Determination of the effective length of interaction in the crystal from the fit of the signal spectral profile at 2.01 µm. The pump energy is 2 mJ corresponding to a pump intensity of 7.5 MW/cm^2.

12.4 FURTHER CONCLUSIONS

This section develops a more subtle analysis of the third set of spectra measured close to 2 µm. We draw two very important conclusions from this analysis.

12.4.1 *Simultaneous QPM*

A (not so careful) observation of the spectra displayed on Figure (72) shows an intriguing dip at 2.043 µm making the full spectra look somewhat "chaotic". We have long thought that this dip in the spectrum was coming from a defect on the grating of the Chromex spectrometer used in the measurements. It turns out that this dip actually provides some very important conclusions on the performances of the partial cylinder OPO.

Figure (78) shows the experimental and calculated angular tuning curves of the partial cylinder OPO as well as the phase-matching curve of the second order SFG process between the signal of the OPO and the 1.064 µm pump. In terms of energy conservation relation, the first order DFG corresponds to:

$$\hbar\omega_p \underset{DFG}{\rightarrow} \hbar\omega_s + \hbar\omega_i \tag{182}$$

while the SFG process corresponds to :

$$\hbar\omega_p + \hbar\omega_s \underset{SFG}{\rightarrow} \hbar\omega_{SFG} \tag{183}$$

Let us recall here that a second order QPM process is a QPM process for which the QPM period is not equal to twice the coherence length as in a first order QPM process (see section 2.2.3) but to four times the coherence length. Such a second order QPM process is possible only if the duty ratio η deviates from its ideal value of 0.5 (see Figure 12).

We see that there is a signal wavelength close to 2 µm and an angle ϕ close to 30° for which the two phase-matching curves intersect. As a consequence, for this specific direction of propagation, there are two processes simultaneously quasi-phase-matched and a pump photon has basically two "options": it can either split into a signal and an idler photons through the QPM DFG condition, but it can also fusion with a signal photon to create a photon of higher energy through the SFG QPM condition. The intensity at the specific signal wavelength for which these two QPM conditions are fulfilled is reduced because such signal photons are consumed through the SFG process, but also because some pump photons are consumed in the SFG process which in turn decreases the conversion efficiency of the DFG. The dip in the spectrum corresponds exactly to the wavelength for which these two processes are quasi-phase-matched simultaneously.

These simultaneous QPM processes have already been reported experimentally: such a dip in a broad spectrum close to 2 µm was observed at 2.044 ± 0.002 µm [121] but with a lower intensity than in our case. This previous value of the signal wavelength is then in perfect agreement with the value that we measured on Figure (72).

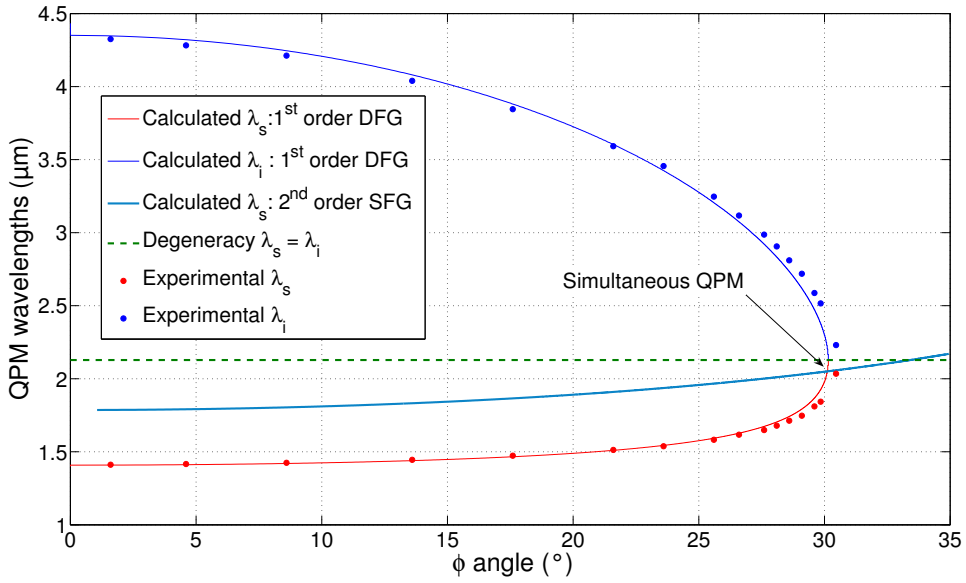

Figure 78: Simultaneous QPM between the first order DFG and the second order SFG between the pump at 1.064 µm and the signal of the OPO. Equation 155 is used for the calculations.

12.4.2 *Collinear versus noncollinear QPM (second proof)*

We now advocate that this simultaneous QPM condition can be a very efficient criteria to discriminate between the collinear and the noncollinear QPM configurations. In this section, we solve the condition for simultaneous QPM in the collinear and noncollinear QPM configurations. And we show that our measurements are closer to the simultaneous QPM phase-matching in the collinear case.

The first order collinear QPM DFG equation is the classical equation used in this chapter:

$$\frac{n^e(\lambda_p)}{\lambda_p} - \frac{n^e(\lambda_s)}{\lambda_s} - \frac{n^e(\lambda_i)}{\lambda_i} = \frac{\cos\phi}{\Lambda_0} \tag{184}$$

The second order QPM SFG condition is now investigated. We said previously that the second order QPM period, Λ_{SFG}^{2nd}, is four times the coherence length of the SFG process:

$$\Lambda_{SFG}^{2nd} = 4L_{c,SFG} = \frac{4\pi}{\Delta k_{SFG}} \tag{185}$$

so that when we impose that the second order QPM period is the effective QPM period $\Lambda_{eff}(\phi)$, we find:

$$\Delta k_{SFG} = \frac{4\pi\cos\phi}{\Lambda_0} \tag{186}$$

from which the second order collinear QPM SFG condition writes:

$$\frac{n^e(\lambda_{SFG})}{\lambda_{SFG}} - \frac{n^e(\lambda_s)}{\lambda_s} - \frac{n^e(\lambda_p)}{\lambda_p} = \frac{\cos\phi}{\left(\frac{\Lambda_0}{2}\right)} \tag{187}$$

The common solution to Equations (184) and (187) gives the condition for which these two parametric processes are simultaneously quasi-phase-matched. We find graphically $\phi = 30.11°$ and $\lambda_s = 2.05\,\mu m$, as shown on Figure (79).

A similar reasoning can be performed to find the angle and wavelength for which simultaneous QPM is possible in the case of a noncollinear QPM configuration. The first order noncollinear QPM DFG equation was given in Equation (173):

$$\frac{n^e(\lambda_p)}{\lambda_p} - \frac{n^e(\lambda_s)}{\lambda_s} - \frac{n^e(\lambda_i)}{\lambda_i}\sqrt{1 - (\frac{\lambda_i \sin\phi}{\Lambda_0 n^e(\lambda_i)})^2} = \frac{\cos\phi}{\Lambda_0} \tag{188}$$

As for the second order QPM SFG equation, it is now the SFG that will adapt both its direction of propagation and wavelength to close the vectorial QPM relation, and not the idler as in the case of DFG. The resulting equation ruling this process is therefore :

$$\frac{n^e(\lambda_{SFG})}{\lambda_{SFG}}\sqrt{1 - (\frac{\lambda_{SFG}\sin\phi}{\left(\frac{\Lambda_0}{2}\right) n^e(\lambda_{SFG})})^2} - \frac{n^e(\lambda_s)}{\lambda_s} - \frac{n^e(\lambda_p)}{\lambda_p} = \frac{\cos\phi}{\left(\frac{\Lambda_0}{2}\right)} \tag{189}$$

And the solution of the simultaneous noncollinear QPM is $\phi = 29.56°$ and $\lambda_s = 2.032$ nm, as shown on Figure (79).

We have compared the theoretical values of collinear and noncollinear simultaneous QPM conditions to our experimental results in Table (15). Experimentally, we found that the signal wavelength at which the two processes are simultaneously phase-matched is 2.043 µm. The corresponding phase-matching angle is $30.5° \pm 0.5°$. The experimental simultaneous QPM phase-matching angle is therefore more than 1° off the noncollinear QPM condition. It is only 0.4° off the theoretical value of the collinear solution. Even with angular error bars of 0.5° the agreement with the collinear solution is better. We do believe that this discussion provides the second proof of a collinear QPM configuration in the partial cylinder OPO. This constitutes one of the main conclusions of the present dissertation.

12.4.3 *Grating characterization*

We have given in Part I some clues about higher order QPM processes. We especially mentioned on Figure (12) that the effective coefficient of a second order QPM process vanishes when the duty ratio of a QPM sample is exactly 0.5, and that it has the highest amplitude when the duty ratio

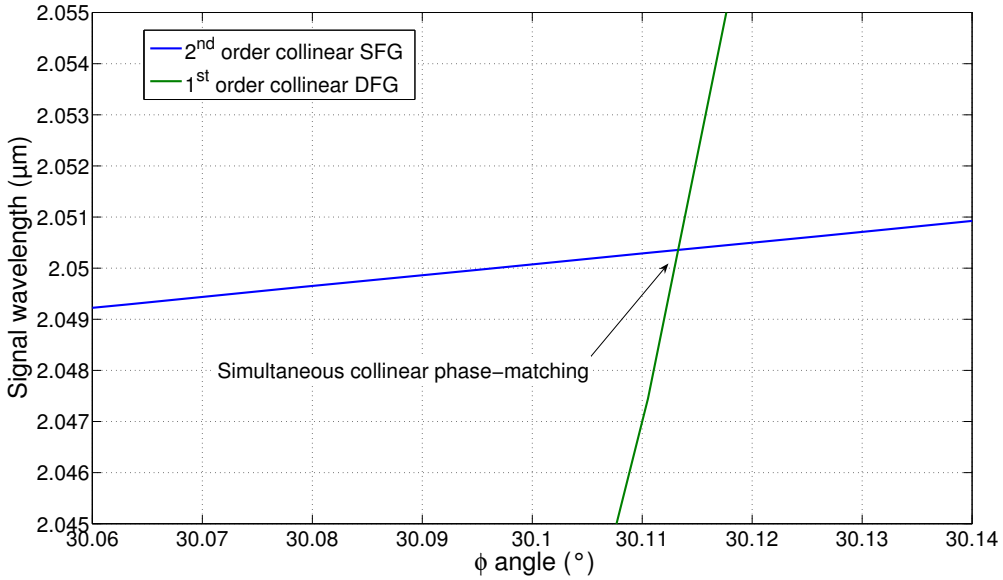

(a) Simultaneous collinear quasi-phase-matching between the first order DFG process and the second order SFG process in a 5%MgO:PPLN crystal with $\Lambda_0 = 28\,\mu m$.

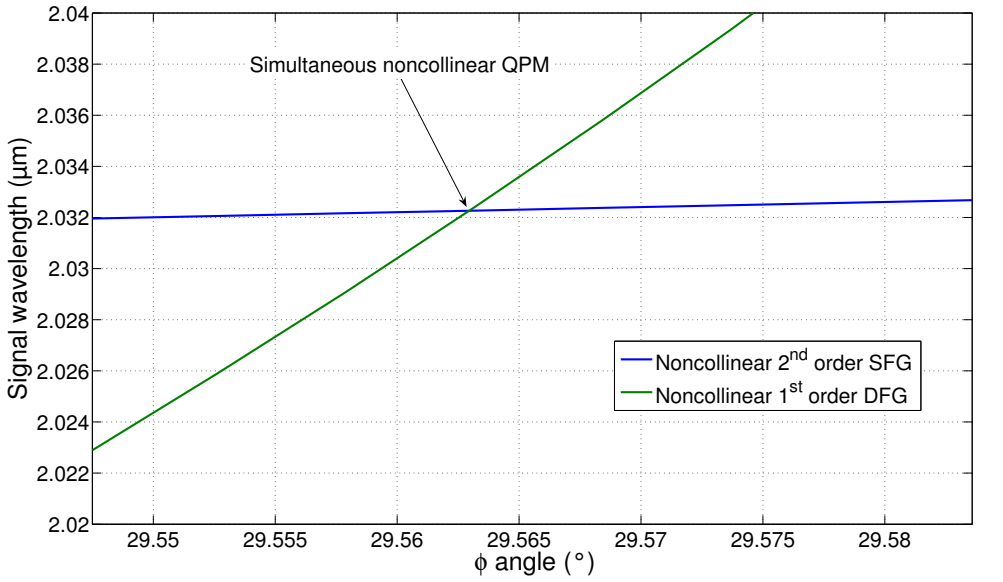

(b) Simultaneous noncollinear quasi-phase-matching between the first order DFG process and the second order SFG process in 5%MgO:PPLN with $\Lambda_0 = 28\,\mu m$.

Figure 79: Comparison between the conditions for collinear or noncollinear simultaneous QPM.

	Collinear QPM case		Noncollinear case (calculation)	Experimental values
	Calculation	Ref.[121]		
Signal wavelength (nm)	2050 nm	2044±2 nm	2032 nm	2043 ± 2 nm
QPM angle ϕ (°)	30.11°	Not relevant	29.56°	30.5±0.5°

Table 15: Comparison between the simultaneous QPM parameters in collinear and noncollinear QPM configurations.

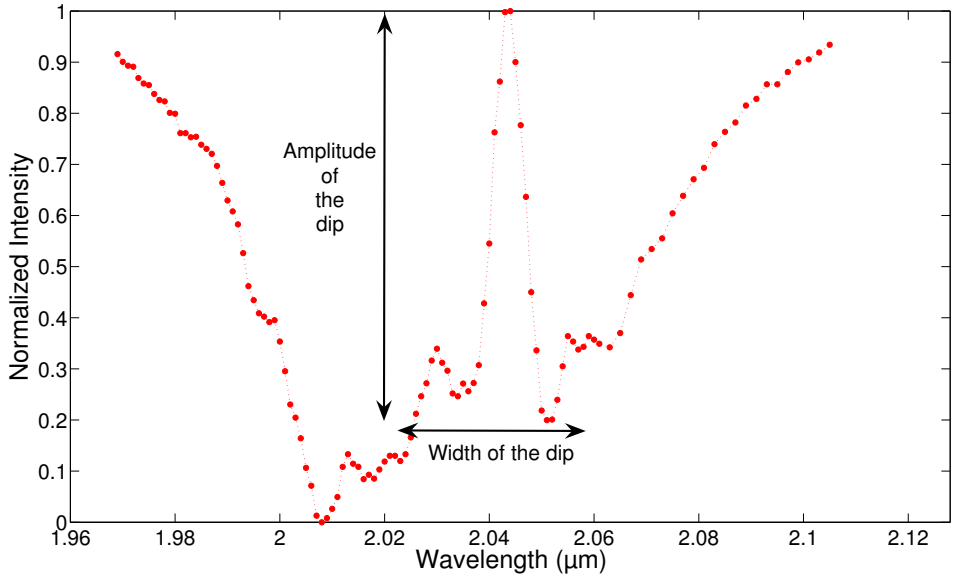

Figure 80: Experimental acceptance of the second order SFG process between the signal and the pump wavelength at 1.064 μm. The pump energy is 6 mJ.

is 0.25. In this section, we investigate the quality of the grating of our sample by analyzing the spectral acceptance of the second order QPM SFG process that we have identified. We have plotted on Figure (80) the spectrum shown on Figure (72) but rotated by 180°, so that the amplitude of the dip is more clearly visible.

We have plotted on Figure (81) the normalized amplitude of the dip shown on Figure (80) for wavelengths between 2.02 and 2.07 μm. Its varies with the signal wavelength as a classical interference function describing low gain parametric conversion processes. If we assume that this normalized amplitude is also the normalized SFG intensity, we can compare this function to theoretical predictions. Based on Sellmeier equations (155), the theoretical acceptance of the QPM SFG between the signal of the OPO and the pump beam, is found to match the shape of the experimental interference function if an interaction length L = 4.2 mm is considered for this SFG process. This is an important conclusion when it comes to assessing the quality of the grating of our sample. We see that the interaction length for this second order SFG process is about one

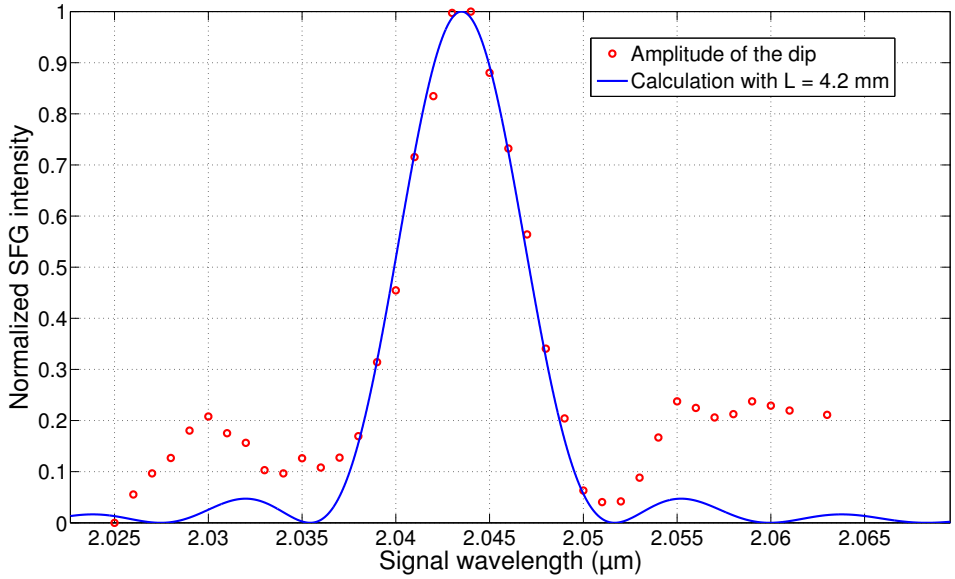

Figure 81: Comparison between the experimental and theoretical acceptance curves of the second-order SFG between the OPO signal wavelength and the pump. The best agreement is obtained for an interaction length L = 4.2 mm.

fourth the interaction length L≈16 mm that we had found previously from the fit of the linewidths of the signal beams. If we consider a QPM crystal with an average duty ratio η such that about one fourth of its interaction length has a duty ratio of 0.25 and the three other fourths have a duty ratio of 0.5, we would find :

$$\eta = 0.44 \tag{190}$$

12.5 CONCLUSION ON THE SPECTRAL PROPERTIES

Let us now summarize the results of the spectral analysis that we have performed so far. First of all, we have potentially identified thermal effects in the cylindrical crystal that lead to a shift of the spectrum of the generated signal wave when the pumping energy is increased. These shifts are higher closer to 2 µm than between 1.43 and 1.64 µm. The subsequent analysis of the linewidth of the signal beams generated in the OPO have shown that far from degeneracy, the linewidths of the signal are higher than what a simple model of optical parametric amplification in a 38 mm long crystal would suggest. A reduced interaction length between 13 and 19 mm gave better adequation between this simple model and the linewidths measured experimentally.

Then, we could analyze the spectral properties of two competitive QPM processes in the crystal. Indeed, there is one signal wavelength for which the SFG with the pump beam at 1.064 µm is simultaneously quasi-phase-matched with the DFG of the OPO. We confirmed the value of the signal wavelength of 2.043 µm measured by our japanese colleagues. On the other hand, we found that this parasitic process was more intense than what they observed previously. However, the

spectral acceptance of this SFG parasitic process correlates well with an interaction length L = 4.2 mm, and we have tried to relate this interaction length to a deviation of duty ratio from the ideal value of 0.5.

CONCLUSION OF THIS CHAPTER

This chapter reports on the first 5%MgO:PPLN optical parametric oscillator based on 5 mm thick partial cylinder with an aperture angle of 45.6°. The tunability achieved with this sample is the highest that can be expected from a monograting QPM sample. It involves only the mechanical rotation of the cylinder, and is therefore truly continuous and agile. It extends from 1.42 µm up to 4.4 µm. The efficiency of the partial cylinder OPO is the highest reported so far for such a device. More than 2.7 mJ have been generated close to degeneracy. And about 2 mJ can be obtained on the entire tuning range. The energetical performance of our OPO has been found to be equivalent to that of a slab OPO. The intensity required to achieve the same efficiency is nevertheless almost 15 times higher in the case of our cylindrical OPO. A poor coupling between the interacting waves inside the resonator can be responsible for this inferior performance: the small size of the resonating signal beam is intrinsically due to the plane mirrors of the cavity. However, the extensive analysis of the spectral properties of the signal generated from the OPO suggests another reason. We have indeed shown that a low interaction length between the signal and the pump beams could explain the linewidths of the generated beams.

In addition to the better agreement between the experimental tuning curve measured in this work and the calculations made under the collinear QPM condition, we were also able to show that the second order QPM SFG of the signal at 2.043 µm with the pump wavelength cannot be explained by a noncollinear QPM configuration of the waves in the OPO. This result is important and validates the theory of Angular Quasi-Phase-Matching. It is also very important for the next Part of this dissertation where the beams of the OPO will be used in DFG experiments. From now on, we will consider that the idler beams are all emitted in the same direction when the partial cylinder is rotated in the cavity.

Part IV

DUAL WAVELENGTH SOURCE FOR VERSATILE DIFFERENCE FREQUENCY GENERATION EXPERIMENTS

INTRODUCTION

At this stage of the dissertation, we have mostly dealt with parametric infrared generation below 8 µm for $CdSiP_2$ (Part II), and below 5 µm for 5%MgO:PPLN (Part III). In this final Part, we tackle the issue of parametric infrared generation in the range 8-12 µm, which corresponds to Band III of transmission of the atmosphere.

We first list the specifications of a source that could lead to a powerful characterization of new nonlinear infrared crystals. Then, we compare these requirements to the existing strategies that have been designed so far to generate infrared coherent radiation above 8 µm. A critical analysis will demonstrate that none of these strategies are fully satisfying when exploratory search and early identification of new and small-sized nonlinear infrared crystals is targeted. We have built a versatile DFG source that should better answer this need. It uses two 5%MgO:PPLN partial cylinder OPOs running in parallel.

We have shown previously that a single OPO based on a 5-mm-thick 5%MgO:PPLN crystal cut as a partial cylinder is well suited for the generation of a continuously tunable coherent beam over the range 1.4-4.4 µm with good conversion efficiencies. When two such partial cylinder OPOs are pumped in parallel, DFG experiments between two widely and independently tunable beams can be performed. And we will show in this final Part that the use of two partial cylinder QPM OPOs makes our strategy much more versatile than any other DFG strategy implemented so far: thanks to the independence of polarizations and wavelengths between the two beams, any parametric mixing process can be investigated. Two different DFG experiments in Band III are reported.

13

THE NEED FOR A NEW TOOL FOR CHARACTERIZING INFRARED CRYSTALS

In this section we list the ideal characteristics of a source that could contribute efficiently to an exploratory search and early identification of nonlinear infrared materials. Then, we compare these requirements to existing DFG setups.

13.1 SPECIFICATIONS

Figure (82) compares the main nonlinear infrared materials for parametric infrared generation above 8 µm on the basis of their long wavelength cut-off and minimum pump wavelength for which two-photon absorption (TPA) is avoided (see Equation 109). This figure confirms that the nonlinear infrared crystals that transmit above 8 µm and that can be pumped with a Nd:YAG laser are scarce. It also shows that most crystals for parametric generation above 8 µm require pump wavelength at least above 1.2-1.4 µm. This first requirement of using longer pump wavelengths for parametric infrared generation was already mentioned on Figure (18) where it was shown that a high nonlinear figure of merit correlates perfectly with small values of the band gap.

It turns out that a pump wavelength in the range 1.2-1.4 µm is usually not long enough to make the best characterizations of most nonlinear infrared crystals. For example, infrared supercontinuum generation requires pump wavelength in the range 2-3 µm (see Table 7). Furthermore, we believe that a tool that could simulate the phase-matching properties of a crystal at different pump wavelengths corresponding to the emission line of mid-infrared lasers (see Table 9) is very valuable. As a consequence, an efficient characterization tool for nonlinear infrared crystals requires a wide and continuous tuning of the pump wavelength possibly in the range 2-3 µm.

Last but not least, it is important for our our new experimental tool to be suited for the characterizations of small crystals. Indeed, it is somewhat unrealistic to expect the first growth attempts of a new nonlinear crystal to yield large size and high quality crystals. Therefore, the low nonlinear gain in small crystals rules out strategies such as pump tunable OPO or OPG as characterization tools. As a consequence, pump tunable DFG is the only available option when the phase-matching properties of a small nonlinear infrared crystal must be characterized.

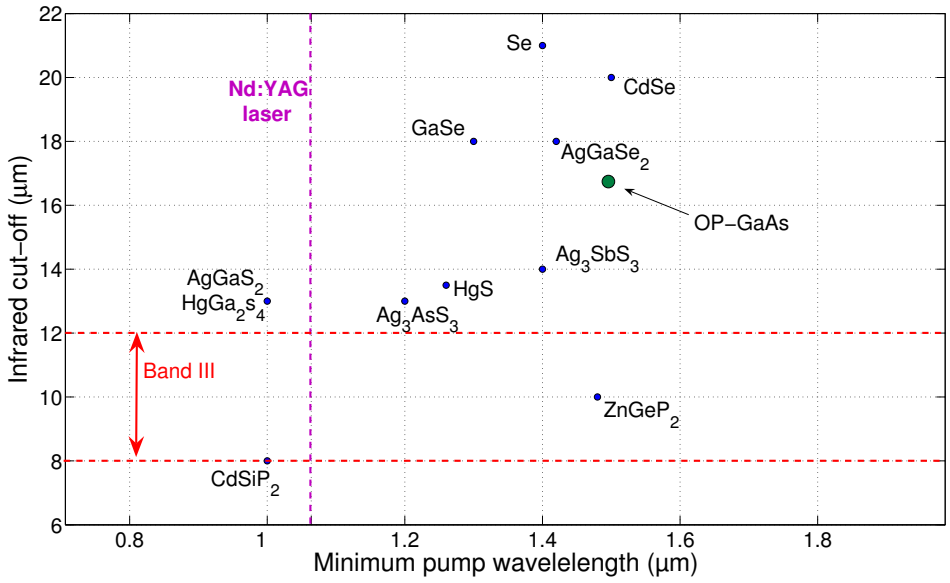

Figure 82: Comparison between some nonlinear infrared materials for Band III applications on the basis of their infrared cut-off wavelength and minimum pump wavelength for which TPA is avoided (twice their band gap). These datas are taken from [9].

13.2 SOURCES FOR DFG: STATE OF THE ART

In this section, we now compare some solutions that have been implemented to perform DFG experiments in nonlinear infrared materials. We discuss the interest in these experimental setups in the light of the main requirement listed above: a wide and continuous tunability of the pump above 1.4 µm and possibly in the range 2-3 µm.

13.2.1 *OPO or OPG at degeneracy*

Mixing together the signal and idler generated from the same OPO (or OPG) in a DFG crystal has been early recognized as a very promising solution to the generation of tunable infrared coherent radiation [122, 123, 124]. Near degeneracy, the signal and idler wavelengths get closer and by mixing these two beams in a suitable nonlinear crystal, DFG in Band III can be easily obtained. Such a strategy was implemented to generate tunable infrared DFG up to 24 µm in CdSe crystals [122], as shown on Figure (83b). It was also implemented in $CdGeAs_2$: DFG between the signal and idler of an OPG pumped by a (Cr,Er):YSGG laser emitting at 2.8 µm yielded a tunability between 7 and 20 µm [125].

These devices are very compact and have given unprecedented results in terms of tunability of the generated DFG beam [122, 125]. However, we advocate that such a strategy is not fully adequate when the goal is to characterize nonlinear infrared crystals. First of all, the pump wavelength that can be used for these DFG experiments is restricted to a limited range near

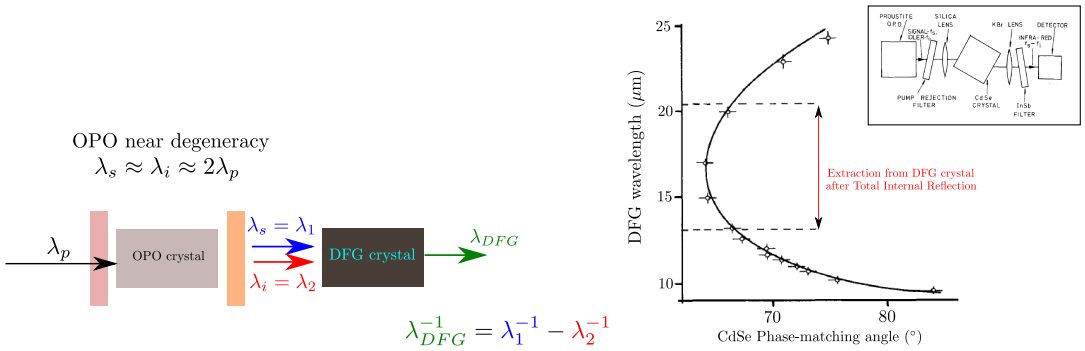

Figure 83: Sketch of the apparatus for DFG between the signal and idler beams emitted from the same OPO (a) and corresponding tuning curve (b) obtained by Hanna et al. [122] when DFG between the signal and idler beams from a proustite OPO pumped at 1.064 µm is performed in CdSe.

degeneracy. Then, one of the main drawbacks of this strategy is the poor control over the polarizations of the waves for the DFG. Actually, the polarizations of these two incident waves are dictated by the type of phase-matching that is used in the OPO crystal, and when the two types of phase-matching in the OPO and in the DFG crystal do not match, it is difficult to control the polarization of the two waves independently [11].

Eventually, in this strategy, the two incident wavelengths $\lambda_1 = \lambda_s$ and $\lambda_2 = \lambda_i$ (see Figure 83a) for the DFG must fulfill the classical energy conservation relation :

$$\lambda_1^{-1} + \lambda_2^{-1} = \lambda_p^{-1} \tag{191}$$

where λ_p is the pump wavelength of the OPO or OPG. This implies that the two wavelengths cannot be tuned *independently*, which inevitably limits the DFG experiments that can be performed.

13.2.2 *Non-parametric sources*

Other solutions have therefore been implemented in order to improve the control over both the wavelengths and polarizations of the beams used for the DFG. Such a control is usually obtained thanks to two independent arms.

13.2.2.1 *Two dye lasers tunable around 700 nm*

As far as we know, the first DFG setup with independent control of the wavelengths was built in 1992 [126]. It is a CW DFG setup between two beams emitted by different dye lasers (see Figure 84a). The main interest in this apparatus is that the two beams emitted by the dye lasers are both tunable independently in the ranges 0.58 - 1.1 µm and 0.58 - 0.9 µm, respectively. CW DFG

experiments could be performed in a AGS crystal cut for angular noncritical DFG (see Figure 84b). On the other hand, this setup has two major limitations : first of all, the incident wavelengths for the DFG are in the range 0.5-1.1 µm, then, because of the operation in the CW regime, we find this setup inadequate for small size crystals.

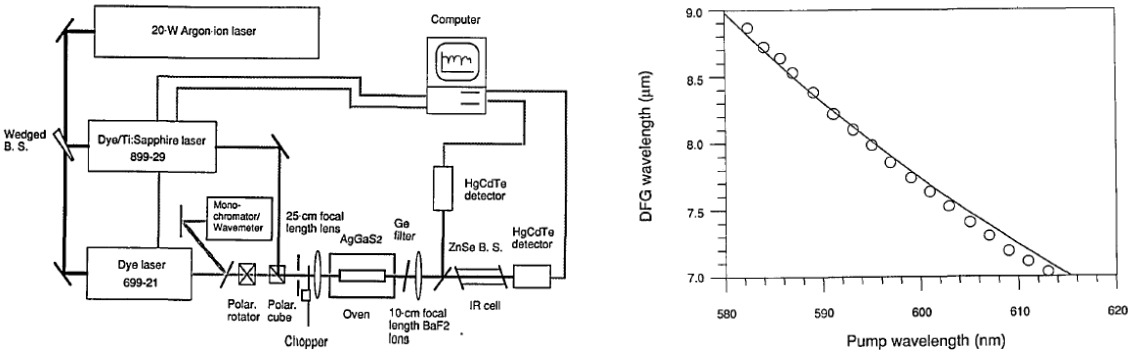

Figure 84: Experimental setup allowing DFG experiments between two dye lasers (a). The corresponding angular noncritical tunability obtained in AGS is shown on Figure (b). These graphs are taken from [126].

13.2.2.2 *DFG between two laser diodes*

Another option to increase the wavelengths for the DFG is to use two beams emitted from two different laser diodes, as shown on Figure (85a). This setup was implemented to demonstrate the first QPM DFG process in OP-GaAs (See Figure 85b). In terms of characterizations, this setup can prove useful only if the nonlinear crystal can be phase-matched over the limited tuning range of the laser diodes. Since the period of a QPM material can be engineered, this setup is better suited for QPM crystals than BPM crystals.

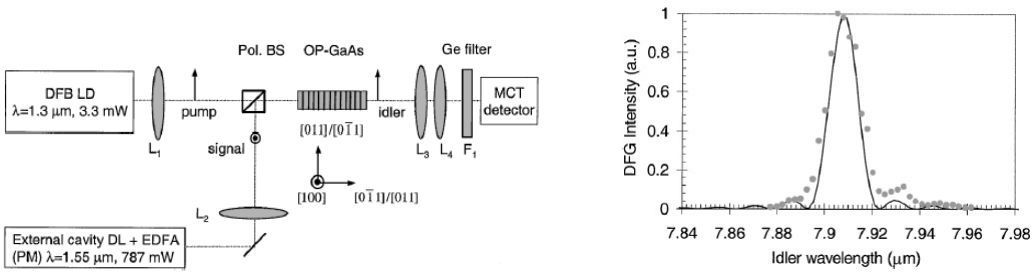

Figure 85: Experimental setup allowing DFG experiments between two diode lasers (a). The corresponding spectral acceptance that was measured in OP-GaAs is shown on Figure (b). These graphs are taken from [127].

13.2.3 *Two independent arms*

More recently, the need to perform DFG experiments at longer pump wavelength in nonlinear infrared crystals led to the design of a new source for DFG experiments in $ZnGeP_2$. This source uses a pump wavelength at 2.128 µm, with a narrow spectral linewidth and a tunable signal in the range 2.6-4 µm. The potentialities of this source for spectroscopic applications were demonstrated. However, its main limitation comes from the fact that the pump wavelength is not tunable at all.

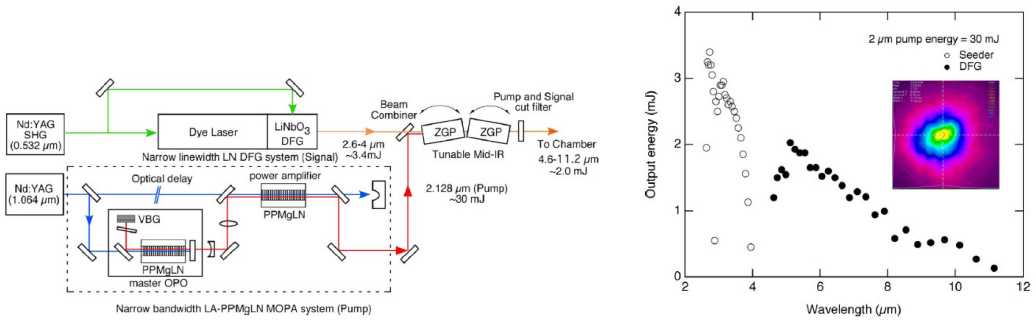

(a) (b)

Figure 86: Experimental set-up used to perform DFG experiments in $ZnGeP_2$ (a). The tunability of the signal and DFG wavelengths are shown on (b). These graphs are taken from [128].

13.3 CONCLUSION

This brief comparison between the existing setups used for performing DFG experiments reveals that a source with two independent arms is the most promising route when versatile DFG experiments need to be performed. However, we believe that the existing setups presented here do not meet one of the most important requirements for nonlinear infrared materials characterization which is the ability to perform DFG experiments at any pump wavelength in the mid-infrared.

14

DUAL WAVELENGTH SOURCE WITH TWO OPOS IN PARALLEL

Based on the limitations of existing setups that we identified, we now justify our decision to build a source with two partial cylinder OPOs running in parallel. Then, we discuss some experimental challenges related to the conception of such a source. The corresponding DFG results are given in the two next two chapters.

14.1 OUR SOLUTION: PRINCIPLE

We take advantage of the encouraging results presented in Part III with a single 5%MgO:PPLN partial cylinder OPO and build an all-parametric source with two such OPOs, as shown on Figure (87). We believe that the wide and continuous tunability of these two devices is well-suited for the design of a source dedicated to the early characterization of nonlinear crystals. The combination of two partial cylinder OPOs in parallel leads to the following advantages listed below:

- Contrary to the operation of an OPO close to degeneracy, the wavelengths of the beams emitted from the first partial cylinder OPO are not related to the wavelengths emitted from the second OPO through the energy conservation relation.
- The beams emitted from the two OPOs are widely tunable between 1.4 and 4.4 µm (See Figure 56), which is adapted to most nonlinear infrared crystals shown on Figure (82). More specifically, the idler beam of these OPOs being tunable between 2.1 and 4.4 µm, our source increases the pump wavelengths at which DFG experiments can be performed.
- We have given strong arguments supporting the collinear QPM configuration (see Part III) in the partial cylinder OPO. This is very important because contrary to all the devices involving rotation of crystals cut as slabs, the rotation of the cylinder will not modify the direction of propagation of the beams. As a consequence, there is no need to compensate for the effects of refraction, and this makes our source easier to use and align.
- The polarizations of the beams emitted from each OPO are also independent. This means that it is very easy to rotate the polarization of the beam emitted by one of the OPO without modifying that of the beam emitted by the second OPO. This has a tremendous advantage because any type of parametric mixing (Type 0, I, II or III) can be considered: this makes our source ideal in the context of the characterization of BPM as well as QPM new nonlinear materials.

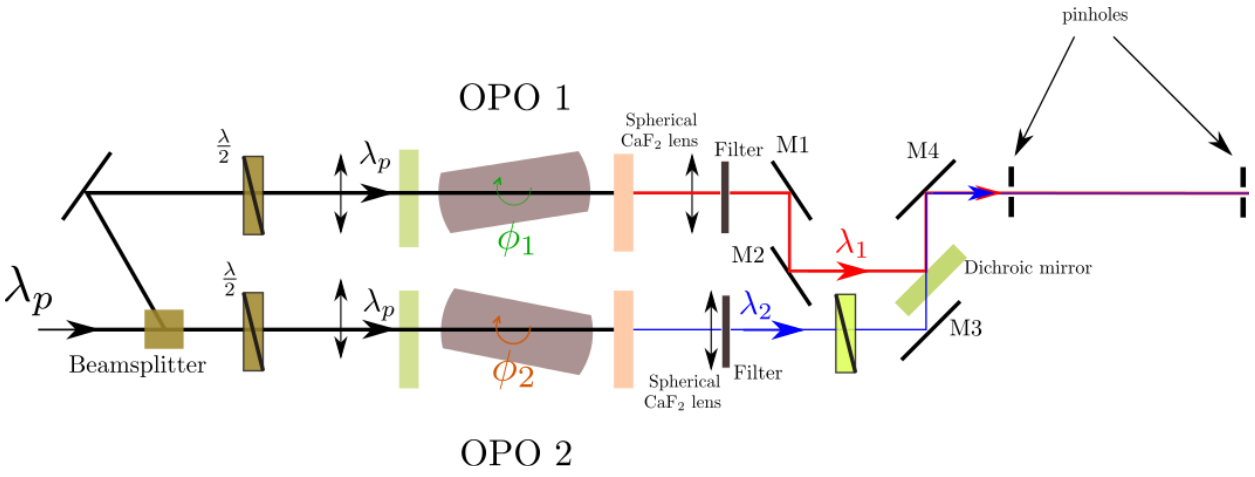

Figure 87: Sketch of the dual wavelength source based on two cylindrical OPOs. The pump wavelength is $\lambda_p = 1.064\,\mu m$.

– Eventually, the output of these two OPOs (see Figure 66) is high enough to perform DFG experiments in small crystals.

As far as we know, the experimental realization of such a dual wavelength source for DFG has not been reported. The first trace of this concept dates back to 2000 [129] when it was patented at the NASA. At that time, terahertz wave generation was targeted and birefringent phase-matched (BPM) OPOs pumped at 355 nm were considered. However, we are not aware of the realization of this source. The apparatus that we have built is very different for two reasons at least. First of all, we have been using QPM OPOs and not BPM OPOs. Then, the interest of pumping the two OPOs at 1.064 µm leads to a reduction of the overall quantum defect between the DFG photons and the primary pump photons at 1.064 µm.

14.2 EXPERIMENTAL APPARATUS OF THE DUAL WAVELENGTH SOURCE

Building such a source took quite some time, and in this section, we give a hint about some of the challenges that had to be tackled in order to perform DFG experiments.

14.2.1 *Experimental set-up*

The experimental apparatus of the dual wavelength source is shown on Figure (87). We use the same Nd:YAG laser at 1.064 µm as the one taken to pump the partial cylinder OPO described in Part III. Its maximum output energy per pulse is now 16 mJ. The pump beam is splitted in two parts of equal energy to pump simultaneously the two identical partial cylinder OPOs. The tuning curve of each OPO is shown on Figure (56), and the energetical properties of this device are given on Figures (65), (66) and (67): for 5 mJ pump energy in the OPOs, about 200 µJ incident energy is available for the DFG experiments. Based on the conclusions from Figure (58) and the discussion

in section (12.4.2), we now consider that the signal and the idler beams of each OPO are emitted collinearly. They are both extraordinary polarized, which corresponds to a vertical direction of polarization on the table of experiments. The wavelength emitted from the first OPO and used for DFG will be labelled as λ_1, while the wavelength emitted by the second OPO and used for DFG will be labelled as λ_2, as shown on Figure (87).

Two CaF_2 spherical lenses of 200-mm-focal length are positioned at the output of each OPO in order to correct for the divergence of the generated beams. The positioning of these lenses is performed so that the orange (reddish) spot generated in the cavity (and corresponding to the non-quasi-phase-matched SFG between the signal and the pump) is as parallel as possible after propagation in these lenses. We are aware that this method of positioning might not be ideal especially when we are working with the idler beam of the OPO. It is somehow justified because of the lack of an infrared camera and because of the easy visual criteria of alignment it involves.

Using a spherical lens does correct for the astigmatism of the beams generated in the OPO. The spatial profile of the 1.42 µm signal beam emitted by the first OPO (OPO 1 on Figure 87) was characterized after a second spherical lens of 150 mm. The knife-edge method was implemented to do so, and the resulting profiles were fitted with an erf function to yield the beam waist radius along the direction of propagation. The results are shown on Figure (88): the signal beam is more strongly focused in the horizontal plane and has an elliptical cross-section. These measurements allowed us to extract the values of the M^2 factor of the signal beam in these two directions. We found that the M^2 factor was 8.5 ± 1.0 in the horizontal plane where the beam is the more focused, and 28 ± 2 in the vertical direction. Along the vertical direction, this value is in agreement with typical values of OPOs based on PPLN slabs [130]. In the horizontal direction, it is likely that a filtering effect due to a higher selectivity of the cavity leads to a much lower M^2 factor, as previously reported in the group during the PhD thesis of Olivier Pacaud who worked on the first cylindrical OPO [31, 115].

It is after these two lenses that we can incorporate some selective filters or half-wave plates, as shown on Figure (87). In the rest of this work, we consider only the idler beams emitted by the two partial cylinder OPOs. Anti-reflection coated Germanium filters from Thorlabs are used.

We think that two cylindrical CaF_2 lenses on each arm of the dual wavelength source with different focal lengths might be better suited to correct for the astigmatism of the beams generated in the partial cylinder OPO.

14.2.2 *Beam combiner issue*

In our apparatus, the "price to pay" for using two OPOs in parallel is the need to get the beams at λ_1 and λ_2 together. The optical element on which the two beams recombine is therefore a key element of our setup. In this section, we justify our choice of a dichroic mirror.

The choice of the optical element where the beams at λ_1 and λ_2 are forced to recombine is primarily imposed by the range of wavelengths and states of polarizations of the beams that need to be mixed in the DFG crystal. In addition, this choice must take into account the efficiency

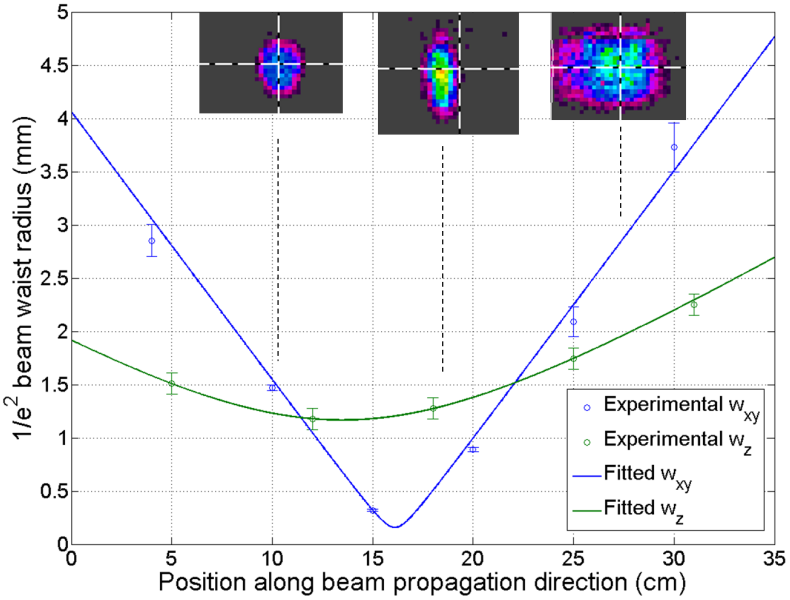

Figure 88: Horizontal and vertical signal beam profiles of the signal at 1.42 µm and for a pump energy of 3 mJ. The zero of the abscissa corresponds to the position of the 150-mm-focal lens.

of recombination i.e. the ratio between the energy of the two waves that are recombined in comparison with their incident energy, and of course the commercial avalibility.

The simplest option to recombine two beams at different wavelengths is a dichroic mirror (See Figure 89a), with cut-on wavelength λ_C. By using one beam in reflexion and one beam in transmission, two beams can be easily recombined. And since the dichroic mirror can be used at 45°, the two beams hit the mirror with perpendicular directions of propagation, which is probably the most convenient solution in terms of alignment. The higher the contrast between the reflected and transmitted intensities the better this option in terms of overall efficiency of recombination. Furthermore, this solution has the huge advantage of allowing beams with any polarizations to be recombined. But since the cut-off wavelength λ_C dictates the maximum value of the first wavelength λ_1 as well as the minimum value of the second wavelength λ_2, this technological solution limits the range of wavelengths that can be recombined. It is especially limited when wide tuning of λ_1 or λ_2 is required, or when very close wavelengths must be recombined.

When closer wavelengths must be recombined, it is better to use polarizing elements that allow two beams in different polarization states to be recombined. Contrary to the use of a dichroic mirror, this solution can be very broadband. However, it will limit the DFG experiments to the types for which the two incident beams are cross-polarized, thus excluding Type 0 in QPM materials for example. Two types of polarizing elements can be imagined. The first one is a rutile polarizer, while the second one is a Germanium thin slab positioned at Brewster angle. The interest of using a Germanium thin slab comes from the fact that the recombination efficiency is high, even for the S-polarized wavelength in reflection thanks to the high refractive index of

Germanium (n ≈ 4.0 at 3 µm). It is also a cheap solution available commercially. Due to the low dispersion of Germanium around 3 µm, the Brewster angle is not much dispersive, and the average value of the Brewster angle, i.e. $\theta_B = 76°$ at 3 µm should be satisfactory for a wide range of wavelengths.

In our work, we have chosen a dichroic mirror from Laseroptik that is specially designed for Er:YAG laser cavities. The transmission spectrum of such a mirror is shown on Figure (90). Since an Er:YAG laser emits at 2.94 µm, these mirrors are highly reflective between 2.5 and 3.2 µm. And this will correspond to the range of our first wavelengths λ_1 used in the following experiments (See Figure 87). The wavelengths λ_2 can fall anywhere between 3.5 and 4.5 µm, where the mirror has a moderate transmission (T > 60%). Let us stress that these two ranges of wavelengths for λ_1 and λ_2 (2.5-3.2 µm and 3.5-4.5 µm) are well suited to generate infrared coherent radiation in Band III. For example, the energy conservation between one beam at $\lambda_1 = 3$ µm and one beam λ_2 at 4 µm results in a DFG wavelength at 12 µm.

14.3 OPTIMIZATION OF THE SPATIAL OVERLAP

Making sure that the beams overlap spatially has not been something easy, mostly because of the lack in the lab of technological solutions to "see" the two idler beams emitted from the OPOs. A Spiricon camera was cordially lent by Antoine Godard from ONERA to realize the spatial overlap between the two idlers, but because of the divergence of the beams and the low idler energy at which the alignement was made, it was difficult to get a good result. Rather than using the pyroelectric camera, we used a classical procedure from our group: instead of performing a direct DFG between one beam at λ_1 and one beam at λ_2, we optimize the SFG efficiency between the two same beams in a crystal whose phase-matching properties are well-known. Performing such an experiment has the main advantage of generating a SFG wavelength that can be easily detected with more standard methods. We chose another 5%MgO:PPLN crystal as the SFG crystal, as shown on Figure (91). It is a 40-mm-long crystal with an aperture window of 5 x 5 mm^2, provided by Pr T. Taira [89]. This sample has a classical QPM grating structure perpendicular to the faces of the crystal, and its QPM period is $\Lambda_0 = 32.3\,\mu m$.

For each set of wavelengths (λ_1, λ_2), we optimize the intensity of the SFG through the optimization of the spatial overlap between these two beams. Figure (92) shows the SFG phase-matching wavelength λ_3 that we measured with different sets of wavelengths λ_1 and λ_2, after the optimization of the overlap. Let us stress that the SFG crystal is not rotated throughout this procedure, and that this procedure is a demonstration of the potential of this source to perform bi-tunable SFG (or DFG) in a crystal cut as a slab without any rotation.

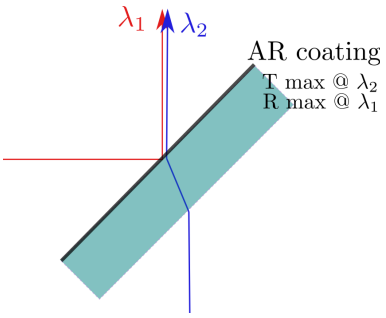

(a) 2D schematic view of a dichroic mirror.

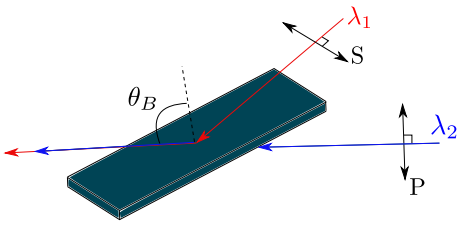

(b) 3D view of a germanium slab at Brewster angle.

Figure 89: Comparison of two solutions for recombing a beam at λ_1 with a beam at λ_2.

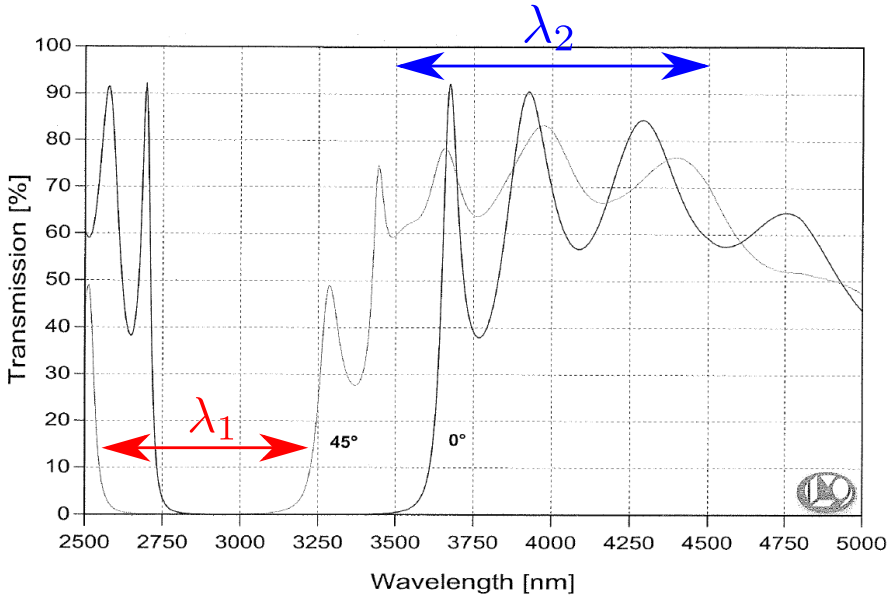

Figure 90: Transmission spectrum of the dichroic mirror with unpolarized light and at 45°. The range of wavelength λ_1 corresponds to the range where the dichroic is highly reflective at 45° while the range of wavelengths λ_2 corresponds to the highest transmission at 45°.

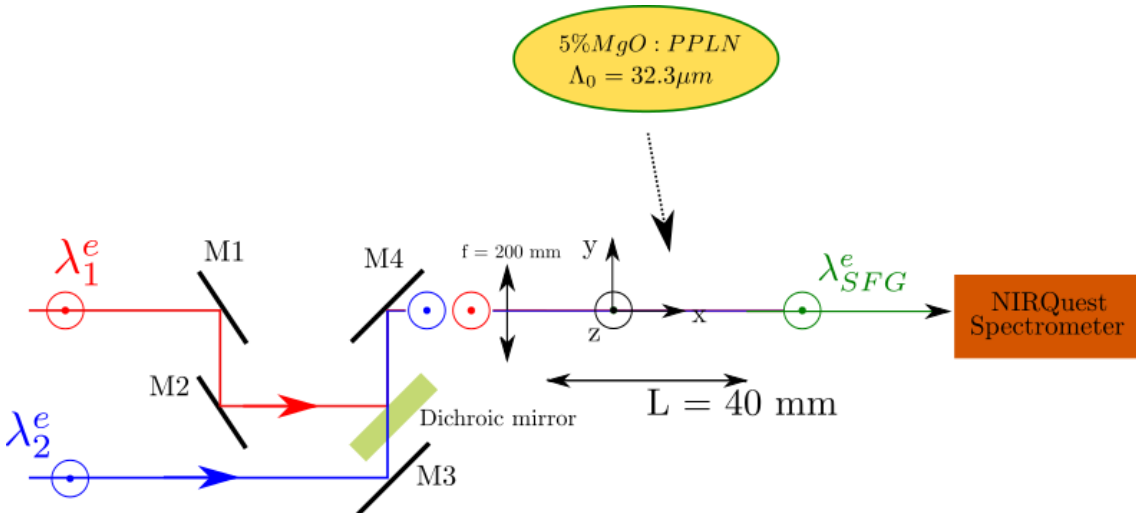

Figure 91: Experimental set-up used for the optimization of the spatial overlap between the two idler beams emitted from the two OPOs.

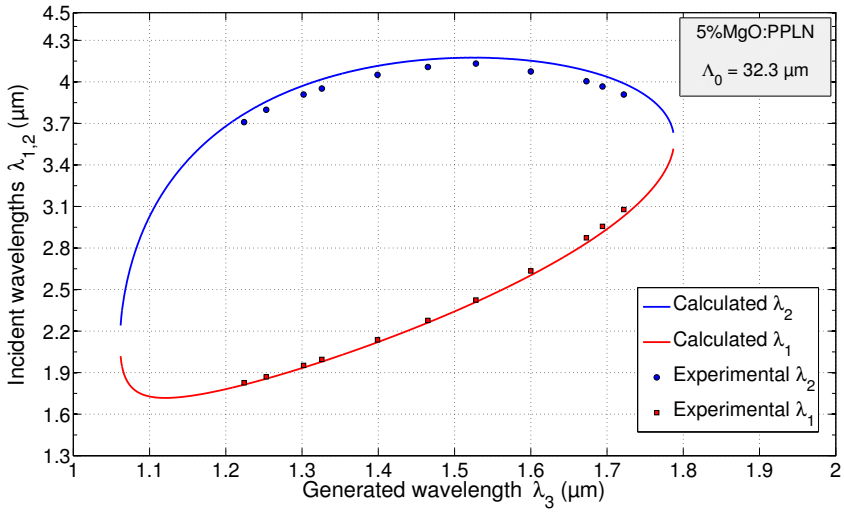

Figure 92: Bi-tunable first order SFG in a 5%MgO:PPLN sample with QPM period $\Lambda_0 = 32.3\,\mu m$

14.4 CONCLUSION

The experimental apparatus of the dual wavelength source has been presented. The main challenge of this all- parametric source is the need to recombine the beams emitted by the two OPOs. To do so, an alignment procedure based on the optimization of the SFG between the two independent beams has been designed. This procedure ensures a good spatial overlap between the two beams. Strictly speaking, the temporal overlap between the two pulses should also be optimized, because the build-up time of the two OPOs could be different and lead to small temporal delay between the two pulses. The successful SFG experiments were a satisfactory validation of the fact that, for the purpose of a proof of principle, no delay line is needed to combine the two pulses together. In fact, since the two OPOs used in these experiments are similar, we can expect that the build up time of the two pulses is equivalent in the two OPOs. This should be checked in future characterizations of this source. The influence of the temporal profile and delay between two pulses on the DFG conversion efficiency has been modelled by Godard et al. [131].

15

ANGULAR NONCRITICAL DFG IN CADMIUM SELENIDE

In this chapter, we give the first DFG results obtained with our source. We start by presenting the optical properties of the material used for the experiments: Cadmium Selenide (CdSe).

15.1 CDSE OPTICAL PROPERTIES

Cadmium Selenide has been identified since the early days of nonlinear optics as a very good candidate for parametric infrared generation [132]. The main advantages of this crystal include a mature technology that allows the growth of crystals with sufficiently large sizes for OPOs and a transmission window extending from 0.75 up to 25 µm, which enables the parametric generation of infrared coherent radiation up to 25 µm. CdSe crystals have a wurtzite structure with 6mm point group. It is an optically uniaxial positive crystal ($n_e > n_o$).

The refractive indices of CdSe have been measured by three different groups in the 60's [133, 134, 135]. And there are two sets of Sellmeier equations available for this crystal. The first set of analytical Sellmeier equations were provided by Bhar et al. in 1972 [136]. A few years later, based on additionnal phase-matching measurements performed by Hanna et al. [122] and Weiss et al. [137], Bhar proposed another set of Sellmeier equations [138] valid a priori in the range 1-12 µm. These are the equations that we will be using:

$$\begin{aligned} n_o^2(\lambda) &= 4.2243 + \frac{1.7680\,\lambda^2}{\lambda^2 - 0.2270} + \frac{3.1200\,\lambda^2}{\lambda^2 - 3380} \\ n_e^2(\lambda) &= 4.2009 + \frac{1.8875\,\lambda^2}{\lambda^2 - 0.2171} + \frac{3.6461\,\lambda^2}{\lambda^2 - 3629} \end{aligned} \tag{192}$$

The birefringence of CdSe, $n_e - n_o$, is between 0.012 and 0.020 over the range 1 and 12 µm. This birefringence is very weak, and too low for example to allow phase-matched SHG of a CO_2 laser at 10.6 µm. The only type of DFG allowed in this crystal is Type III, i.e. $(\lambda_p^o, \lambda_s^e, \lambda_i^o)$. The effective coefficient of this interaction (see Table 2) is given by:

$$d_{eff} = d_{15} \sin\theta \tag{193}$$

It is important to notice that this effective coefficient does not depend on the polar angle ϕ, contrary to CSP for example. For CdSe, d_{15} has been measured at 10.6 µm [139] and is equal to:

$$d_{15} = 18\,pm/V \tag{194}$$

The BPM condition for type III DFG in this crystal writes:

$$\frac{n_o(\lambda_p)}{\lambda_p} = \frac{n_e(\lambda_{s,}\theta)}{\lambda_s} + \frac{n_o(\lambda_i)}{\lambda_i} \tag{195}$$

In addition of a longer interaction length thanks to a vanishing walk-off angle, the choice of angular noncritical phase-matching (ANCPM) in CdSe is very interesting since the effective coefficient of Type III DFG reaches its maximum for $\theta = 90°$ (See Equation 193).

15.2 PUMP WAVELENGTH FOR OUR EXPERIMENTS

OPO in CdSe was demonstrated with many different pump wavelengths including $\lambda_p = 1.833\,\mu m$ [132], $\lambda_p = 1.85 - 1.97\,\mu m$ [140], $\lambda_p = 2.05\,\mu m$ [141], $\lambda_p = 2.36\,\mu m$ [142], $\lambda_p = 2.79\,\mu m$ [143, 144], $\lambda_p = 2.87\,\mu m$ [137], or the idler of a KTA OPO at $\lambda_p = 3.45\,\mu m$ [145]. Such numerous attempts at different pump wavelengths can find an explanation in the fact that there is an optimal range of pump wavelengths for which the tunability of CdSe is the widest, as we will see now.

We have represented on Figure (93) the ANCPM idler wavelength obtained for $\theta = 90°$ in CdSe at different pump wavelengths. It can be seen that the lowest idler wavelength that can be generated in this ANCPM configuration falls slightly below 8 µm and is obtained for a pump wavelength in the range 2.4-2.9 µm. This is the range of pump wavelengths that we have chosen for the two DFG experiments presented in this section.

Let us stress that such a freedom of choice in the pump laser wavelength used for our DFG experiments is probably one the nicest features of the dual wavelength source that we have built. It allows us to measure the phase-matching properties of a crystal at any pump wavelength and more specifically at wavelengths corresponding to the emission line of mid-IR lasers (See Table 9) . Note that this feature of our dual source is made possible thanks to the continuous tunability of the beams emitted from the partial cylinder OPOs.

15.3 DFG RESULTS

In this section, DFG experiments in a 40-mm-long CdSe sample oriented at $\theta = 90°$ are reported. The sample used for these experiments was cordially loaned by Antoine Godard from ONERA. It was previously bought from Moltech. We describe briefly the experimental setup, before presenting the results obtained in terms of spectral acceptances and DFG conversion efficiency.

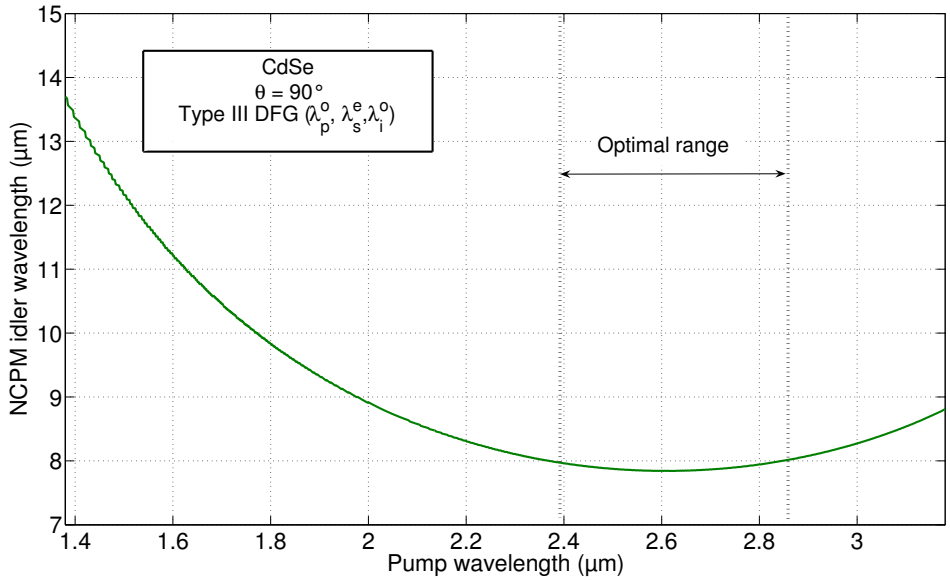

Figure 93: Variations of the minimum idler wavelength that can be generated in CdSe as a function of the pump wavelength. This idler wavelength is obtained for Type III DFG ANCPM ($\theta = 90°$).

15.3.1 *Experimental set-up*

The experimental set-up used for the DFG experiments is shown on Figure (94).

The main difference between the apparatus used for SFG and DFG (see Figures 91 and 94) is that the polarizations of the incident waves must be cross-polarized to achieve Type III DFG in CdSe. An easy way to make sure that the beams are cross-polarized in the previous SFG experiments is to rotate the polarization of the second beam up to the point where the SFG signal disappear.

The DFG beam is detected with a PEM MCT detector from Vigo whose spectral response extends up to 11 µm. This detector was loaned by Antoine Godard from ONERA too. A long-pass filter ($\lambda > 7.3\,\mu m$) from Thorlabs is used to filter out the two incoming wavelengths at the output of the crystal. But several verifications are made to make sure that the voltage measured with the Vigo comes from the DFG generated in the crystal. First of all, we verify that when we switch off the two partial cylinder OPOs successively, the voltage vanishes. This rules out any leaks of the incident wavelengths through the long-pass filter. Secondly, we check that the voltage at the oscilloscope can be switched off when the polarization of the second beam is rotated. The positions for which the voltage decreased below the noise level of the detector (1.5 mV) were found to be in perfect agreement with the neutral lines of the half wave plate, which confirms that no DFG was generated when the second beam was vertically polarized (ordinary polarization for the CdSe crystal).

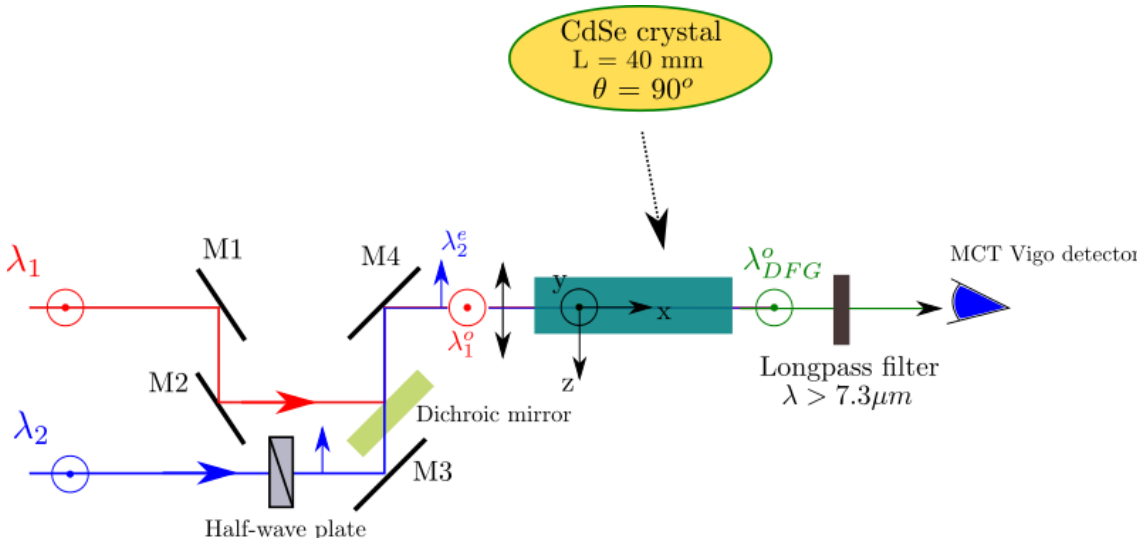

Figure 94: Experimental apparatus used for the first experiments of DFG in CdSe.

15.3.2 *Angular noncritical phase-matching wavelengths*

In this section we present the results of spectral acceptances obtained for two different pump wavelengths at $\lambda_1 = 2.72\,\mu m$ and $\lambda_1 = 2.79\,\mu m$. In each case, we tune the wavelength λ_2 by rotating the OPO 2 (See Figure 94), and we measure the voltage from the MCT detector. The wavelength λ_2 for which the generated intensity is maximum corresponds to the phase-matching wavelength $\lambda_{2,PM}$. The results are shown on Figure (95). For the sake of comparison, we have also plotted the calculated normalized DFG intensity in the (unrealistic) case of a monochromatic pump beam and for a crystal length L = 40 mm.

The ANCPM wavelengths corresponding to pump wavelengths at $\lambda_1 = 2.72\,\mu m$ and $\lambda_1 = 2.79\,\mu m$ were found to be 4.1 μm. and 4.27 μm, respectively. Table (16) compares the ANCPM idler wavelengths measured experimentally to the calculations from Equation (192).

		ANCPM DFG wavelength λ_{DFG} (μm)	
		This work	Calculation with Equation (192)
First beam wavelength	$\lambda_1 = 2.72\,\mu m$	8.08 ± 0.08	7.88
	$\lambda_1 = 2.79\,\mu m$	8.05 ± 0.04	7.93

Table 16: Comparison between the calculated and measured DFG phase-matching wavelengths of CdSe at $\theta = 90°$.

It shows that there is a small discrepancy between the ANCPM DFG wavelength that we measured and the one calculated from Equation (192). For a pump wavelength $\lambda_1 = 2.72\,\mu m$, the discrepancy between the calculations from Equations (192) and our measurements is 50 nm. It is

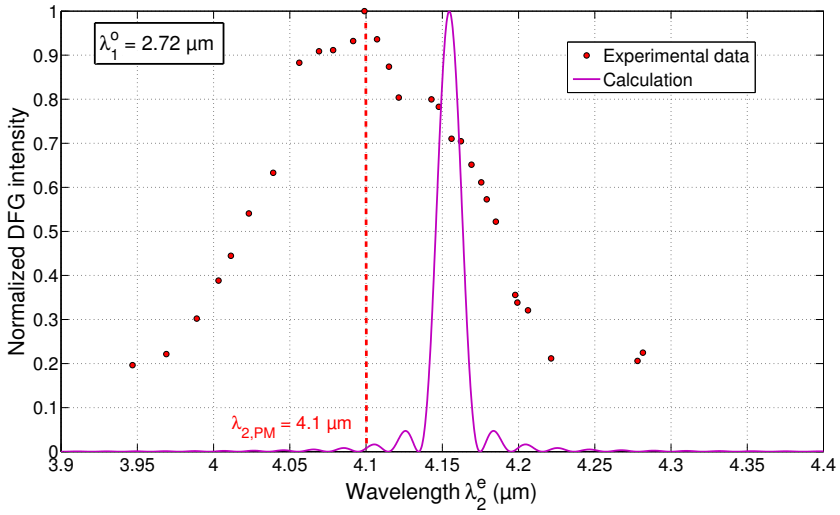

(a) $\lambda_1 = 2.72\,\mu m$

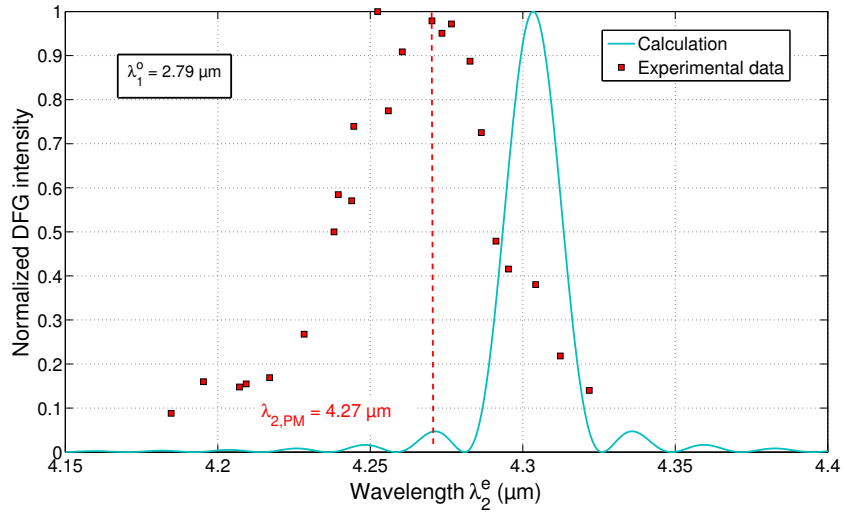

(b) $\lambda_1 = 2.79\,\mu m$

Figure 95: Experimental spectral acceptances of the CdSe crystal measured at two different pump wavelengths The calculations are based on Sellmeier Equations (192). The indices o and e stand for the ordinary and extraordinary polarizations.

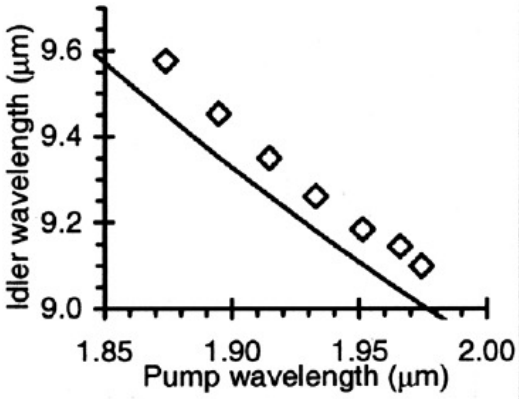

Figure 96: Pump-tunable tuning curve of a CdSe synchronously-pumped OPO with a crystal cut for ANCPM. The deviation between the experimental values and the calculation from Equation (192) is about 100 nm. This graph is taken from [140].

30 nm at 2.79 µm (See Figure 95). Watson et al. in 2003 [140] already reported an overestimation of the ANCPM idler wavelength of a synchronously-pumped OPO with a tunable pump wavelength between 1.8 and 1.9 µm as shown on Figure (96). In our case, the discrepancy between the calculated and experimental idler wavelengths is 200 nm at $\lambda_1 = 2.72$ µm and 120 nm at $\lambda_1 = 2.79$ µm. Nevertheless, a non-collinearity between the two incident beams cannot be ruled out.

15.3.3 *Conversion efficiency*

In this section we present the DFG conversion efficiency obtained in the 40-mm-long CdSe crystal oriented for ANCPM. The pump wavelength λ_1 is set at 2.72 µm, while the second wavelength λ_2 is set to the phase-matching wavelength, i.e. 4.1 µm as shown on Figure (95a), and we measure the DFG energy E_{DFG} for different combinations of incident energies E_1 and E_2. These two incident energies are both varied through an increase of the pumping level in the two partial cylinder OPOs. $E_1$and E_2 are measured right before the uncoated CdSe crystal with a pyroelectric detector PE-10 from Ophir, while the DFG energy E_{DFG} is measured with a calibrated pyroelectric Molectron detector J4-09 after the long pass filter positioned at the ouput of the CdSe crystal. The results showing the DFG energy E_{DFG} as a function of the incident energies E_1 and E_2 on the crystal are shown on Figure (97).

The DFG energy can be seen to increase with the energy of the two beams at λ_1 and λ_2: 500 nJ of DFG were obtained for an overall incident energy of $E_1 + E_2 = 250$ µJ. But contrary to what is expected from a low gain DFG process with two monochromatic incident beams (See equation 39), the DFG energy does not increase linearly with the energy E_2: there is like a saturation effect of the generated energy E_{DFG} when E_2 is increased. Note that since we are only considering the variations in DFG energy following the variations of *one* incident beam, we do not expect a square but a linear dependence of the DFG energy.

Based on these measurements, we calculated the energy conversion efficiency η defined as:

$$\eta = \frac{E_{DFG}}{E_1 + E_2} \tag{196}$$

for different input energies E_2 as shown on Figure (98). It turns out that for the three levels of energy E_1 considered in this work, the conversion efficiency exhibits similar variations with the energy at the second wavelength E_2: when E_2 is increased, the conversion efficiency increases sharply first, then reaches a maximum point and eventually decreases slowly. The maximum efficiencies that we measured are 0.18%, 0.2% and 0.21 % for $E_1 = 25$ µJ, $E_1 = 75$ µJ, and $E_1 = 125$ µJ respectively.

By taking into account the Fresnel losses of the two incident waves at the entrance of the uncoated crystal (18% for n = 2.45 at these wavelengths) as well as the Fresnel losses of the DFG at the exit of the crystal, the overall conversion efficiency is actually 1.5 times higher than what we did measure. It is slightly above 0.3 % then. This efficiency should be compared with what was done in previous DFG experiments in similar CdSe crystals and in the nanosecond regime. In his PhD dissertation, Gabriel Mennerat reported 0.78% conversion efficiency at 12 µm [11]: about 1.1 mJ was generated for a total input of 140 mJ. Andreou et al. measured 5 µJ at 16 µm for 4 mJ input energy, which gives a conversion efficiency of 0.13 % [124]. On the other hand, Godard et al. [131] measured higher conversion efficiencies of 2.5 % since 25 µJ was generated at 12 µm for 1 mJ input energy. Note that in the picosecond regime, Dhirani et al. measured about 40 µJ at 11 µm for an incident overall energy of 0.7 mJ [146], corresponding to a conversion efficiency of 5.7 %. Our measurements therefore lie in the low range of conversion efficiencies measured for DFG experiments in CdSe.

In addition, it is curious to notice on Figure (98) that the maximum conversion efficiency is obtained when the two energies E_1 and E_2 are more or less balanced. Indeed, the highest conversion efficiency is obtained for the following sets of input energies:$E_1 = 25$ µJ, $E_2 = 18$ µJ; $E_1 = 75$ µJ, $E_2 = 68$ µJ, $E_1 = 125$ µJ, $E_2 = 98$ µJ. Such a saturation of the conversion efficiency has already been observed previously by Gabriel Mennerat [11]. But in his experimental set-up, the energies of the two incident beams were much higher than ours. And it was not possible to control the energies of the two incident beams independently. It is therefore difficult to compare the saturation effect he observed with our measurements. We believe that the saturation effect observed in our experiments should be linked to the spectral linewidths and divergence of the incident beams. The measurements presented in Part III have shown that when the pump energy of the partial cylinder OPOs is increased, the FWHM of the beams emitted by the OPOs also increases. At low pumping level, it is likely that the FWHM of the beams is below the spectral acceptances of the DFG process. But when the pumping level gets above a certain value, the FWHM of the beams emitted by the OPOs exceeds the spectral acceptances of CdSe leading to a decrease of the conversion efficiency.

A good way to check for the influence of the linewidth of the incident beams on the conversion efficiency would be to make these measurements again at a constant pump level in the partial cylinder OPOs. Optical densities can be used for example to change the energy of the incident

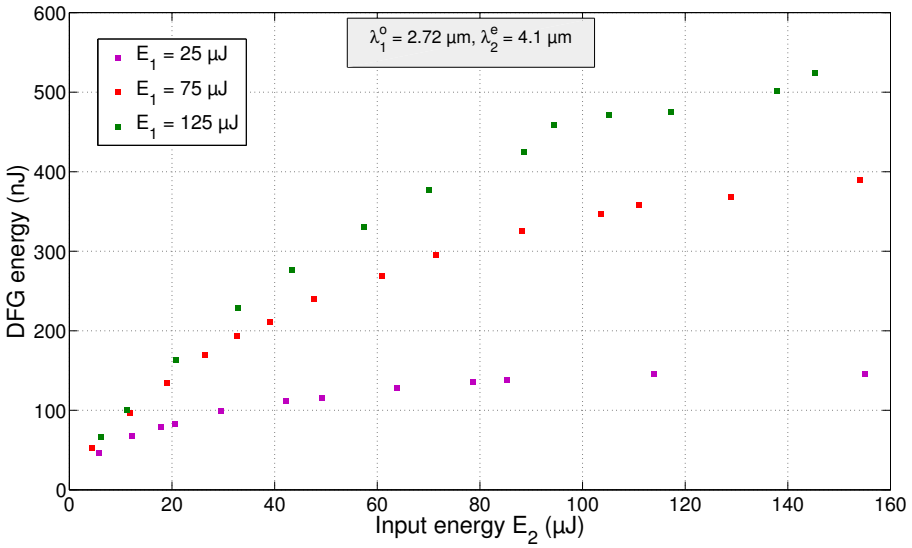

Figure 97: DFG energy as a function of the incident energy E_2 for three different levels of energy E_1.

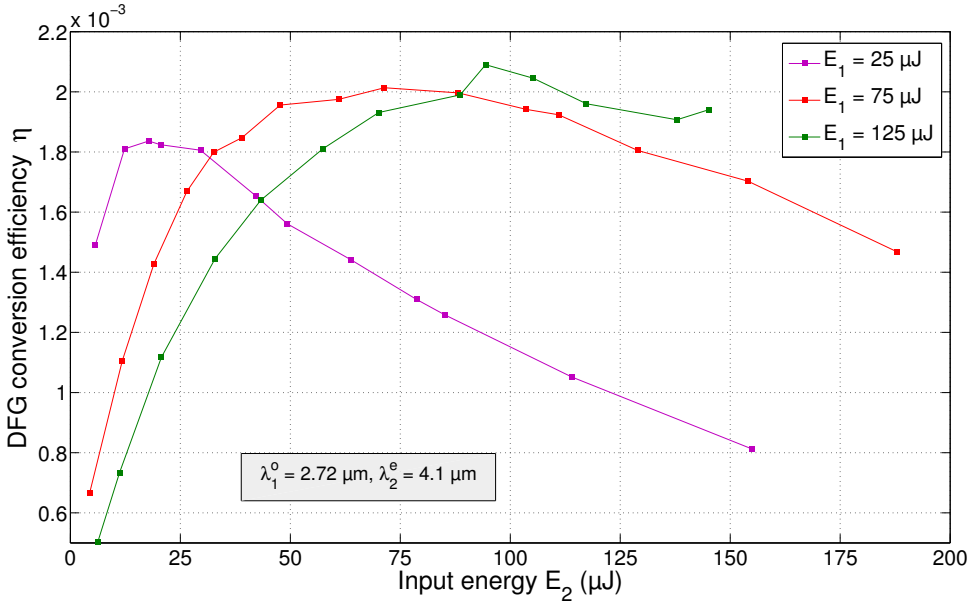

Figure 98: DFG conversion efficiency as a function of the input energy E_2 of the beam at $\lambda_2 = 4.1\,\mu m$, and for different levels of energy E_1 of the beam at $\lambda_1 = 2.72\,\mu m$.

beams. In this case, the linewidths of the incident beams would be constant when their energy is varied.

15.4 DISCUSSION

We are convinced that a fully quantitative analysis that relates the spectral acceptance of the DFG process to the linewidths of the incident beams will be useful for a better understanding of the performance of our dual wavelength source, but we did not have enough time to perform such a study. We rather give some basic and physical insight on the consequences of performing DFG with broad spectra.

We have measured the spectral linewidth of the two incident beams of the DFG process for equivalent pumping levels in the partial cylinder OPOs, and Figure (99) gives the results for a pump energy of 3 mJ. The FWHM of the first beam around 2.7 µm is 41 nm, while the FWHM of the second beam is 21 nm.

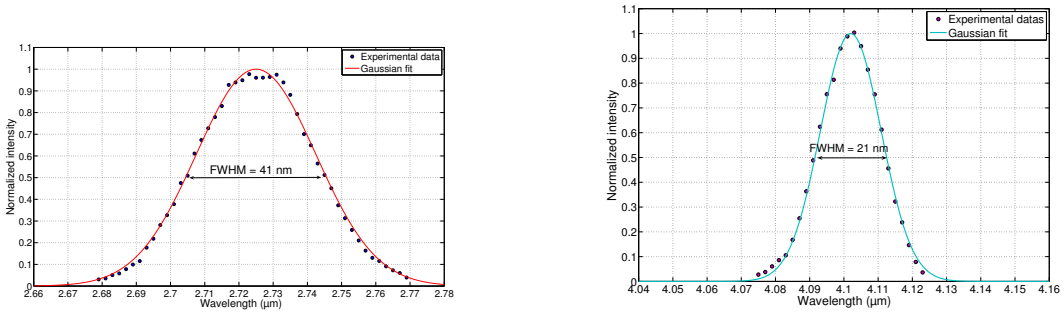

(a) Spectrum of the first beam, at λ_1, used for DFG experiments.

(b) Spectrum of the second beam, at λ_2, used for DFG experiments.

Figure 99: Experimental spectra of the two beams mixed in the DFG experiment when the same pump energy of 3 mJ is used in the two partial cylinder OPOs.

In order to evaluate the influence of these linewidths on the efficiency of conversion, we have also plotted on Figure (100a) the normalized DFG intensity as a function of the two wavelength λ_1 and λ_2:

$$I_{DFG}(\lambda_1, \lambda_2))_{norm} = sinc^2(\frac{\Delta k(\lambda_1, \lambda_2)L}{2}) \tag{197}$$

where Δk is the phase-mismatch of the Type III ANCPM DFG. We see that when the wavelength of the first beam at λ_1 is increased, the corresponding phase-matching wavelength of the second beam increases too. When the wavelength of the first beam is tuned from 2.7 up to 2.73 µm, the phase-matching signal wavelength of the second beam varies from 4.11 up to 4.18 µm. Based on this graph, it is possible to assess graphically and roughly the useful range of wavelength $\Delta\lambda_1$ of the first beam that will efficiently mix with a second beam whose FWHM is 21 nm as shown on Figure (99b). In the first order, this range of wavelength $\Delta\lambda_1$ is determined from the two ends of

the region where DFG is the highest and we see that only 17 nm of the incident spectrum can actually participate in the DFG process. We can therefore consider that a linewidth of 40 nm (as shown on Figure 99b) is too large by a factor of 2.5 for the DFG process studied here so that only the center of the spectrum of the first beam participates in the conversion process. Such a useful linewidth is represented on Figure (100b). Equivalently, this analysis shows that a crystal of 40 mm is slightly too long for our source as it is implemented today. The longest crystals that we can characterize so far are 2.5 times smaller than that i.e. shorter than 16 mm. The implementation of spectral narrowing techniques will solve this current limitation.

We also see from this simple analysis that when the linewidth of the second beam $\Delta\lambda_2$ is varied, through an increase of the pumping level of the OPO for example, the range of useful wavelength $\Delta\lambda_1$ is also increased. And it is likely that there is an optimal FWHM of the first beam for which the useful range of wavelength $\Delta\lambda_1$ can match the real FWHM of the first beam. It would be interesting to investigate whether this optimal situation coincides with the highest conversion efficiency seen on Figure (98). More simulations are required to verify this hypothesis.

15.5 CONCLUSION

The first DFG experiments performed with our source have been presented in this chapter. They are similar in principle to the experimental set-up shown on Figure (84b) and for which ANCPM pump tunable DFG was achieved in AGS [126]. The independent tuning of the two incident beams for DFG allows us to choose the direction in the crystal at which the DFG is performed. We have chosen the angular noncritical phase-matching direction because of the vanishing walk-off angle and highest magnitude of the effective coefficient in CdSe.

These experiments validate our DFG strategy but also highlight the limitations of the current setup. The linewidths of the beams emitted by the OPOs are so far too large to perform DFG in large size crystals. Two options can be envisioned to work around this issue: we can either perform DFG in smaller crystals and thus larger spectral acceptances, or implement spectral narrowing techniques. In the next section, we perform DFG in smaller crystals, since this corresponds to one of our specifications for nonlinear infrared materials characterization. The implementation of spectral narrowing techniques is anticipated as future work in our group.

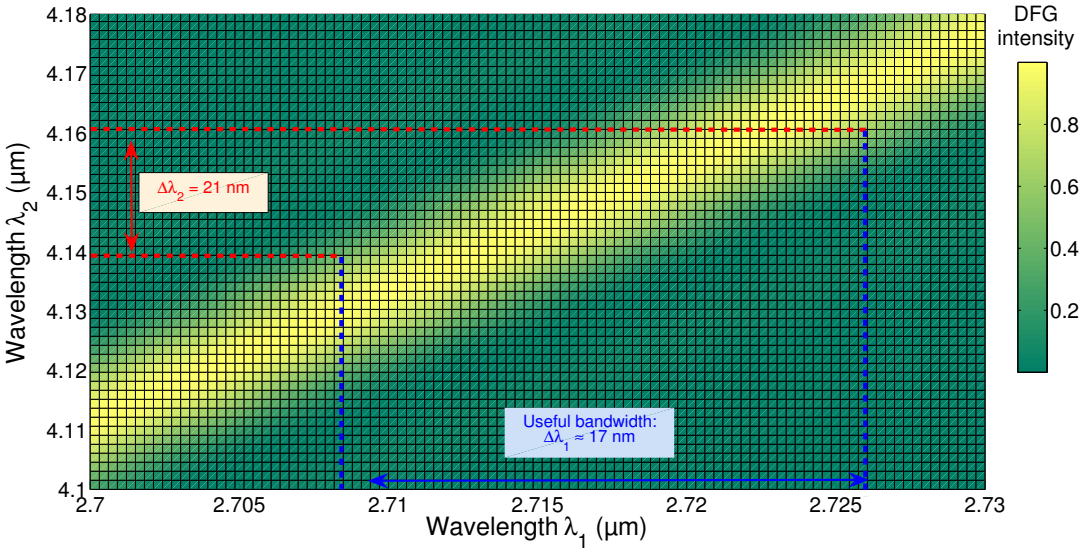

(a) Determination of the "useful" range of pump wavelengths when a signal linewidth of 40 nm is considered.

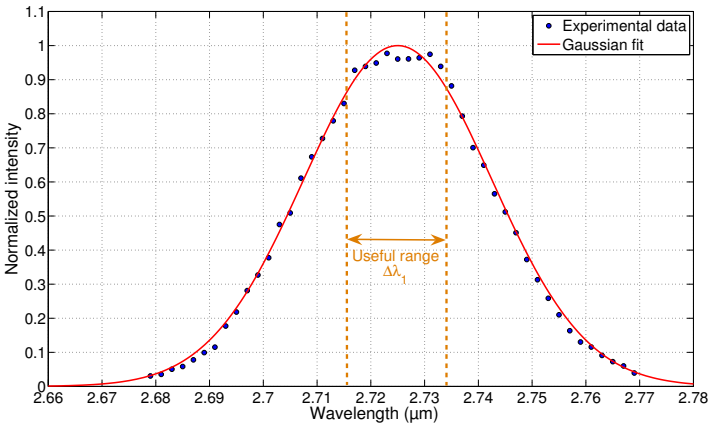

(b) Comparison between the useful range of pump wavelengths and the actual spectrum.

Figure 100: Influence of the spectral linewidth of the second beam $\Delta\lambda_2$ on the range of useful wavelengths $\Delta\lambda_1$ of the first beam.

16

DFG EXPERIMENTS IN SMALL CDSE CRYSTALS

The previous chapter dealt with the first DFG results obtained in a 40-mm-long CdSe crystal. This chapter is now devoted to DFG experiments performed in a 5-mm-diameter CdSe crystal cut as a cylinder. These results constitute the ultimate outcome of this entire dissertation.

16.1 CDSE CYLINDER

We have been the first group to cut and polish a CdSe crystal as a full cylinder, as shown on Figure (101).

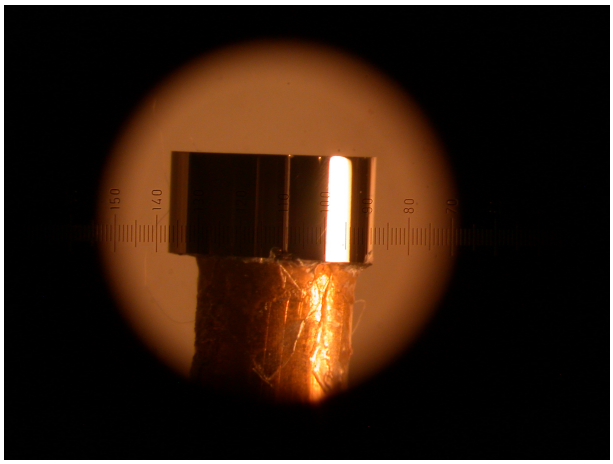

Figure 101: Picture of the oriented 4.9-mm-diameter CdSe cylinder used for DFG experiments.

The original sample was a $5 \times 5 \times 5\,mm^3$ cube from Cleveland Crystals and kindly provided by Gabriel Mennerat from CEA through a collaboration. The experimental setup to make the full cylinder was described in section 9.3.2. But contrary to the samples of 5%MgO:PPLN that were engineered as partial cylinders for the OPOs, the CdSe sample that we received was poorly oriented, so that we had to carry out in a first step the orientation of the upper face of the CdSe cylinder. For a higher tunability of the beam generated through DFG in a cylinder, it is necessary to orient the upper face so that the optical axis, i.e. the 6-fold symmetry axis, of the crystal lies in the plane of rotation of the cylinder (See Figure 102a). Furthermore, if we want a good accuracy of the orientation of this face, it is better to choose the upper face of the cylinder so that it coincides

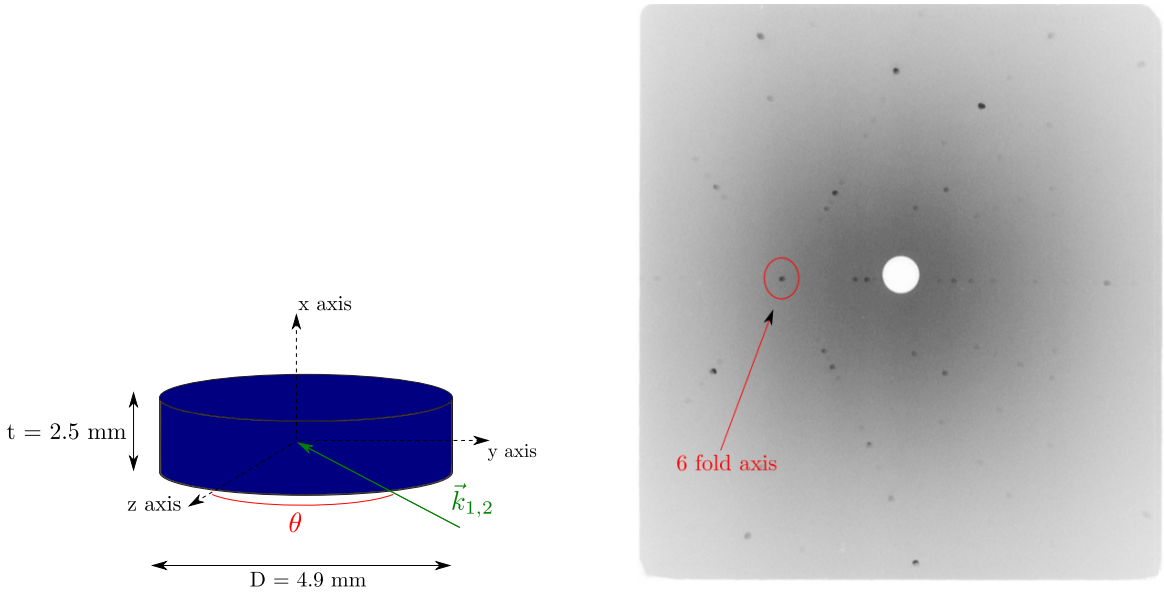

(a) Sketch of the orientation of the cylinder.

(b) Laue diffraction diagram measured on the CdSe cylinder.

Figure 102: Crystallographical orientation of the 4.9-mm-diameter CdSe cylinder.

with diffracting planes. That is why we have chosen the direction $< 110 >$ in the CdSe crystal to be the rotation axis of the cylinder. It corresponds to the x-axis of the crystal and it has a good diffraction efficiency. As a consequence, the rotation of the cylinder is done in the (yz) plane, as shown on Figure (102a). The orientation under X-rays using the Secasi method enabled us to match the axis of rotation of the cylinder with this specific crystallographic direction within an accuracy of 0.05°. The Laue diagram that confirms this orientation is shown on Figure (102b). The z-axis, which corresponds to the 6-fold symmetry axis can be seen to lie perfectly in the plane of rotation of the cylinder. This Laue diagram also confirms the crystalline surface quality of the cylinder.

16.2 PHASE-MATCHING MEASUREMENTS

The experimental setup used for the DFG experiments in the CdSe cylinder is shown on Figure (103). The phase-matching measurements are done by setting the first wavelength λ_1 at 2.79 µm for two main reasons: this wavelength corresponds to the emission line of the (Cr,Er):YSGG laser and optical parametric oscillation with this laser was reported in 1997 on a CdSe slab [143] oriented at $\theta = 73°$. Optical parametric generation (OPG) in CdSe was also demonstrated by Vodopyanov [56] at this specific pump wavelength.

Contrary to the experimental set-up used for DFG experiments in the 40-mm-long slab, a CaF_2 focal length of 50 mm is used. A stronger focusing compensates for the lower conversion efficiency due to the small diameter of the cylinder. Nevertheless, the use of a shorter focal length makes the overlap between the two beams less accurate and also increases the risk of optical damage.

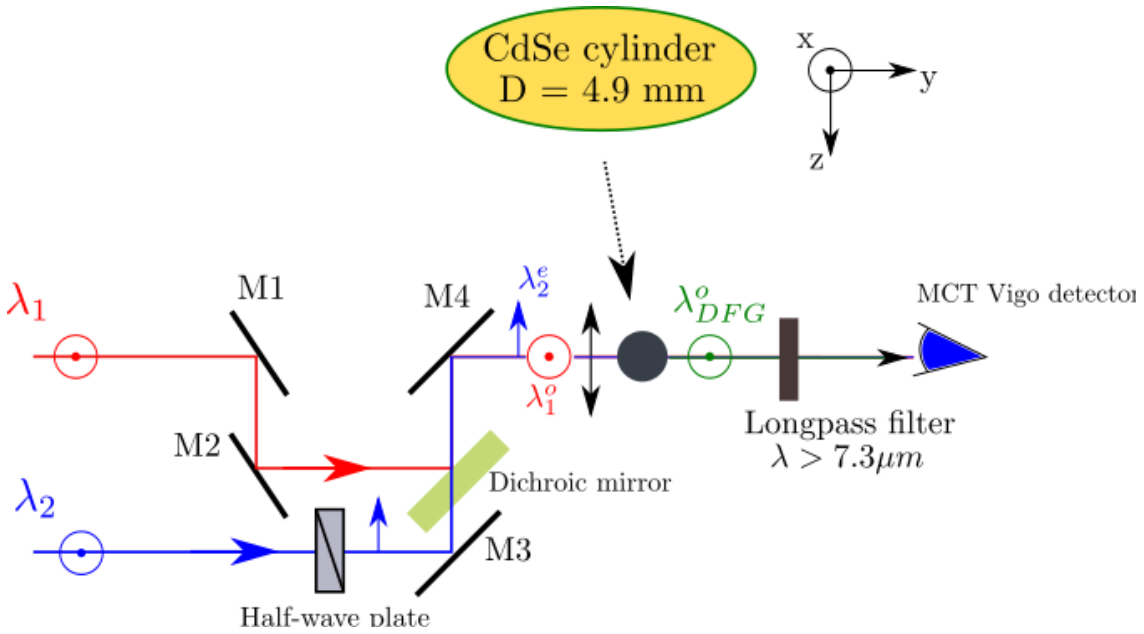

Figure 103: Experimental set-up used for the DFG experiments in the 5-mm-diameter CdSe cylinder

The optical damage threshold for CdSe was found to be 60 MW/cm^2 for 10 ns pulse durations in the case of an uncoated crystal [11, 132].

The alignment of the cylinder is probably the most critical point in this experiment. Unfortunately, since CdSe crystals are not transparent below 750 nm, it is impossible to use a He/Ne laser at 633 nm to perform the alignment in transmission. We rather centered the CdSe cylinder on a goniometric head under a microscope with an accuracy of 15 µm, before positioning the cylinder as accurately as possible in the center of an He/Ne laser spot.

For each angle of rotation, we tune the wavelength of the second beam and find the phase-matching wavelength $\lambda_{2,PM}$ for which the voltage measured with the MCT detector reaches a maximum, as shown on Figure (104). Experimentally, we could measure voltages up to 5 mV which are 3 times above the noise level of the MCT detector. The error bars on the measurements on Figure (104) are due to the fluctuations in intensity of the DFG. The exact position of the x-axis of the crystal can be obtained from the position of the maximum in the interpolation of our 18 measurements: it corresponds to an angle of 149.7° on the goniometer on which the CdSe cylinder is mounted. This value is in good agreement with the value of 150°±1° obtained from X-ray studies.

We have measured the phase-matching wavelengths $\lambda_{2,PM}$ in a range that extends from 3.83 up to 4.18 µm (see Figure 105b) and which corresponds to phase-matching angles θ_{PM} between 72° and 90°. The corresponding idler tuning range is 8.3 - 10.3 µm (see Figure 105a), but measurements at higher DFG wavelengths were not possible because of the lack of an adequate infrared detector above 11 µm. Nevertheless, thanks to the very wide tunability of the idler of the second OPO and transmission spectrum of the dichroic mirror shown on Figure (90), there is a priori no limitations

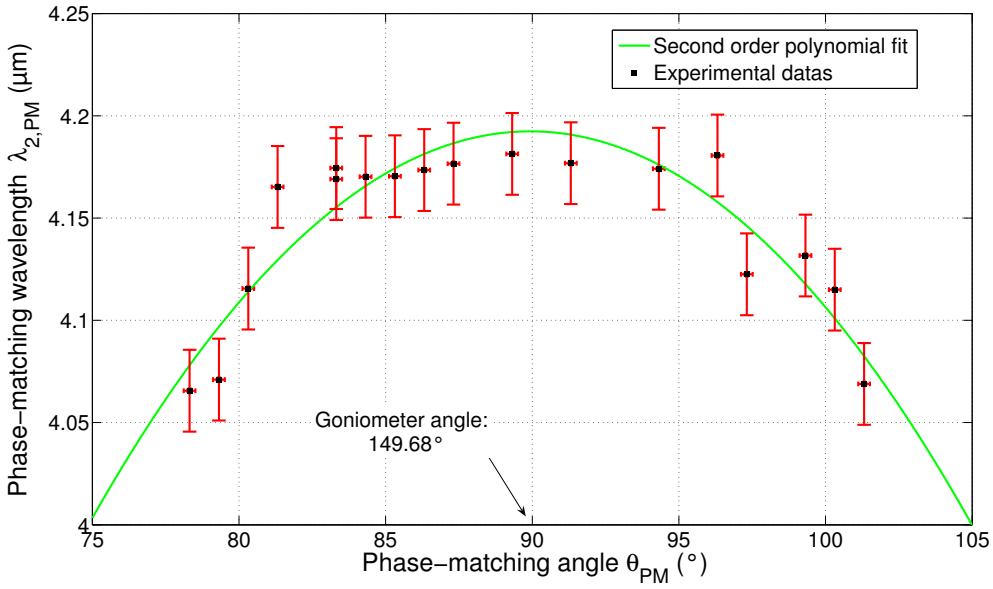

Figure 104: Raw measurements of the phase-matching angles in the CdSe cylinder for a pump wavelength $\lambda_1 = 2.79\,\mu m$. The error bars are due to the noise of the voltage induced by the fluctuations in intensity of the generated beams. The horizontal error bars are 0.5°.

in the incident wavelengths that can be mixed in the crystal. By mixing any wavelengths between 3.2 µm and 4.18 µm, infrared radiation up to 21 µm could be generated as shown on Figures (105b) and (105a). We believe that these measurements are a convincing proof of principle of the interest of cutting a CdSe crystal as a cylinder to generate widely tunable coherent radiation in Band III.

16.3 DISCUSSION

The discussion on the validity of our results is now done through a comparison with the results obtained previously by other groups. Optical Parametric Oscillation in a CdSe slab from Cleveland Crystals cut at $\theta = 73°$ [143, 144] was reported in 1995. Two different values of the phase-matching idler wavelengths in this direction were reported: 9.74 µm and 9.9 µm. We have represented on Figure (106) the two experimental data points corresponding to these two idler wavelengths in comparison with our measurements on cylinder. We see that our measurements performed on cylinder agree well with these two values. It is important to stress that the previous measurements made by Allik et al. and our measurements have been both performed on samples from Cleveland Crystals. The measurements performed by Vodopyanov [56] seem to provide a better agreement with calculation from Equations (192). However, neither the orientation nor the origin of the CdSe sample were reported in this paper.

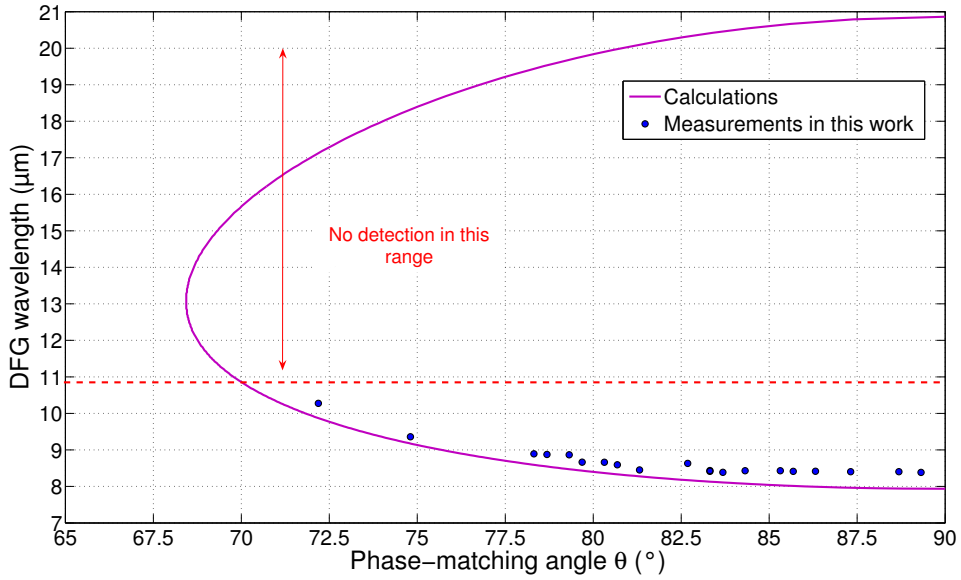

(a) Idler tuning curves

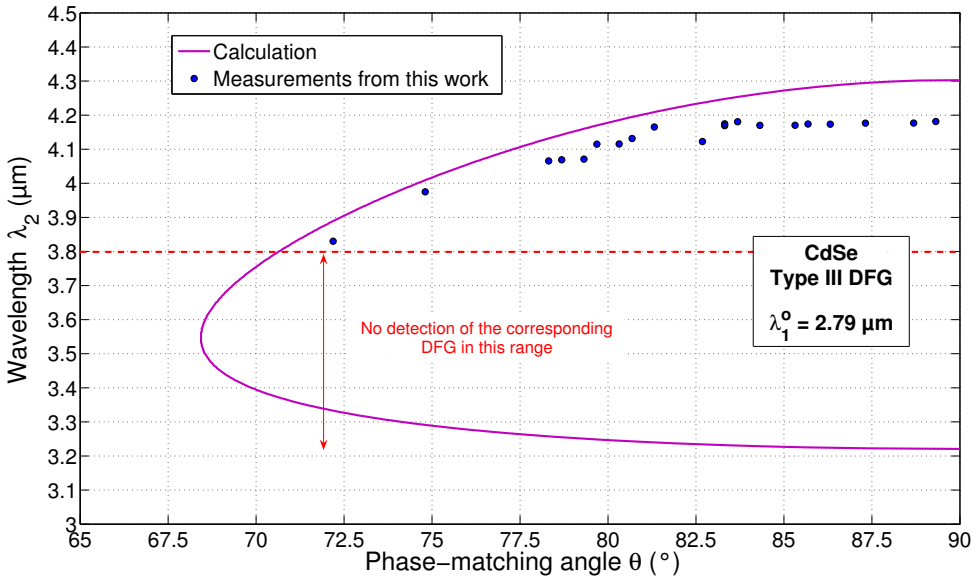

(b) Signal tuning curves

Figure 105: Comparison between the experimental tuning curves and the calculation from Equations (192).

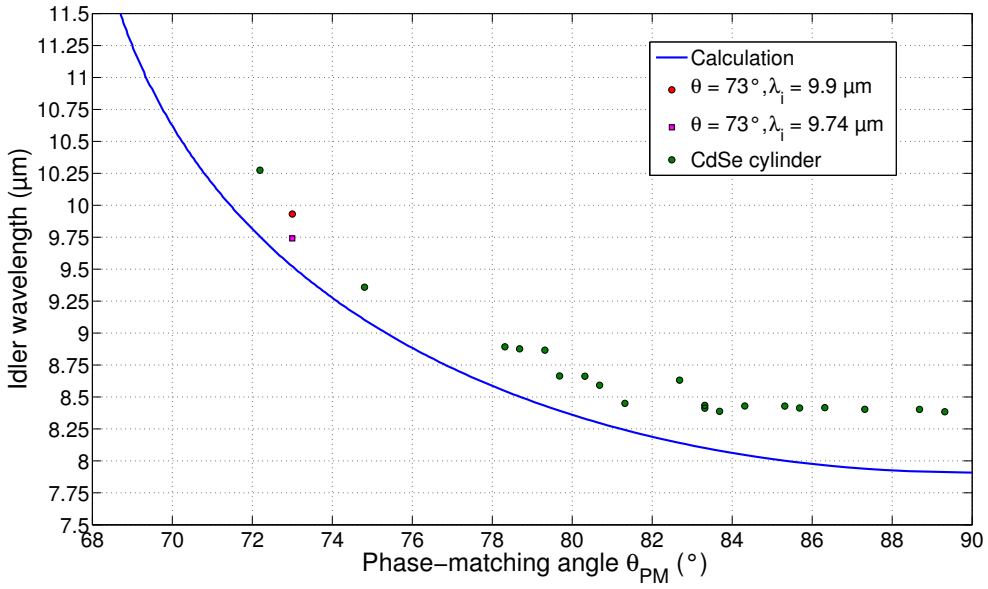

Figure 106: Comparison between the experimental phase-matching values measured by Allik et al. [143] and Rines et al. [144] on a slab cut at $\theta = 73°$, and the measurements performed in this work on a CdSe cylinder.

On the other hand, we would like to mention the influence of some noncollinearity between the two incident beams on the tuning curve of CdSe. It turns out that a noncollinear angle as small as 0.5° modifies the phase-matching wavelengths in the same proportion as the discrepancy between our measurements and the calculation in the collinear case shown on Figure (106). A noncollinearity of 0.5° between the two incident beams is very difficult to check experimentally for the moment since it falls within the experimental error of the alignment procedure of the beams.

16.4 CONCLUSION

We presented the ultimate experimental results of this dissertation: a tunable DFG between 8.3 and 10.3 µm has been generated in a 5-mm-diameter CdSe cylinder. These experiments confirm the potentialities of our strategy to perform DFG experiments in small size nonlinear crystals and at any pump wavelength within the tunability of the partial cylinder OPOs. The use of a crystal of CdSe cut as a cylinder is a very promising route to generate a DFG beam tunable over the entire transmission window of CdSe, i.e. up to 25 µm. Cutting a CdSe crystal as a partial cylinder with larger dimensions will enhance the DFG conversion efficiency while keeping a wide and continuous tunability (see Part III).

CONCLUSION OF PART IV

In this final Part, a quick comparison between the experimental setups for DFG above 8 µm has been given. We found that none of them does actually meet our specifications for the characterization of new materials for parametric infrared generation above 8 µm. As a consequence, a new versatile DFG setup that meets better these requirements has been designed and built: a wide and continuous tunability of two independent beams was specifically targeted. Our strategy is based on the use of two 5%MgO:PPLN partial cylinder OPOs pumped in parallel and with the same Nd:YAG laser.

We started by a DFG experiment in a 40-mm-long CdSe crystal oriented for angular noncritical phase-matching (ANCPM), which is well-suited for Type III DFG in CdSe since it is in this direction that the amplitude of the effective coefficient is the highest. Two different measurements were performed at two different pump wavelengths λ_p = 2.72 µm and λ_p = 2.79 µm. We advocate that spectral narrowing of the partial cylinder OPOs will not only result in a narrower linewidth, but also in higher DFG conversion efficiencies. More numerical simulations that relate the spectral and spatial performance of the two OPOs to the efficiency of the DFG stage should prove useful.

DFG experiments in a CdSe cylinder were then performed for the first time to our knowledge. By rotating the cylinder over a range of 18°, we were able to tune the DFG wavelength between 8.3 and 10.3 µm. The corresponding phase-matching directions are in good agreement with some "recent" measurements [144] performed on CdSe crystals from the same supplier.

The two experiments reported in this chapter are very encouraging and come to validate our unusual DFG strategy. The prospect of DFG experiments with pump wavelengths above 3 µm should lead to the characterizations of new crystals such as $PbIn_6Te_{10}$ [147], but also to a renewed interest in "older" crystals such as Tl_3AsSe_3 [148].

MAIN CONCLUSION

This dissertation deals with the generation of parametric light in the range 1 to 12 µm. Parametric infrared generation turns out to be a challenge at the interface between the fields of nonlinear optics and materials science embodied by the two approaches used to achieve efficient frequency conversion. Birefringent Phase-Matching (BPM) in anisotropic materials has been the traditional solution used in most frequency converter devices. But since the 90's, the quick success of microstructured materials has paved the way for Quasi-Phase-Matching (QPM) even in isotropic materials, leading to a renewed interest in Optical Parametric Oscillators (OPO). The high degree of engineering offered by this technology is now widely recognized as a key competitive advantage. We obtained original results concerning parametric infrared (IR) generation using BPM as well as QPM.

We have built the first OPO pumped by a Nd:YAG laser at 1.064 µm and based on a 5-mm-thick crystal of 5%MgO:PPLN cut as a partial cylinder. This OPO combines a wide and continuous tunability over the range 1.4 µm - 4.4 µm with a good conversion efficiency, up to 30%. Despite the need to resort to pump intensities almost an order of magnitude higher than in a slab OPO, we have shown that the energetical performance of a partial cylinder OPO is now equivalent to that of a slab OPO besides a wider tunability that can be continuously addressed. When the same Nd:YAG laser pumps two such *independent* OPOs in parallel, we dispose of a highly versatile QPM dual wavelength source with two widely and independently tunable beams. We have built this unique source allowing versatile Difference Frequency Generation (DFG) towards the mid- and far- IR. We carried out the first BPM DFG experiments with this source in a CdSe slab oriented for angular noncritical phase-matching at two different pump wavelengths, respectively 2.72 µm and 2.79 µm. The second set of DFG experiments were performed in a CdSe crystal cut and polished as a 5-mm-diameter full cylinder. Using a pump wavelength of 2.79 µm, we were able to tune the DFG wavelength from 8.3 µm up to 10.3 µm by rotating the crystal over an angular range of 18°. Contrary to all the BPM DFG experiments reported so far in the single crystal CdSe, tuning was achieved while keeping normal incidence of both the incident and generated beams in the crystal. The implementation of spectral narrowing techniques is already anticipated and will contribute to more accurate measurements of the phase-matching directions of a crystal as well as to a higher DFG conversion efficiency.

These experiments with our dual wavelength source are preliminary and encouraging validations of our capability of performing DFG in small crystals and at any pump wavelength between 1.4 µm and 3.5 µm. Even though we investigated the promises held by $CdSiP_2$ when it is only pumped with a Nd:YAG laser at 1.064 µm, there is tremendous prospect in terms of tunable infrared generation between 3.5 µm and 8 µm when this crystal is pumped around 2.4 µm. Such early demonstrations will be highly valuable for future applications requiring compact and tunable sources spanning the infrared spectrum. From a more fundamental point of view, performing DFG experiments at different pump wavelengths in the mid-IR can lead to a highly accurate determination of the values of the refractive indices of a nonlinear crystal. In this dissertation, we have cast the first stone of a method that leads to the determination of the values of the refractive

indices of a nonlinear crystal in the mid- to far- IR. This new method is based on the unique measurements of the DFG phase-matching angles in spheres or cylinders, and should contribute to further advances in the field of phase-matching metrology.

We have already identified two BPM crystals that will undoubtedly benefit from the association of the new analytical and experimental tools developed in this work: $PbIn_6Te_{10}$ [147] and Tl_3AsSe_3 [148]. On the one hand, because of the small band gaps of these crystals, it is necessary to perform DFG experiments with a pump wavelength above 2 µm; and our source is so far the only source that allows such measurements. On the other hand, these crystals transmit up to 25 µm and 17 µm respectively, where the lack of IR sources prevents accurate measurements of their refractive indices. Our new analytical method based on the measurements of the DFG phase-matching angles can solve this problem beautifully. Note that these two crystals have been grown recently in large size compatible with the requirements of DFG studies [149, 147], but with not enough good quality for OPO to be demonstrated, thus confirming the interest in our strategy of pump tunable DFG using the sphere or cylinder method.

Lastly, the recent success in the development of Orientation-Patterned Gallium Arsenide (OP-GaAs) shows that new QPM techniques can be advantageously implemented when parametric generation in the far IR region is targeted. However, there are still too few materials allowing QPM DFG in the terahertz region. Some demonstrations have been performed in bonded plates of isotropic materials such as ZnSe or GaP, but it is still a long way before this technique reaches the level of maturity of periodic poling. The original DFG strategy implemented in this work can contribute efficiently to the development of these new QPM strategies for far infrared parametric generation, for which we see a future as bright as for mid-IR parametric generation.

BIBLIOGRAPHY

[1] E.V. Browell, S. Ismail, and W.B. Grant. Differential absorption lidar (dial) measurements from air and space. *Applied Physics B*, 67(4):399–410, 1998.

[2] Julien Jaeck. *Emission infrarouge sous champ électrique dans le cristal de ZnSe dopé au chrome*. PhD thesis, Ecole Polytechnique, 2009.

[3] F. K. Tittel, D. Richter, and A. Fried. Mid-Infrared Laser Applications in Spectroscopy. In IrinaT. Sorokina and KonstantinL. Vodopyanov, editors, *Solid-State Mid-Infrared Laser Sources*, volume 89 of *Topics in Applied Physics*, pages 458–529. Springer Berlin Heidelberg, 2003.

[4] C.I. Rablau, J.-O. Ndap, X. Ma, A. Burger, and N.C. Giles. Absorption and photoluminescence spectroscopy of diffusion-doped ZnSe:Cr^{2+}. *Journal of Electronic Materials*, 28(6):678–682, 1999.

[5] V. Petrov. Parametric down-conversion devices: The coverage of the mid-infrared spectral range by solid-state laser sources. *Optical Materials*, 34(3):536 – 554, 2012.

[6] A. Godard. Infrared (2-12 μm) solid-state laser sources: a review. *Comptes Rendus Physique*, 8(10):1100 – 1128, 2007.

[7] V. Pasiskevicius, G. Strömqvist, F. Laurell, and C. Canalias. Quasi-phase matched nonlinear media: Progress towards nonlinear optical engineering. *Optical Materials*, 34(3):513–523, 2012.

[8] B. Boulanger and J. Zyss. Chapter 1.7. Nonlinear optical properties. *International Tables for Crystallography*, D, 2006.

[9] V.G Dimitriev, G. G. Gurzadyan, and D. N. Nikogosyan. *Handbook of nonlinear optical crystals*. Springer-Verlag, 1991.

[10] J. A. Armstrong, N. Bloembergen, J. Ducuing, and P. S. Pershan. Interactions between light waves in a nonlinear dielectric. *Physical Review*, 127(6):1918–1939, 1962.

[11] Gabriel Mennerat. *Conception , Modélisation et Réalisation d une Source Cohérente de Forte Energie Accordable dans le Moyen Infrarouge*. PhD thesis, 2000.

[12] I. Shoji, T. Kondo, A. Kitamoto, M. Shirane, and R. Ito. Absolute scale of second-order nonlinear-optical coefficients. *J. Opt. Soc. Am. B*, 14(9):2268–2294, 1997.

[13] J-P. Fève, B. Boulanger, and G. Marnier. Calculation and classification of the direction loci for collinear types I , II and III phase-matching of three-wave nonlinear optical parametric interactions in uniaxial and biaxial acentric crystals. *Optics Communications*, 99:284–302, 1993.

[14] D. A. Kleinman. Nonlinear dielectric polarization in optical media. *Phys. Rev.*, 126:1977–1979, 1962.

[15] By B Boulanger and J Zyss. Nonlinear optical properties. In *International Tables for Crystallography*, volume D, pages 178–219. 2006.

[16] M. M. Fejer, G. A. Magel, D. H. Jundt, and R. L. Byer. Quasi-phase-matched second harmonic generation: tuning and tolerances. *Quantum Electronics, IEEE Journal of*, 28(11):2631–2654, 1992.

[17] R. Haïdar, N. Forget, P. Kupecek, and E. Rosencher. Fresnel phase matching for three-wave mixing in isotropic semiconductors. *J. Opt. Soc. Am. B*, 21(8):1522–1534, 2004.

[18] B. Boulanger, J-P. Fève, G. Marnier, B. Ménaert, X. Cabirol, P. Villeval, and C. Bonnin. Relative sign and absolute magnitude of $d^{(2)}$ nonlinear coefficients of KTP from second-harmonic-generation measurements. *J. Opt. Soc. Am. B*, 11(5):750–757, 1994.

[19] R. L. Byer. Quasi-phasematched nonlinear interactions and devices. *Journal of Nonlinear Optical Physics & Materials*, 6(4):549–592, 1997.

[20] K. L. Vodopyanov, O. Levi, P. S. Kuo, T. J. Pinguet, J.S. Harris, M. M. Fejer, B. Gerard, L. Becouarn, and E. Lallier. Optical parametric oscillation in quasi-phase-matched GaAs. *Optics letters*, 29(16):1912–4, 2004.

[21] J. A. Giordmaine and R. C. Miller. Tunable coherent parametric oscillation in $LiNbO_3$ at optical frequencies. *Phys. Rev. Lett.*, 14:973–976, 1965.

[22] R. G. Smith, G. E. Geusic, H. J. Levinstein, J. J. Rubin, S. Singh, and L. G. Van Uitert. Continuous optical parametric oscillation in $Ba_2NaNb_5O_{15}$. *Applied Physics Letters*, 12(9):308–310, 1968.

[23] S. Chaitanya Kumar, R. Das, G. K. Samanta, and M. Ebrahim-Zadeh. Optimally-output-coupled, 17.5 W, fiber-laser-pumped continuous-wave optical parametric oscillator. *Applied Physics B*, 102:31–35, 2011.

[24] H. Ishizuki and T. Taira. Half-joule output optical-parametric oscillation by using 10-mm-thick periodically poled Mg-doped congruent $LiNbO_3$. *Opt. Express*, 20(18):20002–20010, 2012.

[25] W. H. Louisell, A. Yariv, and A. E. Siegman. Quantum fluctuations and noise in parametric processes. I. *Phys. Rev.*, 124:1646–1654, 1961.

[26] A. Yariv. *Quantum Electronics*. John Wiley & Sons, 2^{nd} edition, 1975.

[27] Y. R. Shen. *The principles of nonlinear optics*. John Wiley & sons, 1967.

[28] Y. R. Shen. Quantum statistics of nonlinear optics. *Phys. Rev.*, 155:921–931, 1967.

[29] Anthony. E. Siegman. *Lasers*. University Science Books, 1986.

[30] G. Hansson, H. Karlsson, and F. Laurell. Unstable resonator optical parametric oscillator based on quasi-phase-matched $RbTiOAsO_4$. *Applied Optics*, 40(30):5446–5451, 2001.

[31] J-P. Fève, O. Pacaud, B. Boulanger, and M. Renard. Tunable phase-matched optical parametric oscillators based on a cylindrical crystal. *Journal of the Optical Society of America B*, 19(2):222–233, 2002.

[32] S. Brosnan and R. Byer. Optical parametric oscillator threshold and linewidth studies. *Quantum Electronics, IEEE Journal of*, 15(6):415 – 431, jun 1979.

[33] S.E. Harris. Tunable optical parametric oscillators. *Proceedings of the IEEE*, 57(12):2096 – 2113, 1969.

[34] E. Rosencher and C. Fabre. Oscillation characteristics of continuous-wave optical parametric oscillators: beyond the mean-field approximation. *J. Opt. Soc. Am. B*, 19(5):1107–1116, 2002.

[35] A. Yariv and W. Louisell. 5A2 - Theory of the optical parametric oscillator. *Quantum Electronics, IEEE Journal of*, 2(9):418 –424, 1966.

[36] A. Godard and E. Rosencher. Energy yield of pulsed optical parametric oscillators: a rate-equation analysis. *Quantum Electronics, IEEE Journal of*, 40(6):784 – 790, 2004.

[37] J. E. Bjorkholm. Efficient optical parametric oscillation using doubly and singly resonant cavities. *Applied Physics Letters*, 13(2):53–56, 1968.

[38] V. Petrov, P. G. Schunemann, K. T. Zawilski, and T. M. Pollak. Noncritical singly resonant optical parametric oscillator operation near 6.2 μm based on a $CdSiP_2$ crystal pumped at 1064 nm. *Opt. Lett.*, 34(16):2399–2401, 2009.

[39] V. Kemlin, P. Brand, B. Boulanger, P. Segonds, P. G. Schunemann, K. T. Zawilski, B. Ménaert, and J. Debray. Phase-matching properties and refined Sellmeier equations of the new nonlinear infrared crystal $CdSiP_2$. *Opt. Lett.*, 36(10):1800–1802, 2011.

[40] N. Itoh and T. Fujinaga and T. Nakau. Birefringence in $CdSiP_2$. *Japanese Journal of Applied Physics*, 17(5):951–952, 1978.

[41] P. G. Schunemann, K. T. Zawilski, T. M. Pollak, D. E. Zelmon, N. C. Fernilius, and F. K. Hopkins. New mid-IR nonlinear optical crystal: $CdSiP_2$. In *Conference on Lasers and Electro-Optics/Quantum Electronics and Laser Science Conference and Photonic Applications Systems Technologies*, page CFX7. Optical Society of America, 2008.

[42] K. T. Zawilski, P. G. Schunemann, T. C. Pollak, D. E. Zelmon, N. C. Fernelius, and F. K. Hopkins. Growth and characterization of large $CdSiP_2$ single crystals. *Journal of Crystal Growth*, 312(8):1127 – 1132, 2010.

[43] G. Marnier and B. Boulanger. The sphere method: a new technique in linear and non-linear crystalline optical studies. *Optics Communications*, 72(3 - 4):139 – 143, 1989.

[44] B. Boulanger, P. Segonds, J-P. Fève, O. Pacaud, B. Ménaert, and J. Zaccaro. Spheres and cylinders in parametric nonlinear optics. *Optical Materials*, 26(4):459 – 464, 2004. Third International Symposium on Lasers and Nonlinear Optical Materials.

[45] Pierre Brand. *Study of 5%MgO:PPLN and $CdSiP_2$ for infrared parametric generation*. PhD thesis, Université Joseph Fourier Grenoble, 2010.

[46] J-P. Fève, B. Boulanger, O. Pacaud, I. Rousseau, B. Ménaert, G. Marnier, P. Villeval, C. Bonnin, G.M. Loiacono, and D. N. Loiacono. Phase-matching measurements and Sellmeier equations over the complete transparency range of $KTiOAsO_4$, $RbTiOAsO_4$, and $CsTiOAsO_4$. *J. Opt. Soc. Am. B*, 17(5):775–780, 2000.

[47] P. Segonds and B. Boulanger and B. Ménaert and J. Zaccaro and J.P. Salvestrini and M.D. Fontana and R. Moncorgé and F. Porée and G. Gadret and J. Mangin and A. Brenier and G. Boulon and G. Aka and D. Pelenc. Optical characterizations of $YCa_4O(BO_3)_3$ and $Nd:YCa_4O(BO_3)_3$ crystals. *Optical Materials*, 29(8):975 – 982, 2007.

[48] V. Kemlin, B. Boulanger, V. Petrov, P. Segonds, B. Ménaert, P. G. Schunneman, and K. T. Zawilski. Nonlinear, dispersive, and phase-matching properties of the new chalcopyrite $CdSiP_2$ [Invited]. *Opt. Mater. Express*, 1(7):1292–1300, Nov 2011.

[49] L. Fan, S. Zhu, B. Zhao, B. Chen, Z. He, H. Yang, G. Liu, and X. Wang. Growth of $CdSiP_2$ single crystals by double-walled quartz ampoule technique. *Journal of Crystal Growth*, 364(0):62 – 66, 2013.

[50] G. Marchev, F. Pirzio, R. Piccoli, A. Agnesi, G. Reali, P. G. Schunemann, K. T. Zawilski, A. Tyazhev, and V. Petrov. Narrow-bandwidth, mid-infrared, seeded optical parametric generation in 90 phase-matched $CdSiP_2$ crystal pumped by diffraction limited 500 ps pulses at 1064 nm. *Opt. Lett.*, 37(15):3219–3221, 2012.

[51] G. Ambrazyavichyus, G. Babonas, and V. Karpus. Optical activity of $CdSiP_2$. *Soviet Physics: Semiconductors*, 12:1210–1211, 1978.

[52] K. L. Vodopyanov, S. B. Mirov, V. G. Voevodin, and P. G. Schunemann. Two-photon absorption in GaSe and $CdGeAs_2$. *Optics Communications*, 155(1–3):47–50, 1998.

[53] S. Chaitanya Kumar, A. Agnesi, P. Dallocchio, F. Pirzio, G. Reali, K. T. Zawilski, P. G. Schunemann, and M. Ebrahim-Zadeh. Compact, 1.5 mJ, 450 MHz, $CdSiP_2$ picosecond optical parametric oscillator near 6.3 μm. *Opt. Lett.*, 36(16):3236–3238, 2011.

[54] V. Petrov, F. Noack, I. Tunchev, P. Schunemann, and K. Zawilski. The nonlinear coefficient d_{36} of $CdSiP_2$. In *Society of Photo-Optical Instrumentation Engineers (SPIE) Conference Series*, volume 7197, 2009.

[55] P. D. Mason, D. J. Jackson, and E. K. Gorton. CO_2 laser frequency doubling in $ZnGeP_2$. *Optics Communications*, 110(1–2):163 – 166, 1994.

[56] K. L. Vodopyanov. Mid-infrared optical parametric generator with extra-wide (3–19-μm) tunability: applications for spectroscopy of two-dimensional electrons in quantum wells. *J. Opt. Soc. Am. B*, 16(9):1579–1586, 1999.

[57] A. Douillet and J.J. Zondy. Low threshold, self frequency stabilized $AgGaS_2$ continuous-wave subharmonic optical parametric oscillator. *Opt Lett*, 23(16):1259–61, 1998.

[58] K. L. Vodopyanov, J. P. Maffetone, I. Zwieback, and W. Ruderman. $AgGaS_2$ optical parametric oscillator continuously tunable from 3.9 to 11.3 μm. *Applied Physics Letters*, 75(9):1204–1206, 1999.

[59] V. V. Badikov, A. K. Don, K. V. Mitin, A. M. Seregin, V. V. Sinaiskii, and N. I. Schebetova. Optical parametric oscillator on an $Hg_{1-x}Cd_xGa_2S_4$ crystal. *Quantum Electronics*, 35(9):853, 2005.

[60] V. Petrov, G. Marchev, P. G. Schunemann, A. Tyazhev, K. T. Zawilski, and T. M. Pollak. Subnanosecond, 1 kHz, temperature-tuned, noncritical mid-infrared optical parametric oscillator based on $CdSiP_2$ crystal pumped at 1064 nm. *Opt. Lett.*, 35(8):1230–1232, 2010.

[61] A. Peremans, D. Lis, F. Cecchet, P. G. Schunemann, K. T. Zawilski, and V. Petrov. Noncritical singly resonant synchronously pumped OPO for generation of picosecond pulses in the mid-infrared near 6.4 μm. *Opt. Lett.*, 34(20):3053–3055, 2009.

[62] O. Chalus, P. G. Schunemann, K. T. Zawilski, J. Biegert, and M. Ebrahim-Zadeh. Optical parametric generation in $CdSiP_2$. *Opt. Lett.*, 35(24):4142–4144, 2010.

[63] Henri Gavin. The Levenberg-Marquardt method for nonlinear least squares curve fitting problems. http://people.duke.edu/~hpgavin/ce281/lm.pdf.

[64] M. C. Ohmer. Response to "Comment on '$ZnGeP_2$ birefringence and its temperature dispersion using polarized interference' " [J. Appl. Phys. [bold 87], 4638 (2000)]. *Journal of Applied Physics*, 87(9):4640–4641, 2000.

[65] H. Imam. Metrology: Broad as a lamp, bright as a laser. *Nature Photonics*, 2, 2008.

[66] Y. Hiraoka, T. Shimi, and T. Haraguchi. Multispectral imaging fluorescence microscopy for living cells. *Cell Structure and Function*, 27(5):367–374, 2002.

[67] N. Savage. Supercontinuum sources. *Nature Photonics*, 3:114–115, 2009.

[68] J. M. Dudley, G. Genty, and S. Coen. Supercontinuum generation in photonic crystal fiber. *Rev. Mod. Phys.*, 78:1135–1184, 2006.

[69] C. Xia, M. Kumar, O. P. Kulkarni, M. N. Islam, M. J. Terry Jr, F. L.and Freeman, M. Poulain, and G. Mazé. Mid-infrared supercontinuum generation to 4.5 μm in ZBLAN fluoride fibers by nanosecond diode pumping. *Opt. Lett.*, 31(17):2553–2555, 2006.

[70] K. L. Vodopyanov, E. Sorokin, I. T. Sorokina, and P. G. Schunemann. Mid-IR frequency comb source spanning 4.4–5.4 μm based on subharmonic GaAs optical parametric oscillator. *Opt. Lett.*, 36(12):2275–2277, 2011.

[71] M. W. Haakestad, T. P. Lamour, N. Leindecker, A. Marandi, and K. L. Vodopyanov. Intracavity trace molecular detection with a broadband mid-IR frequency comb source. *J. Opt. Soc. Am. B*, 30(3):631–640, 2013.

[72] C. R. Phillips. *Broadband optical sources based on highly nonlinear quasi-phasematched interactions*. PhD thesis, Stanford University, 2012.

[73] V. Petrov, M. Ghotbi, O. Kokabee, A. Esteban-Martin, F. Noack, A. Gaydardzhiev, I. Nikolov, P. Tzankov, I. Buchvarov, K. Miyata, A. Majchrowski, I.V. Kityk, F. Rotermund, E. Michalski, and M. Ebrahim-Zadeh. Femtosecond nonlinear frequency conversion based on BiB_3O_6. *Laser & Photonics Reviews*, 4(1):53–98, 2010.

[74] K. Kato. Second-harmonic and sum-frequency generation in $ZnGeP_2$. *Appl. Opt.*, 36(12):2506–2510, 1997.

[75] J.-J. Zondy and D. Touahri. Updated thermo-optic coefficients of $AgGaS_2$ from temperature-tuned noncritical $3\omega,\omega - > 2\omega$ infrared parametric amplification. *J. Opt. Soc. Am. B*, 14(6):1331–1338, 1997.

[76] J.-J. Zondy, D. Touahri, and O. Acef. Absolute value of the d_{36} nonlinear coefficient of $AgGaS_2$: prospect for a low-threshold doubly resonant oscillator-based 3:1 frequency divider. *J. Opt. Soc. Am. B*, 14(10):2481–2497, Oct 1997.

[77] D. A. Roberts. Dispersion equations for nonlinear optical crystals: KDP, $AgGaSe_2$, and $AgGaS_2$. *Appl. Opt.*, 35(24):4677–4688, 1996.

[78] J.-J. Zondy. Experimental investigation of single and twin $aggase_2$ crystals for cw 10.2 μm shg. *Optics Communications*, 119(3–4):320 – 326, 1995.

[79] T. Skauli, K. L. Vodopyanov, T. J. Pinguet, A. Schober, O. Levi, L. A. Eyres, M. M. Fejer, J. S. Harris, B. Gerard, L. Becouarn, E. Lallier, and G. Arisholm. Measurement of the nonlinear coefficient of orientation-patterned GaAs and demonstration of highly efficient second-harmonic generation. *Opt. Lett.*, 27(8):628–630, 2002.

[80] T. Skauli, P. S. Kuo, K. L. Vodopyanov, T. J. Pinguet, O. Levi, L. A. Eyres, J. S. Harris, M. M. Fejer, B. Gerard, L. Becouarn, and E. Lallier. Improved dispersion relations for GaAs and applications to nonlinear optics. *Journal of Applied Physics*, 94(10):6447–6455, 2003.

[81] P. S. Kuo, K. L. Vodopyanov, M. M. Fejer, D. M. Simanovskii, X. Yu, J. S. Harris, D. Bliss, and D. Weyburne. Optical parametric generation of a mid-infrared continuum in orientation-patterned GaAs. *Opt. Lett.*, 31(1):71–73, Jan 2006.

[82] M. Eichhorn. Quasi-three-level solid-state lasers in the near and mid infrared based on trivalent rare earth ions. *Applied Physics B*, 93:269–316, 2008.

[83] S. Mirov, V. Fedorov, I. Moskalev, D. Martyshkin, and C. Kim. Progress in Cr^{2+} and Fe^{2+} doped mid-IR laser materials. *Laser & Photonics Reviews*, 4(1):21–41, 2010.

[84] W. S. Pelouch, G. J. Wagner, and T. J. Carrig. Mid-wave ZGP OPOs pumped by a Cr:ZnSe laser. In *Advanced Solid-State Lasers*, page PD1. Optical Society of America, 2001.

[85] M. N. Cizmeciyan, H. Cankaya, A. Kurt, and A. Sennaroglu. Kerr-lens mode-locked femtosecond Cr^{2+}:ZnSe laser at 2420 nm. *Opt. Lett.*, 34(20):3056–3058, 2009.

[86] G. Edwards, R. Logan, M. Copeland, L. Reinisch, J. Davidson, B. Johnson, R. Maciunas, M. Mendenhall, R. Ossoff, J. Tribble, J. Werkhaven, and D. O'Day. Tissue ablation by a free-electron laser tuned to the amide II band. *Nature*, 371(6496):416–419, 1994.

[87] H. Karlsson, M. Olson, G. Arvidsson, F. Laurell, U. Bäder, A. Borsutzky, R. Wallenstein, S. Wickström, and M. Gustafsson. Nanosecond optical parametric oscillator based on large-aperture periodically poled $RbTiOAsO_4$. *Opt. Lett.*, 24(5):330–332, 1999.

[88] A. Zukauskas, N. Thilmann, V. Pasiskevicius, F. Laurell, and C. Canalias. 5 mm thick periodically poled Rb-doped KTP for high energy optical parametric frequency conversion. *Opt. Mater. Express*, 1(2):201–206, 2011.

[89] Hideki Ishizuki and Takunori Taira. High-energy quasi-phase-matched optical parametric oscillation in a periodically poled MgO:LiNbO3 device with a 5 mm×5 mm aperture. *Opt. Lett.*, 30(21):2918–2920, 2005.

[90] Hideki Ishizuki and Takunori Taira. High energy quasi-phase-matched optical parametric oscillation using Mg-doped congruent $LiTaO_3$ crystal. *Opt. Express*, 18(1):253–258, Jan 2010.

[91] Raicol Crystals Ltd. http://www.raicol.com/index.php?option=com_content&view=article&id=118&Itemid=445.

[92] HC Photonics Corp. http://www.hcphotonics.com/bulk.htm.

[93] L. E. Myers, R. C. Eckardt, M. M. Fejer, R. L. Byer, W. R. Bosenberg, and J. W. Pierce. Quasi-phase-matched optical parametric oscillators in bulk periodically poled $LiNbO_3$. *J. Opt. Soc. Am. B*, 12(11):2102–2116, 1995.

[94] M. Peltz, U. Bäder, A. Borsutzky, R. Wallenstein, J. Hellström, H. Karlsson, V. Pasiskevicius, and F. Laurell. Optical parametric oscillators for high pulse energy and high average power operation based on large aperture periodically poled KTP and RTA. *Applied Physics B*, 73(7):663–670, 2001.

[95] A. Kuroda, S. Kurimura, and Y. Uesu. Domain inversion in ferroelectric MgO:$LiNbO_3$ by applying electric fields. *Applied Physics Letters*, 69(11):1565–1567, 1996.

[96] J. C. Jacco and G. M. Loiacono. Nature of the infrared spectrum in band-edge region of $KTiOPO_4$. *Applied Physics Letters*, 58(6):560–561, 1991.

[97] L. Lefort, K. Puech, G. W. Ross, Y. P. Svirko, and D. C. Hanna. Optical parametric oscillation out to 6.3 μm in periodically poled lithium niobate under strong idler absorption. *Applied Physics Letters*, 73(12):1610–1612, 1998.

[98] M. Sato, T. Hatanaka, S. Izumi, T. Taniuchi, and H. Ito. Generation of 6.6 μm optical parametric pscillation with periodically oled $LiNbO_3$. *Appl. Opt.*, 38(12):2560–2563, 1999.

[99] M. Henriksson, M. Tiihonen, V. Pasiskevicius, and F. Laurell. Mid-infrared ZGP OPO pumped by near-degenerate narrowband type-I PPKTP parametric oscillator. *Applied Physics B*, 88(1):37–41, 2007.

[100] Y. Furukawa, K. Kitamura, S. Takekawa, A. Miyamoto, M. Terao, and N. Suda. Photorefraction in $LiNbO_3$ as a function of [Li]/[Nb] and MgO concentrations. *Applied Physics Letters*, 77(16):2494–2496, 2000.

[101] D. A. Bryan, Robert Gerson, and H. E. Tomaschke. Increased optical damage resistance in lithium niobate. *Applied Physics Letters*, 44(9):847–849, 1984.

[102] M. V. Pack, D. J. Armstrong, and A. V. Smith. Measurement of the $\chi^{(2)}$ tensors of $KTiOPO_4$, $KTiOAsO_4$, $RbTiOPO_4$, and $RbTiOAsO_4$ crystals. *Appl. Opt.*, 43(16):3319–3323, 2004.

[103] Hideki Ishizuki and Takunori Taira. Mg-doped congruent $LiTaO_3$ crystal for large-aperture quasi-phase matching device. *Opt. Express*, 16(21):16963–16970, 2008.

[104] D. E. Zelmon, D. L. Small, and D. Jundt. Infrared corrected Sellmeier coefficients for congruently grown lithium niobate and 5 mol.% magnesium oxide –doped lithium niobate. *J. Opt. Soc. Am. B*, 14(12):3319–3322, 1997.

[105] H. Y. Shen, H. Xu, Z. D. Zeng, W. X. Lin, R. F. Wu, and G. F. Xu. Measurement of refractive indices and thermal refractive-index coefficients of $LiNbO_3$ crystal doped with 5 mol. % MgO. *Appl. Opt.*, 31(31):6695–6697, 1992.

[106] O. Paul, A. Quosig, T. Bauer, M. Nittmann, J. Bartschke, G. Anstett, and J. A. L'huillier. Temperature-dependent Sellmeier equation in the MIR for the extraordinary refractive index of 5% MgO doped congruent $LiNbO_3$. *Applied Physics B*, 86(1):111–115, 2007.

[107] L. E. Myers, G. D. Miller, R. C. Eckardt, M. M. Fejer, R. L. Byer, and W. R. Bosenberg. Quasi-phase-matched 1.064-μm-pumped optical parametric oscillator in bulk periodically poled $LiNbO_3$. *Opt. Lett.*, 20(1):52–54, 1995.

[108] K. C. Burr, C. L. Tang, M. A. Arbore, and M. M. Fejer. High-repetition-rate femtosecond optical parametric oscillator based on periodically poled lithium niobate. *Applied Physics Letters*, 70(25):3341–3343, 1997.

[109] L. E. Myers, R. C. Eckardt, M. M. Fejer, R. L. Byer, and W. R. Bosenberg. Multigrating quasi-phase-matched optical parametric oscillator in periodically poled $LiNbO_3$. *Optics letters*, 21(8):591–593, April 1996.

[110] Covesion Ltd. http://www.covesion.com,.

[111] P. E. Powers, T. J. Kulp, and S. E. Bisson. Continuous tuning of a continuous-wave periodically poled lithium niobate optical parametric oscillator by use of a fan-out grating design. *Optics letters*, 23(3):159–161, 1998.

[112] Y. Petit, B. Boulanger, P. Segonds, and T. Taira. Angular quasi-phase-matching. *Phys. Rev. A*, 76:063817, Dec 2007.

[113] J.-P. Fève, O. Pacaud, B. Boulanger, B. Ménaert, J. Hellström, V. Pasiskevicius, and F. Laurell. Widely and continuously tunable optical parametric oscillator based on a cylindrical periodically poled $KTiOPO_4$ crystal. *Opt. Lett.*, 26(23):1882–1884, 2001.

[114] J.-P. Fève, B. Boulanger, B. Ménaert, and O. Pacaud. Continuous tuning of a microlaser-pumped optical parametric generator by use of a cylindrical periodically poled lithium niobate crystal. *Optics letters*, 28(12):1028–1030, 2003.

[115] Olivier Pacaud. *Oscillateurs paramétriques optiques basés sur des cristaux de géométrie cylindrique*. PhD thesis, Université Joseph Fourier - Grenoble 1, 2001.

[116] H. Ishizuki, I. Shoji, and T. Taira. Periodical poling characteristics of congruent MgO:$LiNbO_3$ crystals at elevated temperature. *Applied Physics Letters*, 82(23):4062–4064, 2003.

[117] Hideki Ishizuki and Takunori Taira. Large-aperture, axis-slant quasi-phase matching device using Mg-doped congruent $LiNbO_3$ [Invited]. *Opt. Mater. Express*, 1(7):1376–1382, 2011.

[118] X. Liang, J. Bartschke, M. Peltz, and J. A. L'huillier. Non-collinear nanosecond optical parametric oscillator based on periodically poled LN with tilted domain walls. *Applied Physics B*, 87(4):649–653, 2007.

[119] A. Fix and R. Wallenstein. Spectral properties of pulsed nanosecond optical parametric oscillators: experimental investigation and numerical analysis. *J. Opt. Soc. Am. B*, 13(11):2484–2497, Nov 1996.

[120] J. G. Haub, M. J. Johnson, A. J. Powell, and B. J. Orr. Bandwidth characteristics of a pulsed optical parametric oscillator: application to degenerate four-wave mixing spectroscopy. *Opt. Lett.*, 20(15):1637–1639, 1995.

[121] J. Saikawa, M. Fujii, H. Ishizuki, and T. Taira. 52 mJ narrow-bandwidth degenerated optical parametric system with a large-aperture periodically poled MgO:$LiNbO_3$ device. *Opt. Lett.*, 31(21):3149–3151, 2006.

[122] D. C. Hanna, B. Luther-Davies, R. C. Smith, and R. Wyatt. Cdse down-converter tuned from 9.5 to 24 mu m. *Applied Physics Letters*, 25(3):142–144, 1974.

[123] Ph. Kupecek, H. Le Person, and M. Comte. A multipurpose efficient tunable infrared coherent source with tuning range from 0.8 to 25 ÎŒm and peak powers in the range 50 to 200 kw. *Infrared Physics*, 19(3-4):263 – 271, 1979.

[124] 16 μm tunable source using parametric processes in non-linear crystals. *Optics Communications*, 23(1):37 – 43, 1977.

[125] K. L. Vodopyanov and P. G. Schunemann. Efficient difference-frequency generation of 7-20-μm radiation in $CdGeAs_2$. *Opt. Lett.*, 23(14):1096–1098, 1998.

[126] P. Canarelli, Z. Benko, R. Curl, and F. K. Tittel. Continuous-wave infrared laser spectrometer based on difference frequency generation in aggas2 for high-resolution spectroscopy. *J. Opt. Soc. Am. B*, 9(2):197–202, Feb 1992.

[127] O. Levi, T. J. Pinguet, T. Skauli, L. A. Eyres, K. R. Parameswaran, Jr. J. S. Harris, M. M. Fejer, T. J. Kulp, S. E. Bisson, B. Gerard, E. Lallier, and L. Becouarn. Difference frequency generation of 8-µm radiation in orientation- patterned gaas. *Opt. Lett.*, 27(23):2091–2093, Dec 2002.

[128] J. Saikawa, M. Miyazaki, M. Fujii, H. Ishizuki, and T. Taira. High-energy, broadly tunable, narrow-bandwidth mid-infrared optical parametric system pumped by quasi-phase-matched devices. *Opt. Lett.*, 33(15):1699–1701, 2008.

[129] S. H. Herman and N. P. Barnes. Method and apparatus for providing a coherent terahertz source, Nov 2000.

[130] J. Saikawa, M. Fujii, H. Ishizuki, and T. Taira. High-energy, narrow-bandwidth periodically poled Mg-doped $LiNbO_3$ optical parametric oscillator with a volume Bragg grating. *Opt. Lett.*, 32(20):2996–2998, 2007.

[131] Antoine Godard, Myriam Raybaut, Olivier Lambert, Jean-Pierre Faleni, Michel Lefebvre, and Emmanuel Rosencher. Cross-resonant optical parametric oscillators: study of and application to difference-frequency generation. *J. Opt. Soc. Am. B*, 22(9):1966–1978, Sep 2005.

[132] R.L. Herbst and R.L. Byer. Singly resonant CdSe infrared parametric oscillator. *Applied Physics Letters*, 21(5):189–191, 1972.

[133] W. L. Bond. Measurement of the refractive indices of several crystals. *Journal of Applied Physics*, 36(5):1674–1677, 1965.

[134] R. L. Herbst and R. L. Byer. Efficient Parametric Mixing in CdSe. *Applied Physics Letters*, 19(12):527–530, 1971.

[135] V. N. Malinko M. P. Lisitsa, L. F. Gudymenko and S. F. Terekhova. Dispersion of the refractive indices and birefringence of CdS_xSe_{1-x} single crystals. *Phys.Status Solidi*, 31:389–399, 1969.

[136] G.C. Bhar, D.C. Hanna, B. Luther-Davies, and R.C. Smith. Tunable down-conversion from an optical parametric oscillator. *Optics Communications*, 6(4):323 – 326, 1972.

[137] J. A. Weiss and L. S. Goldberg. Singly resonant CdSe parametric oscillator pumped by an HF laser. *Applied Physics Letters*, 24(8):389–391, 1974.

[138] G. C. Bhar. Refractive index interpolation in phase-matching. *Appl. Opt.*, 15(2):305–307, 1976.

[139] G. D. Boyd, E. Buehler, and F. G. Storz. Linear and nonlinear optical properties of $ZnGeP_2$ and CdSe. *Applied Physics Letters*, 18(7):301–304, 1971.

[140] M. A. Watson and M. V. O'Connor and D. P. Shepherd and D. C. Hanna. Synchronously pumped CdSe optical parametric oscillator in the 9–10 μm region. *Opt. Lett.*, 28(20):1957–1959, 2003.

[141] Y. Bao-Quan, L. Gang, Z. Guo-Li, M. Pei-Bei, J. You-Lun, and W. Yue-Zhu. Comparative investigation of long-wave infrared generation based on $ZnGeP_2$ and CdSe optical parametric oscillators. *Chinese Physics B*, 21(3):034213, 2012.

[142] A tunable infrared parametric oscillator in a cdse crystal. *Optics Communications*, 9(3):234 – 236, 1973.

[143] T. H. Allik, S. C., D. M. Rines, P. G. Schunemann, J. A. Hutchinson, and R. Utano. Tunable 7 12-μm optical parametric oscillator using a Cr,Er:YSGG laser to pump CdSe and $ZnGeP_2$ crystals. *Opt. Lett.*, 22(9):597–599, 1997.

[144] D. M. Rines, G. A. Rines, and P. F. Moulton. CdSe OPO Pumped by a 2.79 μm Cr,Er:YSGG Laser. In *Advanced Solid State Lasers*, page PO7. Optical Society of America, 1995.

[145] Y. Isyanova, G. A. Rines, D. Welford, and P. F. Moulton. Tandem OPO source generating 1.5-10-µm wavelengths. In *Advanced Solid State Lasers*, page OP10. Optical Society of America, 1996.

[146] A. Dhirani and P. Guyot-Sionnest. Efficient generation of infrared picosecond pulses from 10 to 20 µm. *Opt. Lett.*, 20(10):1104–1106, May 1995.

[147] Samvel Avanesov, Valeriy Badikov, Aleksey Tyazhev, Dmitrii Badikov, Vladimir Panyutin, Georgi Marchev, Galina Shevyrdyaeva, Konstantin Mitin, Frank Noack, Polina Vinogradova, Nadezhda Schebetova, Valentin Petrov, and Albert Kwasniewski. $Pbin_6te_{10}$: new nonlinear crystal for three-wave interactions with transmission extending from 1.7 to 25 μm. *Opt. Mater. Express*, 1(7):1286–1291, Nov 2011.

[148] J. D. Feichtner and G. W. Roland. Optical Properties of a New Nonlinear Optical Material: TI_3AsSe_3. *Appl. Opt.*, 11(5):993–998, 1972.

[149] Thierry Salva. *Elaboration et charactérisations de monocristaux de TI_3AsSe_3 matériau optique polyfonctionnel pour l'infrarouge*. PhD thesis, Université de Bourgogne, 1997.